The deep Critical Zone as a source of mineral nutrients to montane, temperate forest ecosystems

Dissertation

zur Erlangung des Grades eines

Doktors der Naturwissenschaften (doctor rerum naturalium)

am Fachbereich Geowissenschaften

der Freien Universität Berlin

vorgelegt von

David Uhlig

Berlin 2018

Erstgutachter:	Prof. Dr. Friedhelm von Blanckenburg (Freie Universität Berlin)
Zweitgutachter:	Prof. Dr. Wulf Amelung (Universität Bonn)
Tag der Disputation:	09.11.2018

Eidesstattliche Erklärung

Hiermit versichere ich, die vorliegende Dissertation selbstständig und ohne unerlaubte Hilfe angefertigt zu haben. Bei der Verfassung der Dissertation wurden keine anderen als die im Text aufgeführten Hilfsmittel verwendet. Beiträge von Koautoren zu publizierten und zur Publikation vorbereiteten Manuskripten sind im „Preface“ dieser Arbeit dargelegt. Ein Promotionsverfahren zu einem früheren Zeitpunkt an einer anderen Hochschule oder bei einem anderen Fachbereich wurde nicht beantragt.

Berlin, 30. Juli 2018

_____

David Uhlig

Danksagung

Zu Beginn danke ich meinem Doktorvater Prof. Dr. Friedhelm von Blanckenburg. Seine wissenschaftliche Kompetenz, fachliche Betreuung, inspirierenden Diskussionen, und seine stetige Unterstützung waren eine große Hilfe in der Anfertigung dieser Arbeit. Für sein Vertrauen, mich die vorliegende Dissertation eigenständig entwickeln und gestalten zu lassen, danke ich ihm sehr. Auch danke ich ihm für den Antrag des DFG-Projektes „Isotopengeochemische Bestimmung von Verwitterungs- Phosphorquellen und Phosphorflüssen in Waldökosystemen“, der DFG zur Förderung des Projektes (Förderkennzeichen: BL 562/14-1) und den Kollegen im SPP 1685 für ihre Unterstützung.

Ein besonderer Dank gilt Dr. Jan A. Schüssler für seine Unterstützung zur Entwicklung massenspektrometrischer Messmethoden und seiner unermüdlichen Arbeit zur Instandhaltung der Neptune. Ebenso danke ich ihm für wissenschaftliche Diskussionen. Weiterer Dank gilt Dr. Hella Wittmann-Oelze für die organisatorische Hilfe zur Analyse von ^{10}Be und ^{9}Be. Dr. Geerke Floor danke ich für die Unterstützung zur Entwicklung einer Messmethode für ^{9}Be in Pflanzen mit der iCAP-Q.

Den Technikerinnen Jutta Schlegel, Josi Buhk und Cathrin Schulz danke ich für die Reinigung unzähliger Verbrauchsmaterialen, Apex, der Instandhaltung der ICP-OES sowie der unterhaltenden Gespräche während stupider Laborarbeit. Darüber hinaus danke ich Dipl.-Min. Rudolf Naumann und Andrea Gottsche für RFA und RDA sowie der Analyse von S und C. Weiterhin danke ich den Mitarbeitern des von der Universität Köln betriebenen AMS für die Messung von ^{10}Be.

Meinen aktuellen und ehemaligen Kollegen und Mitdoktoranden der Arbeitsgruppe für die Geochemie der Erdoberfläche danke ich für anregende Diskussionen. Besondere Aufmerksamkeit verdienen Dr. Nadine Dannhaus, M.Sc. Hanna Haedke, und Dr. Marcus Oelze, mit welchen ich stets fachliche Diskussionen und aufmunternde Gespräche führen konnte. Dr. Maja Tesmer danke ich für immerwährende aufbauende Worte sowie ihrer Hilfe zur Genehmigung der Kernbohrung im Bayerischen Wald. M.Sc. René Kapannusch danke ich für seine Masterarbeit in meinem Doktorarbeitsprojekt und der damit einhergehenden Feld- und Laborarbeiten. Für Feld- und Laborarbeiten im Rahmen des Sierra Nevada Projektes danke ich Dr. Julien Bouchez und Dr. Jean L. Dixon. Dr. Patrick Frings, Dr. Michael Henehan sowie Prof. Dr. Friedericke Lang danke ich für die kritische Auseinandersetzung meiner Manuskripte. Prof. Dr. Wulf Amelung und Kollegen danke ich für die Analyse und Bereitstellung von P Konzentrationen (Hedley Methode) und fachlichen Diskussionen.

Abschließend danke ich meinen Eltern, die mit der Finanzierung des Grundstudiums den Grundstein meiner akademischen Laufbahn gelegt haben. Ihnen und meiner Schwester danke ich auch für die ausdauernde Geduld, Verständnis und seelische Motivation. Weiteren Rückhalt erfuhr ich von meinen Sportsfreunden im SSV Rotation Berlin. Zu guter Letzt danke ich dem engsten Freund und Begleiter meiner Promotion, Daniel Kirchhof für bierselige Abende mit tiefgründigen Gesprächen.

Summary

Forest ecosystems persist over thousands of years. The prevailing paradigm describes how a tight nutrient re-utilisation loop (recycling) from organic matter stored in the forest floor into trees ensures forest ecosystem nutrition. However, these nutrients are constantly lost by drainage during storage on the forest floor. This nutrient loss must be balanced on the long-term, because otherwise ecosystems would run into a deficit of mineral nutrients. In supply-limited weathering regimes, which are often found in non-eroding, well-drained settings, chemical weathering has run to completion and the nutrient loss from the forest floor is counterbalanced by external atmospheric wet and dry deposition. In kinetically limited weathering regimes, which are often found in eroding, temperate settings, the regolith (comprising soil, saprolite and weathered rock) still contains mineral nutrients, as mineral dissolution kinetics are slower than the advection of minerals from deep, unweathered rock to the Earth's surface. At the surface, minerals and plant litter are removed by erosion. The mechanisms by which forest ecosystem nutrition is maintained in the face of these losses is the topic of this thesis. I explore the role of the deeper regolith and the mechanisms and fluxes by which this deep reservoir serves to sustain ecosystems over the long-term. I use geochemical mass balances and innovative metal isotope proxies to derive fluxes and sources from rock weathering into forest trees in montane, eroding and temperate forest ecosystems.

How montane, temperate forest ecosystems are nourished was explored at two study sites in the Schwarzwald (site CON) and the Bayerischer Wald (site MIT). Both sites are underlain by paragneiss of contrasting mineralogy, mantled by Cambisols developed on periglacial slope deposits and covered by *Fagus sylvatica* and *Picea abies*. At both sites I quantified nutrient availability, nutrient accessibility, fluxes of nutrient supply by chemical weathering, and nutrient uptake by forest trees. The regolith at site CON experienced substantially more nutrient loss through chemical weathering than at site MIT. Nevertheless, nutrient uptake fluxes from forest trees are virtually identical at both sites. Considering a forest ecosystem in a mass balance comprising a shallow `organic nutrient cycle´ and a belowground `geogenic nutrient pathway´ shows that the nutrient inventory in the forest floor is of finite size that lasts only for decades, because persistent nutrient loss through plant litter drainage and erosion occurs from the forest floor. This permanent nutrient loss is balanced by fluxes from a reservoir consisting of the biologically available fraction (water-soluble and easily exchangeable fractions for the metal elements, and exchangeable and calcium-bound phosphorus fractions for phosphorus) from the upper regolith (<3 m), and even more significantly from the deep regolith (>3 m). This reservoir of nutrients ensures forest ecosystem nutrition over millennia, because it can replace the nutrient loss from the forest floor and is continually replenished through chemical weathering. Supply from this deep reservoir is linked to the organic nutrient cycle which is regulated by uptake into forest trees through

the adjustment of the number of nutrient re-utilisation cycles from plant litter depending on nutrient supply fluxes. Thus, uniform uptake of mineral nutrients emerges despite large differences in their release through rock weathering.

With this new concept in mind I constrained the uptake depth of the most plant-essential mineral nutrient phosphorus (P). While biologically accessible P forms, namely exchangeable P, are negligible throughout the regolith, the Ca-bound P, biologically available as PO_4^{3-} through mineral dissolution, increases with depth and dominates in the lower part of the regolith and in unweathered rock. To test whether this deep P and other mineral nutrients from this depth are utilised by trees, I applied isotopic tracing methods. To track the depth of nutrient uptake radiogenic Strontium (Sr), namely the $^{87}Sr/^{86}Sr$ ratio, an established isotope proxy for source tracing was used together with the first application of the meteoric cosmogenic Beryllium (Be) isotope system, namely $^{10}Be_{meteoric}/^{9}Be_{stable}$. From the agreement in these isotope ratios between plant tissue and the forest floor´s biologically accessible fraction I demonstrate that these elements, and by inference also P and other mineral nutrients, are turned over between the forest floor and trees. I also show that these elements initially originate from the lower part of the regolith. Because this depth lies beyond reported rooting depths of the prevalent tree species it is speculated that nutrient uplift occurs through a combination of root-mycorrhiza symbiosis, dimorphic root systems and capillary rise of pore water.

Nutrient export after rock weathering was explored in the montane, temperate forest ecosystems of the Southern Sierra Critical Zone Observatory, California, underlain by granodiorite bedrock, mantled by Entisols and Inceptisols and covered mainly by *Pinus ponderosa*. Magnesium (Mg) stable isotopes are sensitive indicators of Mg utilisation by biota. Mg utilisation takes place from up to 6 m depth, as evidenced by the light Mg isotopic composition of the easily exchangeable fraction. It was further found that trees, in particular wood, are isotopically heavy, whereas stream water is isotopically light. Converting this difference into a mass balance shows that 50-100 % of the Mg released by chemical weathering is utilised by trees. From the comparison between the river dissolved fluxes of other plant-essential and plant-beneficial elements (K, Ca, P and Si) with their weathering release fluxes a deficit is found in the river dissolved fluxes that is attributed to nutrient uptake by forest trees. Thus, either the mineral nutrients are accumulating today in re-growing forest biomass after clear cutting, or they are exported in plant litter and coarse woody debris, rather than appearing in drainage.

The two major outcomes of this thesis are that the permanent nutrient loss at the Earth surface by plant litter drainage and erosion is balanced by nutrient uptake from the deep regolith, and that erosion and weathering are coupled through nutrient uptake at depth and erosion of these nutrients in plant debris at the surface.

Zusammenfassung

Waldökosysteme überdauern Tausende von Jahren. Das gegenwärtige Paradigma zur Ernährung von Waldökosystemen besagt, dass deren Ernährung durch die Wiederaufnahme von Mineralnährstoffen aus im Waldboden lagernder Pflanzenstreu und deren Zersetzungsprodukten gewährleistet wird. Während der Lagerung von Pflanzenstreu kommt es jedoch durch Auflösung kontinuierlich zu Nährstoffverlusten. Damit Waldökosysteme langfristig kein Nährstoffdefizit erleiden, müssen diese Nährstoffverluste kompensiert werden. In verfügbarkeitslimitierten Verwitterungsregimen, die in nicht-erodierenden und gut-drainierten Gebieten vorkommen, sind die Böden durch intensive chemische Verwitterung nährstoffverarmt, sodass stetige Nährstoffverluste nur durch atmosphärische nasse und trockene Deposition kompensiert werden können. In kinetisch limitierten Verwitterungsregimen, die häufig in erodierenden, gemäßigten Klimazonen vorkommen, enthält der Regolith (bestehend aus Boden, Saprolith und verwittertem Gestein) jedoch noch reichlich Mineralnährstoffe, weil die Mineralauflösungskinetik langsamer ist als der Transport von Mineralen aus der Tiefe an die Erdoberfläche durch Erosion erfolgt. An der Erdoberfläche gehen Minerale und Pflanzenstreu durch Erosion verloren. In der vorliegenden Dissertation befasse ich mich mit den Mechanismen, durch die die Ernährung von Waldökosystemen angesichts dieser Nährstoffverluste dauerhaft gewährleistet werden kann. Dafür ermittelte ich den Einfluss des tiefen Regoliths auf die Waldökosystemernährung sowie die Mechanismen und Stoffflüsse, mit denen dieses tiefe Reservoir zur Nährstoffversorgung eines Waldökosystems beiträgt. Ich wendete geochemische Massenbilanzen und innovative Metallisotopenproxies an, um Nährstoffflüsse und -quellen aus der Gesteinsverwitterung für Bäume in gebirgigen, erodierenden und gemäßigten Waldökosystemen abzuleiten.

Die Ernährung von Waldökosystemen dieser Art wurde an zwei Untersuchungsstandorten im Schwarzwald (Standort CON) und im Bayerischen Wald (Standort MIT) untersucht. An beiden Standorten liegt als Grundgestein Paragneis unterschiedlicher Mineralogie vor, auf dem sich Braunerden aus periglazialen Deckschichten entwickelt haben. *Fagus sylvatica* (Buche) und *Picea abies* (Fichte) stellen die dominierende Pflanzenspezies beider Standorte dar. An beiden Standorten quantifizierte ich die Nährstoffverfügbarkeit, Nährstoffzugänglichkeit, Nährstoffzufuhr durch chemische Verwitterung und Nährstoffaufnahme der Bäume. Während die Nährstoffverluste im Regolith durch chemische Verwitterung am Standort CON wesentlich größer sind als am Standort MIT, sind die Nährstoffaufnahmeflüsse von Bäumen an beiden Standorten nahezu identisch. Die Betrachtung eines Waldökosystems in einer Massenbilanz, bestehend aus einem oberflächennahen „organischen Nährstoffkreislauf“ an der Waldoberfläche und einem „geogenen Nährstoffweg“ im tiefen Regolith, verdeutlicht, dass der Nährstoffbestand des Waldbodens eine endliche Größe darstellt,

die nur über Jahrzehnte ein Waldökosystem ernähren kann. Grund hierfür sind die kontinuierlichen Nährstoffverluste des Waldbodens durch Erosion und Entwässerung von Pflanzenstreu. Dieser permanente Nährstoffverlust wird durch Stoffflüsse aus einem Reservoir ausgeglichen, welches aus biologisch verfügbaren Nährstoffen besteht – gemeint sind wasserlösliche und leicht austauschbare Fraktionen von Metallelementen und austauschbare sowie Calcium-gebundene Fraktionen von Phosphor – und sich im oberen Regolith (<3m) und noch deutlicher im tiefen Regolith (>3m) befindet. Dieses Nährstoffreservoir gewährleistet die Ernährung des Waldökosystems über Jahrtausende, da es den Nährstoffverlust aus dem Waldboden ersetzen kann und durch chemische Verwitterung kontinuierlich aufgefüllt wird. Die Nährstoffversorgung aus diesem tiefen Reservoir ist insofern mit dem organischen Nährstoffkreislauf verbunden als dass die Anzahl der Nährstoffwiederaufnahmezyklen aus der Pflanzenstreu in die Bäume in Abhängigkeit der Nährstoffzuflüsse aus dem Tiefenreservoir reguliert wird. Durch diesen Mechanismus lassen sich gleichförmige Nährstoffaufnahmeflüsse von Bäumen trotz großer Unterschiede in ihrer Freisetzung durch Gesteinsverwitterung erklären.

Auf der Grundlage dieses neuen Konzeptes zur Waldökosystemernährung untersuchte ich die Aufnahmetiefe des essenziellsten Mineralnährstoffs Phosphor (P). Während der Gehalt biologisch zugänglicher P-Formen (austauschbares P) im gesamten Regolith vernachlässigbar gering ist, nimmt der Gehalt Ca-gebundenen P, das durch Mineralauflösung biologisch verfügbar wird, mit der Tiefe zu und stellt im unteren Teil des Regoliths sowie in unverwittertem Gestein die vorherrschende P-Form dar. Um nachzuweisen, ob P und andere Mineralnährstoffe tatsächlich aus dieser Tiefe von Bäumen aufgenommen werden, benutzte ich Isotopenverhältnisse als Fingerabdrücke. Dafür nutzte ich einerseits einen etablierten Isotopenproxy des Elements Strontium (Sr), nämlich das radiogene Strontiumverhältnis $^{87}Sr/^{86}Sr$, und andererseits das auf diese Art erstmals angewandte Isotopensystem des Elements Beryllium (Be), nämlich das meteorische kosmogene Berylliumverhältnis $^{10}Be_{meteorisch}/^{9}Be_{stabil}$. Aus der Übereinstimmung der Isotopenverhältnisse zwischen Pflanzengewebe und der biologisch zugänglichen Fraktion des Waldbodens wies ich nach, dass diese Elemente und damit auch P und andere Mineralnährstoffe zunächst vom Waldboden von den Bäumen aufgenommen werden. Darüber hinaus wies ich ebenso nach, dass diese Elemente ursprünglich aus dem unteren Teil des Regoliths stammen. Da diese Tiefe jenseits der bislang bekannten Wurzeltiefe der vorherrschenden Baumspezies liegt, mutmaße ich, dass ein „Hochpumpen“ der Nährstoffe aus der Tiefe an die Erdoberfläche durch eine Kombination aus symbiotischen Beziehungen von Wurzeln mit Mykorrhizen, dimorphen Wurzelsystemen und dem Kapillaranstieg von Porenwasser erfolgt.

Der Nährstoffexport infolge von Gesteinsverwitterung wurde fernerhin in dem gebirgigen, gemäßigten Waldökosystem des Southern Critical Zone Observatory in Kalifornien untersucht. Dieser Untersuchungsstandort ist durch die Lithologie Granodiorit und die Bodentypen Entisol und Inceptisol

charakterisiert und ist von einem Wald mit der Hauptspezies *Pinus ponderosa* (Kiefer) bedeckt. Stabile Isotope von Magnesium (Mg) sind empfindliche Indikatoren für die Aufnahme von Mg durch Vegetation. Die Aufnahme von Mg durch Pflanzen findet in einer Tiefe von bis zu sechs Metern statt und wird durch die leichte Mg-Isotopenzusammensetzung der leicht-austauschbaren Fraktion belegt. Weiterhin wies ich nach, dass Bäume, insbesondere deren Holz, isotopisch schwer sind, wohingegen Flusswasser isotopisch leicht ist. Diese Differenz habe ich in eine Massenbilanz übertragen, die zeigt, dass 50 bis 100 Prozent des durch chemische Verwitterung freigesetzten Mg von Bäumen aufgenommen werden. Aus dem Vergleich der in Flusswasser gelösten Stoffflüsse von anderen pflanzenessentiellen und pflanzennützlichen Elementen (K, Ca, P und Si) mit ihren chemischen Freisetzungsflüssen aus der Gesteinsverwitterung identifizierte ich ein Defizit in den in Flusswasser gelösten Stoffflüssen, welches ich der Nährstoffaufnahme durch Bäume zuschrieb. So akkumulieren sich Mineralnährstoffe heute entweder in nachwachsender Waldbiomasse infolge einer Waldrodung oder sie werden in Pflanzenstreu und Totholz erodiert, anstatt in den gelösten Flussfrachten zu erscheinen.

Die beiden bedeutsamsten Ergebnisse dieser Dissertation sind, dass der permanente Nährstoffverlust an der Erdoberfläche durch Entwässerung und Erosion von Pflanzenstreu durch Nährstoffaufnahme aus dem tiefen Regolith ausgeglichen wird, und dass Erosion und chemische Verwitterung durch Nährstoffaufnahme in der Tiefe und Erosion von Nährstoffen in Pflanzenstreu und Totholz an der Erdoberfläche miteinander verbunden sind.

Preface

In this dissertation I present an introductory chapter and three further chapters prepared as journal manuscripts. Each manuscript is either published or in the final stage of preparation for submission to a scientific journal. Here I briefly summarise the contents of the manuscripts and the contributions of the co-authors.

- **Chapter 1** presents a general introduction into forest ecosystem nutrition over short (decadal) and long (millennia) timescales. It provides an overview of the isotope systems, fluxes into, from and within forest ecosystems, and sequential extraction methods used in this thesis.

- **Chapter 2** reports on the presence of a deep (>3 m) and large reservoir of biologically available mineral nutrients that is suggested to balance the permanent nutrient loss from the forest floor of slowly eroding and well-drained forested hillslopes in the German Schwarzwald (Conventwald) and the Bayerischer Wald (Mitterfels). This reservoir ensures forest ecosystem nutrition over millennia. A manuscript entitled "*How slow rock weathering balances nutrient loss during fast forest floor turnover in montane, temperate forest ecosystems*" is in the final stage of preparation for submission. Friedhelm von Blanckenburg is the sole co-author.

  Measurements of the fluxes, inventories and turnover times of mineral nutrients provide evidence for the fast turnover of mineral nutrients at the forest floor (referred to as `organic nutrient cycle´) that experiences permanent nutrient loss by erosion and drainage. A deep (>3 m) and large reservoir of biologically available mineral nutrients (referred to as a `geogenic nutrient pathway´) is coupled to the organic nutrient cycle, and thereby balances nutrient loss over millennia as it is continuously replenished by slow rock weathering. The organic nutrient cycle adjusts its tightness according to the replenishment fluxes from the deep geogenic nutrient pathway.

  Regolith sampling from 0-3 m depth was assisted by René Kapannusch (GFZ-Potsdam) and Jakob Sohrt (University of Freiburg). Core drilling was conducted by "BOG Bohr- und Umwelttechnik GmbH". XRF and XRD analyses were performed by Rudolf Naumann. Phosphorus Hedley sequential fractionation data was obtained from Andrej Rodionov and Sara Bauke at the Institute for Soil Science and Soil Ecology, INRES, University of Bonn. I conducted the drilling campaigns, sample preparation, sequential extractions, ICP-OES analyses, $^{87}Sr/^{86}Sr$ analyses, soil pH measurement, processing of bedload sediment for *in situ* ^{10}Be analyses, and data evaluation. I interpreted data and wrote the manuscript with input from Friedhelm von Blanckenburg. Figure 2-1 was designed by Manuela Dziggel (GFZ-Potsdam). This chapter was conducted within the framework of the SPP 1685 "Ecosystem Nutrition".

- **Chapter 3** reports isotope geochemical evidence for the uplift and replenishment of the most plant-essential mineral nutrient P from a deep (2-17m) reservoir of biologically accessible P in the German Schwarzwald (Conventwald) and the Bayerischer Wald (Mitterfels). A manuscript entitled "*Phosphorus supply by deep rock weathering sustains temperate forest ecosystem functioning*" is in the final stage of preparation for submission. Co-authors are Wulf Amelung (Institute for Soil Science and Soil Ecology, INRES, University of Bonn) and Friedhelm von Blanckenburg.

  This study builds on chapter 2 by focussing on the replenishment of the often plant-growth limiting mineral nutrient P. Uplift of deep weathered rock is suggested to balance losses from the leaky forest floor. The depth distribution of calcium-bound P in combination with the comparison of the isotope ratios $^{87}Sr/^{86}Sr$ and $^{10}Be_{(meteoric)}/^{9}Be$ between plant tissue and the regolith reveals that P utilised by forest trees originates from several meters depth, where primary phosphate minerals are still present.

  I supplemented the dataset of chapter 2 with $^{87}Sr/^{86}Sr$ on the biologically available fraction and $^{10}Be/^{9}Be$, both of which are analysed and evaluated by me. I interpreted the data and wrote the manuscript with support from Friedhelm von Blanckenburg, who designed the study, and Wulf Amelung (Institute for Soil Science and Soil Ecology, INRES, University of Bonn).

- **Chapter 4** reports on the coupling between erosion at the surface and chemical weathering at depth through biogenic nutrient uptake. This manuscript is published in *Biogeosciences* ('Quantifying nutrient uptake as driver of rock weathering in forest ecosystems by magnesium stable isotopes' by David Uhlig, Jan A. Schuessler, Julien Bouchez, Jean L. Dixon and Friedhelm von Blanckenburg; doi.org/10.5194/bg-14-3111-2017).

  From the partitioning of Mg stable isotopes in the compartments of the Critical Zone (Southern Sierra Critical Zone Observatory, USA) I estimated that 50-100 % of Mg released from rock weathering is taken up from up to 6 m depth by forest trees. The comparison of the dissolved elemental fluxes in rivers with the elemental solubilisation fluxes from rock reveals a deficit in the dissolved flux that I attribute to nutrient utilisation by forest trees without return into the drainage. This deficit is either stored in biomass re-growing after logging or is eroded as coarse woody debris.

  This study was designed by Friedhelm von Blanckenburg. Field work was conducted by Jan A. Schuessler, Julien Bouchez, Jean L. Dixon and Friedhelm von Blanckenburg. Samples were analysed by Jan A. Schuessler, Julien Bouchez and me. I interpreted data and wrote the manuscript with input from all co-authors. Figure 4-1 was designed by Manuela Dziggel (GFZ-Potsdam). This manuscript was reviewed by two anonymous reviewers.

Table of contents

1 Introduction

The thin, dynamic, habitable, but fragile skin of the Earth, the zone where air, rock, and water meet and interact to enable life is called the “Critical Zone” of the Earth (e.g. Brantley et al. 2007; Chorover et al. 2007). This zone is defined to extend from the top of the vegetation canopy, through the regolith comprising mobile soil, immobile saprolite and weathered bedrock down to the upper boundary of groundwater and to the lower boundary of unweathered parent bedrock (Chorover et al. 2007; Lin 2010; Riebe et al. 2017). At the timescales of minutes to millennia, physical, chemical and biological reactions shape the Critical Zone. A prominent component that reacts sensitively to the environmental state of the Critical Zone is a forest ecosystem, which grows and recedes with glacial and interglacial cycles (Birks and Birks 2004). Forest ecosystems shape the Critical Zone as they emerge along interfaces of the Critical Zone´s spheres (Figure 1-1), and thus combine a suite of geomaterials such as various gases, fluids and solids that contain nutrients for plant growth.

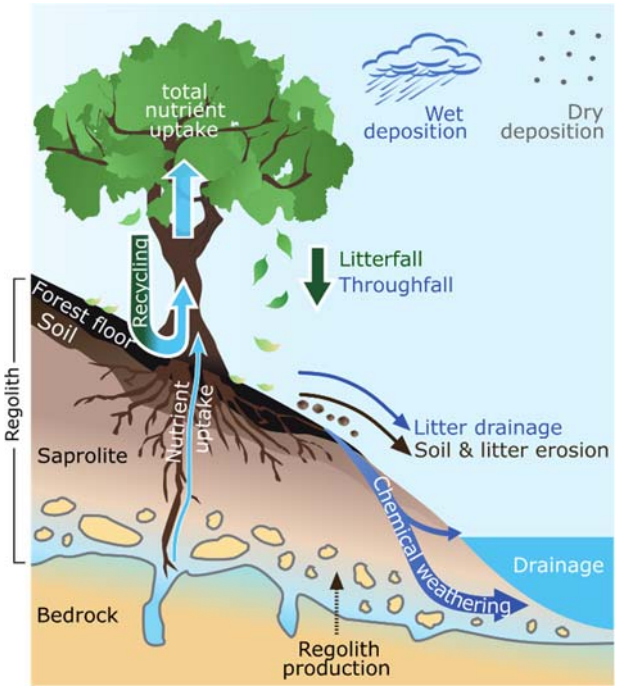

Figure 1-1 Schematic illustration of a montane forest ecosystem showing the vertical structure of the weathering zone and inbound, outbound and internal nutrient fluxes. Figure is not drawn to scale.

The relevance of nutrients to the physiological needs of higher plants can be divided into three categories of nutrients: Macronutrients (nitrogen (N), potassium (K), calcium (Ca), magnesium, (Mg), phosphorus (P), sulphur (S)), micronutrients (iron (Fe), manganese (Mn), copper (Cu), zinc (Zn), nickel (Ni), molybdenum (Mo), boron (B), chlorine (Cl)) and plant-beneficial elements (aluminium (Al), silicon

(Si), cobalt (Co), selenium (Se), sodium (Na)) (Marschner 2011). The most plant-essential mineral nutrient is P. Phosphorus often limits primary productivity in terrestrial ecosystems (Elser et al. 2000, 2007), because P fulfils diverse functions in all living organisms, yet occurs only in trace amounts of about 700 µg/g in the upper continental crust (Taylor and McLennan 1995). Moreover, the accessibility of P to forest trees declines with `soil age' (a term that is only applicable for static geomorphic surfaces). With soil age P is transformed from readily biologically accessible Ca-bound P, such as apatite, into biologically accessible non-occluded P (easily exchangeable fraction), less biologically accessible organic-bound P, and biologically inaccessible occluded P (Walker and Syers 1976; Crews et al. 1995). In the latter case, P is irreversibly adsorbed to Al and Fe sesquioxide clays (Brady and Weil 2002).

Forest ecosystems are open systems with respect to mineral nutrient transport pathways as nutrients are acquired and permanently lost. Mineral nutrients are gained either from local or external sources. Mineral nutrients from local sources derive mainly from primary minerals hosted in parent bedrock and regolith that are liberated and supplied to forest trees by chemical weathering (Figure 1-1) – a process that operates over millennia. External sources are atmospheric depositions either as solutes (wet deposition) or as particulates (dry deposition) (Figure 1-1), where dry deposition is derived mainly from anthropogenic emissions, desert dust or biogenic particles (e.g. Mahowald et al. 2008; Tipping et al. 2014). External wet deposition is augmented when passing through the leaf canopy and bark and its chemical composition is modified through leaching processes. Thus, apart from litterfall, wet deposition via throughfall (Figure 1-1) and stemflow contributes to nutrient return from the forest tree to the forest floor (e.g. Wilcke et al. 2002). Mineral nutrients returned to the forest floor can be lost from forest ecosystems by the drainage of decomposed and solubilised plant litter (Figure 1-1), and in sloping settings by erosion of plant litter (e.g. Scatena and Lugo 1995; Heartsill Scalley et al. 2012) (Figure 1-1).

1.1 Short-term forest ecosystem nutrition

The internal fluxes of nutrients in forest ecosystems – such as nutrient uptake into forest trees and nutrient return via throughfall, stemflow and litterfall to the forest floor – are generally large, relative to nutrient input and output fluxes (e.g. Cole and Rapp 1981; Attiwill and Adams 1993). For example, the largest turnover of mineral nutrients in forest ecosystems occurs within the forest floor that, particularly in tropical rain forests, provides the highest amount of biologically available nutrients (Cuevas and Medina 1986; Grubb 1995; Kauffman et al. 1998). Thus, on the short timescale (years) the predominant nutrient acquisition strategy of forest trees is to tighten the element cycles to minimise water-bound nutrient loss (Jordan et al. 1980; Jordan 1982; Jobbágy and Jackson 2001, 2004; Riotte et al. 2014; Lang et al. 2016; Wilcke et al. 2017). This process is often called nutrient recycling and involves nutrient re-utilisation from organic matter after plant litter decomposition, solubilisation and

mineralisation (e.g. Swift et al. 1979; Cadisch and Giller 1997; Jobbágy and Jackson 2004; Cleveland et al. 2006; Buendía et al. 2010; Wilcke et al. 2017). However, organic-bound nutrients cannot be utilised directly by plants (George et al. 2011; Jansa et al. 2011). For this reason, mycorrhizal fungi and other decomposing organisms such as earthworms (Wardle et al. 2004b) promote the breakdown of organic matter into plant-accessible inorganic forms that are utilisable by tree roots.

1.2 Long-term forest ecosystem nutrition

In response to the periodic variation of the parameters of the Earth´s orbit around the Sun (Milankovitch cycles) the Northern Hemisphere experienced recurrent glacial-interglacial, or cold-stage/ warm-stage cycles throughout the Pleistocene. Consequently, forest ecosystems in the Northern Hemisphere persist at least over the millennia of an interglacial (Birks and Birks 2004). In contrast, palynological evidence suggests that some tropical rainforests, such as those in India, survived as `Plant Refugia´ (Farooqui et al. 2010) throughout the Pleistocene, thus over a few millions of years, whereas shifts in the distribution and composition of, for example, the Amazon rainforest (representing the best studied tropical forest) during the Pleistocene cold stages are more ambiguous (Colinvaux 1987, 1997; van der Hammen and Absy 1994; Colinvaux et al. 1996; Hooghiemstra 1997). Thus, regardless of the shifts in ecosystem properties with climate, forest trees must have developed nutrient acquisition strategies to ensure forest ecosystem nutrition over thousands to millions of years; cycles that supplement short-term nutrient recycling from organic matter. Such strategies depend on the properties of the prevailing weathering regime. Two endmember weathering regimes with entirely different vectors of nutrient supply are known, namely supply-limited weathering regimes (e.g. Riebe et al. 2004; West et al. 2005; Dixon and von Blanckenburg 2012) and kinetically limited weathering regimes (e.g. Stallard and Edmond 1983; West et al. 2005; Dixon and von Blanckenburg 2012).

Supply-limited weathering regimes are typically found in the tropical belt that experienced neither Quaternary glaciation nor periglacial processes, and are located in tectonically quiescent landscapes, where erosion rates are low or non-existent. In such landscapes primary minerals can have soil residence times of up to millions of years so that chemical weathering results in complete dissolution of primary minerals. The transformation of Ca-bound P into organic-bound P, occluded P and some non-occluded P is also complete (Crews et al. 1995). If in such landscapes nutrient supply by exogenous nutrient inputs is less than nutrient loss by seepage and transformation of P into biologically inaccessible forms, plant growth will be limited particularly by the mineral nutrient P (Vitousek and Farrington 1997; Tanner et al. 1998; Porder et al. 2007; Vitousek et al. 2010; Menge et al. 2012; Augusto et al. 2017). However, in supply-limited weathering regimes nutrient supply by dilute sea aerosols (Newman 1995; Kennedy et al. 1998; Chadwick et al. 1999; Whipkey et al. 2000) or atmospheric dust from, for example, the Sahara or Asian deserts, contributes substantially to

ecosystem nutrition (e.g. Chadwick et al. 1999; Boy and Wilcke 2008; Mahowald et al. 2008; Aciego et al. 2017; Arvin et al. 2017).

Kinetically limited weathering regimes are found in montane landscapes of temperate and tropical climate. Such landscapes are characterised by soil residence times that range from a few hundred years in rapidly uplifting collisional mountain belts (e.g. the Himalaya) to a few hundred kiloyears in inactive mountain belts (e.g. the Appalachians). In this regime the upward transport of primary minerals from depth (weathering front) to the eroding Earth surface (organic soil) is sufficiently fast for primary minerals in topsoil to remain undissolved. Hence, fresh minerals advect into the rooting zone, which is thereby continuously replenished by mineral nutrients (Porder et al. 2007). Such uplift has also been suggested to be caused by plants, demonstrated by the concentration increase of the easily exchangeable fraction from subsoil to shallow soil (Jobbágy and Jackson 2004). Importantly, exogenous inputs into forest ecosystems in kinetically limited weathering regimes play a minor role to forest ecosystem nutrition, when their supply fluxes are low compared to long-term nutrient supply through chemical weathering (Aciego et al. 2017). While erosion causes the advection of mineral nutrients into topsoil, it also causes the removal of organic-bound nutrients, such as N. For this reason and because soil in temperate forest ecosystems on the Northern Hemisphere was rejuvenated through the geomorphic processes resulting from Quaternary glaciation and periglacial processes, plant growth in temperate forest ecosystems is often limited by N (e.g. Vitousek and Farrington 1997; Tanner et al. 1998; Menge et al. 2012). Even though in the kinetically limited setting nutrient-containing primary minerals are present in sufficient abundance, they are not always directly accessible to trees. Tree roots have thus developed acquisition strategies to access such nutrients. For example, forest trees utilise barely accessible nutrients through the symbiosis of roots with mycorrhizal fungi that can penetrate directly into minerals, such as feldspars and hornblende (Jongmans et al. 1997), apatite for P acquisition (Smits et al. 2012) or biotite for K acquisition (Balogh-Brunstad et al. 2008; Bonneville et al. 2009). Roots can also excrete weathering agents, such as low molecular weight organic acids (carboxylates) into the rhizosphere (Landeweert et al. 2001; Brantley et al. 2011) to enhance mineral dissolution kinetics. A further nutrient acquisition strategy of roots is to extend the rooting zone by the development of carboxylate excreting cluster roots (Lambers et al. 2008).

1.3 Constraining the research question and defining the main objectives

Despite these acquisition strategies and the ability of forest trees to retain nutrients in the ecosystem by recycling, the question arises whether the ensemble of these strategies suffices to ensure forest ecosystem nutrition over the timescale of millennia. Thus, the overarching question of this thesis is whether these acquisition strategies can compensate for the permanent nutrient loss via seepage, plant litter dissolution and loss into drainage, and plant litter erosion in eroding landscapes. More

specifically, my first question is whether this compensation could be ensured by nutrient uptake either from a nutrient-rich reservoir at depth (considering the uplift of fresh minerals from depth in eroding landscapes) or even from the weathering front, where most chemical weathering takes place and liberates nutrients in a form that is accessible to forest trees. If that is the case, my second question is whether nutrients that are multiple times returned via litterfall to the forest floor and re-utilised from plant litter have their ultimate source at these depths. My final question is whether nutrients leave a forest ecosystem as solutes or in particulate form. To explore these questions I use geochemical methods to quantify total mass fluxes and nutrient fluxes; apply three different isotope systems comprising radiogenic isotope ratios of strontium (Sr), the cosmogenic radionuclide beryllium (Be), and stable isotopes of magnesium (Mg), and assess the accessibility of nutrients to forest trees by sequential extractions.

1.4 Geochemical methods

1.4.1 Total mass loss fluxes from forest ecosystems

Consider a weathering profile on the hillslope of a montane and well-drained setting. The vertical structure comprises soil underlain by saprolite, beneath which weathered bedrock overlies unweathered parent bedrock. Here, soil, saprolite and weathered rock are collectively referred to as regolith (Figure 1-1). The thickness of the regolith is constant over time if regolith production (RP) is balanced by regolith mass loss (Heimsath et al. 1997, 1999, 2006; Lebedeva et al. 2010). In this case, the landscape's lowering rate, i.e. total denudation (D), represents the absolute mass loss flux from the weathering profile that consists of a particulate component, namely physical erosion (E), and a dissolved component, namely chemical weathering (W). Landscape lowering rates are typically reported in units of either length per time (e.g. mm kyr^{-1}) or mass per area per time (e.g. t km^{-2} yr^{-1}). The catchment-wide denudation rate integrates mass loss over the entire catchment area over timescales of about 10^3 to 10^5 years and can be quantified by measuring the concentration of cosmogenic nuclides such as $^{10}Be_{in\ situ}$ in quartz from bedload sediment, sampled at the outlet of the watershed (e.g. Granger et al. 1996; Riebe et al. 2000, 2004; von Blanckenburg 2005; Binnie et al. 2007; Norton et al. 2011). To disentangle the proportions of mass loss from a forest ecosystem by chemical weathering (occurring along the entire regolith) and physical erosion (from the surface) the degree of chemical depletion of the regolith must be quantified and multiplied by total denudation. A measure of the degree of chemical alteration of the regolith relative to parent bedrock is the chemical depletion fraction (CDF, Riebe et al. (2003)). The CDF is the concentration ratio of a refractory element (e.g. Zr, Nb, Ti) in regolith relative to parent material. These elements are hosted mostly in inert minerals and are concentrated in weathered material relative to parent bedrock by the loss of more soluble elements (Brimhall and Dietrich 1987). Since total denudation is the sum of chemical weathering and

physical erosion, the total particulate mass loss flux by physical erosion can be calculated by simple mass balance.

1.4.2 Elemental chemical release fluxes in forest ecosystems

Total mass fluxes can be converted into elemental fluxes. For example, the total mass flux of an element of interest X from parent bedrock into the regolith (RP^X) is computable from the regolith production flux (RP) by multiplication with the concentration of element X in unweathered parent bedrock. RP^X in turn can be converted into an elemental chemical release flux ($W^X_{regolith}$) by multiplication with the fractional loss of the element of interest X from the regolith. The so-called mass transfer coefficient (τ^X) must thus be quantified. τ^X is a measure to quantify elemental loss or gain in weathered material relative to unweathered parent bedrock (Brimhall and Dietrich 1987; Anderson et al. 2002). Because the formation of secondary weathering products is accounted for in τ^X, this elemental chemical release flux is a net release flux of dissolved nutrients into forest ecosystems.

1.4.3 Radiogenic isotopes – strontium

Strontium (Sr) is one of the most abundant trace elements in the upper continental crust, occurring at approximately 350 µg/g (Taylor and McLennan 1995). Due to its high solubility, it is also strongly partitioned as a trace element in water and vegetation. Natural Sr consists of the four stable isotopes ^{84}Sr, ^{86}Sr, ^{87}Sr, ^{88}Sr with respective atomic masses of 83.913426 u, 85.909265 u, 86.908881 u, 87.905617 u (Audi and Wapstra 1993) and natural relative abundances of 0.56 at.%, 9.86 at.%, 7.00 at.%, 82.58 at.% (De Biévre and Taylor 1993). Among the four stable Sr isotopes, ^{87}Sr is a so-called radiogenic isotope, because it is the product of the radioactive ß$^-$ decay of ^{87}Rb with a decay constant λ of about 1.42×10^{-11} yr^{-1} (Steiger and Jager 1977) corresponding to a half-life of about 4.88×10^{10} yr (Holden 1990). After Rb and Sr were incorporated into minerals at their formation the amount of ^{87}Sr increases over time, whereas the amounts of ^{84}Sr, ^{86}Sr and ^{88}Sr remain constant (Capo et al. 1998). Shifts in the relative amounts of ^{87}Sr by isotopic fractionation can be neglected, because these minute natural shifts are corrected for during mass spectrometry by the normalisation of the $^{87}Sr/^{86}Sr$ ratio to the known ratio of $^{88}Sr/^{86}Sr = 8.375209$ (e.g. Faure and Mensing 2005) that is routinely employed to correct instrumental isotopic fractionation. Thus, the $^{87}Sr/^{86}Sr$ ratio of bedrock varies only with geologic age and the initial Rb/Sr ratio.

1.4.3.1 Applications of the radiogenic Sr isotope ratio ($^{87}Sr/^{86}Sr$)

There are three main applications of radiogenic Sr in isotope geochemistry. First, the Rb-Sr system is used as one of the oldest and best-established methods for isotopic dating (e.g. Hahn et al. 1943; Bowen 1994). Second, the radiogenic Sr isotope ratio ($^{87}Sr/^{86}Sr$) is widely used as fingerprint for the magma source to igneous rocks, deep crustal recycling, and the source of Ca in the precipitation of

calcite from seawater. Third, this ratio is used as a conservative source tracer in environmental studies (Figure 1-2), in particular on soil profile to catchment scales to identify the geogenic source of dissolved and biogeochemically cycled Sr. For example, $^{87}Sr/^{86}Sr$ is applied as ecological tracer to fingerprint the calcium (Ca) source in forest ecosystems (e.g. Åberg et al. 1990; Miller et al. 1993; Bailey et al. 1996; Stewart et al. 1998; Capo et al. 1998; Poszwa et al. 2000, 2004; Blum et al. 2002; Kennedy et al. 2002; Bullen and Bailey 2005; Drouet et al. 2005a, b; Pett-Ridge et al. 2009a; Bélanger et al. 2012; Meek et al. 2016; Bedel et al. 2016; Schmitt et al. 2017). Using the radiogenic Sr ratio to fingerprint the Ca source for forest trees is justified by the similar chemical behaviour of Ca and Sr with respect to ionic charge, radius and electron configuration, thus allowing organisms to utilise Sr along with Ca. To identify not only the source, but also the depth of Ca uptake by forest trees Poszwa et al. (2004) and McCulley et al. (2004) applied $^{87}Sr/^{86}Sr$ as a depth tracer. Investigations on $^{87}Sr/^{86}Sr$ in watersheds focus on mixing proportions of dissolved Sr, labile or soil exchangeable Sr, and plant-utilised Sr from endmembers such as carbonate and silicate bedrock, and atmospheric dry and wet deposition (e.g. Graustein and Armstrong 1983; Miller et al. 1993; Bain and Bacon 1994; Åberg 1995; Kennedy et al. 1998, 2002; Chadwick et al. 1999; Jacobson et al. 2000; Blum et al. 2002; Pett-Ridge et al. 2009b, a; Pierson-Wickmann et al. 2009; Reynolds et al. 2012; Bélanger et al. 2012; Andrews et al. 2016; Aciego et al. 2017). The foundation of these studies was laid by Grousset et al. (1992), Grousset and Biscaye (2005), Chen et al. (2007), Erel and Torrent (2010), Scheuvens et al. (2013), and Gross et al. (2016), among others, who used the radiogenic Sr isotope ratio to explore key source areas of Saharan and Asian dust. Moreover, in hydrology $^{87}Sr/^{86}Sr$ is used to investigate flow pathways of dissolved Sr (e.g. Hogan and Blum 2003; Shand et al. 2007).

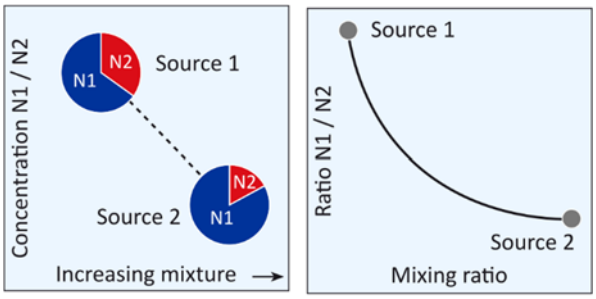

Figure 1-2 Schematic illustration showing the physical principles of an isotope ratio N1/N2 as source tracer (left panel) and the dependency of isotope abundance on mixing ratio (right panel). Modified from von Blanckenburg (2017).

In this thesis I apply the radiogenic Sr isotope ratio in two ways. First, $^{87}Sr/^{86}Sr$ is used as proxy for the intensity of chemical weathering. To use $^{87}Sr/^{86}Sr$ as a proxy for the intensity of chemical weathering, minerals must differ in their Sr content, the radiogenic Sr isotope ratio and in their mineral dissolution kinetics. If these conditions are met, the radiogenic Sr isotope ratios of unweathered bedrock and weathered rock progressively diverge the greater the degree of chemical alteration. Second, $^{87}Sr/^{86}Sr$ is applied as conservative source tracer to identify the depth of nutrient uptake by forest trees. For this purpose, I compare the radiogenic Sr isotope ratio of the biologically available fraction that is assumed to be representative of soil water, which is utilised by forest trees at a given

depth, with the $^{87}Sr/^{86}Sr$ ratio of living plant tissue. The radiogenic Sr isotope ratio was measured on a multi collector inductively coupled plasma mass spectrometer (MC-ICP-MS) after sample digestion and purification from matrix elements by ion chromatography using Sr Spec resin.

1.4.4 Cosmogenic nuclides – beryllium

Beryllium (Be) is a rare trace element i) in the upper continental crust, occurring at approximately 3 µg/g (Taylor and McLennan 1995), ii) in surface waters with concentrations in the order of ng/L (references in Vesely et al. (2002)) and iii) in vegetation with concentrations in the order of ng/g (Skrivan et al. 2000). Beryllium has only one stable isotope (^{9}Be) with an atomic mass of 9.012182 u (Audi and Wapstra 1993), and eleven radioactive isotopes. Of these only two radionuclides have half-lives ($T_{1/2}$) longer than seconds, namely the relatively short-lived ($T_{1/2}$ ~ 53 d) radionuclide ^{7}Be with an atomic mass of 7.016929 u (Audi and Wapstra 1993) and the relatively long-lived ($T_{1/2}$ = 1.387 ± 0.012 Myr (Chmeleff et al. 2010; Korschinek et al. 2010)) radionuclide ^{10}Be with an atomic mass of 10.013534 u (Audi and Wapstra 1993). While ^{7}Be decays by electron capture to stable lithium-7 (^{7}Li), ^{10}Be decays by $ß^-$ emission to stable boron-10 (^{10}B). Both ^{7}Be and ^{10}Be are of cosmogenic origin and are produced by spallation reactions, when high-energy secondary cosmic ray particles like neutrons, protons or muons interact with target nuclides like oxygen (O) or nitrogen (N) (Figure 1-3). There are two sources of target nuclides: gases in the atmosphere and minerals in the lithosphere. A larger amount of ^{10}Be is produced in the atmosphere and deposited at a flux of about 0.01 to 4.0 x 10^6 atoms cm^{-2} yr^{-1} (Heikkilä and von Blanckenburg 2015) onto the Earth surface and oceans, giving it the name meteoric beryllium-10 ($^{10}Be_{meteoric}$). The minority of ^{10}Be ($^{10}Be_{in\ situ}$) is produced at the Earth surface, when cosmic ray particles interact with target nuclides in the crystal-lattice of minerals, such as quartz, at a production rate of ~ 4 atoms $g^{-1}_{(Qtz)}$ yr^{-1} at sea level high latitude (SLHL; Dunai (2000), Gosse and Phillips (2001), Muzikar et al. (2003), Phillips et al. (2016)). The production of $^{10}Be_{in\ situ}$ depends on atmospheric shielding, and hence altitude, geomagnetic latitude, and geomagnetic field strength, and so needs to be scaled for these factors. Thanks to the seminal work of Lal (1991) $^{10}Be_{in\ situ}$ is now routinely applied in geomorphological studies on quartz-containing lithologies to determine soil erosion or production rates, catchment-wide denudation rates (for which $^{10}Be_{in\ situ}$ is used in this thesis), exposure ages and burial ages (e.g. Bierman and Nichols 2004; von Blanckenburg 2005;

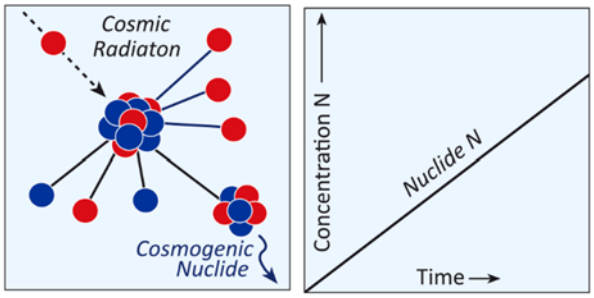

Figure 1-3 Schematic illustration showing the physical principles of the production of cosmogenic nuclides (left panel) and the accumulation of a nuclide's isotope concentration with time (right panel). Modified from von Blanckenburg (2017).

Portenga and Bierman 2011; Dixon and Riebe 2014; Granger and Schaller 2014; von Blanckenburg and Willenbring 2014).

1.4.4.1 Principles and applications of meteoric beryllium-10

Once $^{10}Be_{meteoric}$ is produced by spallation reactions mainly in the stratosphere, where its production rate is a function of geomagnetic latitude and geomagnetic field strength (Lal and Peters 1967), $^{10}Be_{meteoric}$ occurs mostly as the molecules ^{10}BeO or $^{10}Be(OH)_2$. Due to the reactive nature of these molecules, $^{10}Be_{meteoric}$ is quickly scavenged by aerosols, such as sulphates originating from e.g. volcanic eruptions (Mészáros 1981). After entering the troposphere, the $^{10}Be_{meteoric}$-containing aerosols are deposited to the Earth´s surface by rainfall as wet deposition or in aerosols as dry deposition (Field et al. 2006). The residence time of $^{10}Be_{meteoric}$ in the atmosphere is about one year in the stratosphere (Raisbeck et al. 1981), but only a few weeks in the troposphere and depends on scavenging by aerosols and rainfall, troposphere-stratosphere mixing and intertropospheric mixing (Lal and Peters 1967). Because of atmospheric circulation of $^{10}Be_{meteoric}$-containing aerosols, the delivery of $^{10}Be_{meteoric}$ to the Earth surface is highly dependent on climate and thus its flux needs to be determined empirically from interpolated ^{10}Be precipitation measurements or from atmospheric nuclide production models that are combined with General Circulation Models (GCMs) (Willenbring and von Blanckenburg 2010). Once $^{10}Be_{meteoric}$ is deposited on land it spends several months on the vegetation canopy (Monaghan et al. 1983), indicated by ^{7}Be, before it is either exported by overland flow through the fluvial system (c.f. McHargue and Damon (1991)) or infiltrates into soil, where its retentivity strongly depends on soil properties such as the presence of humic acids (Takahashi et al. 1999), pH (Takahashi et al. 1999) and grain size distribution (e.g. Wallbrink and Murray 1996; Shen et al. 2004; Willenbring and von Blanckenburg 2010a). In the absence of humic acids and at a pH above five Be is mainly present in its hydrolysed form, i.e. as $BeOH^+$ or $Be(OH)_2$ (Takahashi et al. 1999). Dissolved hydrolysed $^{10}Be_{meteoric}$ is highly surface-reactive. Thus, hydrolysed $^{10}Be_{meteoric}$ is either adsorbed to the negatively charged surfaces of clay minerals or soil organic matter, or co-precipitates with oxy-hydroxides of iron (Fe) and aluminium (Al). The depth distribution of the soil pH and grain size distribution dictates the $^{10}Be_{meteoric}$ concentration depth profile that commonly takes one of two profile shapes: an exponential profile (e.g. Pavich and Vidic 1993; Balco 2004; Willenbring and von Blanckenburg 2010a) or a bulge-shape profile (e.g. Pavich et al. 1986; Monaghan et al. 1992; Graly et al. 2010). In the exponential profile, the $^{10}Be_{meteoric}$ concentration declines with depth as the topsoil is highly retentive with respect to $^{10}Be_{meteoric}$. In contrast, in a bulge-shape profile the topsoil is less retentive, due to the acidic soil pH. Thus, in a bulge-shaped profile the $^{10}Be_{meteoric}$ concentration increases from topsoil with depth to a maximum concentration that is typically located in a clay-rich soil horizon and then decreases below the topsoil $^{10}Be_{meteoric}$ concentration with increasing depth. However, some regoliths provide the

conditions for the infiltration of $^{10}Be_{meteoric}$ below ten meters depth (e.g. Bacon et al. 2012; West et al. 2013).

Because of the dependencies of $^{10}Be_{meteoric}$ concentrations on grain size and pH, recent studies circumvent this complicating factor by normalising the $^{10}Be_{meteoric}$ concentrations to its stable counterpart ^{9}Be. ^{9}Be is released by chemical weathering from parent bedrock, mixes with dissolved $^{10}Be_{meteoric}$ to a certain ratio of $^{10}Be_{meteoric}/^{9}Be_{stable}$ and adsorbs onto clay minerals or soil organic matter, co-precipitates with amorphous and crystalline oxides or remains in the dissolved form under acidic conditions (von Blanckenburg et al. 2012). Thus, the $^{10}Be_{meteoric}/^{9}Be_{stable}$ ratio depends on the $^{10}Be_{meteoric}$ deposition rate, the concentration of ^{9}Be in parent bedrock and its release by chemical weathering and the weathering front advance rate (Maher and von Blanckenburg 2016). von Blanckenburg et al. (2012) provided a conceptual framework for the application of the $^{10}Be_{meteoric}/^{9}Be_{stable}$ ratio to measure total denudation rates from bulk soil and bedload sediment, and Wittmann et al. (2012) provided the methods, modified from Tessier et al. (1979) and Wiederhold et al. (2007), to sequentially extract Be contained in amorphous and crystalline oxides. This conceptual framework was successfully applied, for example, at the large scale in the Amazon River basin by Wittmann et al. (2015) and at the small scale in upland forest catchments in the Czech Republic by Dannhaus et al. (2018).

In this thesis I apply the $^{10}Be_{meteoric}/^{9}Be_{stable}$ ratio for the first time as a conservative source tracer to identify the nutrient uptake depth of forest trees. For this purpose, I assume that the $^{10}Be_{meteoric}/^{9}Be_{stable}$ ratio in amorphous oxides is representative of the dissolved $^{10}Be_{meteoric}/^{9}Be_{stable}$ ratio in soil water at a given depth from which forest trees utilise nutrients. The $^{10}Be_{meteoric}/^{9}Be_{stable}$ ratio in amorphous oxides therefore represents the $^{10}Be_{meteoric}/^{9}Be_{stable}$ ratio of the biologically available fraction. Consequently, in a similar manner as for the radiogenic Sr isotope ratio I compare the $^{10}Be_{meteoric}/^{9}Be_{stable}$ ratio of amorphous oxides with living wood (sapwood) of the prevailing tree species to identify the depth of nutrient utilisation. After sample digestion and purification of Be from matrix elements by anion and cation chromatography methods (where the minor amounts of $^{10}Be_{in\ situ}$ contained in the samples can be neglected), followed by alkaline precipitation, ^{10}Be was measured by accelerator mass spectrometry (AMS) and ^{9}Be by inductively coupled plasma optical emission spectrometry (ICP-OES) or by quadrupole inductively coupled plasma mass spectrometry (iCAP Q-ICP-MS). For measurements of $^{10}Be_{in\ situ}$ a few grams of the mineral quartz were first etched in hydrofluoric acid (HF) to remove adsorbed $^{10}Be_{meteoric}$ after which the entire quartz fraction was dissolved with HF and the procedure as described for $^{10}Be_{meteoric}$ was followed.

1.4.5 Metal stable isotopes – magnesium

Magnesium (Mg) is approximately 1.33 wt.% of the upper continental crust, making it the eighth most abundant chemical element there (Taylor and McLennan 1995). Apart from hydrogen, carbon and oxygen Mg is also the fourth most-abundant element in plants (Epstein and Bloom 2005) and a major

constituent of various water types such as soil water, groundwater and river water. The chemical properties of Mg mainly depend on the atomic number (12), valance (2) and atomic radius. The Mg nucleus can contain 12, 13 or 14 neutrons, thereby producing the three stable isotopes ^{24}Mg, ^{25}Mg, ^{26}Mg with respective atomic masses of 23.985042 u, 24.985837 u, 25.982593 u (Audi and Wapstra 1993) and natural relative abundances of 78.99 at.%, 10.00 at.%, 11.01 at.% (De Biévre and Taylor 1993). Even though the relative mass difference between ^{26}Mg and ^{24}Mg is relatively high at about 8 %, the determination of absolute isotope ratios by mass spectrometry is very difficult. For this reason, relative isotopic ratios are determined by reporting the per mil deviation of the isotope ratio of a sample from the isotope ratio of a reference material. As reference material for Mg stable isotopes the pure Mg solution DSM3 (provided by Dead Sea Magnesium Ltd., Israel) is preferred to the heterogeneous metal chips SRM980 from the National Institute for Standards and Technology (NIST, Galy et al. (2003)). Mg isotope ratios are reported according to the common delta notation (O'Neil 1986) by Equation 1-1, where x denotes to 25 or 26.

$$\delta^{x}\mathrm{Mg} = \left[\frac{\left(\frac{^{x}\mathrm{Mg}}{^{24}\mathrm{Mg}}\right)_{\mathrm{sample}} - \left(\frac{^{x}\mathrm{Mg}}{^{24}\mathrm{Mg}}\right)_{\mathrm{DSM3}}}{\left(\frac{^{x}\mathrm{Mg}}{^{24}\mathrm{Mg}}\right)_{\mathrm{DSM3}}} \right] \qquad \textbf{Equation 1-1}$$

δ^{x}Mg is commonly presented in the ‰ (per mil) notation by multiplying the left-hand term in Equation 1-1 by 1000, and mostly the δ^{26}Mg is reported. Positive δ^{26}Mg values indicate that the sample has a higher isotope ratio than the reference material, because the sample is enriched in the heavy isotope relative to the reference material and vice versa for negative δ^{26}Mg values. To date, reported δ^{26}Mg values of natural materials range from about -5.6 to +1.8 ‰ (Teng 2017). The lower limit of δ^{26}Mg is represented by carbonate rock with δ^{26}Mg values ranging from about -1.0 to -5.6 ‰ (Teng 2017) and the upper limit is represented by silicate rock with δ^{26}Mg values ranging from about -0.6 to 0.0 ‰ (Galy et al. 2002; Tipper et al. 2006a; Brenot et al. 2008). During chemical, physical and biological reactions Mg is incompletely transferred from one compartment into another (Figure 1-4). Thereby, the minute isotope mass differences cause mass-dependent isotope fractionation. Essentially, two types of isotopic fractionation effects can be distinguished: equilibrium effects and

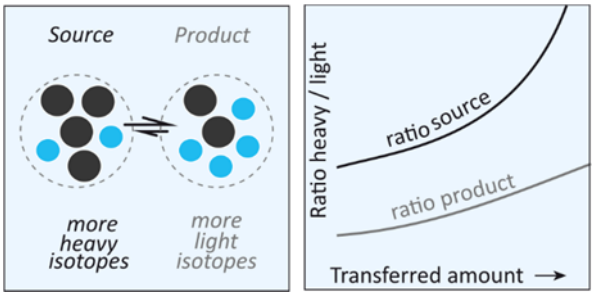

Figure 1-4 Schematic illustration showing the physical principles of isotope fractionation (left panel) and the dependency of transferred amount with isotope ratio (right panel). Modified from von Blanckenburg (2017).

kinetic effects. Equilibrium effects are reversible, temperature-dependent and rely on the dependency of bond strengths on atomic mass. In contrast, kinetic effects rely on fast, incomplete or unidirectional processes such as evaporation, diffusion, or fast, non-equilibrium forward reactions during the breaking of bonds or attachment of Mg to surfaces. The magnitude of Mg isotopic fractionation between compartment A and B is, according to Equation 1-2, expressed by an isotopic fractionation factor $\alpha_{A\text{-}B}$.

$$\alpha_{A-B} = \frac{1000 + (\delta^{26}\mathrm{Mg})_A}{1000 + (\delta^{26}\mathrm{Mg})_B} \qquad \textbf{Equation 1-2}$$

1.4.5.1 Behaviour of Mg isotopes in the Critical Zone

In the Critical Zone substantial Mg isotope fractionation occurs during Mg uptake by vegetation and during chemical weathering, when secondary minerals are newly formed (references in reviews from Schmitt et al. (2012); Bullen (2014); Teng (2017)). In both processes with few exceptions, ^{24}Mg is relatively enriched in the solution, whereas ^{26}Mg is preferentially partitioned into the neo-formed secondary minerals and vegetation. Here, I briefly review the literature on Mg stable isotope partitioning during low-temperature reactions at the Earth surface. I exclude carbonate systems, as carbonate formation and dissolution do not play a role in this thesis.

The partitioning of Mg isotopes in the Critical Zone begins with primary mineral dissolution. Wimpenny et al. (2010), Maher et al. (2016) and Ryu et al. (2016) showed experimentally that ^{24}Mg is preferentially released from forsterite. Indeed, the release of light isotopes is often observed in the early stages of mineral dissolution experiments (e.g. for Si by Ziegler et al. (2005)), because in interfacial reactions the detachment of light isotopes from bonds have a lower activation energy barrier to overcome (Schauble 2004). Yet, as weathering proceeds beyond the initial stage, mineral dissolution affects the entire grain and mass balance dictates that dissolved Mg will obtain the composition of the original primary mineral (Bouchez et al. 2013). A different case of isotope-selective mineral dissolution was shown by Ryu et al. (2011) who concluded from their granite dissolution experiments that temporal patterns in δ^{26}Mg rely on mineralogical effects: Mg-containing primary minerals vary in their isotope ratio and mineral dissolution kinetics. Thus, solutes formed will be preferentially enriched in the isotope ratio of the fastest dissolving and most abundant Mg mineral.

Tipper et al. (2006a) and (2008) demonstrated in sparsely vegetated catchments that δ^{26}Mg of stream water is isotopically lighter than silicate rock and attributed this finding to the preferential partitioning of ^{24}Mg into water and ^{26}Mg into the neoformation of clay minerals during chemical weathering. Indeed, numerous studies confirmed that rivers draining silicate bedrock are isotopically lighter than silicate bedrock and that heavy Mg isotopes are retained in soil in clay minerals and

amorphous phases (Tipper et al. 2006b, 2010, 2012a, b; Brenot et al. 2008; Teng et al. 2010; Pogge von Strandmann et al. 2012; Huang et al. 2012; Opfergelt et al. 2012, 2014; Liu et al. 2014; Mavromatis et al. 2014; Dessert et al. 2015; Ma et al. 2015; Chapela Lara et al. 2017; Kimmig et al. 2018). Among these are studies on weathering profiles, which contain contrasting results. For example, Opfergelt et al. (2012) found that bulk soil and clay minerals are both isotopically heavier than bedrock, but also that δ^{26}Mg of bulk soil is negatively correlated with the concentration of adsorbed Mg. Based on this finding, Opfergelt et al. (2012) concluded that δ^{26}Mg of Mg-containing clay minerals results from the mixture of isotopically heavy structural Mg and isotopically light exchangeable Mg. In contrast, Mg isotope fractionation by adsorption on and desorption from exchangeable sites of isotopically heavy Mg was observed by Opfergelt et al. (2014) in a basaltic system, causing the formation of isotopically light Mg clays. In another contradictory study Pogge von Strandmann et al. (2012) concluded that isotopically heavy Mg preferentially adsorbs onto the exchangeable complex. Because none of these studies measured δ^{26}Mg of exchangeable Mg directly, Wimpenny et al. (2014) performed experiments to systematically investigate the partitioning of Mg isotopes into the octahedral sheets (`structural´) and the exchangeable sites of clay minerals. They demonstrated that Mg-containing clay minerals preferentially incorporate isotopically heavy Mg into the clay structure, leaving isotopically light Mg in solution, which adsorbs with little to no isotopic fractionation to the negatively charged interlayer surfaces. Finally, Wimpenny et al. (2014) concluded that the mass balance between structural and exchangeable Mg determines the Mg isotopic composition of newly formed secondary minerals.

As a nutrient Mg activates more enzymes than any other element in plants; Mg is also the central ion of chlorophyll. Thus, Mg plays an important role in photosynthesis. The isotopic composition of Mg in chlorophyll is species-dependent as δ^{26}Mg in chlorophyll can either be lower than the growth media as shown for experimentally grown cyanobacteria, coccolithophores and wheat (Black et al. 2006, 2008; Ra et al. 2010) or higher than, for example, in leaves of English ivy (Black et al. 2007). At the whole-plant scale, laboratory growth experiments revealed that relative to the growth media heavy Mg is preferentially utilised by wheat (Black et al. 2008), rye grass and clover (Bolou-Bi et al. 2010). Also, naturally grown plants preferentially incorporated heavy Mg isotopes into grass, larch and spruce relative to the source Mg. Mg isotopes are fractionated within plants, as Mg in leaf foliage is consistently isotopically lighter than in roots (Black et al. 2008; Tipper et al. 2010, 2012b; Bolou-Bi et al. 2012; Mavromatis et al. 2014; Opfergelt et al. 2014). Also, microcolonial fungi like *Knufia petricola* preferentially take up heavy Mg from growing media (Pokharel et al. 2017). In contrast, Kimmig et al. (2018) shows that maple is isotopically lighter than its bedrock source. Overall, the δ^{26}Mg of whole organisms including higher plants, is higher than the Mg source, but during redistribution within the plant the higher plant organs can receive lighter isotopes.

In summary, the partitioning of Mg isotopes in the natural environment makes Mg an excellent proxy to quantify biogeochemical cycles of Mg in the Critical Zone. In this thesis I apply Mg stable isotopes to quantify the biogeochemical cycling of Mg and to quantify the proportions of Mg export in the dissolved and particulate form in and from a montane, temperate forest ecosystem. Mg isotopes are measured by multi collector inductively coupled plasma mass spectrometry (MC-ICP-MS) after sample digestion and purification by cation chromatography.

1.4.6 Sequential extractions

Sequential extractions are commonly applied to forest and arable soils, sewage sludges, bedload, suspended and marine sediments, among others (Filgueiras et al. 2002). Their aim is to characterise pollution sources, evaluate metal mobility and bioavailability, or to identify binding sites of metals to assess metal accumulation (Filgueiras et al. 2002). In general, most sequential extraction procedures can be traced back to the methods of Tessier et al. (1979) and the Community Bureau of Reference (BCR) and were adapted according to the properties of the sample material, the element of interest and its binding form. For example, in this thesis three different sequential extraction methods are applied, each adapted to specific elements of interest: strontium and magnesium (see chapter 2 and 4), phosphorus (see chapter 3), and beryllium (see chapter 3). The results of sequential extractions depend on many factors including homogeneity of the sample, sample drying method, pH of the extractant, temperature, extraction time, reagent concentration, stirring system, particle size, or the ratio of solid to volume of extractants (e.g. Förstner 1993; Hursthouse 2001).

For this thesis the overarching aim of applying sequential extractions is to trace the depth distribution of nutritive elements that are principally available for uptake by trees. For this purpose, sequential extraction methods are generally designed to extract progressively more strongly bound nutrients with each extraction step, for example: 1.) water-soluble fraction, 2.) exchangeable fraction, 3.) acid-soluble (carbonate) fraction, 4.) reducible fraction, 5.) oxidizable fraction. In doing so, it is assumed that the order of the extraction procedure mirrors the increasing effort a forest tree must exert to access a nutrient from the regolith.

The *water-soluble fraction* represents the most labile soil compartment. It is assumed that a forest tree exerts the least effort to utilise nutrients contained in soil water that are present in the form of free ions and ions complexed with soluble organic matter. Although some studies argue that the water-soluble fraction is significant only in evaporitic salts and negligible elsewhere (Chao 1984; Hall et al. 1996) the water-soluble fraction represents the soil reservoir that is most accessible to plants (He et al. 1995). Even though the water-soluble fraction is extractable by deionised water, deionised water has no buffering capacity and re-adsorption is likely to occur for very insoluble elements (Rauret et al. 1999).

The *exchangeable fraction* consists of elements that form weak electrostatic bonds between the hydrated surfaces of phyllosilicates, oxyhydroxides minerals, or organic matter. These weakly adsorbed elements are commonly extracted by changing the ionic strength of the medium with chloride salts ($MgCl_2$, $CaCl_2$, $BaCl_2$), ammonium salts (CH_3COONH_4 (hereafter NH_4OAc), NH_4NO_3, NH_4Cl), or nitrate salts ($NaNO_3$, KNO_3, $Ca(NO_3)_2$, $Sr(NO_3)_2$). While ammonium salts can lower the pH of the suspension and favour the hydrolysis of clay minerals (Filgueiras et al. 2002), chlorine and acetate salts result in complexation of metals. In contrast, using nitrate salts as the extractant avoids complexing metals (Krishnamurti et al. 1995). However, since acetate prevents re-adsorption or precipitation of the extracted metal ions (Filgueiras et al. 2002), NH_4OAc is used in this thesis to extract the exchangeable fractions after the water-soluble fraction, where the extraction efficiency follows the order: $H < Ca < Mg < Na < NH_4$ (Pickering 1986). The extraction efficiency increases with increasing molarity of the extractant. For example, the extraction efficiency of 1 M NH_4OAc (used in this thesis) is four times higher than that for the often-used 0.01 M NH_4OAc (Arunachalam et al. 1996). The optimum extraction time to extract the easily exchangeable fraction is about 1-3 h (Arunachalam et al. 1996).

The *carbonate fraction* is accessible to forest trees if roots excrete carboxylates, i.e. low-molecular organic acids into the rhizosphere to decrease soil pH (Landeweert et al. 2001; Brantley and Lebedeva 2011). Minerals with slow dissolution kinetics can thus be dissolved. In this thesis a weak low molecular weight organic acid (Baruah et al. 2011), namely 1 M CH_3COOH (acetic acid), is used to extract the carbonate fraction. However, this extraction is known to have some potential to attack primary minerals and to dissolve Fe- and Mn-oxides if the pH of the solution falls below 5 (Filgueiras et al. 2002).

The *reducible fraction* is not extracted in this thesis for three reasons. First, under common soil conditions the reducible fraction is relatively stable and thus biologically inaccessible (Lee and Kittrick 1984). Second, hydroxylamine hydrochloride ($NH_2OH{\cdot}HCl$) in nitric acid medium is widely used to extract the reducible fraction. However, $NH_2OH{\cdot}HCl$ is known to liberate substantial amounts of trace metals bound to organic matter leading to an underestimation of the oxidisable fraction extracted after the reducible fraction (Ahnstrom and Parker 1999). Third, if the pH of the extraction solution falls below 1.5 primary silicate minerals are attacked (Tessier et al. 1979).

The *oxidisable fraction* is accessible to forest trees if tree roots develop a symbiotic relationship with organic matter decomposing organisms such as mycorrhiza fungi (Wardle et al. 2004a) that break down organic matter into plant-accessible inorganic forms. In this thesis the oxidisable fraction comprising stable, high molecular weight humic substances from the remaining soil compartments is extracted by applying hydrogen peroxide in dilute nitric acid medium (e.g. Tessier et al. 1979; Gibson and Farmer 1986) at 85°C and re-adsorption is avoided by addition of NH_4OAc to a final molarity of 1 M. This procedure represents a compromise between the mutually exclusive aims of i) complete

oxidisation of organic matter, and ii) minimal attack of primary silicate minerals (Tessier et al. 1979). However, if carbonates were not extracted in previous steps, they may be attacked here (Anderson 1961), along with oxides (Lavkulich and Wiens 1970; Shuman 1985) and sulphides (Marin et al. 1997).

1.4.7 Choice of field sites

To explore the sources and fluxes of mineral nutrients in terrestrial ecosystems I selected two study sites in the uplands of southern Germany, namely the Black Forest (Schwarzwald, Conventwald) and the Bavarian Forest (Bayerischer Wald, Mitterfels), and a study site in the uplands of the Californian Sierra Nevada (Southern Sierra Critical Zone Observatory, SSCZO). All study sites are mountainous, well-drained as a result of temperate climate, and experience erosion because of their location on hillslopes. Thus, all sites fulfil the characteristics of a kinetically limited weathering regime. Moreover, the study sites are underlain by silicate bedrock, mantled by weakly developed soils and covered by mixed deciduous and coniferous forests. Apart from their site characteristics, the main reasons for choosing these study sites were i) that they are part of long-term monitoring programs and ii) that interdisciplinary research programs are linked to them. For example, the German sites are part of the long-term forest ecosystem monitoring program “International Co-operative Program on assessment and monitoring of air pollution effects on forests (ICP Forest Level II)”. An interdisciplinary Priority Program (SPP) of the German Research Foundation, i.e. SPP 1685 “Ecosystem Nutrition – Forest Strategies for limited Phosphorus Resources” collaborates with this monitoring programs to benefit from the large background datasets. A similar situation exists with the Critical Zone Exploration Networks (CZEN) and their Critical Zone Observatories (CZO), including the SSCZO. The wealth of background data and the potential for scientific collaborations within the frameworks of the SPP or the CZEN makes these study sites ideal to explore the sources and fluxes of forest ecosystem nutrition in this thesis.

2 How slow rock weathering balances nutrient loss during fast forest floor turnover in montane, temperate forest ecosystems

Abstract

Mineral nutrient cycling between trees and the forest floor is key to forest ecosystem nutrition. However, in sloping, well-drained landscapes the forest floor experiences permanent nutrient loss by drainage and erosion. To prevent nutrient deficit, a replenishing mechanism must be in operation that we suggest being sourced in the subsoil and the weathering zone beneath it, provided that atmospheric input is insufficient. To explore such a mechanism, we quantified deep (up to 20 m depth) weathering and mineral nutrient cycling in two montane, temperate forest ecosystems in Southern Germany: Black Forest and Bavarian Forest. From measurements of the inventories, turnover times, and fluxes of macronutrients (K, Ca, Mg, P) we found evidence for a fast, shallow `organic nutrient cycle´, and a slow, deep `geogenic nutrient pathway´. We found that the forest floor nutrient inventory is of finite size and persists for less than ten years. Despite this loss, foliar nutrient concentrations in *Picea abies* and *Fagus sylvatica* do not indicate deficiency. We infer that ultimately the biologically available fraction in the deep regolith (CON: 3 - 7 m, MIT: 3 - 17 m) balances nutrient loss. However, although the nutrient supply fluxes from chemical weathering at CON are twice those of MIT, nutrient uptake fluxes into trees do not differ. The organic nutrient cycle apparently adjusts its efficiency to cater for differences in its replenishment by the deep geogenic nutrient pathway, and thereby provides potentially an alternative feedback mechanism to the acceleration of biogenic weathering to ensure long-term forest ecosystem nutrition.

2.1 Introduction

A fundamental aspect of forest ecosystems is that mineral nutrient demand of forest trees vastly exceeds nutrient supply from chemical weathering and atmospheric deposition for most nutritive elements. Thus, over time forest ecosystems run into nutrient limitation (e.g. Elser et al. 2007; Vitousek et al. 2010; Augusto et al. 2017) if no strategies exist to handle high nutrient demand in face of low nutrient supply. Several nutrient acquisition, storage and allocation strategies (Aerts and Chapin 1999) have been suggested that all contribute to satisfy nutrient demand through a cycle, that we call here the "*organic nutrient cycle*". The most common strategy is efficient re-utilisation of nutrients from plant litter in the forest floor (e.g. Jobbágy and Jackson 2004; Lang et al. 2016). In fact, the present paradigm is that the fast turnover of the forest floor ensures forest ecosystem nutrition. Because organic-bound nutrients are not directly utilisable by plants (George et al. 2011; Jansa et al. 2011), microbial activity is central in ensuring the fast turnover required at the forest floor (e.g. Lang et al. 2016). For example, mycorrhizal fungi promote the breakdown of organic matter into plant-available inorganic forms that are subsequently taken up by tree roots (e.g. Chapin et al. 2012).

But, in sloping, well-drained landscapes that characterise large parts of the global land surface, these forest ecosystems experience permanent loss of nutrients contained in plant litter into drainage (e.g. Moore et al. 2005; Chaudhuri et al. 2007) or by erosion (Scatena and Lugo 1995; Heartsill Scalley et al. 2012). Thus within only a few years the finite nutrient inventory of the forest floor is exhausted (Wilcke et al. 2002). For tropical, non-eroding and some temperate, eroding forest ecosystems, external atmospheric dry deposition has been invoked as mitigating nutrient loss on the long-term (e.g. Chadwick et al. 1999; Aciego et al. 2017). However, if, as in these studies, the nutrient loss flux exceeds the replacement flux from atmospheric dry deposition by several times (Uhlig et al. 2017) even atmospheric inputs will fail to prevent the development of nutrient limitation.

Thus, a second flux should become the essential one to ensure long-term forest ecosystem nutrition by the continuous replenishment of the 'leaky' forest floor. To ensure forest ecosystem nutrition throughout the thousands of years of an interglacial period, this second mechanism is a pathway represented by the slow release of "new" mineral nutrients from the mineral soil and bedrock through chemical weathering (e.g. Cleveland et al. 2013), that operates over millennia (Buendía et al. 2010). Here, we call this second mechanism the `geogenic nutrient pathway´ which operates as follows. In landscapes that have attained steady state between the formation of regolith at depth and the removal of nutrient depleted soil by erosion at the surface, the topmost soil experiences a continuous renewal of mineral nutrients from the bedrock source that transit upwards from the weathering front into topsoil (e.g. Porder et al. 2007). However, a relatively high amount of mineral nutrients in the regolith does not necessarily satisfy nutrient demand of forest trees if the nutrient in question is strongly bound to solids and hence inaccessible to forest trees (Walker and Syers 1976).

Nutrients showing such attributes are characteristically P and K (Tripler et al. 2006), as P is frequently occluded to Fe- and Al-containing sesquioxides (Brady and Weil 2002) while K is hosted in minerals with low mineral dissolution kinetics (Chaudhuri et al. 2007), such as potash feldspar. Thus, besides the advection of material by erosion, the release mechanisms by weathering are the essential ingredients of the geogenic nutrient pathway, as they make mineral nutrients available to plants.

The release of nutrients by weathering processes takes place continuously in the regolith and at the weathering front. In the simplest terms these processes require water flow and thus porosity (Brantley and Lebedeva 2011), protons supplied by carbonic acid in water, microbial respiration of CO_2, or sulfide oxidation (Brantley et al. 2017b), and sufficient fluid flow to dissolve primary minerals (Maher 2010). However, biogenic processes are increasingly thought to play a role in weathering (Amundson et al. 2007; Brantley et al. 2011). For example, cluster roots with their densely-packed root hairs can produce and excrete weathering agents into the rhizosphere (e.g. Landeweert et al. 2001; Lambers et al. 2008) to decrease the rhizospheric soil pH and in doing so to increase mineral dissolution rates. Also, symbiotic relationships between roots and mycorrhiza fungi (e.g. Lambers et al. 2008) help to acquire nutrients from the mineral soil. In this symbiosis mycorrhizal fungi can detect and mobilise otherwise biologically-inaccessible nutrients. In doing so mycorrhizal fungi penetrate directly into mineral crystals (Jongmans et al. 1997) such as apatite for P acquisition (Smits et al. 2012) or biotite for K acquisition (Balogh-Brunstad et al. 2008; Bonneville et al. 2009).

That the geogenic nutrient pathway has not gained more importance in forest ecosystem nutrition studies is because it is considered to be miniscule. For example, Cleveland et al. (2013) suggest that geogenic P may supply as little as 2 % of terrestrial net primary productivity (NPP). Similarly, Wilcke et al. (2017) suggest that even in montane, tropical regimes, where erosion and nutrient loss should be high, the proportion of nutrients sourced from bedrock is little. If this little geogenic contribution to forest ecosystem nutrition is of no importance, this would suggest that plants may play little role in accelerating weathering, as has previously been suggested (e.g. Pagani et al. 2009). However, this seems difficult to reconcile with the aforementioned prevalence of mycorrhizal fungi that are demonstrably adapted to mobilise mineral nutrients. In addition, it is unclear how such ecosystems could last over millennia without an important source of nutrition from bedrock given the inevitable loss of plant litter to erosion and drainage through time and the insignificance of atmospheric dry deposition fluxes at many sites when compared to chemical weathering fluxes. In fact, the importance of bedrock-derived nutrients to forest ecosystem nutrition was recently highlighted by Houlton et al. (2018) who show that nutrient supply by rock weathering plays an important role in forest ecosystem nutrition even for nitrogen that is else fixed from atmospheric sources. Also, bedrock P concentrations exert an ecological control (Hahm et al. 2014).

We attempt here to reconcile these disparate views into a revised paradigm similar to the conceptual model of Buendía et al. (2010). The *geogenic nutrient pathway* operates over geologic time scales (between 10 kyr and 1 Myr) by uplift of fresh material into soil. Embedded within this slow cycle is the fast *organic nutrient cycle* between the soil and vegetation (Buendía et al. 2010). While on short timescales the organic nutrient cycle appears to be highly efficient, over millennia, inevitable losses from the organic nutrient cycle must be balanced by nutrient uptake via the geogenic nutrient pathway. To underpin the feasibility of this revised paradigm, we have undertaken a case study with the aim to parameterise all components of the system such as to identify their relative efficiencies. To this end we explored how forest ecosystem nutrition is ensured in two mountainous catchments. Although these sites strongly differ in their nutrient supply fluxes through rock weathering they are characterised by similar primary productivity. We quantified nutrient cycling in forest ecosystems across several reservoirs that extend to the unweathered bedrock that was accessed at up to 30 m depth by drilling, and by using a range of geochemical approaches that we applied to rock, weathered rock, soil, and tissues of trees. As a prerequisite we developed a conceptual framework including a series of simple mass balance equations that combine nutrient fluxes, inventories and turnover times.

2.2 Conceptual framework

Consider a forest ecosystem extending from the top of the vegetation canopy down to unweathered bedrock from a conceptual standpoint (Figure 2-1), a zone now commonly termed the "Critical Zone" (Brantley et al. 2007; Lin 2010). Each box in Figure 2-1 represents a compartment of the forest ecosystem comprising a nutrient inventory and a nutrient turnover time. The turnover time is calculated as the inventory of a given compartment divided by a nutrient input or output flux and describes the mean time a constituent spends in the respective compartment after entry and before exit (Sierra et al. 2017). In explaining the conceptual framework, we follow a given nutrient from its bedrock

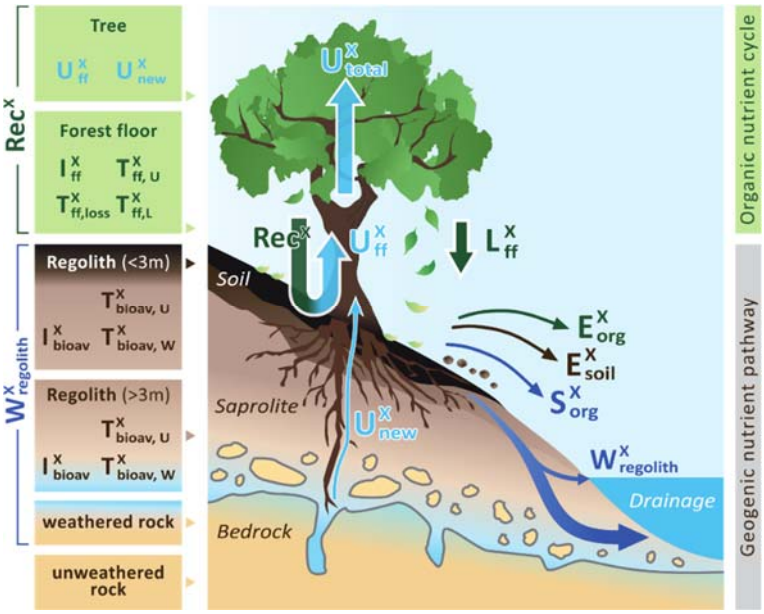

Figure 2-1 A conceptual forest ecosystem. Individual compartments are presented as boxes including the metrics used to quantify their properties: nutrient inventory (I^X) and nutrient turnover time (T^X). Compartments are linked by fluxes (arrows), where the thickness of the arrows indicates the relative proportions. Detailed information on the metrics is provided in Table 2-1. Figure is not drawn to scale.

Table 2-1 Glossary of metrics.

	Total mass fluxes (e.g. in g m^{-2} yr^{-1})
D	Denudation rate; i.e. the sum of chemical and physical denudation; Equation 2-1; Section 2.2.1
E	Erosion rate; physical removal of primary and secondary minerals and biogenic material; Equation 2-1 and Equation 2-3, Figure 2-1; Section 2.2.1
W	Weathering rate; chemical release flux from minerals minus the flux of incorporation into secondary minerals and oxides; Equation 2-3; Figure 2-1; Section 2.2.1
GPP	Gross primary production; gross carbon input to forest ecosystem; Equation 2-9; Section 2.2.2
NPP	Net primary production; carbon fixation by the forest ecosystem minus respiration; Equation 2-9; Section 2.2.2
	Elemental fluxes F^X (e.g. in mg m^{-2} yr^{-1})
$W^X_{regolith}$	Chemical weathering flux of element X; release flux of X from minerals minus the flux of incorporation of X into secondary minerals and oxides; Equation 2-6; Section 2.2.1; Figure 2-1
E^X_{org}	Litter erosion flux of element X; particulate removal of plant litter from forest floor; Equation 2-11; Section 2.2.2; Figure 2-1
S^X_{org}	Drainage flux of element X from organic matter from the forest floor; export of plant litter after decomposition and solubilisation; Equation 2-12; Section 2.2.2; Figure 2-1
L^X	Litterfall flux of element X; nutrient return by leaf litterfall from trees to the forest floor; Figure 2-1
U^X_{total}	Total nutrient uptake flux of element X; uptake of X by forest trees at the ecosystem scale; Equation 2-10; Section 2.2.2; Figure 2-1
U^X_{ff}	Nutrient uptake flux of element X from the forest floor; Figure 2-1
U^X_{new}	Nutrient uptake flux of "new" element X from the biologically available regolith fraction to replace the nutrient loss by E^X_{org} and S^X_{org}; Equation 2-16; Section 2.2.1; Figure 2-1
Dep^X_{wet}	Atmospheric wet deposition flux of element X in open rainfall
	Elemental mass fractions and elemental flux ratio f^X
CDF	Chemical depletion fraction; fractional mass loss by dissolution of elements from the regolith; Equation 2-2; Section 2.2.1
$\tau^X_{X_i}$	Mass transfer coefficient of element X calculated using an immobile X_i (here Zr is used); elemental loss or gain relative to unweathered bedrock; Equation 2-5, Section 2.2.1
Rec^X	Nutrient recycling factor; number of cycles element X is re-utilised from plant litter after its initial release from rock; Equation 2-19, Section 2.4.3.2; Figure 2-1
	Elemental Inventories I^X (e.g. in g m^{-2})
I^X_{ff}	Inventory of element X in the forest floor; Equation 2-7, Section 2.2.2; Figure 2-1
I^X_{bulk}	Inventory of element X in bulk regolith; Equation 2-7, Section 2.2.1
I^X_{bioav}	Inventory of element X in the biologically available fraction; Equation 2-7; Section 2.2.1; Figure 2-1
	Elemental turnover times T^X (e.g. in yr)
$T^X_{i,j}$	Turnover time of element X in compartment I with respect to input or output flux j; the ratio of total stock of element X in I to input or output flux j.
$T^X_{ff,L}$	Turnover time of element X in the forest floor with respect to litterfall; mean time required to replace one inventory of element X in the forest floor through litterfall; Equation 2-15; Section 2.2.2; Figure 2-1
$T^X_{ff,U_{ff}}$	Turnover time of element X in the forest floor with respect to uptake into trees; mean time a nutrient rests in the forest floor before re-utilisation by forest trees; Equation 2-14; Section 2.2.2; Figure 2-1
$T^X_{ff,loss}$	Turnover time of element X in the forest floor with respect to loss by plant litter erosion and drainage after plant litter decomposition and solubilisation; mean time element X can sustain nutrient uptake before loss into the stream; Equation 2-13; Section 2.2.2
$T^X_{bioav,W}$	Turnover time of element X in the biologically available fraction in regolith with respect to adsorption onto clay minerals; mean time over which the inventory of the biologically available fraction is replenished by chemical silicate weathering in the absence of other gains or losses; Section 2.2.1; Equation 2-8; Figure 2-1
$T^X_{bioav,U_{new}}$	Turnover time of element X in the biologically available fraction in regolith with respect to uptake into trees; mean time the nutrient rests in the biologically available regolith fraction before transfer into trees in the absence of other gains or losses; Equation 2-20; Section 2.2.1; Figure 2-1

source through forest trees to the forest floor. In doing so we parameterise nutrient fluxes and inventories in the geogenic nutrient pathway and the organic nutrient cycle to be able to quantify

turnover times. A glossary on the metrics used throughout this paper is provided in Table 2-1 and more detailed information on the calculation and limitations of the metrics is given in Section 2.3.4.

2.2.1 Geogenic nutrient pathway

The geogenic nutrient pathway is characterised by the conversion of bedrock into regolith – defined here to comprise weathered rock, saprolite and soil – through regolith production, nutrient release from primary and secondary minerals by chemical weathering, loss of dissolved species into drainage, erosion of remaining solids, and for the remainder nutrient utilisation by forest trees.

2.2.1.1 Fluxes

At the weathering front unweathered bedrock is converted into regolith by regolith production (RP). Although regolith production occurs at the base of the weathering zone, at steady state RP is coupled to the total mass loss from the weathering profile (e.g. Heimsath et al. 1997; Lebedeva et al. 2010), so as to maintain a constant thickness of regolith. Total mass loss comprises both particulate matter (physical erosion, E) and dissolved material (chemical weathering, W), and the combined mass loss flux is the denudation flux D (Equation 2-1). This denudation flux can be determined, for example, by cosmogenic nuclides such as *in situ* ^{10}Be (Section 2.3.4).

$$\mathrm{RP} = \mathrm{D} = \mathrm{E} + \mathrm{W} \qquad \textbf{Equation 2-1}$$

An estimate of the time-integrated total amount of elements transferable from bedrock to forest trees can be made from the chemical depletion fraction (CDF). The CDF uses the relative enrichment of an inert mineral´s refractory element (X_i) compared to parent bedrock to quantify the relative dissolved mass loss in the regolith. For this purpose, we ratio the concentration of such an immobile element ($[X_i]$) (Merrill 1906; Barth 1961) in unweathered parent bedrock (p) to its concentration in weathered regolith (r) (Brimhall and Dietrich 1987; Riebe et al. 2003) in Equation 2-2. A CDF-value of 0 indicates no chemical depletion, while a CDF-value of 1 would mean that parent bedrock dissolution has run to completion. In reality, since quartz and secondary precipitates remain even in heavily weathered regolith the global observed maximum CDF approaches a value of 0.5 to 0.7, depending on bedrock mineralogy (Dixon and von Blanckenburg 2012).

$$\mathrm{CDF} = 1 - \frac{[\mathrm{X_i}]_\mathrm{p}}{[\mathrm{X_i}]_\mathrm{r}} \qquad \textbf{Equation 2-2}$$

The chemical weathering flux can be disentangled from total denudation by multiplying the CDF by D (Riebe et al. 2003) (Equation 2-3). Accordingly, E can be calculated from the difference between D and W (Equation 2-1 and Equation 2-3).

$$W = D \cdot CDF \qquad \textbf{Equation 2-3}$$

Absolute mass fluxes can be expressed as elemental fluxes, which form the basis to assess the cycling of mineral nutrients between forest ecosystem compartments. For example, RP is expressed as RP^X by multiplying RP with the concentration of the element of interest (X) in unweathered parent bedrock (Equation 2-4).

$$RP^X = D \cdot [X]_{rock} \qquad \textbf{Equation 2-4}$$

Chemical weathering of bedrock and regolith releases elements dissolved from primary minerals into solution. A dissolved element X may follow one of three paths: it may be exported as solute via the stream, it may be utilised by forest trees, or it may be incorporated into or adsorbed onto secondary minerals or (oxy-)hydroxides. An estimate of the time-integrated total amount of an individual element following the first two paths can be made based on the elemental mass transfer coefficient ($\tau^X_{X_i}$). $\tau^X_{X_i}$ quantifies the relative loss or gain of element X in the weathering zone and provides a maximum estimate of dissolved nutrients available to forest trees, as some solute can be lost into drainage prior to uptake. Specifically, $\tau^X_{X_i}$ is the concentration ratio of an immobile element ($[X_i]$) to a mobile element of interest ([X]) in parent bedrock and the regolith (Equation 2-5) (Brimhall and Dietrich 1987; Anderson et al. 2002). If $\tau^X_{X_i}$ is negative, a fraction of element X was lost by mineral dissolution. Conversely, if $\tau^X_{X_i}$ is positive, a fraction of element X was added by accumulating secondary precipitates or by admixing of organic matter or external atmospheric inputs into the regolith. If $\tau^X_{X_i}$ is zero, neither loss nor gain occurred, and unweathered parent bedrock is present, or inputs are balanced by outputs.

$$\tau^X_{X_i} = \frac{[X_i]_p}{[X_i]_r} \cdot \frac{[X]_r}{[X]_p} - 1 \qquad \textbf{Equation 2-5}$$

The elemental chemical weathering flux ($W^X_{regolith}$) provides the time-integrated dissolution flux of element X from primary minerals minus the incorporation flux of X into secondary minerals and (oxy-)hydroxides formed in the regolith. $W^X_{regolith}$ is inferred from the total denudation flux, the mass

transfer coefficient ($\tau^{X}_{X_i}$) and the concentration of element X in unweathered parent bedrock by multiplying Equation 2-4 with the negative of Equation 2-5 (Equation 2-6).

$$W^{X}_{regolith} = D \cdot [X]_{rock} \cdot \left(-\tau^{X}_{X_i}\right) \quad \textbf{Equation 2-6}$$

The fraction of $W^{X}_{regolith}$ which is not involved in secondary mineral or (oxy-)hydroxide formation is either drained into the stream or utilised by vegetation, from which it can also be drained into the stream after solubilisation from litter.

2.2.1.2 Inventories

The conversion of depth-integrated concentrations of element X into an inventory provides a metric on the availability of element X in the regolith. The inventory of element X in compartment j (I^{X}_{j}, where j denotes bulk regolith (bulk), the forest floor (ff), or the biologically available fraction of regolith (bioav)), is calculated by the integral of the depth interval´s concentration of element X in compartment j ($[X]_j$), the soil density (ρ) and the thickness (dz) of the respective depth interval (Equation 2-7).

$$I^{X}_{j} = \int_{z=0}^{z} [X]_j \cdot \rho \cdot dz \quad \textbf{Equation 2-7}$$

2.2.1.3 Turnover times

Following the terminology suggested for terrestrial ecosystem ecology by Sierra et al. (2017) and Spohn and Sierra (2018), the turnover time is a quantification of the capacity of an ecosystem to store and cycle an element. In other words, the turnover time of element X in compartment j represents the mean time an element X remains in a given compartment before being transferred from this source compartment into another compartment. In this sense it may be considered analogous to the concept of a residence time in hydrology or geochemistry. Turnover time can thus be defined as the ratio of the inventory of a compartment (pool) to the input flux into the pool or output flux from the pool. We do not require the balance of inbound and outbound fluxes and thus do not assume the steady state of inventories. Yet, over the timescale of a few turnover times the fluxes must attain some balance to avoid total depletion. The total turnover time in the compartments we consider is governed by several in- and outbound fluxes. We do not consider total turnover (or residence) times for these compartments. Rather, we calculate turnover times with respect to one specific flux (denoted by the second subscript). For example, $T^{X}_{bioav,W}$ represents the mean time element X spends in the biologically

available inventory with respect to supply from dissolution of primary minerals and secondary precipitates ($W^X_{regolith}$) (Equation 2-8). Thereby, $T^X_{bioav,W}$ provides the minimum turnover time estimate, as some fraction of $W^X_{regolith}$ could be directly drained via groundwater into streams instead of arriving in the biologically available fraction by e.g. adsorption.

$$T^X_{bioav,W} = \frac{I^X_{bioav}}{W^X_{regolith}} \qquad \textbf{Equation 2-8}$$

2.2.2 Organic nutrient cycle

Put simply, the organic nutrient cycle incorporates nutrient uptake from forest trees, nutrient return to the forest floor followed by either nutrient re-utilisation or nutrient export from the forest ecosystem by drainage.

2.2.2.1 Fluxes

The total nutrient uptake flux of the entire forest ecosystem (U^X_{total}) can be quantified from estimates of gross primary production (GPP). As GPP includes the release of carbon by plant mitochondrial respiration (R_{plant}), which accounts for about half of the GPP flux (Chapin et al. 2012), GPP must be converted into net primary productivity (NPP) (Equation 2-9). We determined U^X_{total} from Equation 2-10, where $[X]_{tree}$ is the bulk tree nutrient concentration in dry biomass and $[C]_{tree}$ is the carbon concentration of bulk tree, typically 50 %. Equation 2-10 converts the carbon-based NPP flux into a total annual dry biomass production flux of the element of interest.

$$NPP = GPP - R_{plant} \qquad \textbf{Equation 2-9}$$

$$U^X_{total} = \frac{NPP \cdot [X]_{tree}}{[C]_{tree}} \qquad \textbf{Equation 2-10}$$

After nutrient utilisation, nutrients are returned to the forest floor by litterfall (L^X) – comprising mainly non-woody foliage (leaves and needles) and some woody foliage (twigs). Subsequently these nutrients are either re-utilised or lost from the forest ecosystem in particulate form by plant litter erosion (E^X_{org}) or in solute form after plant litter decomposition and solubilisation (S^X_{org}).

In the absence of difficult field-based measurements the elemental plant litter erosion flux (E^X_{org}) can be estimated from the cosmogenic *in situ* ^{10}Be-derived erosion flux (E) in units t km^{-2} yr^{-1}, the concentration of element X in the litter layer ($[X]_{litter}$) and a density ratio of bedrock to plant litter that converts the annual ^{10}Be-derived mass per area erosion flux of bedrock into an annual mass per area erosion flux of plant litter (Equation 2-11).

$$E_{org}^{X} = E \cdot \frac{\rho_{rock}}{\rho_{litter}} \cdot [X]_{litter}$$ **Equation 2-11**

The elemental plant litter solubilisation flux (S_{org}^{X}) can be estimated from the inventory of the forest floor (I_{ff}^{X}, Equation 2-7) and a plant litter decay rate constant (k, yr^{-1}) (Equation 2-12), where 1/k represents the overall and non-element specific turnover time of plant litter.

$$S_{org}^{X} = I_{ff}^{X} \cdot k$$ **Equation 2-12**

2.2.2.2 Turnover times

The turnover time of element X in the forest floor with respect to loss by plant litter erosion and drainage of decomposed and solubilised plant litter is $T_{ff,loss}^{X}$. We note that $T_{ff,loss}^{X}$ merely presents a rough estimate, as neither E_{org}^{X} nor S_{org}^{X} can be estimated with certainty, and because both parameters also depend on the time X is cycled through forest trees where it is not prone to loss (see Section 2.3.4).

$$T_{ff,loss}^{X} = \frac{I_{ff}^{X}}{E_{org}^{X} + S_{org}^{X}}$$ **Equation 2-13**

The turnover time of element X in the forest floor with respect to the outbound nutrient uptake flux by forest trees is $T_{ff,U_{ff}}^{X}$ (where U_{ff}^{X} represents the major fraction of the total nutrient uptake flux, see Section 2.2.3).

$$T_{ff,U_{ff}}^{X} = \frac{I_{ff}^{X}}{U_{ff}^{X}}$$ **Equation 2-14**

The turnover time of element X in the forest floor with respect to the inbound litterfall flux (L^{X}) through the annual nutrient return from forest trees to the forest floor is $T_{ff,L}^{X}$.

$$T_{ff,L}^{X} = \frac{I_{ff}^{X}}{L^{X}}$$ **Equation 2-15**

2.2.3 Coupling the geogenic nutrient pathway with the organic nutrient cycle

2.2.3.1 Fluxes

In our conceptual forest ecosystem, the fluxes of E_{org}^{X} (plant litter erosion flux) and S_{org}^{X} (plant litter drainage flux) must be replaced. Following the terminology in Cleveland et al. (2013) we term this nutrient uptake replacement flux that stems from fresh nutrients "new" (U_{new}^{X}), as it comprises nutrients that are utilised by forest trees for the first time and are not re-utilised from the forest floor. Such new nutrients could be sourced from external atmospheric wet and dry deposition or, if these external fluxes are negligible relative to $W_{regolith}^{X}$, from $W_{regolith}^{X}$ itself. We have no *a priori* means to assess how much of $W_{regolith}^{X}$ is used for nutrient uptake by forest trees, as some of the weathering flux is likely drained via groundwater into the stream. By assuming that U_{new}^{X} at best balances nutrient losses from the organic nutrient cycle, we instead equate U_{new}^{X} with the sum of nutrient loss from plant litter erosion and drainage by Equation 2-16.

$$U_{new}^{X} = E_{org}^{X} + S_{org}^{X} \qquad \textbf{Equation 2-16}$$

However, for most mineral nutrients "new" nutrients derived from rock weathering represent only a minor fraction of U_{total}^{X}. Vice versa, the major flux to U_{total}^{X} originates from the forest floor. For this purpose, we disentangled U_{total}^{X} in Equation 2-17 to reflect both the fraction of element X utilised from the forest floor (U_{ff}^{X}) and the "new" nutrient (U_{new}^{X}).

$$U_{total}^{X} = U_{ff}^{X} + U_{new}^{X} \qquad \textbf{Equation 2-17}$$

2.2.3.2 Nutrient recycling factor

The fraction of nutrient X that is returned to the forest floor by litterfall (L^{X}) and is neither eroded as plant litter nor lost into drainage after being leached from plant litter can be re-utilised by forest trees. We term this re-utilisation process `nutrient recycling´ and assess the efficiency of the nutrient recycling loop with the `nutrient recycling factor´ (Rec^{X}). Rec^{X} is a metric that quantifies the number of utilisation and return cycles of a nutrient from organic matter by forest trees after its release by chemical weathering from parent bedrock or atmospheric dry and wet deposition. We parameterise this nutrient recycling factor by the ratio of the total nutrient uptake flux of element X (U_{total}^{X}) relative to U_{new}^{X} (Equation 2-18). Because measuring U_{new}^{X} is principally impossible we substitute U_{new}^{X} by the sum of E_{org}^{X} and S_{org}^{X} (Equation 2-16) in the right-hand term in Equation 2-18, instead.

$$\mathrm{Rec^X} = \frac{\mathrm{U^X_{total}}}{\mathrm{U^X_{new}}} = \frac{\mathrm{U^X_{total}}}{\mathrm{E^X_{org}} + \mathrm{S^X_{org}}} \qquad \textbf{Equation 2-18}$$

Because over millennia the replacement flux for $\mathrm{E^X_{org}}$ and $\mathrm{S^X_{org}}$ must originate from the geogenic pathway, hence $\mathrm{W^X_{regolith}}$, unless atmospheric wet and dry deposition are non-negligible, we parameterise $\mathrm{Rec^X}$ by dividing $\mathrm{U^X_{total}}$ by $\mathrm{W^X_{regolith}}$ (Equation 2-19, Uhlig et al. 2017). This parameterisation of $\mathrm{Rec^X}$ provides the advantage of circumventing the impossibility of measuring $\mathrm{U^X_{new}}$ directly and the methodological challenges involved in estimating $\mathrm{U^X_{new}}$ indirectly through $\mathrm{E^X_{org}}$ and $\mathrm{S^X_{org}}$ (see Section 2.3.4). Note that $\mathrm{Rec^X}$ therefore represents a minimum estimate of the number of nutrient uptake and re-utilisation cycles of element X through forest trees. This is because not all of the weathering release flux may be available to forest trees, if some of this flux is lost, for example, into groundwater before nutrient uptake.

$$\mathrm{Rec^X} = \frac{\mathrm{U^X_{total}}}{\mathrm{W^X_{regolith}}} \qquad \textbf{Equation 2-19}$$

2.2.3.3 Turnover times

In a conceptual forest ecosystem in which the organic nutrient cycle is coupled to the geogenic nutrient pathway, the inventory of the biologically-available fraction of the regolith represents a source for the forest trees´ $\mathrm{U^X_{new}}$. The turnover time of element X in the biologically available fraction of the regolith with respect to new nutrient utilisation by forest trees is $\mathrm{T^X_{bioav,U_{new}}}$ (Equation 2-20).

$$\mathrm{T^X_{bioav,U_{new}}} = \frac{\mathrm{I^X_{bioav}}}{\mathrm{U^X_{new}}} \qquad \textbf{Equation 2-20}$$

2.3 Methods

2.3.1 Study sites

Our two study sites are in the uplands of southern Germany: Conventwald (CON) in the Black Forest (Schwarzwald) and Mitterfels (MIT) in the Bavarian Forest (Bayerischer Wald). Both are part of the long-term forest ecosystem monitoring program “International Co-operative Program on assessment and monitoring of air pollution effects on forests (ICP Forest Level II)”. For details of location, climatic regime, vegetation, geomorphology and mineralogy at each catchment see Table 2-2. While most aspects of the sites are similar, critically the catchments differ in the chemical composition of their bedrock and in their elemental atmospheric supply fluxes. Even though neither study site was glaciated

during the Quaternary, periglacial slope deposits developed and provide the source material for pedogenesis.

Table 2-2 Characteristics of the study sites in the Black Forest (CON, Schwarzwald) and the Bavarian Forest (MIT, Bayerischer Wald).

Study site	Conventwald (CON)	Mitterfels (MIT)
Longitude[a] Latitude[a]	48°1.20222'N 7°57.93996'E	48°58.54860'N 12°52.49388'E
Altitude (m.a.s.l.) Slope (°)	733 - 863 17 (south-facing)	985 - 1037 10 (west-facing)
Mean annual temperature (°C)[b]	6.8	5.5
Mean annual precipitation (mm)[b]	1749	1580
Main vegetation type	Fagus sylvatica, Picea abies	Fagus sylvatica, Picea abies
Soil type (WRB)[c]	Dystric Cambisol	Dystric Cambisol
Lithology	Paragneiss	Paragneiss
Mineralogy[d]	Quartz: 12% Anorthite: 27% Albite: 25% K-feldspar: 12% Pyroxene: 9% hbl*, crd^{+}, chl*, bt*	Quartz: 20% Anorthite: 16% Albite: 31% K-feldspar: 16% Pyroxene: 5% Bt*
Denudation rate (t km^{-2} yr^{-1})[e]	125 ± 11 (SE)	57 ± 5 (SE)
Weathering rate (t km^{-2} yr^{-1})	71 ± 19 (SE)	8 ± 8 (SE)
Erosion rate (t km^{-2} yr^{-1})	54 ± 15 (SE)	49 ± 50 (SE)
Chemical depletion fraction (CDF)	0.57	0.14

[a] catchment coordinates at the outlet of the catchment (WGS84)
[b] data for CON from Forest Research Institute of Baden-Wuerttemberg (FVA) and data for MIT from State Institute of Bavaria for Forestry and Silviculture (LWF)
[c] WRB: World Reference Base for Soil Resources
[d] Modal mineralogy (vol-%) was inferred from CIPW calculations
[e] measured with cosmogenic *in situ* ^{10}Be
Hbl: hornblende, crd: cordierite, chl: chlorite, bt: biotite
* hydrous minerals are not considered in CIPW calculations
[+] identified by X-ray diffraction

Elemental atmospheric supply fluxes from unpublished data from the Bayerische Landesanstalt für Wald und Forstwirtschaft (LWF) for MIT and from the Forstliche Versuchsanstalt Baden-Wuerttemberg (FVA) show higher wet atmospheric deposition fluxes at MIT with $\mathrm{Dep}_{\mathrm{wet}}^{\mathrm{X}}$ of K, Ca, and Na all being in the range of 300-600 mg m^{-2} yr^{-1} at MIT and 200-300 mg m^{-2} yr^{-1} at CON (Table 2-3). At MIT the relative elemental abundances do not resemble any natural dust source and are most likely caused by anthropogenic inputs. Thus, we consider wet atmospheric deposition fluxes to contribute to tree nutrition at MIT only since industrialisation and modern land use. Over the time scales of this study atmospheric inputs can be considered negligible compared to rock weathering sources (Table 2-2, (Table 2-3).

Table 2-3 Elemental fluxes at CON and MIT.

	K		Ca		Mg		P		Na		Al		Fe		Mn		Zn	
	CON	MIT	CON	MIT	CON	MIT	CON	MIT	CON	MIT	CON	MIT	CON	MIT	CON	MIT	CON	MIT
	(mg m^{-2} yr^{-1})		(mg m^{-2} yr^{-1})		(mg m^{-2} yr^{-1})		(mg m^{-2} yr^{-1})		(mg m^{-2} yr^{-1})		(mg m^{-2} yr^{-1})		(mg m^{-2} yr^{-1})		(mg m^{-2} yr^{-1})		(mg m^{-2} yr^{-1})	
RP^X	2200	1300	5600	1600	2900	730	120	110	2900	1500	12000	5100	7000	2600	120	40	11	7.1
(uncertainty)	*320*	*200*	*580*	*280*	*380*	*240*	*27*	*70*	*410*	*200*	*1000*	*610*	*1100*	*770*	*17*	*13.0*	*1.6*	*2.60*
$W^X_{regolith}$	1000	240	5500	980	2000	400	84	65	2400	780	7100	280	4500	160	80	14	2.4	3.0
(uncertainty)	*150*	*130*	*470*	*150*	*210*	*33*	*10*	*12*	*240*	*200*	*860*	*230*	*510*	*190*	*8.3*	*1.2*	*1.2*	*0.24*
Dep^X_{wet} [a]	160	340	380	580	53	73	7.1	46	290	360	n.d.	48	n.d.	58	10	35	42	n.d.
(uncertainty)	*57*	*220*	*79*	*270*	*11*	*27*	*5.5*	*35*	*88*	*180*	*n.d.*	*26*	*n.d.*	*18*	*5.1*	*35*	*45*	*n.d.*
U^X_{total}	6400	5000	8700	2400	830	650	960	900	48	68	190	150	*66*	*72*	600	160	42	23
(uncertainty)	*1200*	*1200*	*2400*	*430*	*87*	*130*	*54*	*120*	*9.3*	*70*	*110*	*93*	*24*	*23*	*170*	*39*	*13*	*5.1*
L^X [a]	1700	1700	1700	1400	430	320	330	410	n.d.	n.d.	170	54	110	54	230	180	15	14
(uncertainty)	*980*	*500*	*280*	*310*	*150*	*100*	*120*	*170*	*n.d.*	*n.d.*	*66*	*18*	*46*	*16*	*50*	*43*	*0.57*	*3.2*
U^X_{ff}	6000	4700	8200	1900	680	550	820	750	n.d.	31	n.d.	n.d.	n.d.	n.d.	540	99	n.d.	n.d.
U^X_{new}	380	250	590	480	150	100	140	140	52	37	420	370	220	180	58	58	n.d.	n.d.
E^X_{org}	150	110	230	220	46	36	28	49	7.7	5.0	24	23	15	17	25	26	n.d.	n.d.
S^X_{org}	240	140	370	260	100	68	120	95	45	32	390	350	200	170	33	32	n.d.	n.d.

RP^X = regolith production flux, $W^X_{regolith}$ = chemical weathering flux, Dep^X_{wet} = wet atmospheric deposition flux, U^X_{total} = ecosystem nutrient uptake flux, L^X = litterfall flux, U^X_{ff} = forest floor nutrient uptake flux, U^X_{new} = nutrient uptake flux from the biologically available fraction, E^X_{org} = plant litter erosion flux, S^X_{org} = plant litter solubilisation flux

[a] data provided by the State Institute of Bavaria for Forestry and Silviculture (LWF) for MIT and the Forest Research Institute Baden-Wuerttemberg (FVA) for CON.

Uncertainties of $W^X_{regolith}$ and U^X_{total} are estimated by Monte-Carlo simulations (see section 2.3.4) and of RP^X by conservative error propagation.

2.3.2 Sampling

Forest floor samples originate from soil pits sampled by Lang et al. (2017) some tens of meters upslope from the drill sites at each study site. Regolith was sampled at depth increments of 20 cm from a 3 m deep trench. Regolith beyond 3 m depth was sampled from 20 m (CON) and 30 m (MIT) deep drill cores, with each regolith sample integrating a drilled depth of about 0.5 m to about 1 m (Figure 2-2). Diesel-powered wireline core-drilling was required, as thick regolith containing periglacial slope deposits separated soil from unweathered parent bedrock. Dry core-drilling was performed at CON from 0 m depth to the regolith-bedrock interface at 7 m depth, and only to a depth of 5.5 m at MIT, which is not the regolith-bedrock interface, but where the abundance of fragmented rocks increased significantly. Hydraulic-rotary drilling using creek water as drilling fluid from the neighbouring watersheds was used to sample bedrock at both sites from drill-cores. However, at MIT hydraulic rotary drilling was also performed within regolith above the regolith-bedrock interface. This practice could have led to alteration of regolith properties such as soil pH and the chemical composition of the easily exchangeable fraction, and so where possible samples from hydraulically-drilled regolith sections were taken from the interior of coherent core pieces. Where this was impossible, samples were taken from wet cuttings integrating over ~2 m depth.

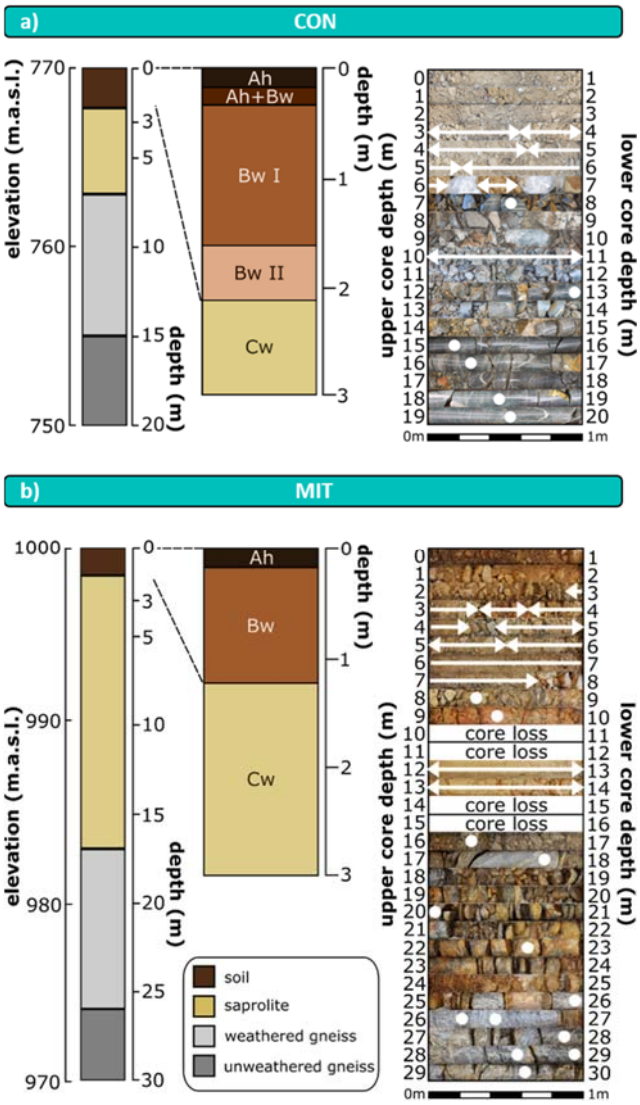

Figure 2-2 Schematic depth distribution of drill cores and soil profiles (left hand side); stacked photographs of drill core sections with labelled sampling points and sampled depth intervals (right hand side) at CON (panel a) and MIT (panel b). Arrows and cycles illustrate sampling points and depth intervals, respectively. Sampled depth intervals were selected to correspond to drill sections and changes in regolith appearance. Polyethylene bags at CON between 6 m and 7 m depth contain coherent regolith. m.a.s.l.: meter above sea level. Ah, Bw, Cw: soil horizons according to IUSS/ISRIC/FAO 2006. Boundary of soil to saprolite is defined to be represented by the boundary between Bw horizon to Cw horizon. Colour scheme of schematic drill cores is used in subsequent profile figures to assign data to soil, saprolite and bedrock.

Living wood, leaves and needles were sampled from representative mature trees of the prevailing species European beech (*Fagus sylvatica)* and Norway spruce (*Picea abies)*. Living wood was sampled by using an increment borer. Leaves and needles were sampled from young branches nearest the forest floor in September 2014.

2.3.3 Analytical methods

Element concentration and radiogenic Sr isotope analyses were performed at the Helmholtz Laboratory for the Geochemistry of the Earth Surface (HELGES) at GFZ Potsdam (von Blanckenburg et al. 2016). X-ray fluorescence spectrometry was performed with the Isotope Geochemistry section at GFZ Potsdam. Phosphorus Hedley sequential fractionation was done at the University of Bonn, INRES.

2.3.3.1 Chemical composition of regolith and bedrock

The bulk chemical composition of regolith, bedrock, and international reference materials including GM (granite, ZGI), TB (clay shale, ZGI), SRM 2709a (San Joaquin soil, NIST) and TILL-1 (soil, CCRMP) were analysed at GFZ Potsdam. Prior to analyses, representative sections of the drill core were cut into fist-sized pieces, weathering rinds removed, and bedrock pieces crushed and pulverised to <60 µm using an agate planetary mill. From representative soil and saprolite samples, rock fragments were removed, oven-dried (60 °C, 24 h), homogenised, split by using a sample divider, sieved to <2 mm and pulverised to <60 µm. Glass tablets were made by alkali fusion using Li-metaborate and stepwise-heating to 1200 °C. The chemical composition of the samples and reference materials was analysed by X-ray fluorescence spectroscopy (XRF, PANalytical Axios Advanced) with a relative uncertainty of 5 % for major elements and 10 % for trace elements. The loss on ignition (LOI) of each sample was determined by weighing the glass tablets after fusion. Concentration data and respective uncertainties are reported in Supplementary Table 2-1a and 2-1b.

2.3.3.2 Chemical composition of vegetation

Leaves and needles were rinsed in the field with deionised water (Milli-Q, 18 MΩ) to avoid contamination by dust particles. Prior to analysis, leaves, needles and bulk wood were oven-dried (60 °C, 24h), and leaves and needles crushed and homogenised. Sections of heartwood (dead part of stem wood) and sapwood (living part of stem wood) spanning several consecutive annual rings were sampled from core wood and cut into pieces of ~5 cm length. Samples were digested in PFA vials using a microwave (MLS start) and ultrapure concentrated acid mixtures comprising H_2O_2, HNO_3, HCl and HF. The HF treatment was performed to destroy any Si-containing precipitates that may have formed after total evaporation of the dissolved sample. Chemical compositions were analysed by inductively coupled plasma optical emission spectrometry (ICP-OES, Varian 720ES) for major and trace element

concentrations, with relative uncertainties of 10 % (see Supplementary Table 2-3). The international reference material SRM 1515 (apple leaves, NIST) was processed with each sample batch.

2.3.3.3 In situ ^{10}Be concentrations in quartz

To determine *in situ* ^{10}Be concentrations bedload sediment was sampled at the outlet of the catchment. This averaged the spatially heterogeneous *in situ* ^{10}Be concentrations of soil over the entire catchment area and ensured that flux estimates are representative over all possible topographic positions. Bedload sediment was sieved to 125-250 µm and this aliquot was purified from matrix minerals to 10 g of pure quartz. Then 400 µg of an in-house ^{9}Be "phenakite" carrier with a ^{9}Be concentration of 372.5 µg/g was added to each sample, before the pure quartz sample was digested with 14 M HF and Be was separated from matrix elements by cation chromatography following the method described in von Blanckenburg et al. (2004). Finally, Be was further purified by alkaline precipitation following von Blanckenburg et al. (1996), oxidised, pressed into accelerator mass spectrometer (AMS) cathodes and analysed at the University of Cologne Centre for Accelerator Mass Spectrometry (AMS). Procedural blanks were run with each sample batch and subtracted from the samples. The ^{10}Be Blank contribution was about 5 %.

2.3.3.4 Soil pH

The pH of soil and saprolite (hereafter termed "soil pH" for ease, although the pH of saprolite is also referred to soil pH) was analysed after suspension in 0.01 M $CaCl_2$. Specifically, soil pH was measured in a suspension of 1 g oven-dried (60 °C, 24 h) bulk soil/saprolite (<2 mm) in 5 ml 0.01 M $CaCl_2$ with a WTW pH meter, 3-point-calibrated using Merck buffer solutions. To monitor stability, accuracy and reproducibility, Merck pH 4 buffer solution and the international reference material IRMM-443-7 (Cambisol, BCR/IRMM representing the same soil type as those at our study sites) were measured every tenth sample. Reproducibility of measurements was better than ± 1.5 %. Soil pH values are reported in Supplementary Table 2-1c.

2.3.3.5 Sequential extraction procedure and chemical analyses

Sequential extractions were performed to trace the depth distribution of nutritive elements available for uptake by trees. The procedure was designed to extract increasingly stronger-bound nutrients with each extraction step to mimic the increasing effort a forest tree and symbiotic organisms must exert to access a nutrient from the regolith. For extracting the metal group of nutritive elements the method from Tessier et al. 1979 was adapted (note, because binding behaviour of biologically-available phosphorus differs, a separate procedure was required for P; see below). Sample to extractant ratios of 1:7 were used throughout (14 ml of reactants to 2 g of dried bulk soil, sieved to <2 mm), consistent with previous studies (e.g. Baruah et al. 2011). Each extraction step (except the oxidisable extraction

step) was performed by mild agitation. After each extraction step, the suspension was centrifuged at 4200 rpm for 30 min and the supernatant pipetted off and filtered through a 0.2 µm acetate filter. Between each extraction step, soil samples were rinsed with 10 ml deionised water. The sequential extraction method was performed in two parallel aliquots of soil and saprolite, of which the supernatants were combined for analyses. Finally, the samples were re-dissolved with concentrated acid mixtures (HF, HCl, HNO_3) and prepared for ICP-OES analyses. The element concentration of each extracted fraction was measured with ICP-OES following the procedure described in Schuessler et al. (2016), with relative uncertainties better than 5 % (Al, Ba, Ca, Fe, Mn, Na, S, Sr) and 10 % (K, Mg) based on repeat analyses of the international reference materials SLRS-5 (river water, NRC CNRC), SRM 1640a (river water, NIST) and M212 (USGS) and synthetic in-house standards. Data from each extraction step are listed in Supplementary Table 2-2.

The *water-soluble fraction* represents the most labile soil compartment, most accessible to plants (He et al. 1995) and was extracted by suspending in deionised water (Milli-Q, 18 MΩ) for 24 h, with 1h of ultrasonication prior to extraction. The *exchangeable fraction* consists of elements that form weak electrostatic bonds between the hydrated surfaces of primary phyllosilicates, secondary clay minerals, or organic matter and was extracted with 1 M NH_4OAc for 2h. We cannot exclude that elements that were structurally bonded with organic matter could have accidently been extracted by 1M NH_4OAc too. The *carbonate fraction* is accessible to forest trees if roots excrete low-molecular weight organic acids into the rhizosphere to decrease pH and dissolve minerals of low dissolution kinetics and was extracted with such an acid, namely 1 M CH_3COOH for 24 h. The *oxidisable fraction* is accessible to forest trees if tree roots develop a symbiotic relationship with organic matter decomposing organisms such as mycorrhiza fungi (Wardle et al. 2004a) that break down organic matter into plant-accessible inorganic forms. The oxidisable fraction was extracted with hydrogen peroxide in dilute nitric acid medium (4 ml 30 % H_2O_2 in 0.01 M HNO_3; following e.g. Tessier et al. 1979; Gibson and Farmer 1986)) and incubated at 85°C. After 2 hours 3 ml 30 % H_2O_2 in 0.01 M HNO_3 was added and the oxidisation was continued at 85 °C for 3 hours. Finally, 5 ml of 2.4 M NH_4OAc was added and the mixture was agitated for 30 min to desorb any part of the oxidisable fraction that might have bound to exchangeable sites. The *reducible fraction* was not extracted here so as to avoid attacking primary silicate minerals (Tessier et al. 1979). Since under common soil conditions the reducible fraction is relatively stable and thus biologically inaccessible (Lee and Kittrick 1984), this should not compromise our interpretation of these data.

2.3.3.6 Phosphorus Hedley sequential fractionation

Sieved and ground aliquots from core samples were extracted sequentially in duplicate according to a modified Hedley procedure (Tiessen and Moir 1993) at the University of Bonn, INRES. This method assesses P availability via stepwise extraction of 0.5 g soil at a 1:60 soil:solution ratio (w/v) using anion

exchange resin (termed ´resin P´), 0.5 M $NaHCO_3$ (termed ´P-$NaHCO_3$´), 0.1 M NaOH (termed ´P-NaOH´) and 1 M HCl (termed ´P-HCl´) over 16 hours. Samples are then centrifuged and filtered through ashless quantitative paper filters (Albet LabScience, Dassel, Germany). Subsequently, the ´P-HCl_{conc}´ fraction was extracted with hot concentrated HCl (80 °C, 20 minutes). For the final extraction of ´residual P´, *aqua regia* (following Lauer et al. 2013) was used. For each fraction, inorganic P (P_i) was determined by the molybdenum-blue method (Murphy and Riley 1962) and total P by ICP-OES (Ultima 2, HORIBA Jobin Yvon, Longjumeau, France). Organic P (P_o) was then calculated as the difference of total P and P_i. P concentrations are reported in Supplementary Table 2-2e.

2.3.3.7 Radiogenic strontium ($^{87}Sr/^{86}Sr$) ratios

Radiogenic Sr analyses were performed on unweathered and weathered bedrock, bulk soil and bulk saprolite after sample digestion in PFA vials. Sr was separated from matrix elements using inverted disposable pipettes packed with 200 µl Sr Spec resin (TrisKem SR-B50-S (50-100 µm)). Matrix elements were removed by elution with 5.5 ml 7.5 M HNO_3 and Sr was eluted with 2 ml deionised water (Milli-Q water, 18 MΩ). To destroy any organic crown-ether released from the Sr Spec resin, the Sr fraction was dried, re-dissolved and treated in closed PFA vials for more than 12 h in a concentrated acid mixture (H_2O_2, HNO_3) at 85 °C and then in concentrated HNO_3 at 170 °C. The purity of the Sr fraction was monitored by ICP-OES analyses. Impurities were significant only for Ba and were kept below a Ba/Sr ratio of less than 5. Doping tests (not shown here) with SRM 987 demonstrate the absence of analytical bias below this threshold. $^{87}Sr/^{86}Sr$ was measured as 40 ppb pure Sr solutions in 0.3 M HNO_3 on a multi collector inductively coupled plasma mass spectrometer (MC-ICP-MS, Thermo Neptune) in low mass resolution using an APEX-Q (ESI), and a nickel sampler cone. $^{87}Sr/^{86}Sr$ ratios were determined over 8 blocks of 10 cycles with an integration time of 4.194 seconds. The sequence of a sample run consisted of 5-12 blocks where each block comprised a blank, four samples or reference materials and SRM 987 (not processed through chemistry). Blank correction of samples and reference material during the sequence was less than 0.4 % of sample signal. Simultaneously to the signals of ^{84}Sr (L2), ^{86}Sr (central Faraday Cup), ^{87}Sr (H1) and ^{88}Sr (H2) the signals of ^{82}Kr (L4) and ^{83}Kr (L3) and ^{85}Rb (L1) were monitored to correct for Kr and Rb interferences on the masses 84 and 87 with the Kr and Rb isotope ratios measured prior to the sequence run. The measured $^{87}Sr/^{86}Sr$ ratio was normalised to the $^{88}Sr/^{86}Sr$ ratio of 8.375209 by using an exponential law to correct for natural and instrumental isotope fractionation. Repeat analyses of SRM 987 both processed the same way as samples and without chemistry was used to determine the long-term accuracy of the method. Averages and two standard deviations are SRM 987 = 0.71029 ± 0.00001 (N=240, without chemistry) and SRM 987 = 0.71026 ± 0.00011 (N=32, including chemistry) and are identical to published values for SRM 987 = 0.71029 ± 0.00033 (N=247, Jochum et al. 2005) measured with MC-ICP-MS.

2.3.4 Calculation of Fluxes and Inventories in Forest Ecosystems

2.3.4.1 Total Denudation rates (D)

Catchment wide denudation rates (D) were determined from *in situ* ^{10}Be concentrations of quartz sampled from bedload sediment at the outlet of the catchment (following the approach of von Blanckenburg (2005)). D was calculated from Equation 2-21, where PROD is the production rate (at g^{-1} yr^{-1}) of cosmogenic ^{10}Be at the Earth surface in quartz, $[^{10}Be]_{in\ situ}$ the measured cosmogenic nuclide concentration (at g^{-1}), λ is the decay constant (yr^{-1}) of ^{10}Be and Λ the cosmic ray absorption mean free path (150 g cm^{-2}) in rock. To calculate D a PROD of 4.01 at g^{-1} yr^{-1} at sea-level high latitude (SLHL) (Lal 1991; Stone 2000) was used and scaled for altitude and latitude (Stone 2000). The total denudation rate is reported in Table 2-2.

$$D = \left(\frac{PROD}{[^{10}Be]_{in\ situ}} - \lambda\right)\Lambda \qquad \textbf{Equation 2-21}$$

2.3.4.2 Chemical Depletion Fraction (CDF)

The calculation of CDF requires the presence of an immobile element. We tested the deviation of supposedly immobile elements from the diagonal lines in Figure 2-3 that were inferred from unweathered bedrock concentrations and indicate the weathering enrichment line (Hewawasam et al. 2013; Oeser et al. 2018). At both study sites Zr is considered the most immobile element, as its concentration increase from unweathered bedrock to regolith is most pronounced. Weathered rock or regolith samples that originated from a chemically distinct parent bedrock were disclosed if their Zr concentration was lower than the mean of unweathered bedrock by more than two standard deviations (2SD). These samples were excluded from further consideration. Saprolite and weathered rock samples were also excluded from our dataset if the Cr, Ni, Nb and Ti concentrations are twice those of unweathered parent bedrock (+2SD). Elevated concentrations of these elements indicate the presence of mafic precursor rock such as present in bedrock enclaves. All such excluded samples are labelled in red in Figure 2-3 and are highlighted in Supplementary Table 2-1a and 2-1b.

To estimate the profile's representative chemical depletion fraction, each sites CDF value was estimated by averaging the Zr concentration through the weathering profile from below 1.4 m depth to the regolith-weathered bedrock interface at 7 m depth at CON and at 17 m depth at MIT. The topmost 1.4 m were excluded for this estimate, because there Zr concentrations decrease, which is presumably due to a dilution effect caused by the biological uplift of mainly Al, Fe, Mn, Zn and P, and accumulation in secondary precipitates. All CDF-values were calculated from Equation 2-2 and reported in Supplementary Table 2-1b and 2-1c.

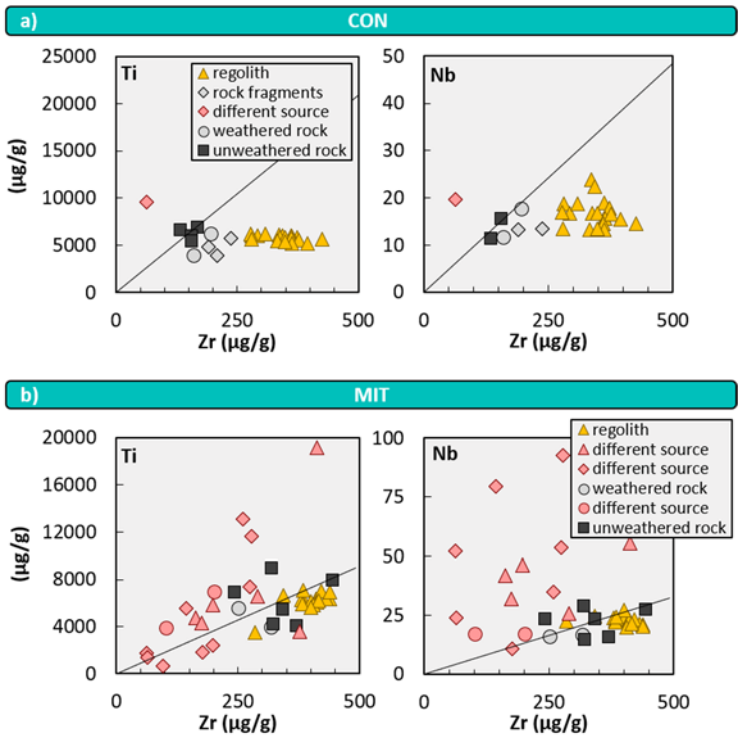

Figure 2-3 Concentrations of elements of very low mobility (y-axis) to Zr (x-axis) in unweathered rock, weathered rock, rock fragments and regolith to identify the immobile element best-suited to calculate mass loss relative to parent bedrock. The diagonal line indicates the weathering enrichment line and is inferred from unweathered rock concentrations. Samples with red symbols denoted as ´different source´ were excluded from the calculation of metrics relying on the concentration of an immobile element, such as the chemical depletion fraction (CDF) and the mass transfer coefficient (τ^{X}_{Xi}), as justified in Section 2.3.4.

2.3.4.3 Elemental chemical weathering fluxes ($W^{X}_{regolith}$)

$W^{X}_{regolith}$ was calculated from Equation 2-6 and reported in Table 2-3. To estimate $W^{X}_{regolith}$ mean τ^{X}_{Zr}-values (calculated from Equation 2-5 and reported in Supplementary Table 2-1c) were used from the entire depth of soil and saprolite from τ^{X}_{Zr}-profiles that exhibit uniform depth distributions. From τ^{X}_{Zr}-profiles that exhibit strong depth dependencies either the most negative τ^{X}_{Zr}-values from the shallowest mineral soil sample (for depletion profiles at MIT) or average τ^{X}_{Zr}-values from below the enrichment horizons from 1.4 m to 7.0 m depth (for depletion-enrichment profiles at CON) were used. Such depth dependencies are characteristic for depletion profiles, depletion-enrichment profiles and biogenic profiles (Brantley and Lebedeva 2011).

2.3.4.4 Ecosystem nutrient uptake fluxes (U^{X}_{total})

U^{X}_{total} was calculated from Equation 2-10 and fluxes are reported in Table 2-3. An elemental bulk tree nutrient concentration was estimated by averaging leaf foliage and wood nutrient concentrations in both prevailing tree species (*Fagus sylvatica* and *Picea abies*) and reported in Table 2-4. The sampling and analyses of roots was excluded in this study, because of the difficulties related to their purification from soil particles, and because the accurate apportionment of elements into different root compartments is notoriously difficult. For example, nutrient concentrations in fine roots are

substantially higher than in coarse roots (Hellsten et al. 2013), but the relative proportions of fine to coarse roots are largely unknown. We nevertheless suggest that the nutrient content in roots is adequately estimated. GPP was not measured at our study sites. Instead, mean annual (1982−2008) GPP data from a global empirical upscaling model, based on FLUXNET data (Jung et al. 2011) were used. For both study sites this equates to about 1260 g m^{-2} yr^{-1} ± 60 (SE, N=360).

Table 2-4 Biomass growth and element concentrations of bulk tree at CON and MIT.

	GPP [a]	K	Ca	Mg	P	Na	Al	Fe	Mn	Zn
	(g m^{-2} yr^{-1})	(µg/g)	(µg/g)	(µg/g)	(µg/g)	(µg/g)	(µg/g)	(µg/g)	(µg/g)	(µg/g)
CON	1260	5100	6900	660	760	38	150	52	480	33
MIT	1260	4000	1900	520	710	54	120	57	120	18

GPP = gross primary productivity
[a] GPP data from a global empirical upscaling model based on FLUXNET data from Jung et al. (2011)

2.3.4.5 Litter erosion flux (E_{org}^{X})

E_{org}^{X} was calculated from Equation 2-11 and reported in Table 2-3. Data on the density of the litter layer was taken from Supplement 2 in Lang et al. (2017). Because the metric E_{org}^{X} includes the cosmogenic nuclide derived denudation rate (D) that integrates over millennia, the litter erosion flux represents an underestimation of E_{org}^{X}. The reason is that the litter layer is of lower density than the soil beneath it that contains quartz on which D was measured.

2.3.4.6 Litter solubilisation flux (S_{org}^{X})

S_{org}^{X} was calculated from Equation 2-12 and reported in Table 2-3. Leaf foliage litter decomposition rate constants (k, yr^{-1}) from litterbag experiments in 30 to 120 years old pure and mixed stands of *Fagus sylvatica* and *Picea abies* from Albers et al. (2004) were used. Decomposition rate constants used for non-woody foliage at pure stands were 0.0257 yr^{-1} for *Picea abies* and 0.0187 yr^{-1} for *Fagus sylvatica*, and at mixed stands 0.0244 yr^{-1} for *Picea abies* and 0.0202 yr^{-1} for *Fagus sylvatica (*Albers et al. 2004). This non-woody foliage derived decomposition rate constants are by about an order of magnitude lower than *in situ* derived decomposition rate constants of woody tissue of, for example, about 0.097 yr^{-1} (Johnson et al. 2014). We note that the litter solubilisation flux S_{org}^{X} provides a maximum approximation of the drainage of nutrients from plant litter, because some fraction of S_{org}^{X} is likely immediately re-utilised by forest trees or infiltrates into soil where it adsorbs onto exchangeable sites. In any case the turnover time of element X in the forest floor with respect to litterfall is sufficiently long to cause substantial nutrient loss by plant litter drainage (see Section 2.4.3.1).

2.3.4.7 Determination of inventories (I_j^X)

I_j^X was calculated from Equation 2-7 for each of the compartments: the biologically available fraction (I_{bioav}^X), forest floor (I_{ff}^X) and bulk regolith including nutrients contained in fragmented rocks (I_{bulk}^X). I_j^X are reported in Table 2-5.

The biologically available fraction comprises the water-soluble and exchangeable fraction that is weakly adsorbed to soil minerals and organic matter. In the case of P the biologically available fraction refers to the inorganic products of the Hedley sequential P fractionation method, namely resin-P, HCO_3-Pi and 1M HCl-Pi. I_{bioav}^X was estimated for two depth intervals that we believe to be principally accessible to tree roots: from 0 m to 3 m (called "<3 m") and from 3 m depth until the interface of saprolite and weathered bedrock (called ">3 m"). The >3 m depth intervals range from 3 m to 7 m at CON and 3 m to 17 m at MIT.

The fine-earth soil density of the soil horizons Ah, Bw and Cw, required to calculate the inventory of the biologically available fraction (I_{bioav}^X) via Equation 2-7, was taken from Lang et al. (2017) and reported in Table 2-5. The bulk soil densities, required to calculate the nutrient inventory of bulk regolith including fragmented rocks (I_{bulk}^X) via Equation 2-7 were taken from unpublished data (Friederike Lang, personal communication) and reported in Table 2-5. To account for fragmented rocks in I_{bulk}^X the concentration in rock fragments was multiplied by the rock fragment content (69 % at CON, 25 % at MIT; Lang et al. (2017)); the nutrient concentration in fine earth multiplied by its percent abundance (100 % minus % rock fragments) was added; this sum was then multiplied by bulk soil densities (>2 mm, including rock fragments). To calculate I_{ff}^X, density data from Lang et al. (2017) and element concentrations from the Oh layer were excluded, because the chemical composition of the Oh layer indicates that the dissolved sample contained not only organic material, but also silicate minerals accidently dissolved during microwave digestion. Hence, data from the Of layer was used instead.

2.3.4.8 Nutrient recycling factor (Rec^X)

Rec^X was calculated from Equation 2-19 and reported in Table 2-6. Note that Rec^X might represent an underestimate. Because Rec^X is parameterised with $W_{regolith}^X$, some fraction of which circumvents nutrient uptake, due to drainage via groundwater into the stream. Rec^X could also be underestimated for some elements, because Rec^X does not account for throughfall and stemflow fluxes, which are generally highest for K compared to other nutrients (e.g. Wilcke et al. 2017). Similarly, the process of nutrient resorption and excretion into the rhizosphere during leaf senescence, followed by re-utilisation in the subsequent growing season, might also lead to underestimation of Rec^X. Note that Rec^X is not affected by intra-plant cycling of nutrients such as storage in perennial wood of nutrients resorbed during senescence of leaves (Aerts 1996; Killingbeck 1996) or wood (Meerts 2002).

Conversely, Rec^X as parameterised in this study could represent an overestimate, if, for example, atmospheric wet deposition fluxes contribute substantially to forest ecosystem nutrition. Wet deposition is believed to be negligible in this study, based on data shown in Table 2-3 and discussed in Section 2.4.1.1.

Table 2-5 Inventories at CON and MIT.

	depth	K		Ca		Mg		P		Na		Al		Fe		Mn	
	interval	CON	MIT	CON	MIT	CON	MIT	CON	MIT	CON	MIT	CON	MIT	CON	MIT	CON	MIT
	(m)	(kg m^{-2})		(kg m^{-2})		(kg m^{-2})		(kg m^{-2})		(kg m^{-2})		(kg m^{-2})		(kg m^{-2})		(kg m^{-2})	
I^X_{bulk} [a]	<3	110	62	8.0	63	73	40	2.7	4.5	44	47	430	280	230	140	2.9	2.3
I^X_{bulk} [a]	3-7	190	150	18	160	120	100	4.4	14	78	72	680	530	360	260	4.4	5.4
I^X_{bulk} [a]	>3[d]	190	370	18	570	120	300	4.4	40	78	160	680	1500	360	980	4.4	20
		(g m^{-2})		(g m^{-2})		(g m^{-2})		(g m^{-2})		(g m^{-2})		(g m^{-2})		(g m^{-2})		(g m^{-2})	
I^X_{ff} [b]		11	6.2	16	12	4.6	3.1	5.2	4.3	2.0	1.4	18	16	9.1	7.6	1.5	1.4
I^X_{bioav} [c]	<3	81	70	220	19	85	19	82	250	22	16	44	43	2.6	11	35	9.5
I^X_{bioav} [c]	>3[d]	190	840	2600	15000	780	860	100	8700	50	220	10	60	7.4	22	13	150

I^X_{bulk} = inventory of element X in bulk regolith, I^X_{ff} = inventory of element X in the forest floor, I^X_{bioav} = inventory of element X in the biologically available fraction

a: Fine soil density data used to calculate I^X_{bioav} was taken from Lang et al. 2017 and are reported here for each soil horizon. MIT: 0.59 g cm^{-3} (Ah), 0.72 g cm^{-3} (Ah+Bw), 0.85* g cm^{-3} (Bw I + Bw II), 1.04 g cm^{-3} (Cw). CON: 0.375 g cm^{-3} (Ah+Bw), 0.65** g cm^{-3} (Bw I), 0.71*** g cm^{-3} (Bw II, Cw).

b: Fine soil density data used to calculate I^X_{ff} was taken from Lang et al. 2017 and are reported here. MIT: 0.02 g cm^{-3} (L), 0.08 g cm^{-3} (Of, Oh+Of). CON: 0.03 g cm^{-3} (L), 0.06 g cm^{-3} (Of, Oh).

c: Bulk soil density data used to calculate I^X_{bulk} was taken from unpublished data (F. Lang, personal communication) and are reported here for each soil horizon. MIT: 0.73 g cm^{-3} (Ah), 0.86 g cm^{-3} (Ah+Bw), 0.98 g cm^{-3} (Bw), and 1.24 g cm^{-3} (Cw). CON: 0.67 g cm^{-3} (Ah+Bw), 1.31 g cm^{-3} (BwI), and 1.90 g cm^{-3} (BwII, Cw).

d: depth interval ranging from 3 m to the boundary of regolith to weathered bedrock

* average value from the Bw horizon from Lang et al. 2017
** from 23-36 cm depth in Lang et al. 2017
*** from 48-78 cm depth in Lang et al. 2017

Table 2-6 Nutrient recycling factor (Rec^X) at CON and MIT.

	K	Ca	Mg	P	Na	Al	Fe	Mn	Zn
CON	6.3	1.6	0.41	11	0.02	0.03	0.01	7.5	18
MIT	21	2.4	1.6	14	0.09	0.53	0.46	11	7.5

2.3.4.9 Uncertainty estimation of nutrient fluxes

The analytical uncertainties of measured data are reported in Supplementary Table 2-1 - 2-3 and in Section 2.3.3. Assigned uncertainties on $\mathrm{Dep}^{\mathrm{X}}_{\mathrm{wet}}$ and L^X are 1 standard deviation (SD) of the entire datasets from Bayerische Landesanstalt für Wald und Forstwirtschaft (LWF) for MIT and from the Forstliche Versuchsanstalt Baden-Wuerttemberg (FVA). For GPP, a much larger dataset is available allowing us to assign 1 standard error (SE). Uncertainty on RP^X incorporates the SE of the catchment-wide denudation rate propagated with the SD of unweathered bedrock concentration. The uncertainties of the nutrient fluxes of $\mathrm{W}^{\mathrm{X}}_{\mathrm{regolith}}$ and $\mathrm{U}^{\mathrm{X}}_{\mathrm{total}}$ were estimated by performing Monte Carlo simulations: 1000 random datasets were sampled within the SD and SE of all input parameters, generated by a Box-Muller transform (Box and Muller 1958). Specifically, input uncertainties into Monte Carlo simulations for $\mathrm{U}^{\mathrm{X}}_{\mathrm{total}}$ were the SE of GPP and the SD of nutrient concentrations in woody and non-woody foliage. Input variable uncertainties for $\mathrm{W}^{\mathrm{X}}_{\mathrm{regolith}}$ were the SE of the catchment-wide denudation rate and the SD of the mean of the weathering profile's elemental loss/gain fraction. Resultant uncertainties on nutrient fluxes are reported in Table 2-3.

2.4 Results and discussion

To evaluate the significance of the various geogenic and organic nutrient reservoirs and cycles for long-term forest ecosystem nutrition we use the sequence of metrics developed in our conceptual framework (Section 2.2). First, we follow this sequence to guide through the values obtained for them and second, we discuss their contribution to the entire system.

2.4.1 Geogenic nutrient pathway

2.4.1.1 Mineral nutrient availability of the regolith

2.4.1.1.1 Denudation (D) and regolith production rates (RP)

The absolute mass loss from the regolith by denudation (sum of weathering flux and erosion flux) is substantially higher at CON (125 t km^{-2} yr^{-1}) than at MIT (57 t km^{-2} yr^{-1}; Table 2-2). Provided that the

weathering profiles are at steady state (meaning quasi-steady regolith thickness over 10 kyr timescale) the denudation rates correspond to the regolith production rates. On a global comparison, both denudation rates are within the range of fast regolith production rates (Dixon and von Blanckenburg 2012). According to the nutrient supply framework for eroding settings (Porder et al. 2007), this mass loss should translate to effective rejuvenation of the topsoil´s nutrient availability by erosion. However, besides advection by erosion the abundance of primary minerals and thus of mineral nutrients remaining at the top of the profile ultimately also depends on water flow and the dissolution kinetics of primary minerals (Maher 2010). To shed light on the nutrient availability we quantified the degree of chemical alteration along the regolith profile.

2.4.1.1.2 Chemical depletion fraction (CDF)

The chemical depletion fraction (CDF, Equation 2-2) at CON is 0.57 (Figure 2-4a), which is close to the global reported maximum CDF for granitic rock in sloping landscapes of ~0.6 (Dixon and von Blanckenburg 2012). This CDF value indicates that dissolution of rock-forming minerals, such as plagioclase, virtually run to completion. At MIT the CDF is substantially lower at 0.14, indicating that rock-forming minerals remain in large quantities and the regolith is only weakly altered. To determine

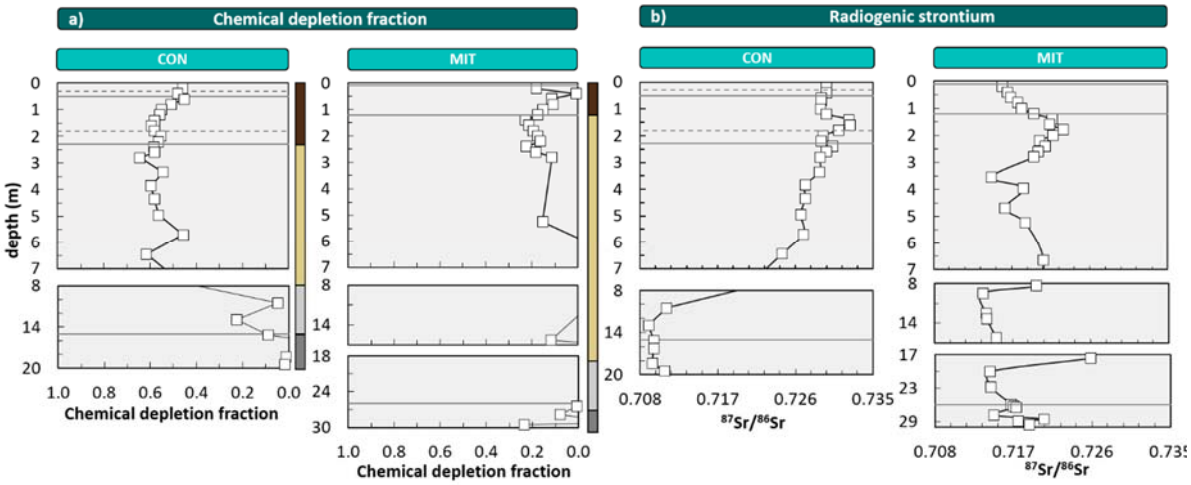

Figure 2-4 Depth distribution of the chemical depletion fraction (CDF, panel a) and the radiogenic strontium isotope ratio ($^{87}Sr/^{86}Sr$, panel b). Solid lines illustrate soil horizon boundaries and the interface of weathered rock to unweathered rock. Dashed lines indicate soil horizon subdivision (see Figure 2-2). Coloured bars at the right site of panel a refer to colour coding of drill core sections from Figure 2-2. For ease of display we changed the y-axis spacing with depth, yet all data are shown continuously. At MIT some CDF-values are negative; these are not displayed for simplicity

whether erosion at the surface sets this difference we used the catchment's CDF values to disentangle D into W and E (see Equation 2-1 and Equation 2-3). We find that soil erosion rates on the millennial timescale are similar at both sites (54 t km^{-2} yr^{-1} at CON and 49 t km^{-2} yr^{-1} at MIT). Given this similarity and given that climate parameters like temperature and precipitation also do not differ strongly between the sites (Table 2-2), we suggest that the parent bedrock's mineralogical composition sets

the susceptibility to chemical weathering. Indeed, the paragneiss at MIT contains more minerals of slow mineral dissolution kinetics. For example, whereas the paragneiss at CON contains only 12 % quartz by vol., MIT contains 20 %. The composition of plagioclase is shifted towards slow mineral dissolution kinetics at MIT. There, plagioclase contains about 31 % albite by vol. and 16 % anorthite by vol., as opposed to about equal proportions of albite (25 %) and anorthite (27 %) at CON. Also, minerals with high dissolution kinetics like hornblende, cordierite, and chlorite were identified in parent bedrock at CON (based on of X-ray diffraction analyses; Supplementary Figure 2-1), but they are absent at MIT. As a result, the weathering rates are 71 t km^{-2} yr^{-1} at CON and only 8 t km^{-2} yr^{-1} at MIT (Equation 2-3). In terms of nutrient availability to the forest ecosystem, we conclude that CON apparently lost a higher fraction of nutrients relative to bedrock than MIT; yet they are also supplied at much higher rates by chemical weathering at CON than at MIT.

2.4.1.1.3 Radiogenic strontium isotope ratio ($^{87}Sr/^{86}Sr$)

As an independent proxy for the overall nutrient availability of the regolith that does not depend on an index element like Zr we use the ratio of the radiogenic Sr isotope ^{87}Sr to the stable Sr isotope ^{86}Sr. $^{87}Sr/^{86}Sr$ of bulk parent bedrock and bulk regolith differ if bedrock mineralogy comprises minerals that are distinct in their dissolution kinetics, Sr contents and $^{87}Sr/^{86}Sr$ compositions (Blum and Erel 1995). For example, the $^{87}Sr/^{86}Sr$ of bulk regolith shifts from low ratios in unweathered rock to high ratios in regolith, as plagioclase with low $^{87}Sr/^{86}Sr$ and high Sr concentration is lost and biotite with high (radiogenic) $^{87}Sr/^{86}Sr$ and low Sr concentrations remains. Thus, the higher the intensity of chemical weathering, the larger the difference between $^{87}Sr/^{86}Sr$ of bulk bedrock and bulk regolith. At CON, $^{87}Sr/^{86}Sr$ of bulk regolith ranges from 0.7245 - 0.7327 and is distinct from that of bulk parent bedrock, which ranges from 0.7094 - 0.7109 (Figure 2-4b). Conversely, at MIT, $^{87}Sr/^{86}Sr$ of bulk regolith is similar to bulk parent bedrock (which ranges from 0.7148 - 0.7205), with values of 0.7136 - 0.7230 (Figure 2-4b). Consequently, $^{87}Sr/^{86}Sr$ of bulk regolith is only at CON substantially more radiogenic than bulk parent bedrock, implying a high degree of chemical alteration relative to parent bedrock and thus more nutrient loss at this site. Yet CDF and $^{87}Sr/^{86}Sr$, both being indicators of bulk mass loss from the regolith, do not per se inform on nutrient availability.

2.4.1.1.4 Elemental loss and gain fractions (τ_{Zr}^{X})

Indicators of the availability of individual nutrients and plant-beneficial elements are τ_{Zr}^{X}-values (Equation 2-5). In agreement with the higher CDF and the difference in $^{87}Sr/^{86}Sr$ we find substantially greater losses at CON among all considered elements (Figure 2-5). The degree of nutrient loss is most striking for Ca at CON, where Ca loss runs to completion, whereas at MIT about 35 % of Ca remain in the regolith. At both study sites most elements exhibit depletion profiles (Figure 2-5), defined as weathering profiles showing the continuous loss of soluble elements from bedrock as one moves from

the weathering front to topsoil (Brantley and Lebedeva 2011). For P and Zn at CON, there is a remarkable enrichment towards the forest floor in the Bw horizon that can be ascribed to nutrient uplift by biota. At both sites, the elemental losses can be attributed to a "kinetically limited weathering regime" (Brantley and Lebedeva 2011), where the erosion rate is sufficiently high to keep the nutrient stock of minerals that transit vertically through the weathering profile at moderate levels. The higher nutrient depletion of the regolith at CON is attributed to i) the complete dissolution of cordierite and hornblende, and ii) the presence of a slowly altering anorthite-poor plagioclase at MIT.

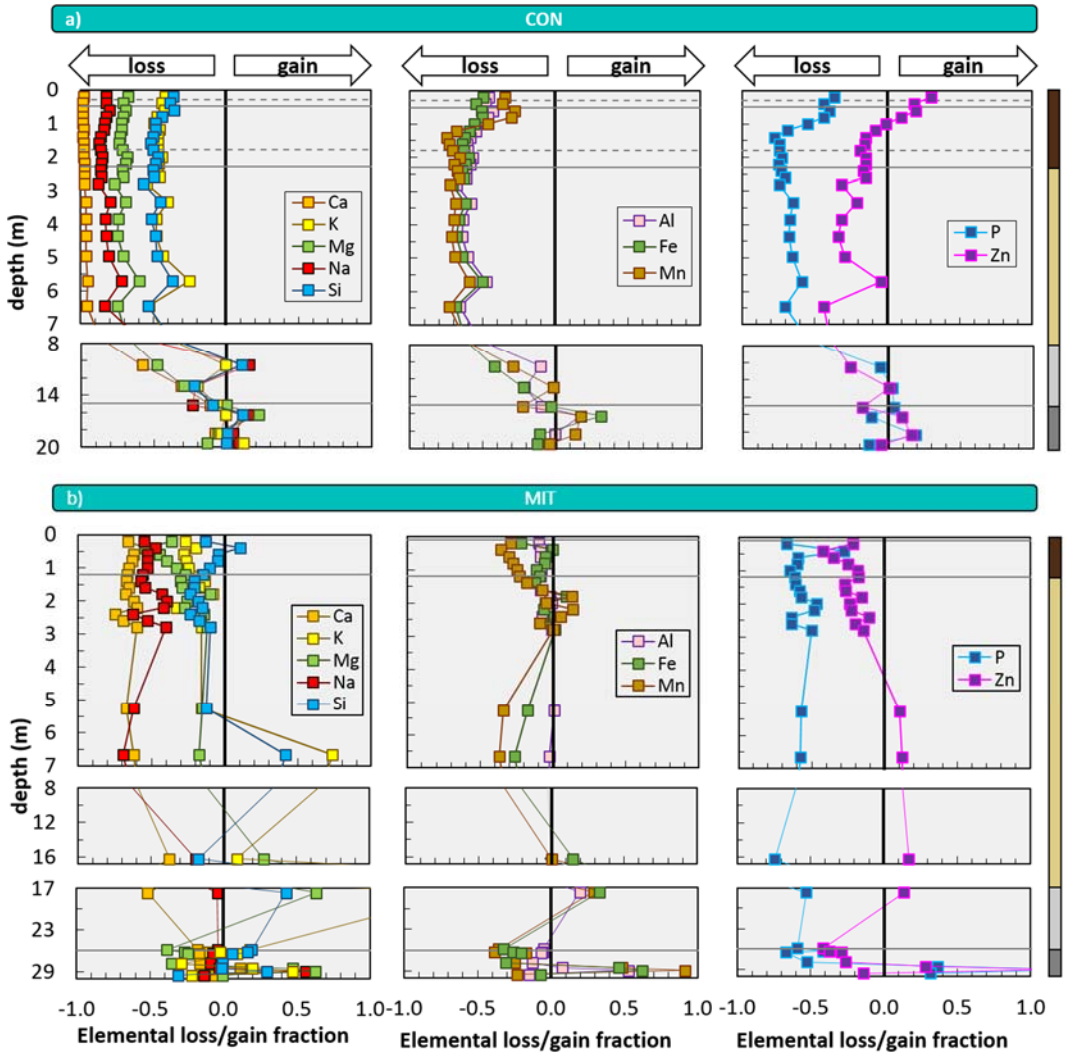

Figure 2-5 Depth distribution of elemental loss/gain fractions (mass transfer coefficients, τ^{X}_{Xi}) at CON (panel a) and MIT (panel b). The vertical line indicates a τ^{X}_{Xi}-value of zero and represents unweathered parent bedrock. Solid horizontal lines illustrate soil horizon boundaries and the interface of weathered rock to unweathered rock. Dashed horizontal lines indicate soil horizon subdivision (see Figure 2-2). Coloured bars at the right site of panel a refer to colour coding of drill core sections from Figure 2-2. For ease of display we changed the y-axis spacing with depth, yet all data are shown continuously. X-axis scale in panel a (not shown) is the same as in panel b.

Importantly, CDF, $^{87}Sr/^{86}Sr$, and τ^{X}_{Zr}-values all inform about the depth of the weathering front. At CON, all these indicators point at the weathering front to be located beneath 7 m depth, within the diffuse

saprolite/gneiss boundary (Table 2-2). But also, at MIT, where overall loss is low, τ^{X}_{Zr} of the most soluble elements Ca and Na indicate a weathering front at > 7 m depth. Thus, the intriguing possibility arises that nutrients are indeed released at these depths and are transported into the rooting zone for uptake into forest trees. To begin an evaluation of this possibility we convert these elemental loss and gain fractions into elemental fluxes, and we note that these present upper flux limits of nutrient transfer from rock into forest trees as some nutrient may be lost into drainage before it is captured by trees.

2.4.1.1.5 Nutrient supply by $W^{X}_{regolith}$

The weathering supply for the most plant-essential mineral nutrient phosphorus $W^{P}_{regolith}$ is similar between both study sites and amounts to 84 mg m^{-2} yr^{-1} at CON and to 65 mg m^{-2} yr^{-1} at MIT. For the other nutritive elements, the fluxes of $W^{X}_{regolith}$ (Equation 2-6) are considerably higher at CON, where the regolith experiences more chemical alteration (Table 2-3, Figure 2-6). For example, $W^{X}_{regolith}$ of the second most essential mineral nutrient potassium (K) amounts to 1000 mg m^{-2} yr^{-1} at CON, but only to 240 mg m^{-2} yr^{-1} at MIT. These geogenic supply fluxes exceed atmospheric supply fluxes (Dep^{X}_{wet}) by an order of magnitude at CON and by several times at MIT, as atmospheric supply is dominated by anthropogenic sources today (see Section 2.3.1 above). Forest trees are thus considered to be nourished from a nutrient stock fed by chemical weathering, some of which is sourced at substantial depth. To quantify whether this stock is a reservoir of sufficient size and also available to tree roots we proceed to quantify the inventories of these regolith nutrient stocks.

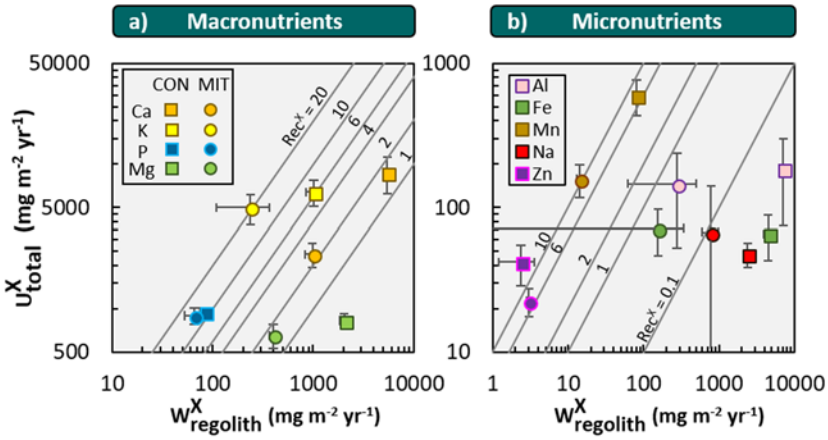

Figure 2-6 Chemical weathering fluxes ($W^{X}_{regolith}$) and ecosystem nutrient uptake fluxes (U^{X}_{total}) for macronutrients (panel a) and micronutrients + Na (panel b) at CON (squares) and MIT (circles). Contour lines illustrate the nutrient recycling factor (Rec^{x}), which is the ratio of U^{X}_{total} to $W^{X}_{regolith}$. Uncertainty bars show one standard deviation (see Section 2.3.4).

2.4.1.2 Accessibility of mineral nutrients to forest trees

2.4.1.2.1 Regolith nutrient inventories (I^X_{bulk}) and nutrient availability

The first and most simple assessment is to budget the maximum amount of nutrients in form of their inventories in bulk regolith ($I^X_{regolith}$). For most elements inventories are substantially higher at CON than at MIT (Table 2-5). The exceptions are Ca and P. $I^{Ca}_{regolith}$ is an order of magnitude higher at MIT than at CON because at CON most of the fast-dissolving anorthite-rich plagioclase has been depleted (Table 2-2). $I^{P}_{regolith}$ is higher at MIT than at CON because of the two to three-fold higher concentration of P in unweathered bedrock (MIT: ~2000 µg/g, CON: ~950 µg/g) and fragmented rocks (MIT: ~2900 µg/g, CON: ~470 µg/g) at MIT relative to CON. However, only a minor fraction of this bulk nutrient inventory is biologically available to forest trees. Our sequential extractions disclose this biologically available fraction. Element concentrations of all extracted regolith fractions are orders of magnitude below the bulk regolith concentrations (Figure 2-7). They are also generally higher at CON than at MIT. Thus, only a minor fraction (much less than 1 %) of the bulk regolith nutrient and plant-beneficial content is accessible to forest trees (Figure 2-7).

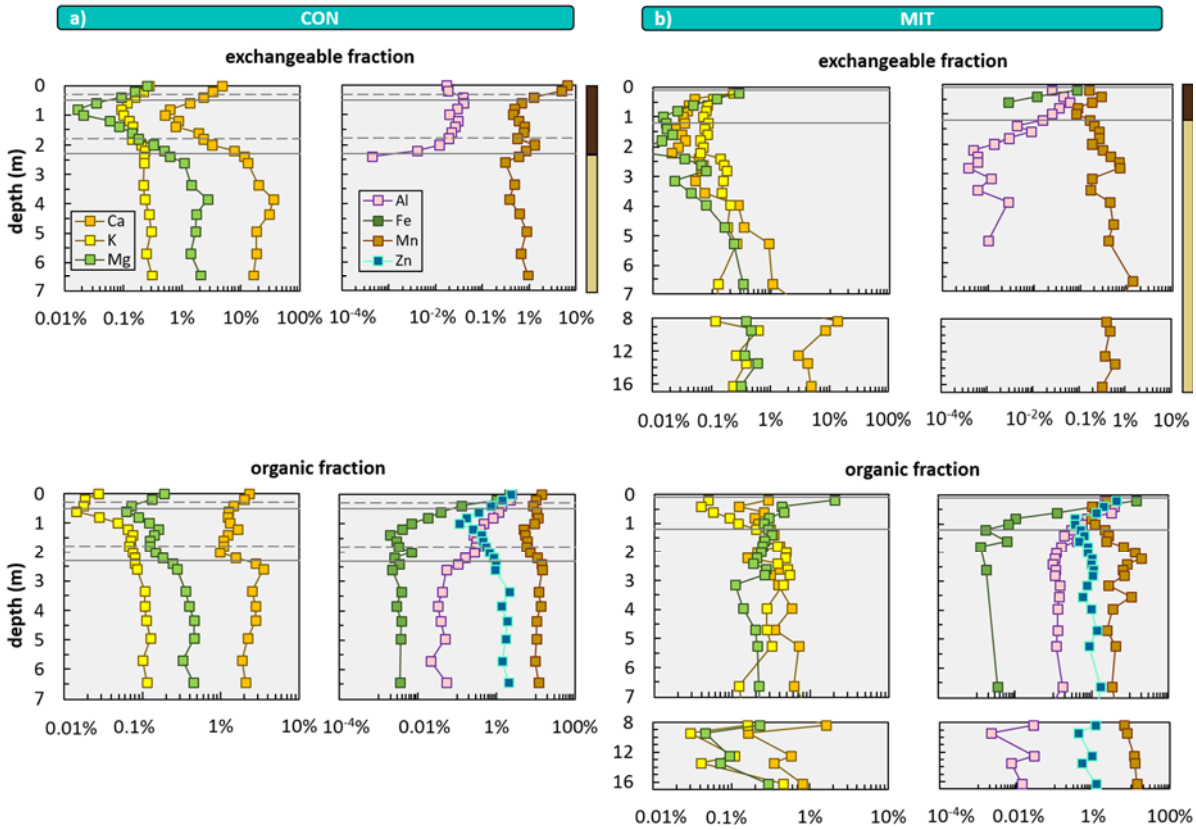

Figure 2-7 Depth distributions of sequentially extracted fractions comprising the exchangeable fraction (1 M NH_4OAc) and organic fraction (30 % H_2O_2 in 0.01 M HNO_3) at CON (panel a) and MIT (panel b). Shown are total concentrations relative to bulk soil and saprolite samples. Data gaps occur when extractant was below limit of detection. Solid lines illustrate soil horizon boundaries and the interface of weathered rock to unweathered rock. Dashed lines indicate soil horizon subdivision (see Figure 2-2). Coloured bars at the top of the panel refer to colour coding of drill core sections from Figure 2-2. For ease of display we changed the y-axis spacing with depth, yet all data are shown continuously.

To provide further insight into the biological availability of these nutrients we discuss the depth distribution of their chemical forms by focusing on the exchangeable and organic-bound fractions. The exchangeable fraction is considered as the best representation of plant-available nutrients. The most striking feature is an increase in Al towards the surface, particularly in the acidic Bw soil horizon (4.3 - 4.7 at CON and 3.6 - 4.7 at MIT (Figure 2-8)), which is a trend opposite to the depth distribution of Ca, K, Mg within the Bw horizon. At depth > 2 m no exchangeable Al is found whereas Ca, K, Mg occur in concentrations that exceed those in the central part of the Bw horizon by an order of magnitude. These depth profiles are dictated by both the soil pH and the cation exchange capacity

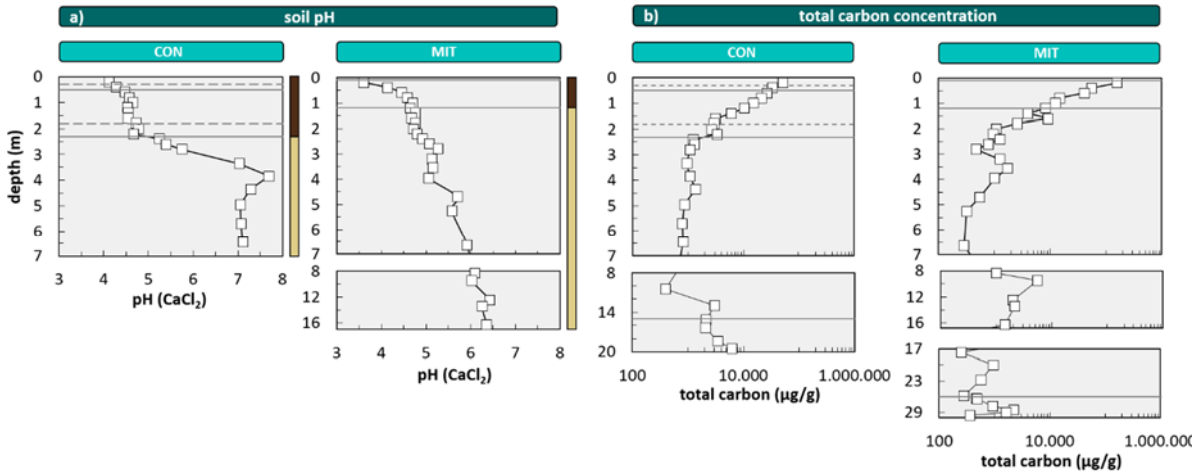

Figure 2-8 Depth distribution of the soil pH (panel a) and depth distribution of total carbon concentrations at CON and MIT. Soil pH is analysed in 0.01 M $CaCl_2$. Solid lines illustrate soil horizon boundaries and the interface of weathered rock to unweathered rock. Dashed lines indicate soil horizon subdivision (see Figure 2-2). Coloured bars at the right site of panel a refer to colour coding of drill core sections from Figure 2-2. For ease of display we changed the y-axis spacing with depth, yet all data are shown continuously.

(CEC). At low soil pH acidic cations that are less plant-essential (such as Fe, Mn and Al), inhibit the adsorption of basic cations that are more plant-essential (such as Ca, Mg and K). Hence, where the soil pH is acidic, plant-essential basic cations are replaced by elements of less nutritive character. Indeed, the soil pH decreases from ~6 to ~7 at a depth > 3 m to ~4 m at the surface at both sites (Figure 2-8). However, contrary to these findings the concentrations of K, Ca and Mg in the exchangeable fraction increase from a depth of 1 m towards the forest floor at both sites, where the soil pH is most acidic (Figure 2-7, Figure 2-8). At this level total carbon (C_{total}), considered to be organic, as pedogenic carbonate is absent at this low pH, also increases (Figure 2-8). Thus, the depth distribution of Ca, K, Mg, and Al suggests the adsorption of these nutritive elements onto organic matter (as humus exhibits the highest CEC). Such depth profiles are indicative of biological uplift of nutrients from depth through plants (Jobbágy and Jackson 2001). According to our conceptual framework these features contribute towards the *organic nutrient cycle*. The elevated concentrations and thus higher inventories of these elements at >3 m depth (Table 2-5), potentially providing another reservoir of biologically available

nutrients, have been released by chemical weathering within the saprolite below 3 m depth and are subsequently adsorbed onto clay minerals. These nutrients contribute to the *geogenic nutrient pathway*.

Concentrations in the organic fractions, featuring similar depth distributions to the exchangeable fraction, support this interpretation. However the concentrations of some organic-extractable nutritive elements (mainly Ca, K, Mg, and Mn) do not mirror the pattern of C_{total} that steadily increases from depth to topsoil (Figure 2-8), where organic carbon of true biological origin is present only in the Bw horizon and above. Note that C_{total} at depth can be attributed to lithogenic sources such as graphite. One potential explanation is that the oxidative extraction step partially attacked residual phyllosilicates such as biotite, chlorite or illite.

The chemical form of the biologically available fraction of P differ from the other elements. Concentrations of biologically available Ca-bound P increase with depth and approach maximum concentrations in the lower regolith (>3 m) where it dominates over the entirety of P species (Supplementary Table 2-2e).

In summary, even though most plant-accessible nutrients and plant-beneficial elements amount to only a very small fraction of the bulk regolith concentrations, the plant-accessible nutritive elements occur throughout the regolith profiles and are enriched at the surface in organic-rich layers, participating in the *organic nutrient cycle*, and beneath 3 m depth up to > 7 m depth at both sites (particularly Ca). Thereby, they potentially provide a deep nutrient reservoir for the suggested *geogenic pathway* of forest ecosystem nutrition.

2.4.2 Organic nutrient cycle

2.4.2.1 Chemical composition of picea abies and fagus sylvatica

The so called “critical” leaf and needle foliage concentrations discloses the nutrient status of a forest ecosystem; whether it is nutrient deficient, in the normal range, or in surplus (Göttlein et al. 2011). The foliar concentrations at CON and MIT (Figure 2-9) reveal that for most elements the nutrient level of both tree species is in the normal range, when compared to critical leaf and needle concentrations determined by Göttlein et al. (2011). The foliar and wood concentrations are similar to those compiled by Jacobsen et al. (2002) in more than a dozen independent studies performed on *Fagus sylvatica* and *Picea abies* forests. An exception are the Ca concentrations of *Picea abies* needles at MIT that exceed the range found in Jacobsen et al. (2002) by about 50 %. Only Ca levels for *Picea abies* and K levels for both tree species are indicative of nutrient surplus (Figure 2-9).

Another indicator for the nutrient status of forest trees is nutrient resorption during sapwood senescence. The concentrations in wood from *Fagus sylvatica* are generally higher than those in *Picea abies* at both sites, apart from K at MIT. This pattern agrees with the generally higher nutrient

concentrations in Angiosperms (e.g. *Fagus sylvatica*) than in Gymnosperms (e.g. *Picea abies*) reviewed by Meerts (2002). Nutrient concentrations in sapwood (living part of stem wood) are higher than in heartwood (dead part of stem wood) in both study sites and tree species. This effect is most pronounced for P in *Picea abies* at both sites, where P concentrations in sapwood are 6-fold higher at MIT and 17-fold higher at CON than in heartwood (Figure 2-9). Such elevated nutrient concentrations in sapwood are indicative of nutrient resorption during sapwood senescence (heartwood formation). Because P is resorbed during heartwood formation, we argue that P is efficiently used and not in deficit. This observation is consistent with critical leaf and needle concentrations found for P in *Picea abies* at MIT. In contrast, we found higher concentrations of Ca, Mg, K in heartwood over those in sapwood at both sites. We attribute the partitioning of particularly bivalent cations into heartwood to its accumulation into crystals such as oxalates, which are typically found in wood (Hillis 2006).

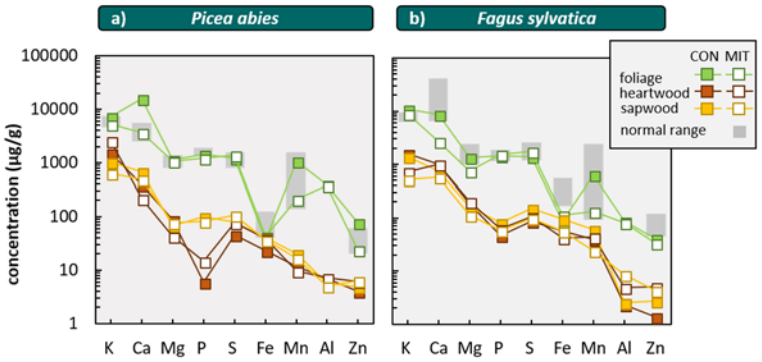

Figure 2-9 Elemental concentrations in leaves, needles, heartwood (dead part of wood) and sapwood (living part of wood) of Picea abies (panel a) and Fagus sylvatica (panel b) at CON and MIT. We did not illustrate data of sample MIT-V-7 and MIT-V-8 as P and S were not analysed in these samples. "normal range" denotes the critical leaf and needle concentration at normal range (data from Göttlein et al. 2011)). Elements on x-axis are sorted from left to right by macronutrients, micronutrients and plant-beneficial elements.

2.4.2.2 Is the biologically available fraction of the regolith setting tree stoichiometry?

The chemical composition of bulk tree allows us to test whether their chemical composition is driven by nutrient availability (the `you are what you root in´ model (Elser et al. 2010)) or by nutrient demand (the `physiological needs´ model (Elser et al. 2010)). For this test we compared the bulk tree element concentrations (Table 2-4) with the chemical composition of the nutrient supplying reservoirs parent bedrock, bulk regolith and the biologically available fractions in the upper regolith (<3 m) and the lower regolith (>3 m) (Figure 2-10).

Bulk rock and regolith element concentrations exceed those of trees by one order of magnitude or more, and their relative abundance patterns do in no way resemble those of trees (Figure 2-10). The reason is that elements contained in bulk rock or regolith are not readily available to forest trees. In contrast, the concentrations of biologically available elements, comprising here the water-soluble and the exchangeable fractions (Figure 2-7) are of relevance to forest trees. Nearly all these concentrations are lower than those of bulk trees. Intriguingly, the patterns of the chemical composition of bulk trees mirror the patterns of the biologically available fractions in both the upper and the lower regolith

(Figure 2-10). While this resemblance in pattern is apparent when plotting elemental concentrations, it is even more striking when all element concentrations are normalised to those of the most plant-essential mineral nutrient P (Figure 2-10 c,d); in a presentation of ecologic stoichiometry comparable to C:N:P ratios. Two explanations for this similarity are possible. In the first explanation the stoichiometry of mineral nutrients in plants is set by forest trees that utilise nutrients to their physiological needs (the `physiological needs´ model of Elser et al. (2010)), followed by the excretion of mineral nutrients through deep roots. Thereby forest trees would supply the biologically available

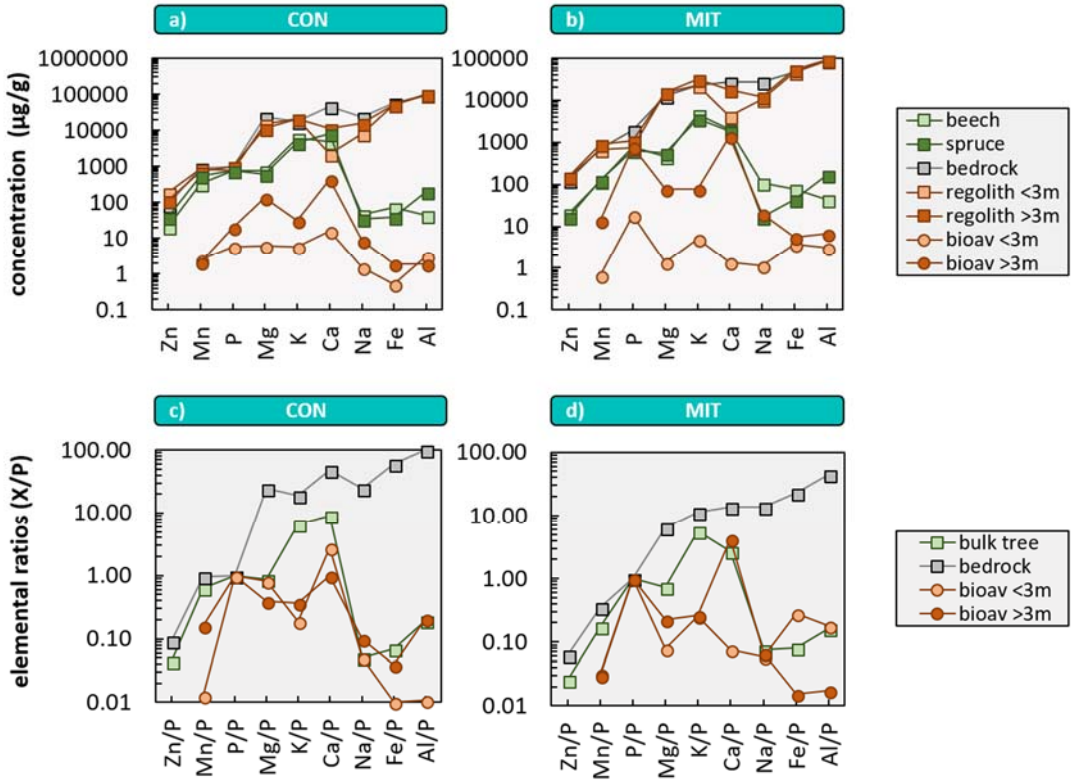

Figure 2-10 Concentrations of unweathered bulk bedrock, bulk regolith above (<3 m) and below 3 m (>3 m) depth, biologically available fractions above and below 3 m depth, bulk tree of Fagus sylvatica (beech) and Picea abies (spruce) at sites CON (panel a) and MIT (panel b). Element ratios of element X to P of bulk tree, bulk parent bedrock and the biologically available fraction above and below 3 m depth at CON (panel c) and MIT (panel d). Element sorting on x-axis reflects increasing element concentrations in parent bedrock from left to right.

fraction in the regolith. In the second explanation nutrient stoichiometry of forest trees is governed by the elemental abundance in the biologically available fraction (the 'you are what you root in' model of Elser et al. 2010)). We consider the second model to be applicable because we regard it as unlikely that forest trees excrete such substantial amounts of all mineral nutrients without running into deficit. More importantly, we observe that concentrations of the biologically available mineral nutrients in the >3 m deep regolith fraction are about one order of magnitude higher than those in the < 3 m interval. In this shallower depth interval, we would expect that the excretion of nutrients is highest because in this depth root density is highest. This is not the case, and we thus regard it as likely that the

stoichiometry of the biologically available regolith fraction is set by the weathering flux from primary minerals, where the flux is higher at greater depth. If this analysis is valid, the important conclusions are that a) tree roots extract their mineral nutrients from either the <3 m or from 3 m depth up to the weathering front, which would be a much deeper uptake depth than hitherto thought. b) The trees' stoichiometry is largely set by the biologically available fraction, and smaller differences of less than one order of magnitude between X/P in the biologically available fraction and the bulk tree composition result from differences in physiological demand. Given that we have identified the forest trees' potential nutrient source we can proceed to compare the nutrient uptake fluxes between study sites.

2.4.2.3 Nutrient uptake and loss fluxes

That nutrient uptake fluxes into forest trees (U^{X}_{total}) exceed weathering fluxes ($W^{X}_{regolith}$) by several times for K, Ca, P, Mn, Zn at both study sites, and for Mg at MIT (Figure 2-6), means that after uptake, nutrients are returned to the forest floor by annual litterfall from which they can be re-utilised multiple times. We return to the quantification of this cycle in Section 2.4.3.2. However, such cycling cannot proceed infinitely. Nutrients contained in plant litter can be lost from the forest ecosystem's forest floor as solute after litter decomposition and solubilisation (S^{X}_{org}), or as particulates by plant litter erosion (E^{X}_{org}). Neither loss flux is well known, but both can be fast. Plant litter is particularly vulnerable to erosion, because the litter layer is – in contrast to the mineral soil – directly exposed to erosive forces such as overland flow, storm events, and wild fires. The export of particulate organic matter and coarse woody debris in sloping forest ecosystems can be substantial (Hilton 2017) and significant for biogenic material including plant litter (Bormann et al. 1969; Webster et al. 1990; Heartsill Scalley et al. 2012). Uhlig et al. (2017) have used chemical and stable isotope mass balances in a forested ecosystem to show that, depending on ecological stoichiometry, up to more than 50 % loss of elements can take place by erosion of plant debris. The litter layer is also constantly exposed to precipitation and is prone to microbial decomposition. Decomposition time scales for non-woody foliage at pure stands were about 40 yr for both *Picea abies* and *Fagus sylvatica* at mixed stands (Albers et al. (2004), but in detail depend on water flow and microbial abundance.

In the absence of exact measurements of nutrient losses we roughly estimated the fluxes of plant litter erosion (E^{X}_{org}) and plant litter drainage (S^{X}_{org}) (Equation 2-11 and Equation 2-12) (reported in Table 2-3). For the most plant-essential mineral nutrient P, S^{P}_{org} amounts to ~120 mg m^{-2} yr^{-1} at CON and to ~95 mg m^{-2} yr^{-1} at MIT. Also, E^{P}_{org} is not negligible and amounts to ~30 mg m^{-2} yr^{-1} at CON and to ~50 mg m^{-2} yr^{-1} at MIT. The sum of these fluxes is very similar to the P weathering flux $W^{P}_{regolith}$ that amounts to 84 mg m^{-2} yr^{-1} at CON and to 65 mg m^{-2} yr^{-1} at MIT (Table 2-3). Also, for the second-most plant-essential mineral nutrient K, the weathering flux and the loss flux from the forest floor are

roughly similar. In contrast, for the other elements Ca, Mg, Na, Al, and Fe loss fluxes are lower than the weathering flux $W^{X}_{regolith}$ (Table 2-3).

We can conclude with high confidence that all elements lost from the forest floor can be balanced by fresh nutrients released by weathering. In addition, we can speculate that for those elements for which S^{X}_{org} + E^{X}_{org} is lower than $W^{X}_{regolith}$ a fraction of their loss takes place via groundwater drainage before being utilised by forest trees, and that in turn those nutrients in highest demand like P and K are transferred with the highest efficiency from their weathering source into trees.

2.4.3 A revised paradigm for long-term forest ecosystem nutrition

We summarise the above discussed estimates of fluxes. The geogenic nutrient pathway differs between the two sites: The degree of chemical alteration (based on CDF, $^{87}Sr/^{86}Sr$, τ^{X}_{Zr}), and nutrient supply fluxes ($W^{X}_{regolith}$) are all higher at CON than at MIT. A large reservoir of biologically available nutrients (I^{X}_{bioav}) exists below 3 m depth that is larger at MIT than at CON. In contrast, the properties of the organic nutrient cycle do not differ between the two sites. Foliar and wood concentrations are similar, NPP estimates are almost identical, and as a result, the nutrient uptake fluxes (U^{X}_{total}) do not differ significantly between the sites. Also, the substantial nutrient losses by plant litter drainage (S^{X}_{org}) and plant litter erosion (E^{X}_{org}) from the forest floor do not differ much between the study sites. These similarities in the ecosystem nutrient status and organic nutrient cycle in the face of substantial differences in geogenic nutrient supply now allow us to revise the paradigm described in the introduction. Namely that to date, according to the common paradigm, the importance of the geogenic supply of nutrients to forest ecosystem nutrition has been considered miniscule and ecosystem nutrition is mostly viewed to between trees and the forest floor. The revised paradigm states that ecosystems cannot persist over millennia without an important source of mineral nutrients from bedrock. We guide this final discussion by three important questions. 1) How is nutrient loss from the forest floor balanced to prevent nutrient deficit? 2) How is a healthy nutrient status maintained when nutrient supply rates from rock differ? 3) Does a forest nutrition feedback operate through nutrient recycling or through biogenic weathering?

2.4.3.1 Balancing nutrient loss from the forest floor by geogenic-derived nutrients

Here we provide quantitative evidence for the importance of the geogenic nutrient source to forest ecosystem nutrition by combining nutrient inventories (Table 2-5) in the forest floor (I^{X}_{ff}) and in the biologically available fraction in the regolith (I^{X}_{bioav}) with nutrient fluxes (Table 2-3) of weathering, uptake, and loss. This combination allows us to estimate the timescale over which a given inventory lasts (Table 2-7). We reiterate that nutrient loss and nutrient supply fluxes do not need to balance over the short-term, as for this assessment steady state is required only over extended periods. For simplicity, we limit this discussion to the frequently plant-growth limiting mineral nutrient P. Yet these

calculations are applicable to all nutrients (Table 2-7), and in Figure 2-11 we also illustrate how they apply to K, the second-most important mineral nutrient.

Table 2-7 Turnover times at CON and MIT.

	depth interval	K		Ca		Mg		P		Na		Al		Fe		Mn	
		CON	MIT	CON	MIT	CON	MIT	CON	MIT	CON	MIT	CON	MIT	CON	MIT	CON	MIT
	(m)	(yr)		(yr)		(yr)		(yr)		(yr)		(yr)		(yr)		(yr)	
$T^X_{ff,L}$		6.2	3.7	10	8.4	11	9.7	16	10	n.d.	n.d.	100	290	84	140	6.3	7.8
$T^X_{ff,U_{ff}}$ *		1.8	1.3	2.0	6.1	6.8	5.5	6.4	5.7	n.d.	46	n.d.	n.d.	n.d.	n.d.	2.7	14
$T^X_{ff,loss}$		28	25	28	25	31	30	36	30	38	39	42	42	42	41	26	25
$T^X_{bioav,U_{new}}$	<3	210	280	360	41	570	190	570	1800	410	440	110	120	12	62	610	160
$T^X_{bioav,U_{new}}$	>3	500	3400	4400	32000	5200	8300	700	60000	960	6100	23	160	34	120	230	2600
$T^X_{bioav,W}$	<3	80	280	40	22	42	48	990	4100	9.0	19	6.2	160	0.58	59	440	670
$T^X_{bioav,W}$	>3	190	3300	480	17000	390	2100	1200	140000	21	270	1.4	220	1.7	110	160	11000

$T^X_{ff,L}$ = turnover time of element X in the forest floor with respect to litterfall, $T^X_{ff,U_{ff}}$ = turnover time element X in the forest floor with respect to uptake into trees, $T^X_{ff,loss}$ = turnover time of element X in the forest floor with respect to loss by erosion and drainage of plant litter, $T^X_{bioav,W}$ = turnover time of element X in the biologically available fraction in regolith with respect to adsorption onto clay minerals, $T^X_{bioav,U_{new}}$ = turnover time of element X in the biologically available fraction in regolith with respect to uptake into trees

* negative data occur, if the fluxes of E^X_{org} and S^X_{org} exceed U^X_{total}

The need to replace nutrient losses arises because in the organic nutrient cycle the timescale of P in the forest floor until loss by plant litter erosion (E^{P}_{org}) and drainage (S^{P}_{org}) is about 30 yr at both study sites (Figure 2-11). One can argue, however, that any P leached within the forest floor is immediately re-utilised by renewed uptake to minimise dissolved nutrient loss (e.g. Jobbágy and Jackson 2001, 2004). We indeed have evidence for such cycling. Because total P uptake fluxes (U^{P}_{total}) from forest trees (900-960 mg m^{-2} yr^{-1}) are an order of magnitude higher than P supply fluxes from chemical weathering (60-80 mg m^{-2} yr^{-1}), efficient re-utilisation of P from the forest floor takes place to ensure forest ecosystem nutrition. However, despite such intense re-utilisation, P turnover, or residence times in the forest floor can be estimated to be about 6 yr at both study sites before re-utilisation ($T^{P}_{ff,U_{ff}}$, Figure 2-11) and about 10 to 20 yr with respect to replenishment by litterfall ($T^{P}_{ff,L}$, Figure 2-11). This residence time in the forest floor suffices for P to experience continuous nutrient loss by S^{P}_{org} and E^{P}_{org}. Thus, unless another nutrient inventory exists that provides a flux that permanently replaces the continuous nutrient loss from the forest floor, I^{P}_{ff} would run out over decadal timescales, thus on a timescale shorter than the life cycle of a forest tree of about 150 - 200 yr.

We have found such a potential reservoir through the geogenic nutrient pathway in the form of the inventory of the biologically available fraction (I^{X}_{bioav}). In the upper regolith (<3 m) I^{P}_{bioav} lasts for ~0.6 kyr at CON and for ~1.8 kyr at MIT (Figure 2-11) to replace the P loss incurred in the forest floor. In the lower regolith (>3 m) I^{P}_{bioav} lasts even longer: ~0.7 kyr at CON and for ~60 kyr at MIT (Figure 2-11). We have also found that the chemical composition of this fraction exerts a first-order control over the stoichiometry of mineral nutrients in forest trees (Section 2.4.2.2) which serves as evidence for the likelihood of this deep source. However, if the biologically available P fraction permanently replenishes the forest floor over millennial timescales a deficit of P will develop there too. We suggest that the biologically available P fraction is in turn replenished by P release through chemical weathering. In the upper regolith (<3 m) the turnover timescale with respect to chemical weathering ($T^{P}_{bioav,W}$) is about 1.0 kyr at CON and about 4 kyr at MIT (Figure 2-11). In the lower regolith (>3 m) $T^{P}_{bioav,W}$ is about 1.2 kyr at CON and about 140 kyr at MIT (Figure 2-11). The fact that the turnover time of the biologically available fraction of P from weathering ($T^{P}_{bioav,W}$) is so similar to the "new" P required to balance P losses ($T^{P}_{bioav,U_{new}}$) strongly suggests that U^{P}_{new} can be supplied from I^{P}_{bioav} over millennial timescales.

We suggest that, despite the fast turnover of plant litter in the forest floor, the permanent loss of nutrients from the forest floor is replaced by the deep regolith's biologically available nutrient inventory. This reservoir is in turn continuously replenished by slow rock weathering. Thus, even though the nutrient uptake flux (U^{X}_{new}) from the geogenic nutrient pathway is small compared to the total nutrient uptake (U^{X}_{total}), this flux is of key importance in ensuring forest ecosystem nutrition over millennia. In terms of mechanisms, the organic nutrient cycle and the geogenic nutrient pathway are

connected through dimorphic root systems comprising a surficial dense root network and deep taproots, which enable forest trees to access a groundwater table even at a depth of several meters (Fan et al. 2017). Thereby, deep roots ensure water supply during summer droughts (Brantley et al. 2017a) and aid tree nutrition as groundwater is often chemically equilibrated with respect to forming and dissolving secondary precipitates (e.g. Maher 2011). Hence, pore water presents a reservoir of biologically available nutrients, which can be uplifted by roots and stored in the forest floor (e.g. Jobbágy and Jackson 2004).

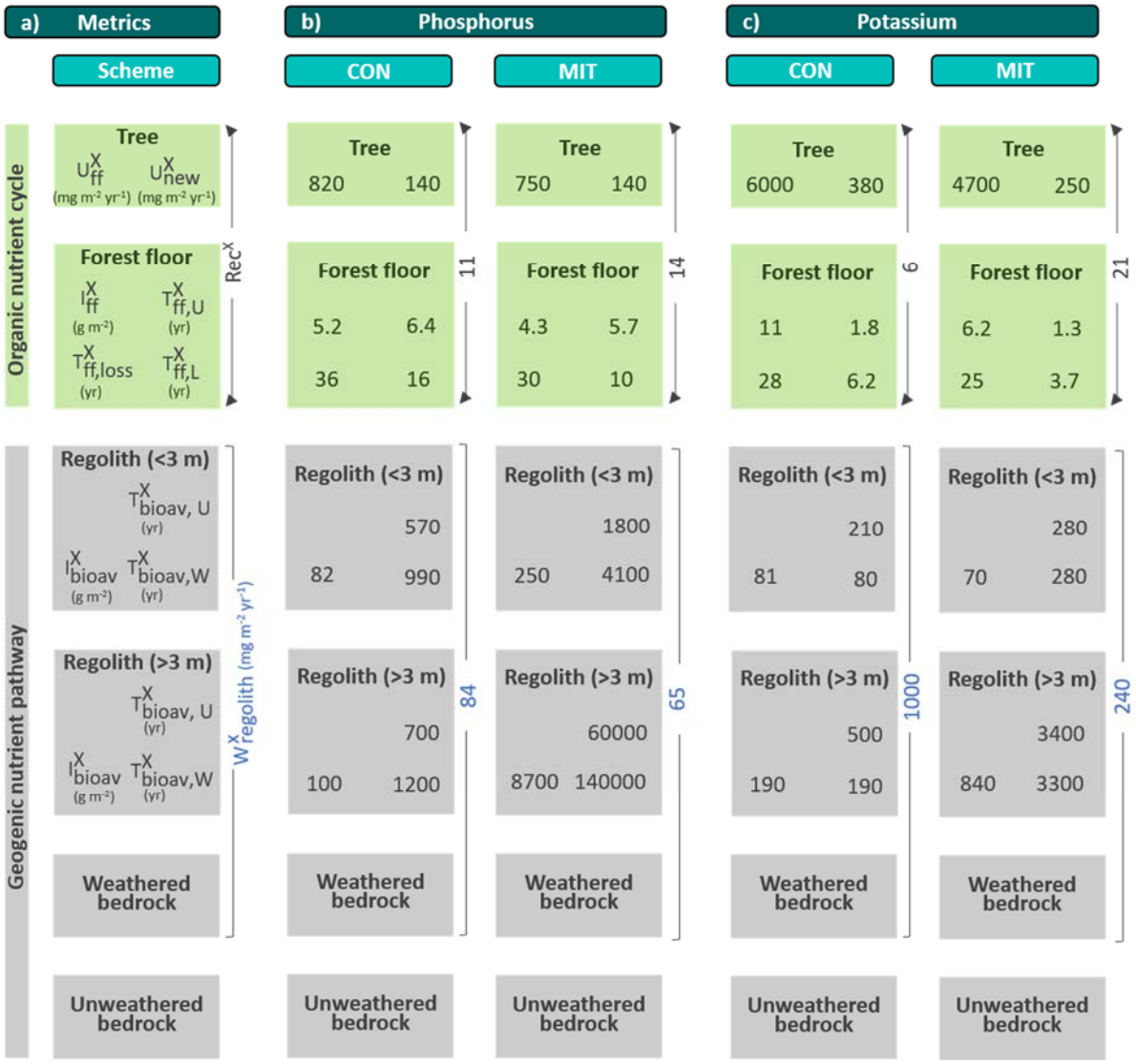

Figure 2-11 Fluxes (U^X_{new}, U^X_{ff}, $W^X_{regolith}$), inventories (I^X_{ff}, I^X_{bioav}), turnover times ($T^X_{ff,loss}$, $T^X_{ff,U}$, $T^X_{ff,L}$, $T^X_{bioav,W}$, $T^X_{bioav,U}$) and recycling factors (Rec^X) of nutrients in the organic nutrient cycle and geogenic nutrient pathway (overview in panel a) for phosphorus (panel b) and potassium (panel c). $W^X_{regolith}$ is shown in vertical blue labels to the right of regolith boxes; Rec^X in black vertical labels to the right of organic cycle boxes. For detailed description on the metrics see Figure 2-1 and Table 2-1. Units of the metrics are given in left panels (Rec^X is dimensionless).

2.4.3.2 Maintaining a healthy nutrient status by adjustment of nutrient recycling loops

Regardless of the importance of the geogenic nutrient source, nutrient re-utilisation from plant litter still presents the dominant source to short-term forest ecosystem nutrition. This source, however, has a limited lifetime due to permanent loss that correspondingly limits the number of possible recycling loops. As we suggest that the replenishment of this forest floor compartment originates from chemical weathering, we speculate that the number of nutrient recycling loops between forest trees and the forest floor is a function of the nutrient supply through chemical weathering (where $U^{X}_{new} \sim W^{X}_{regolith}$). As at our two study sites nutrient uptake fluxes are identical but nutrient supply fluxes from rock weathering are higher at CON than at MIT we can explore whether nutrient recycling between forest trees and the forest floor indeed reflects these differences. For example, the nutrient supply flux from rock weathering of the second-most plant-essential mineral nutrient K ($W^{K}_{regolith}$) is about 1000 mg m^{-2} yr^{-1} at CON and only about 240 mg m^{-2} yr^{-1} at MIT. Yet, the nutrient uptake fluxes of K (U^{K}_{total}) are similar between sites. Because we have defined the nutrient recycling factor (Rec^{X}) as the ratio of U^{X}_{total} to $W^{X}_{regolith}$, the Rec^{X} of K suggests 6 re-utilisation cycles between the forest floor and forest trees at CON, but 21 re-utilisation cycles at MIT (Figure 2-11). For the other macronutrients Ca, Mg and P the nutrient recycling factor Rec^{X} at MIT exceeds Rec^{X} at CON (Table 2-6, Figure 2-6). We note, however, that for the less essential mineral nutrients Ca and Mg a substantial fraction of weathering fluxes is potentially directly drained via groundwater into the stream. Thus, the actual supply of these nutrients to forest trees presents a maximum flux and the calculated Rec^{X} provides correspondingly a minimum estimate.

We conclude that forest trees persist with similar primary production through highly variable nutrient re-utilisation loops. In other words, in the organic nutrient cycle nutrient loss is minimised to an extent that depends on nutrient supply by $W^{X}_{regolith}$. With this efficient nutrient use the physiological needs of forest ecosystems are sustained.

2.4.3.3 A forest nutrition feedback through nutrient recycling or through biogenic weathering?

That at low nutrient availability efficient nutrient recycling must prevail to handle nutrient limitation was suggested previously, in particular for forest ecosystem research in tropical, non-eroding settings (e.g. Vitousek et al. 2003; Cleveland et al. 2006; Buendía et al. 2010). With our new metric Rec^{X} we have now provided a simple means to quantify the efficiency of this recycling. This Rec^{X} is an estimator of regulation via a feedback mechanism located within the organic nutrient cycle. If supply by the geogenic nutrient pathway is low, recycling is efficient, and vice versa, such that forest ecosystem nutrition is maintained throughout at optimal levels. But what are the actual ecological strategies enabling this regulation? Root-microbe interaction was suggested as an ecological strategy for this regulation. Higher plants are known to supply energy for the microbial rhizospheric communities,

which in return alter plant health and nutrition (Hinsinger et al. 2011). For our two study sites, the processes that regulate the efficiency of this recycling were explored in detail by Lang et al. (2017): phosphorus in fine-root biomass increased relative to microbial P with decreasing P stocks. Concomitantly, phosphodiesterase activity decreased, which might explain increasing proportions of diester-P remaining in the soil organic matter. Fast mining of nutrients from leaf litter by mycorrhizal fungi to outpace bacterial decomposition that would otherwise lead to dissolved nutrient loss is another suggested strategy (Hättenschwiler et al. 2011).

Would biogenic weathering provide an alternative feedback that ensures forest ecosystem nutrition? The accelerated decomposition of primary and secondary minerals that contain nutrients indirectly by root exudates or reduced soil pH, or directly by "rock-eating" fungi, has gained increasing scientific importance in past years (e.g. Jongmans et al. 1997; Landeweert et al. 2001; Balogh-Brunstad et al. 2008; Lambers et al. 2008; Bonneville et al. 2009; Smits et al. 2012). In fact, it has been hypothesised that "in eroding landscapes, weathering-front advance at depth is coupled to surface denudation via biotic processes" (c.f. Brantley et al. 2011). Indeed, biogenic weathering provides an alternative powerful feedback located in the geogenic nutrient pathway that potentially regulates nutrient provision to counter nutrient limitation: to prevent nutrient limitation, forest trees and their microbial communities regulate mineral dissolution by nutrient mining. Our study offers a direct test of this feedback hypothesis. Owing to subtle differences in mineral composition between CON and MIT, site MIT is weathering with much lower intensity than CON, yet nutrient uptake is the same at both sites. If biogenic weathering were to regulate the feedback, we would expect similar degrees of weathering. Thus, it is instead the organic nutrient cycle that regulates the feedback without accelerating biogenic weathering. If this were a globally common nutrition feedback the impact of biogenic weathering to regulate CO_2 withdrawal over geologic timescales (Pagani et al. 2009) might require some reconsideration.

2.5 Conclusions

Our results indicate that the regolith at CON experienced substantially more nutrient loss through chemical weathering than MIT. We found that even though the nutrient supply fluxes from rock weathering differ substantially among study sites, the nutrient uptake fluxes from forest trees are astonishingly similar. We explored the mechanisms that regulate the uptake fluxes by considering the forest ecosystem in a mass balance comprising the shallow organic nutrient cycle and the belowground geogenic nutrient pathway. The major outcome of this analysis is that the nutrient inventory in the forest floor is of finite size that lasts only for decades to nourish forest trees, because continuous nutrient loss through plant litter drainage and erosion occurs. Because an additional inorganic nutrient supplying flux in the form of atmospheric inputs is negligible this permanent nutrient loss is balanced

by fluxes from a reservoir in the deep regolith. However, only a minor fraction of the nutrient inventory in soil and saprolite is biologically available to forest trees, but its inventories in the upper regolith (<3 m) and even more pronounced in the deep regolith (>3 m) exceed the nutrient inventory in the forest floor by orders of magnitude. This reservoir of nutrients lasts for centuries to millennia, replaces the nutrient loss from the forest floor, and is in turn permanently replenished through chemical weathering. The stoichiometry of this deep biologically available regolith nutrient reservoir also sets the stoichiometry of the forest trees to within an order of magnitude. According to a revised paradigm forest ecosystems are nourished if nutrient losses from the forest floor in the organic nutrient cycle are replaced through the geogenic nutrient pathway. Finally, we found a potential feedback in which the efficiency of nutrient recycling as measured by the nutrient re-utilisation cycles from plant litter ensures forest ecosystem nutrition even when nutrient supply or loss vary. This feedback is potentially stronger than one that invokes biogenic weathering as regulating mechanism. This study adds to the increasing evidence for the importance of a geological cycle, driven by erosion that sustains forest ecosystem nutrition.

2.6 Acknowledgements

We are grateful to the German Research Foundation Priority Program (SPP 1685) “Ecosystem Nutrition: Forest strategies for limited phosphorus resources” and Friederike Lang (Albert-Ludwigs-University of Freiburg) for its coordination and discussion. We also thank the State Institute of Bavaria for Forestry and Silviculture (LWF) and the Forest Research Institute Baden-Wuerttemberg (FVA) for providing wet deposition and litterfall data. For X-ray fluorescence analyses and X-ray diffraction analyses we are thankful to R. Naumann (GFZ) and A. Gottsche (GFZ). For phosphorus Hedley sequential fractionation we are grateful to A. Rodionov (INRES), S. L. Bauke (INRES) and W. Amelung (INRES). J. A. Schuessler (GFZ) and H. Wittmann (GFZ) are acknowledged for analytical support and R. Kapannusch (GFZ) is acknowledged for sample preparation. M. Henehan (GFZ) is thanked for a review of an early version of this manuscript.

2.7 Supplements

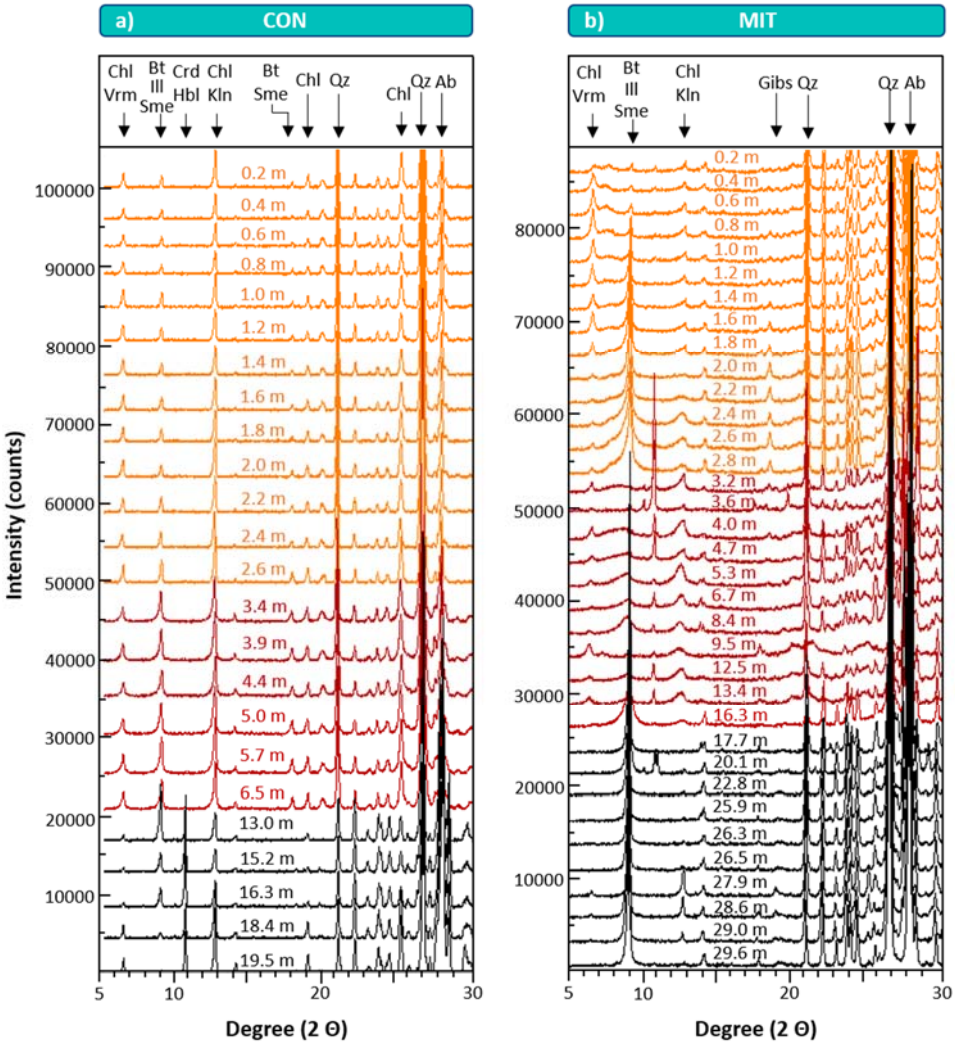

Supplementary Figure 2-1 X-ray diffractograms at CON (panel a) and MIT (panel b). X-ray diffraction analyses (XRD, Siemens D5000) was performed at 40 kV and 40 mA with a Cu-Kα radiation at a rate of 1.2° min^{-1} in the range of 5-85° 2Θ with a relative identification limit of detection of 5 %. For XRD analyses <63 µm grain-sized bulk soil, saprolite and bedrock samples were used. Qualitative data evaluation was done with the software EVA from Bruker. Ab = albite, Bt = biotite, Chl = chloride, Crd = cordierite, Gibs = gibbsite, Hbl = hornblende, Ill = illite, Kln = kaolinite, Qz = quartz, Sme = smectite, Vrm = vermiculite.

Supplementary Table 2-1a Chemical composition of soil, saprolite and rock samples at CON and MIT (for colour coding see table caption).

				XRF analyses: Raw data (major oxides)												XRF analyses: Raw data (trace elements)										
sample ID	**IGSN†**	**brief sample description**	**mean depth**	**SiO_2**	**TiO_2**	**Al_2O_3**	**Fe_2O_3**	**MnO**	**MgO**	**CaO**	**Na_2O**	**K_2O**	**P_2O_5**	**LOI**	**Sum**	**Ba**	**Cr**	**Ga**	**Nb**	**Ni**	**Rb**	**Sr**	**V**	**Y**	**Zn**	**Zr**
			(m)	(wt%)	(wt%)	(wt%)	(wt%)	(wt%)	(wt%)	(wt%)	(wt%)	(wt%)	(wt%)	(wt%)	(wt%)	(µg/g)	(µg/g)	(µg/g)	(µg/g)	(µg/g)	(µg/g)	(µg/g)	(µg/g)	(µg/g)	(µg/g)	(µg/g)
CON regolith - bedrock depth profile																										
CON 14	GFDUH00LT	soil, Ah horizon	0.2	57	0.86	15	6.4	0.12	2.0	0.19	0.87	2.0	0.22	15	99.69	445	93	20	16	36	112	58	125	28	178	237
CON 13	GFDUH00LU	soil, Ah + Bw horizon	0.4	60	0.89	16	6.3	0.13	1.9	0.19	0.93	2.1	0.21	12	99.62	467	97	21	15	36	103	56	124	30	176	257
CON 12	GFDUH00LV	soil, Bw I horizon	0.6	51	0.79	14	5.5	0.12	1.6	0.16	0.87	1.7	0.18	24	99.67	381	90	18	13	30	83	49	116	26	145	210
CON 11	GFDUH00LW	soil, Bw I horizon	0.8	58	0.93	18	7.4	0.15	2.1	0.20	1.0	2.1	0.23	9.8	99.64	484	111	22	17	45	122	64	136	36	175	277
CON 10	GFDUH00LX	soil, Bw I horizon	1.0	59	0.94	18	7.3	0.13	2.2	0.24	1.0	2.2	0.20	8.7	99.58	517	109	22	22	49	127	70	137	38	175	306
CON 9	GFDUH00LY	soil, Bw I horizon	1.2	62	0.94	17	6.9	0.08	2.3	0.28	1.1	2.5	0.15	6.9	99.63	464	116	22	21	51	104	66	136	34	169	318
CON 8	GFDUH00LZ	soil, Bw I horizon	1.4	63	0.95	16	6.8	0.07	2.3	0.24	0.95	2.6	0.11	5.8	99.69	412	113	23	18	47	107	62	129	34	167	339
CON 7	GFDUH00M0	soil, Bw I horizon	1.6	64	0.93	16	6.7	0.08	2.4	0.28	0.94	2.7	0.13	5.2	99.64	399	112	20	17	48	107	62	126	34	172	352
CON 6	GFDUH00M1	soil, Bw II horizon	1.8	64	0.94	16	6.9	0.08	2.5	0.30	0.96	2.6	0.13	4.7	99.67	450	116	20	15	51	105	64	122	32	161	344
CON 5	GFDUH00M2	soil, Bw II horizon	2.0	64	0.93	16	6.9	0.09	2.6	0.32	0.98	2.5	0.13	5.3	99.72	467	112	21	16	48	103	68	131	31	157	319
CON 4	GFDUH00M3	soil, Bw II horizon	2.2	64	0.93	16	6.7	0.08	2.6	0.34	0.98	2.5	0.12	5.2	99.70	459	112	21	16	50	98	68	129	35	162	329
CON 3	GFDUH00M4	saprolite, Cw horizon	2.4	65	0.90	16	6.6	0.09	2.5	0.37	0.97	2.6	0.13	4.8	99.65	485	116	18	15	47	101	67	129	36	166	345
CON 2	GFDUH00M5	saprolite, Cw horizon	2.6	65	0.92	16	6.7	0.09	2.6	0.43	1.00	2.7	0.15	4.6	99.69	484	126	21	14	48	106	69	130	41	169	343
CON 1	GFDUH00M6	saprolite, Cw horizon	2.8	66	0.90	15	6.4	0.09	2.4	0.46	1.0	2.6	0.15	4.3	99.65	476	122	20	14	48	102	72	115	42	161	406
CON 19	GFDUH00MB	saprolite, Cw horizon	3.4	66	0.88	16	6.5	0.08	2.5	0.49	1.3	2.7	0.16	3.6	99.72	493	109	21	13	44	108	84	123	41	146	319
CON 20	GFDUH00MC	saprolite, Cw horizon	3.9	66	0.90	15	6.5	0.09	2.4	0.56	1.3	2.7	0.17	3.7	99.62	495	114	21	16	46	108	87	121	42	143	361
CON 21	GFDUH00MD	saprolite, Cw horizon	4.4	68	0.84	15	6.0	0.08	2.3	0.55	1.3	2.6	0.16	3.5	99.68	480	106	19	13	44	97	81	115	37	133	348
CON 22	GFDUH00ME	saprolite, Cw horizon	5.0	60	0.80	14	5.8	0.08	2.3	0.50	1.2	2.5	0.15	12	99.73	460	93	18	12	40	91	81	111	37	125	306
CON 23	GFDUH00MF	saprolite, Cw horizon	5.7	63	0.91	17	7.1	0.09	2.7	0.56	1.5	2.8	0.16	3.8	99.67	536	109	23	13	49	112	91	137	39	148	267
CON 24	GFDUH00MG	saprolite, Cw horizon	6.5	66	0.84	15	6.4	0.08	2.5	0.66	1.3	2.6	0.16	3.6	99.69	499	102	18	15	46	110	99	118	43	123	379
CON 28	GFDUH00MT	weathered rock fragments	0.4	68	0.78	15	6.2	0.05	2.4	0.13	0.9	2.8	0.10	3.4	99.75	525	102	20	13	47	100	44	132	30	117	182
CON 32	GFDUH00MX	weathered rock fragments	1.6	63	0.92	18	7.3	0.05	2.8	0.07	0.5	3.7	0.07	3.9	99.71	555	126	24	13	51	141	37	161	34	128	227
CON 36	GFDUH00N1	weathered rock fragments	2.8	75	0.65	12	4.1	0.03	1.6	0.43	1.8	2.0	0.13	2.1	99.76	408	63	14	<10	29	64	93	71	32	76	203
CON 45	GFDUH00N5	weathered paragneiss	7.6	72	0.08	15	0.94	0.01	0.17	0.38	3.2	4.9	0.18	2.8	99.86	381	17	17	10	<10	184	63	<10	20	28	45
CON 40	GFDUH00N7	weathered paragneiss >63 mm	10.5	69	0.45	16	3.4	0.07	1.3	2.2	4.0	2.2	0.18	1.3	99.73	609	19	16	10	<10	58	456	59	19	52	154
CON 41	GFDUH00N8	weathered paragneiss 20-63 mm	10.5	60	0.83	17	6.2	0.11	2.7	3.2	3.3	2.2	0.25	3.7	99.60	632	33	18	13	<10	71	384	138	20	80	156
CON 47	GFDUH00N9	weathered paragneiss	13.0	54	0.99	17	7.8	0.15	3.3	5.3	3.0	2.1	0.28	4.6	99.06	742	<10	20	17	<10	65	486	187	40	108	186
CON 48	GFDUH00NA	unweathered paragneiss	15.2	54	1.1	17	8.2	0.10	4.0	5.9	2.5	2.1	0.24	5.0	99.58	696	15	19	<10	<10	64	387	267	25	75	158
CON 49	GFDUH00NB	unweathered paragneiss	16.3	52	1.1	17	8.8	0.12	3.9	6.2	3.0	1.8	0.16	5.0	99.45	504	13	18	11	<10	49	321	215	21	79	125
CON 50	GFDUH00NC	unweathered paragneiss	18.4	55	0.95	17	6.9	0.13	3.5	5.6	3.1	2.0	0.25	5.3	99.49	684	41	18	15	<10	63	434	170	28	97	145
CON 51	GFDUH00ND	unweathered paragneiss	19.5	54	0.86	16	6.7	0.11	3.2	6.2	3.2	2.3	0.18	6.3	99.57	644	17	17	<10	<10	67	478	169	26	79	144
CON bedload sediment																										
CON 27	GFDUH00SK	bedload sediment	-	70	0.65	14	4.9	0.07	1.9	0.28	0.84	2.8	0.10	4.7	99.72	560	80	18	10	42	108	63	98	25	187	170

continued next page …

Supplementary Table 2-1a continued - Chemical composition of soil, saprolite and rock samples at CON and MIT (for colour coding see table caption).

				XRF analyses: Raw data (major oxides)												XRF analyses: Raw data (trace elements)										
sample ID	**IGSN†**	**brief sample description**	**mean depth**	**SiO_2**	**TiO_2**	**Al_2O_3**	**Fe_2O_3**	**MnO**	**MgO**	**CaO**	**Na_2O**	**K_2O**	**P_2O_5**	**LOI**	**Sum**	**Ba**	**Cr**	**Ga**	**Nb**	**Ni**	**Rb**	**Sr**	**V**	**Y**	**Zn**	**Zr**
			(m)	(wt%)	(wt%)	(wt%)	(wt%)	(wt%)	(wt%)	(wt%)	(wt%)	(wt%)	(wt%)	(wt%)	(wt%)	(µg/g)	(µg/g)	(µg/g)	(µg/g)	(µg/g)	(µg/g)	(µg/g)	(µg/g)	(µg/g)	(µg/g)	(µg/g)
MIT regolith - bedrock depth profile																										
MIT 14	GFDUH004A	soil, Bw horizon	0.2	42	0.68	12	4.0	0.05	1.1	1.0	1.3	1.5	0.12	36	99.70	422	35	15	14	15	69	88	60	26	77	266
MIT 13	GFDUH004B	soil, Bw horizon	0.4	58	0.93	13	5.5	0.05	0.82	1.5	1.6	1.8	0.28	16	99.68	612	48	22	21	15	65	129	85	27	61	286
MIT 12	GFDUH004C	soil, Bw horizon	0.6	58	0.92	15	6.1	0.06	1.2	1.4	1.7	1.9	0.18	14	99.66	615	47	24	20	19	71	123	80	32	79	330
MIT 11	GFDUH0045	soil, Bw horizon	0.8	60	0.96	17	6.3	0.07	1.3	1.4	1.7	2.0	0.19	9.4	99.64	657	50	20	22	23	88	127	87	33	95	343
MIT 10	GFDUH0046	soil, Bw horizon	1.0	60	0.94	17	6.2	0.07	1.5	1.4	1.8	2.2	0.17	8.6	99.60	622	49	23	22	26	111	124	92	37	110	364
MIT 9	GFDUH0047	soil, Bw horizon	1.2	59	0.99	18	6.7	0.08	1.8	1.4	1.8	2.6	0.20	7.2	99.62	714	52	24	22	26	127	125	96	41	115	380
MIT 8	GFDUH0048	saprolite, Cw horizon	1.4	60	1.00	18	7.0	0.09	1.8	1.5	1.9	2.8	0.22	5.8	99.56	764	46	24	20	24	132	125	94	47	111	412
MIT 7	GFDUH0049	saprolite, Cw horizon	1.6	58	0.98	18	7.2	0.10	1.8	1.6	1.9	2.6	0.22	7.3	99.57	707	47	25	20	22	126	125	95	49	108	398
MIT 6	GFDUH004D	saprolite, Cw horizon	1.8	55	1.1	19	8.3	0.12	2.2	1.4	2.4	2.9	0.23	6.6	99.30	733	68	27	22	30	145	131	135	56	122	392
MIT 5	GFDUH004E	saprolite, Cw horizon	2.0	58	0.96	19	7.1	0.10	1.8	1.7	2.5	2.3	0.28	5.8	99.50	659	44	25	22	20	113	155	102	45	108	386
MIT 4	GFDUH004F	saprolite, Cw horizon	2.2	59	0.91	19	6.9	0.11	1.7	1.7	2.4	2.0	0.26	6.4	99.59	598	37	24	19	15	105	158	105	49	108	378
MIT 3	GFDUH004G	saprolite, Cw horizon	2.4	56	1.1	19	7.9	0.11	2.2	1.2	1.6	2.7	0.20	7.3	99.49	690	51	25	19	31	160	116	109	73	134	405
MIT 2	GFDUH004H	saprolite, Cw horizon	2.6	58	0.96	18	6.9	0.09	2.0	1.3	1.9	2.5	0.19	7.7	99.53	654	42	22	20	21	141	147	100	73	113	382
MIT 1	GFDUH004J	saprolite, Cw horizon	2.8	59	0.93	18	7.0	0.10	2.0	1.6	2.3	2.4	0.24	6.3	99.57	610	37	23	21	19	116	157	103	74	113	357
MIT 19	GFDUH00AT	saprolite, Cw horizon	3.2	60	0.92	17	7.0	0.12	3.2	2.9	1.4	1.3	0.49	5.5	99.68	457	124	24	44	149	108	123	76	48	144	185
MIT 20	GFDUH00AU	saprolite, Cw horizon	3.6	45	0.58	13	14	0.55	6.2	9.5	0.5	1.8	3.04	4.8	99.08	609	957	21	215	523	144	252	129	141	191	357
MIT 21	GFDUH00AV	saprolite, Cw horizon	4.0	62	0.76	17	7.0	0.13	2.8	1.6	1.0	2.1	0.30	5.4	99.66	540	137	23	40	103	160	92	77	58	164	153
MIT 22	GFDUH00AW	saprolite, Cw horizon	4.7	61	0.70	18	5.4	0.08	2.2	2.8	2.2	2.6	0.45	3.9	99.69	664	91	24	31	84	145	168	56	35	134	167
MIT 23	GFDUH00AX	saprolite, Cw horizon	5.3	61	0.90	19	6.0	0.07	2.0	1.4	1.5	2.5	0.22	5.2	99.65	587	54	28	26	50	211	108	71	42	154	378
MIT 24	GFDUH00AY	saprolite, Cw horizon	6.7	71	0.58	13	3.9	0.05	1.4	1.2	0.91	3.8	0.16	3.0	99.72	661	55	18	22	42	186	111	49	24	114	275
MIT 25	GFDUH00AZ	saprolite, Cw horizon	8.4	56	1.1	18	9.0	0.12	2.9	1.2	1.5	5.8	0.13	4.0	99.53	1339	116	26	25	51	227	169	127	25	174	277
MIT 26	GFDUH00B0	saprolite, Cw horizon	9.5	32	7.1	19	19	0.28	2.8	7.1	<0.01	1.5	0.56	9.4	99.31	1103	581	36	114	331	107	233	280	84	168	568
MIT 27	GFDUH00B1	saprolite, Cw horizon	12.5	53	3.0	17	9.2	0.16	3.2	4.8	1.0	2.4	0.47	4.8	99.44	706	237	27	53	127	136	196	149	44	161	478
MIT 28	GFDUH00B2	saprolite, Cw horizon	13.4	56	3.0	16	10	0.22	2.4	4.2	0.58	2.3	0.39	5.0	99.53	882	191	25	53	129	117	198	154	47	161	391
MIT 29	GFDUH00B3	saprolite, Cw horizon	16.3	56	1.2	19	8.3	0.10	3.0	2.6	3.2	3.2	0.13	2.8	99.53	676	92	28	24	62	159	237	121	29	161	372
MIT 41	GFDUH00AG	weathered rock fragments	1.0	58	2.2	13	7.9	0.14	4.1	8.5	2.1	1.8	0.34	1.1	99.55	461	259	20	35	74	85	204	155	31	124	255
MIT 42	GFDUH00B7	weathered rock fragments	1.9	53	1.9	13	10	0.16	5.5	8.2	1.1	2.7	0.86	2.1	99.25	1073	142	18	91	53	77	269	158	38	114	270
MIT 43	GFDUH00AH	weathered rock fragments	2.4	60	1.2	13	6.9	0.13	4.4	7.7	1.8	2.3	0.57	0.0	98.22	857	91	18	54	92	75	232	116	31	98	273
MIT 44	GFDUH00B9	weathered rock fragments	3.2	65	0.92	13	4.9	0.11	3.5	6.4	2.5	1.3	0.71	1.0	99.69	399	96	15	79	92	67	243	53	24	85	140
MIT 45	GFDUH00B8	weathered rock fragments	4.0	63	0.40	13	4.3	0.12	4.0	8.8	2.5	0.53	1.7	1.3	99.49	398	707	17	104	247	26	283	63	47	81	194
MIT 46	GFDUH00AJ	weathered rock fragments	4.6	55	0.29	11	6.5	0.16	5.8	13	0.88	0.31	1.0	6.3	99.56	198	419	17	49	238	16	132	54	30	115	57
MIT 47	GFDUH00B6	weathered rock fragments	5.3	67	0.24	17	2.4	0.06	1.9	5.6	3.4	0.82	0.33	1.2	99.81	399	51	20	24	88	42	453	22	16	50	62
MIT 48	GFDUH00BD	weathered rock fragments	7.9	72	0.32	14	2.2	0.02	0.63	1.3	2.5	5.9	0.26	0.25	99.77	901	14	16	11	<10	182	183	34	13	49	175
MIT 49	GFDUH00BA	weathered rock fragments	8.1	76	0.12	14	0.57	<0.01	0.14	2.3	1.7	5.1	0.12	0.24	99.78	1033	<10	16	<10	<10	140	232	13	<10	17	94

continued next page …

Supplementary Table 2-1a continued - Chemical composition of soil, saprolite and rock samples at CON and MIT (for colour coding see table caption).

				XRF analyses: Raw data (major oxides)												XRF analyses: Raw data (trace elements)										
sample ID	**IGSN†**	**brief sample description**	**mean depth**	**SiO_2**	**TiO_2**	**Al_2O_3**	**Fe_2O_3**	**MnO**	**MgO**	**CaO**	**Na_2O**	**K_2O**	**P_2O_5**	**LOI**	**Sum**	**Ba**	**Cr**	**Ga**	**Nb**	**Ni**	**Rb**	**Sr**	**V**	**Y**	**Zn**	**Zr**
				(wt%)	(wt%)	(wt%)	(wt%)	(wt%)	(wt%)	(wt%)	(wt%)	(wt%)	(wt%)	(wt%)	(wt%)	(µg/g)	(µg/g)	(µg/g)	(µg/g)	(µg/g)	(µg/g)	(µg/g)	(µg/g)	(µg/g)	(µg/g)	(µg/g)
MIT 31	GFDUH00BY	weathered gneiss	17.7	65	0.92	15	6.4	0.09	2.6	1.4	2.6	5.2	0.16	0.8	99.65	727	103	19	16	29	162	202	111	35	104	248
MIT 32	GFDUH00BX	weathered gneiss	20.1	59	1.2	17	7.8	0.10	3.3	4.3	3.4	2.0	0.21	1.1	99.59	503	57	23	17	17	98	216	157	30	128	198
MIT 33	GFDUH00BW	weathered gneiss	22.8	65	0.64	17	4.4	0.05	1.6	3.9	4.0	1.8	0.30	1.5	99.72	329	<10	22	17	<10	92	269	83	17	87	99
MIT 34	GFDUH00BV	weathered gneiss	25.9	69	0.66	15	4.1	0.05	1.2	2.9	3.3	3.0	0.17	0.34	99.47	1034	22	18	17	<10	98	195	55	14	68	315
MIT 35	GFDUH00BU	unweathered gneiss	26.3	68	0.71	15	4.6	0.05	1.5	3.2	3.3	2.5	0.25	0.30	99.64	831	28	19	15	10	98	189	62	20	74	319
MIT 36	GFDUH00BT	unweathered gneiss	26.5	66	0.91	16	5.2	0.08	1.6	3.2	3.4	2.9	0.15	0.34	99.45	938	25	19	24	<10	107	194	62	14	89	339
MIT 37	GFDUH00BS	unweathered gneiss	27.9	66	0.68	16	4.9	0.07	1.5	3.5	3.6	2.1	0.23	0.98	99.52	834	24	21	16	10	76	225	63	17	99	364
MIT 38	GFDUH00BR	unweathered gneiss	28.6	57	1.5	17	8.9	0.12	2.9	4.0	3.3	3.0	0.58	1.1	98.99	673	51	26	29	20	147	188	132	31	149	314
MIT 39	GFDUH00BQ	unweathered gneiss	29.0	57	1.2	18	7.6	0.12	2.5	4.3	4.0	2.8	0.73	neg.	98.40	750	23	27	24	16	131	220	86	37	194	240
MIT 40	GFDUH00BP	unweathered gneiss	29.6	56	1.3	19	7.9	0.09	2.8	4.7	4.1	2.8	0.78	0.44	99.48	524	32	27	28	19	148	219	136	40	140	440
MIT bedload sediment																										
MIT 30	GFDUH0077	bedload sediment	-	73	0.6	13	2.4	0.07	0.6	2.4	2.7	2.2	0.15	3.5	99.66	774	23	13	17	<10	57	182	34	34	41	445
international reference materials for concentration data quality control																										
GM Granite (ZGI) (a)				74	0.20	13	2.0	0.04	0.4	0.9	3.6	4.8	0.06	0.6	99.68	337	<10	16	18	<10	263	136	<10	27	33	136
GM Granite (ZGI) (b)				74	0.20	13	1.9	0.04	0.3	0.9	3.6	4.8	0.06	0.6	99.66	317	<10	16	19	<10	261	134	12	26	31	137
GM Granite (ZGI) (c)				74	0.20	13	1.9	0.04	0.4	0.9	3.8	4.8	0.06	0.6	99.66	333	<10	16	19	<10	262	136	12	27	32	136
GM Granite (ZGI) certified value				73	0.21	14	2.0	0.04	0.37	1.1	3.8	4.8	0.06	0.6	99.91	340	11	15	18	6.8	260	133	11	26	30	149
GM Granite (ZGI) certified relative uncertainty				n.r.	n.r.	n.r.	n.r.	n.r.	n.r.	n.r.	n.r.	n.r.	n.r.	n.r.	n.r.	n.r.	n.r.	n.r.	n.r.	n.r.	n.r.	n.r.	n.r.	n.r.	n.r.	n.r.
TB clay shale (ZGI) (a)				60	0.89	21	6.7	0.05	1.8	0.2	1.4	4.0	0.10	3.9	99.54	783	88	27	18	40	185	166	101	37	95	189
TB clay shale (ZGI) (b)				60	0.90	21	6.7	0.05	1.8	0.2	1.4	4.0	0.10	3.9	99.51	780	90	25	17	41	185	165	104	38	96	186
TB clay shale (ZGI) (c)				60	0.89	21	6.7	0.05	1.8	0.2	1.3	4.0	0.10	3.9	99.54	753	87	26	18	39	184	165	109	38	96	187
TB clay shale (ZGI) certified value				60	0.93	21	6.9	0.05	1.9	n.r.	1.3	3.9	0.10	3.9	99.89	780	82	25	20	40	180	160	107	39	94	180
TB clay shale (ZGI) certified relative uncertainty				n.r.	n.r.	n.r.	n.r.	n.r.	n.r.	n.r.	n.r.	n.r.	n.r.	n.r.	n.r.	n.r.	n.r.	n.r.	n.r.	n.r.	n.r.	n.r.	n.r.	n.r.	n.r.	n.r.
SRM 2709a San Joaquin Soil (a)				63	0.56	14	4.8	0.07	2.4	2.7	1.1	2.5	0.17	8.3	99.40	1049	126	14	20	87	102	229	110	24	100	124
SRM 2709a San Joaquin Soil (b)				51	0.43	11	3.5	0.05	1.9	2.1	1.2	2.0	0.12	26	99.65	687	95	13	<10	57	68	185	85	15	78	126
SRM 2709a San Joaquin Soil certified value				n.r.	n.r.	n.r.	n.r.	n.r.	n.r.	n.r.	n.r.	n.r.	n.r.	n.r.	n.r.	n.r.	n.r.	n.r.	n.r.	n.r.	n.r.	n.r.	n.r.	n.r.	n.r.	n.r.
SRM 2709a San Joaquin Soil certified relative uncertainty				n.r.	n.r.	n.r.	n.r.	n.r.	n.r.	n.r.	n.r.	n.r.	n.r.	n.r.	n.r.	n.r.	n.r.	n.r.	n.r.	n.r.	n.r.	n.r.	n.r.	n.r.	n.r.	n.r.
TILL-1 (CCRMP)				59	0.95	13	6.7	0.18	2.1	2.6	2.2	2.0	0.22	11.1	99.67	651	45	14	25	30	54	275	111	36	92	407
TILL-1 (CCRMP) certified value				61	0.98	14	6.8	0.18	2.2	2.7	2.7	2.2	0.22	7.3	99.90	702	65	n.r.	10	24	44	291	99	38	98	502
TILL-1 (CCRMP) certified relative uncertainty				n.r.	n.r.	n.r.	n.r.	n.r.	n.r.	n.r.	n.r.	n.r.	n.r.	n.r.	n.r.	n.r.	n.r.	n.r.	n.r.	n.r.	n.r.	n.r.	n.r.	n.r.	n.r.	n.r.

n.r. = not reported

Uncertainties on XRF concentration data are estimated to be ±5% relative for major elements (wt%) in rock, ±10% relative for major elements in soil and saprolite, ±10% relative for trace elements in rock, soil and saprolite, and ±15% relative for Na in soil and saprolite (based on accuracy of analysed reference materials). Grey labelled data indicate samples identified to stem from a non-representative source rock as indicated by Zr concentrations that are too low (see Section 2.3.4). These were excluded in metrics that rely on Zr data. Brown labelled data indicate samples that also stem from another source rock as indicated by Cr, Nb, Ni, Ti concentrations that are too high. The metrics derived from these samples that rely on Zr concentrations were excluded.

† IGSN (International Geo Sample Number). Metadata of samples are available under: www.igsn.org by adding the IGSN after igsn.org, e.g. igsn.org/GFDUH00LT

Supplementary Table 2-1b Loss on ignition (LOI) corrected chemical composition of soil, saprolite and rock samples at CON and MIT (for colour coding see table caption).

				LOI corrected data (major oxides)										LOI corrected data (trace elements)										
sample ID	**IGSN[†]**	**brief sample description**	**mean depth**	**SiO_2**	**TiO_2**	**Al_2O_3**	**Fe_2O_3**	**MnO**	**MgO**	**CaO**	**Na_2O**	**K_2O**	**P_2O_5**	**Ba**	**Cr**	**Ga**	**Nb**	**Ni**	**Rb**	**Sr**	**V**	**Y**	**Zn**	**Zr**
			(m)	(wt%)	(wt%)	(wt%)	(wt%)	(wt%)	(wt%)	(wt%)	(wt%)	(wt%)	(wt%)	(µg/g)	(µg/g)	(µg/g)	(µg/g)	(µg/g)	(µg/g)	(µg/g)	(µg/g)	(µg/g)	(µg/g)	(µg/g)
CON regolith - bedrock depth profile																								
CON 14	GFDUH00LT	soil, Ah horizon	0.2	67	1.0	18	7.5	0.14	2.3	0.22	1.02	2.3	0.26	523	109	24	19	42	132	68	147	33	209	279
CON 13	GFDUH00LU	soil, Ah + Bw horizon	0.4	68	1.0	18	7.1	0.15	2.2	0.22	1.05	2.3	0.24	528	110	24	17	41	117	63	140	34	199	291
CON 12	GFDUH00LV	soil, Bw I horizon	0.6	67	1.0	19	7.2	0.16	2.2	0.21	1.14	2.3	0.24	501	118	24	17	39	109	64	152	34	190	276
CON 11	GFDUH00LW	soil, Bw I horizon	0.8	65	1.0	19	8.2	0.17	2.3	0.22	1.1	2.3	0.25	536	123	24	19	50	135	71	151	40	194	307
CON 10	GFDUH00LX	soil, Bw I horizon	1.0	65	1.0	19	7.9	0.14	2.4	0.26	1.1	2.4	0.22	566	119	24	24	54	139	77	150	42	192	335
CON 9	GFDUH00LY	soil, Bw I horizon	1.2	66	1.0	18	7.4	0.09	2.5	0.30	1.1	2.6	0.16	498	125	24	23	55	112	71	146	37	182	342
CON 8	GFDUH00LZ	soil, Bw I horizon	1.4	67	1.0	18	7.3	0.07	2.5	0.25	1.01	2.7	0.12	438	120	24	19	50	114	66	137	36	177	360
CON 7	GFDUH00M0	soil, Bw I horizon	1.6	67	0.98	17	7.1	0.08	2.5	0.30	0.99	2.8	0.14	421	118	21	18	51	113	65	133	36	181	371
CON 6	GFDUH00M1	soil, Bw II horizon	1.8	68	0.99	17	7.2	0.08	2.6	0.31	1.01	2.7	0.13	472	122	21	16	54	110	67	128	34	169	361
CON 5	GFDUH00M2	soil, Bw II horizon	2.0	67	0.98	17	7.2	0.09	2.7	0.34	1.04	2.7	0.13	493	118	22	17	51	109	72	138	33	166	337
CON 4	GFDUH00M3	soil, Bw II horizon	2.2	68	0.98	17	7.1	0.08	2.7	0.36	1.03	2.7	0.13	484	118	22	17	53	103	72	136	37	171	347
CON 3	GFDUH00M4	saprolite, Cw horizon	2.4	68	0.95	17	7.0	0.09	2.6	0.39	1.02	2.7	0.14	509	122	19	16	49	106	70	135	38	174	362
CON 2	GFDUH00M5	saprolite, Cw horizon	2.6	68	0.97	16	7.1	0.10	2.7	0.45	1.05	2.8	0.15	507	132	22	15	50	111	72	136	43	177	360
CON 1	GFDUH00M6	saprolite, Cw horizon	2.8	69	0.94	16	6.6	0.09	2.5	0.48	1.1	2.7	0.16	497	127	21	15	50	107	75	120	44	168	424
CON 19	GFDUH00MB	saprolite, Cw horizon	3.4	68	0.92	16	6.8	0.08	2.6	0.51	1.4	2.8	0.17	511	113	22	13	46	112	87	128	43	151	331
CON 20	GFDUH00MC	saprolite, Cw horizon	3.9	68	0.93	16	6.7	0.09	2.5	0.58	1.3	2.8	0.18	514	118	22	17	48	112	90	126	44	149	375
CON 21	GFDUH00MD	saprolite, Cw horizon	4.4	70	0.87	15	6.2	0.08	2.3	0.57	1.3	2.7	0.17	497	110	20	13	46	100	84	119	38	138	361
CON 22	GFDUH00ME	saprolite, Cw horizon	5.0	68	0.91	16	6.6	0.08	2.5	0.57	1.4	2.8	0.17	521	105	20	14	45	103	92	126	42	141	346
CON 23	GFDUH00MF	saprolite, Cw horizon	5.7	66	0.95	17	7.4	0.09	2.8	0.58	1.6	3.0	0.17	557	113	24	14	51	116	95	142	41	154	278
CON 24	GFDUH00MG	saprolite, Cw horizon	6.5	69	0.87	16	6.6	0.08	2.6	0.68	1.4	2.6	0.17	518	106	19	16	48	114	103	122	45	128	393
CON 28	GFDUH00MT	weathered rock fragments	0.4	70	0.80	16	6.4	0.05	2.5	0.13	0.9	2.9	0.11	543	106	21	13	49	104	46	137	31	121	188
CON 32	GFDUH00MX	weathered rock fragments	1.6	65	0.96	18	7.5	0.05	2.9	0.07	0.5	3.9	0.08	577	131	25	14	53	147	38	167	35	133	236
CON 36	GFDUH00N1	weathered rock fragments	2.8	77	0.66	12	4.2	0.03	1.6	0.44	1.8	2.0	0.13	417	64	14	<lod	30	65	95	72	33	78	207
CON 45	GFDUH00N5	weathered paragneiss	7.6	75	0.08	15	1.0	0.01	0.2	0.4	3.3	5.0	0.18	392	17	17	10	<lod	189	65	<lod	21	29	46
CON 40	GFDUH00N7	weathered paragneiss >63 mm	10.5	70	0.45	16	3.4	0.07	1.4	2.3	4.1	2.3	0.18	617	19	16	10	<lod	59	462	60	19	53	156
CON 41	GFDUH00N8	weathered paragneiss 20-63 mm	10.5	62	0.86	18	6.4	0.11	2.8	3.3	3.4	2.2	0.26	656	34	19	14	<lod	74	399	143	21	83	162
CON 47	GFDUH00N9	weathered paragneiss	13.0	57	1.0	18	8.1	0.15	3.5	5.6	3.2	2.2	0.29	778	<lod	21	18	<lod	68	510	196	42	113	195
CON 48	GFDUH00NA	unweathered paragneiss	15.2	57	1.2	18	8.6	0.10	4.2	6.2	2.6	2.2	0.25	732	16	20	<lod	<lod	67	407	281	26	79	166
CON 49	GFDUH00NB	unweathered paragneiss	16.3	55	1.1	18	9.2	0.12	4.1	6.6	3.1	1.9	0.17	530	14	19	12	<lod	52	338	226	22	83	132
CON 50	GFDUH00NC	unweathered paragneiss	18.4	58	1.0	18	7.3	0.14	3.6	5.9	3.3	2.1	0.26	723	43	19	16	<lod	67	458	180	30	102	153
CON 51	GFDUH00ND	unweathered paragneiss	19.5	58	0.92	18	7.2	0.12	3.4	6.6	3.4	2.4	0.19	687	18	18	<lod	<lod	72	510	180	28	84	154
CON bedload sediment																								
CON 27	GFDUH00SK	bedload sediment	-	73	0.68	15	5.1	0.07	2.0	0.29	0.88	3.0	0.10	588	84	19	10	44	113	66	103	26	196	178

continued next page …

Supplementary Table 2-1b continued - Loss on ignition (LOI) corrected chemical composition of soil, saprolite and rock samples at CON and MIT (for colour coding see table caption) .

				LOI corrected data (major oxides)										LOI corrected data (trace elements)										
sample ID	**IGSN**[†]	**brief sample description**	**mean depth**	**SiO_2**	**TiO_2**	**Al_2O_3**	**Fe_2O_3**	**MnO**	**MgO**	**CaO**	**Na_2O**	**K_2O**	**P_2O_5**	**Ba**	**Cr**	**Ga**	**Nb**	**Ni**	**Rb**	**Sr**	**V**	**Y**	**Zn**	**Zr**
			(m)	(wt%)	(wt%)	(wt%)	(wt%)	(wt%)	(wt%)	(wt%)	(wt%)	(wt%)	(wt%)	(µg/g)	(µg/g)	(µg/g)	(µg/g)	(µg/g)	(µg/g)	(µg/g)	(µg/g)	(µg/g)	(µg/g)	(µg/g)
MIT regolith - bedrock depth profile																								
MIT 14	GFDUH004A	soil, Bw horizon	0.2	66	1.0	19	6.2	0.08	1.7	1.6	2.0	2.4	0.18	655	54	23	22	23	107	136	93	40	119	413
MIT 13	GFDUH004B	soil, Bw horizon	0.4	69	1.1	16	6.6	0.06	0.98	1.8	1.9	2.2	0.33	729	57	26	25	18	77	154	101	32	73	341
MIT 12	GFDUH004C	soil, Bw horizon	0.6	67	1.1	18	7.0	0.07	1.3	1.6	1.9	2.2	0.21	711	54	28	23	22	82	142	92	37	91	382
MIT 11	GFDUH0045	soil, Bw horizon	0.8	66	1.1	18	6.9	0.07	1.4	1.6	1.9	2.2	0.21	725	55	22	24	25	97	140	96	36	105	378
MIT 10	GFDUH0046	soil, Bw horizon	1.0	65	1.0	18	6.8	0.08	1.7	1.6	2.0	2.4	0.19	680	54	25	24	28	121	136	101	40	120	398
MIT 9	GFDUH0047	soil, Bw horizon	1.2	64	1.1	19	7.2	0.08	1.9	1.6	1.9	2.7	0.21	769	56	26	24	28	137	135	103	44	124	409
MIT 8	GFDUH0048	saprolite, Cw horizon	1.4	63	1.1	19	7.4	0.10	1.9	1.6	2.0	3.0	0.23	811	49	25	21	25	140	133	100	50	118	437
MIT 7	GFDUH0049	saprolite, Cw horizon	1.6	62	1.1	20	7.7	0.11	1.9	1.7	2.1	2.8	0.24	763	51	27	22	24	136	135	103	53	117	429
MIT 6	GFDUH004D	saprolite, Cw horizon	1.8	59	1.2	21	8.9	0.13	2.4	1.5	2.6	3.1	0.24	785	73	29	24	32	155	140	145	60	131	420
MIT 5	GFDUH004E	saprolite, Cw horizon	2.0	61	1.0	20	7.5	0.10	1.9	1.8	2.7	2.4	0.30	700	47	27	23	21	120	165	108	48	115	410
MIT 4	GFDUH004F	saprolite, Cw horizon	2.2	63	0.98	20	7.3	0.12	1.8	1.8	2.5	2.2	0.28	639	40	26	20	16	112	169	112	52	115	404
MIT 3	GFDUH004G	saprolite, Cw horizon	2.4	61	1.2	20	8.5	0.12	2.4	1.3	1.7	2.9	0.21	744	55	27	20	33	173	125	118	79	144	437
MIT 2	GFDUH004H	saprolite, Cw horizon	2.6	63	1.0	20	7.4	0.10	2.2	1.4	2.1	2.8	0.20	708	45	24	22	23	153	159	108	79	122	414
MIT 1	GFDUH004J	saprolite, Cw horizon	2.8	63	0.99	19	7.5	0.10	2.1	1.7	2.5	2.6	0.26	651	39	25	22	20	124	168	110	79	121	381
MIT 19	GFDUH00AT	saprolite, Cw horizon	3.2	63	0.98	18	7.4	0.13	3.3	3.0	1.5	1.4	0.52	484	131	25	47	158	114	130	80	51	152	196
MIT 20	GFDUH00AU	saprolite, Cw horizon	3.6	48	0.61	13	15	0.58	6.5	10.0	0.6	1.9	3.19	640	1005	22	226	549	151	265	135	148	201	375
MIT 21	GFDUH00AV	saprolite, Cw horizon	4.0	65	0.80	18	7.4	0.14	2.9	1.7	1.1	2.3	0.32	571	145	24	42	109	169	97	81	61	173	162
MIT 22	GFDUH00AW	saprolite, Cw horizon	4.7	64	0.73	19	5.6	0.08	2.3	2.9	2.3	2.7	0.47	691	95	25	32	87	151	175	58	36	139	174
MIT 23	GFDUH00AX	saprolite, Cw horizon	5.3	64	0.95	20	6.4	0.07	2.1	1.5	1.6	2.7	0.23	619	57	30	27	53	223	114	75	44	162	399
MIT 24	GFDUH00AY	saprolite, Cw horizon	6.7	73	0.59	14	4.1	0.05	1.5	1.2	0.94	3.9	0.16	681	57	19	23	43	192	114	51	25	118	284
MIT 25	GFDUH00AZ	saprolite, Cw horizon	8.4	58	1.1	19	9.4	0.13	3.0	1.2	1.6	6.0	0.13	1395	121	27	26	53	236	176	132	26	181	289
MIT 26	GFDUH00B0	saprolite, Cw horizon	9.5	36	7.9	21	21	0.31	3.1	7.8	<lod	1.6	0.62	1218	641	40	126	365	118	257	309	93	185	627
MIT 27	GFDUH00B1	saprolite, Cw horizon	12.5	56	3.2	18	9.7	0.16	3.4	5.1	1.0	2.5	0.49	742	249	28	56	133	143	206	157	46	169	502
MIT 28	GFDUH00B2	saprolite, Cw horizon	13.4	58	3.2	17	10	0.24	2.5	4.4	0.61	2.5	0.41	928	201	26	56	136	123	208	162	49	169	411
MIT 29	GFDUH00B3	saprolite, Cw horizon	16.3	58	1.2	19	8.5	0.10	3.1	2.7	3.3	3.3	0.13	696	95	29	25	64	164	244	124	30	166	383
MIT 41	GFDUH00AG	weathered rock fragments	1.0	59	2.2	14	8.0	0.14	4.1	8.6	2.1	1.9	0.35	466	262	20	35	75	86	206	157	31	125	258
MIT 42	GFDUH00B7	weathered rock fragments	1.9	54	1.9	13	10	0.16	5.6	8.4	1.1	2.8	0.88	1096	145	18	93	54	79	275	161	39	116	276
MIT 43	GFDUH00AH	weathered rock fragments	2.4	60	1.2	13	6.9	0.13	4.4	7.7	1.8	2.3	0.57	857	91	18	54	92	75	232	116	31	98	273
MIT 44	GFDUH00B9	weathered rock fragments	3.2	66	0.93	13	5.0	0.11	3.6	6.4	2.5	1.3	0.72	403	97	15	80	93	68	245	54	24	86	141
MIT 45	GFDUH00B8	weathered rock fragments	4.0	63	0.40	14	4.3	0.12	4.0	8.9	2.5	0.54	1.7	403	716	17	105	250	26	287	64	48	82	197
MIT 46	GFDUH00AJ	weathered rock fragments	4.6	59	0.31	11	7.0	0.17	6.2	14	0.94	0.33	1.1	211	447	18	52	254	17	141	58	32	123	61
MIT 47	GFDUH00B6	weathered rock fragments	5.3	68	0.25	17	2.4	0.06	1.9	5.6	3.5	0.83	0.34	404	52	20	24	89	43	459	22	16	51	63
MIT 48	GFDUH00BD	weathered rock fragments	7.9	72	0.32	14	2.2	0.02	0.6	1.3	2.5	5.9	0.26	903	14	16	11	<lod	182	183	34	13	49	175
MIT 49	GFDUH00BA	weathered rock fragments	8.1	76	0.12	14	0.57	<lod	0.1	2.3	1.7	5.1	0.12	1035	<lod	16	<lod	<lod	140	233	13	<lod	17	94
MIT 31	GFDUH00BY	weathered gneiss	17.7	65	0.92	15	6.4	0.09	2.6	1.4	2.6	5.2	0.16	732	104	19	16	29	163	204	112	35	105	250
MIT 32	GFDUH00BX	weathered gneiss	20.1	60	1.2	17	7.9	0.10	3.4	4.4	3.4	2.0	0.22	508	58	23	17	17	99	218	159	30	129	200
MIT 33	GFDUH00BW	weathered gneiss	22.8	66	0.65	17	4.5	0.05	1.6	3.9	4.1	1.8	0.31	334	<lod	22	17	<lod	93	273	84	17	88	101
MIT 34	GFDUH00BV	weathered gneiss	25.9	69	0.66	15	4.1	0.05	1.2	2.9	3.3	3.0	0.17	1038	22	18	17	<lod	98	196	55	14	68	316

continued next page …

Supplementary Table 2-1b continued - Loss on ignition (LOI) corrected chemical composition of soil, saprolite and rock samples at CON and MIT (for colour coding see table caption).

				LOI corrected data (major oxides)										LOI corrected data (trace elements)										
sample ID	**IGSN†**	**brief sample description**	**mean depth**	**SiO_2**	**TiO_2**	**Al_2O_3**	**Fe_2O_3**	**MnO**	**MgO**	**CaO**	**Na_2O**	**K_2O**	**P_2O_5**	**Ba**	**Cr**	**Ga**	**Nb**	**Ni**	**Rb**	**Sr**	**V**	**Y**	**Zn**	**Zr**
				(wt%)	(wt%)	(wt%)	(wt%)	(wt%)	(wt%)	(wt%)	(wt%)	(wt%)	(wt%)	(µg/g)	(µg/g)	(µg/g)	(µg/g)	(µg/g)	(µg/g)	(µg/g)	(µg/g)	(µg/g)	(µg/g)	(µg/g)
MIT 35	GFDUH00BU	unweathered gneiss	26.3	68	0.71	15	4.6	0.05	1.5	3.2	3.3	2.5	0.25	834	28	19	15	10	98	190	62	20	74	320
MIT 36	GFDUH00BT	unweathered gneiss	26.5	66	0.91	16	5.2	0.08	1.6	3.2	3.4	3.0	0.15	941	25	19	24	<lod	107	195	62	14	89	340
MIT 37	GFDUH00BS	unweathered gneiss	27.9	67	0.68	16	4.9	0.07	1.5	3.5	3.6	2.1	0.23	842	24	21	16	10	77	227	64	17	100	368
MIT 38	GFDUH00BR	unweathered gneiss	28.6	57	1.5	17	9.0	0.13	2.9	4.0	3.3	3.0	0.58	680	52	26	29	20	149	190	133	31	151	317
MIT 39	GFDUH00BQ	unweathered gneiss	29.0	57	1.2	18	7.6	0.12	2.5	4.3	4.0	2.8	0.73	750	23	27	24	16	131	220	86	37	194	240
MIT 40	GFDUH00BP	unweathered gneiss	29.6	56	1.3	19	8.0	0.09	2.8	4.7	4.1	2.8	0.78	526	32	27	28	19	149	220	137	40	141	442
MIT bedload sediment																								
MIT 30	GFDUH0077	bedload sediment	-	75	0.66	13	2.5	0.07	0.6	2.4	2.7	2.3	0.15	802	24	13	18	<lod	59	189	35	35	43	461
international reference materials and inter lab comparison for concentration data quality control																								
GM Granite (ZGI) (a)				74	0.20	14	2.0	0.04	0.35	0.94	3.7	4.9	0.06	339	<lod	16	18	<lod	265	137	<lod	27	33	137
GM Granite (ZGI) (b)				74	0.20	14	2.0	0.04	0.34	0.94	3.7	4.9	0.06	319	<lod	16	19	<lod	263	135	12	26	31	138
GM Granite (ZGI) (c)				74	0.20	14	1.9	0.04	0.35	0.94	3.8	4.8	0.06	335	<lod	16	19	<lod	264	137	12	27	32	137
GM Granite (ZGI) mean				**74**	**0.20**	**13.5**	**1.95**	**0.04**	**0.35**	**0.94**	**3.7**	**4.9**	**0.06**	**331**	**-**	**16**	**19**	**-**	**264**	**136**	**12**	**27**	**32**	**137**
GM Granite (ZGI) 2SD				*0.14*	*0.00*	*0.02*	*0.02*	*0.00*	*0.01*	*0.00*	*0.18*	*0.02*	*0.00*	*21*	*-*	*0*	*1*	*-*	*2*	*2*	*0*	*1*	*2*	*1*
GM Granite (ZGI) 2SE				*0.2%*	*1.5%*	*0.2%*	*1.0%*	*2.7%*	*3%*	*0%*	*5%*	*0%*	*2%*	*6%*	*-*	*0%*	*6%*	*-*	*1%*	*2%*	*0%*	*4%*	*6%*	*1%*
GM Granite (ZGI) certified value				74	0.21	14	2.0	0.04	0.37	1.1	3.8	4.8	0.06	342	11	15	18	7	262	134	11	26	30	150
GM Granite (ZGI) certified relative uncertainty				n.r.	n.r.	n.r.	n.r.	n.r.	n.r.	n.r.	n.r.	n.r.	n.r.	n.r.	n.r.	n.r.	n.r.	n.r.	n.r.	n.r.	n.r.	n.r.	n.r.	n.r.
relative uncertainty on rock concentrations (%)				**0%**	**-7%**	**-1%**	**-3%**	**-2%**	**-6%**	**-13%**	**-2%**	**1%**	**-1%**	**-3%**	**-**	**7%**	**4%**	**-**	**1%**	**2%**	**9%**	**3%**	**7%**	**-9%**
TB clay shale (ZGI) (a)				62	0.93	21	7.0	0.05	1.9	0.19	1.4	4.1	0.11	815	92	28	19	42	193	173	105	39	99	197
TB clay shale (ZGI) (b)				62	0.93	21	7.0	0.05	1.9	0.19	1.4	4.1	0.11	812	94	26	18	43	193	172	108	40	100	194
TB clay shale (ZGI) (c)				62	0.93	21	7.0	0.05	1.9	0.19	1.4	4.1	0.11	784	91	27	19	41	192	172	113	40	100	195
TB clay shale (ZGI) mean				**62**	**0.93**	**21**	**7.0**	**0.05**	**1.9**	**0.19**	**1.4**	**4.1**	**0.11**	**803**	**92**	**27**	**18**	**42**	**192**	**172**	**109**	**39**	**100**	**195**
TB clay shale (ZGI) 2SD				*0.10*	*0.00*	*0.04*	*0.01*	*0.00*	*0.01*	*0.00*	*0.04*	*0.01*	*0.00*	*34*	*3.2*	*2.1*	*1.2*	*2.1*	*1.2*	*1.2*	*8.4*	*1.2*	*1.2*	*3.2*
TB clay shale (ZGI) 2SE				*0.2%*	*0.2%*	*0.2%*	*0.2%*	*0.0%*	*1%*	*0%*	*3%*	*0%*	*0%*	*4%*	*3%*	*8%*	*7%*	*5%*	*1%*	*1%*	*8%*	*3%*	*1%*	*2%*
TB clay shale (ZGI) certified value				63	0.97	21	7.2	0.05	2.0	n.r.	1.4	4.0	0.10	812	85	26	21	42	187	167	111	41	98	187
TB clay shale (ZGI) certified relative uncertainty				n.r.	n.r.	n.r.	n.r.	n.r.	n.r.	n.r.	n.r.	n.r.	n.r.	n.r.	n.r.	n.r.	n.r.	n.r.	n.r.	n.r.	n.r.	n.r.	n.r.	n.r.
relative uncertainty on rock concentrations (%)				**-1%**	**-4%**	**-1%**	**-3%**	**-8%**	**-6%**	**-**	**2%**	**2%**	**4%**	**-1%**	**8%**	**4%**	**-12%**	**0%**	**3%**	**3%**	**-2%**	**-3%**	**2%**	**4%**
SRM 2709a San Joaquin Soil (a)				69	0.61	15	5.3	0.08	2.6	2.9	1.2	2.7	0.18	1143	137	15	22	95	111	250	120	26	109	135
SRM 2709a San Joaquin Soil (b)				69	0.59	15	4.7	0.07	2.5	2.9	1.6	2.7	0.17	933	129	18	<lod	77	92	251	115	20	106	171
SRM 2709a San Joaquin Soil mean				**69**	**0.60**	**15**	**5.0**	**0.1**	**2.6**	**2.9**	**1.4**	**2.7**	**0.17**	**1038**	**133**	**16**	**22**	**86**	**102**	**250**	**118**	**23**	**107**	**153**
SRM 2709a San Joaquin Soil 2SD				*0.84*	*0.03*	*0.01*	*0.83*	*0.01*	*0.12*	*0.10*	*0.54*	*0.01*	*0.02*	*297*	*12*	*3*	*22*	*25*	*27*	*2*	*6*	*8*	*4*	*51*
SRM 2709a San Joaquin Soil 2SE				*1.2%*	*5.6%*	*0.1%*	*17%*	*8.2%*	*4.5%*	*3.4%*	*40%*	*0.4%*	*12%*	*29%*	*9%*	*21%*	*-*	*29%*	*26%*	*1%*	*5%*	*35%*	*4%*	*33%*
SRM 2709a certified values				65	0.56	13.9	4.8	0.07	2.4	2.7	1.6	2.5	0.16	979	130	n.r.	n.r.	85	99	239	110	n.r.	103	195
SRM 2709a certified absolut uncertainty				*0.9*	*0.01*	*0.3*	*0.10*	*0.01*	*0.03*	*0.13*	*0.04*	*0.1*	*0.00*	*28*	*9*	*n.r.*	*n.r.*	*2*	*3*	*6*	*11*	*n.r.*	*4*	*46*
relative uncertainty soil/saprolite concentrations (%)				**7%**	**7%**	**8%**	**4%**	**9%**	**5%**	**8%**	**-16%**	**5%**	**10%**	**6%**	**2%**	**-**	**-**	**1%**	**3%**	**5%**	**7%**	**-**	**4%**	**-21%**
TILL-1 (CCRMP)				66	1.1	15	7.6	0.20	2.3	2.9	2.4	2.3	0.25	732	51	16	28	34	61	309	125	40	103	458
TILL-1 (CCRMP) certified value				66	1.1	15	7.4	0.19	2.3	2.9	2.9	2.4	0.24	757	70	<lod	11	26	47	314	107	41	106	542
relative uncertainty soil/saprolite concentrations (%)				**0%**	**1%**	**0%**	**3%**	**4%**	**0%**	**-1%**	**-17%**	**-5%**	**6%**	**-3%**	**-28%**	**-**	**161**	**30%**	**28%**	**-1%**	**17%**	**-1%**	**-2%**	**-15%**

lod = below limit of detection (see table S1a), n.r. = not reported

Uncertainties on XRF concentration data are estimated to be ±5% relative for major elements (wt%) in rock, ±10% relative for major elements in soil and saprolite, ±10% relative for trace elements in rock, soil and saprolite, and ±15% relative for Na in soil and saprolite (based on accuracy of analysed reference materials). Grey labelled data indicate samples identified to stem from a non-representative source rock as indicated by Zr concentrations that are too low (see Section 2.3.4). These were excluded in metrics that rely on Zr data. Brown labelled data indicate samples that also stem from another source rock as indicated by Cr, Nb, Ni, Ti concentrations that are too high. The metrics derived from these samples that rely on Zr concentrations were excluded.

† IGSN (International Geo Sample Number). Metadata of samples are available under: www.igsn.org by adding the IGSN after igsn.org, e.g. igsn.org/GFDUH00LT

Supplementary Table 2-1c Soil pH, weathering indices and isotopic composition of soil, saprolite and rock samples at CON and MIT (for colour coding see table caption).

sample ID	IGSN†	brief sample description	mean depth	soil pH	CDF	τ^{Si}_{Zr}	τ^{Ti}_{Zr}	τ^{Al}_{Zr}	τ^{Fe}_{Zr}	τ^{Mn}_{Zr}	τ^{Mg}_{Zr}	τ^{Ca}_{Zr}	τ^{Na}_{Zr}	τ^{K}_{Zr}	τ^{P}_{Zr}	τ^{Sr}_{Zr}	τ^{Zn}_{Zr}	MC-ICP-MS analyses		AMS analyses	
																		(^{87}Sr / ^{86}Sr)	SD	$^{10}Be_{in\ situ}$	uncertainty
			(m)																	(10^3 at/g_{Qtz})	(10^3 at/g_{Qtz})
CON regolith - bedrock depth profile																					
CON 14	GFDUH00LT	soil, Ah horizon	0.2	4.1	0.46	-0.36	-0.48	-0.46	-0.50	-0.35	-0.67	-0.98	-0.82	-0.42	-0.36	-0.91	0.30	0.72956	0.00015	n.a.	n.a.
CON 13	GFDUH00LU	soil, Ah + Bw horizon	0.4	4.3	0.48	-0.38	-0.50	-0.48	-0.54	-0.36	-0.71	-0.98	-0.82	-0.44	-0.44	-0.92	0.19	0.72956	0.00011	n.a.	n.a.
CON 12	GFDUH00LV	soil, Bw I horizon	0.6	4.5	0.45	-0.36	-0.46	-0.43	-0.51	-0.28	-0.69	-0.98	-0.80	-0.42	-0.40	-0.92	0.20	0.72898	0.00018	n.a.	n.a.
CON 11	GFDUH00LW	soil, Bw I horizon	0.8	4.6	0.51	-0.44	-0.51	-0.46	-0.50	-0.30	-0.71	-0.98	-0.82	-0.47	-0.44	-0.92	0.10	0.72901	0.00017	n.a.	n.a.
CON 10	GFDUH00LX	soil, Bw I horizon	1.0	4.7	0.55	-0.49	-0.56	-0.51	-0.56	-0.46	-0.72	-0.98	-0.83	-0.50	-0.55	-0.92	-0.01	0.72895	0.00018	n.a.	n.a.
CON 9	GFDUH00LY	soil, Bw I horizon	1.2	4.5	0.56	-0.49	-0.57	-0.55	-0.59	-0.68	-0.71	-0.98	-0.84	-0.46	-0.68	-0.93	-0.08	0.72961	0.00013	n.a.	n.a.
CON 8	GFDUH00LZ	soil, Bw I horizon	1.4	4.6	0.58	-0.50	-0.60	-0.59	-0.62	-0.75	-0.73	-0.98	-0.86	-0.47	-0.77	-0.94	-0.15	0.73221	0.00017	n.a.	n.a.
CON 7	GFDUH00M0	soil, Bw I horizon	1.6	4.6	0.59	-0.52	-0.62	-0.61	-0.64	-0.73	-0.73	-0.98	-0.87	-0.47	-0.74	-0.94	-0.15	0.73237	0.00021	n.a.	n.a.
CON 6	GFDUH00M1	soil, Bw II horizon	1.8	4.7	0.58	-0.50	-0.61	-0.60	-0.63	-0.71	-0.71	-0.98	-0.86	-0.47	-0.74	-0.93	-0.19	0.73099	0.00019	n.a.	n.a.
CON 5	GFDUH00M2	soil, Bw II horizon	2.0	4.8	0.55	-0.47	-0.58	-0.57	-0.60	-0.66	-0.68	-0.98	-0.85	-0.44	-0.72	-0.92	-0.15	0.72922	0.00017	n.a.	n.a.
CON 4	GFDUH00M3	soil, Bw II horizon	2.2	4.7	0.56	-0.48	-0.59	-0.59	-0.62	-0.70	-0.69	-0.98	-0.85	-0.46	-0.74	-0.93	-0.15	0.72898	0.00018	n.a.	n.a.
CON 3	GFDUH00M4	saprolite, Cw horizon	2.4	5.3	0.58	-0.50	-0.62	-0.61	-0.64	-0.67	-0.71	-0.97	-0.86	-0.47	-0.73	-0.93	-0.17	0.73031	0.00019	n.a.	n.a.
CON 2	GFDUH00M5	saprolite, Cw horizon	2.6	5.4	0.58	-0.50	-0.61	-0.61	-0.63	-0.66	-0.70	-0.97	-0.86	-0.46	-0.70	-0.93	-0.15	0.72957	0.00014	n.a.	n.a.
CON 1	GFDUH00M6	saprolite, Cw horizon	2.8	5.8	0.64	-0.57	-0.68	-0.68	-0.71	-0.72	-0.77	-0.97	-0.88	-0.55	-0.74	-0.94	-0.31	0.72883	0.00018	n.a.	n.a.
CON 19	GFDUH00MB	saprolite, Cw horizon	3.4	7.0	0.54	-0.45	-0.60	-0.58	-0.62	-0.69	-0.69	-0.96	-0.80	-0.40	-0.65	-0.91	-0.21	0.72881	0.00008	n.a.	n.a.
CON 20	GFDUH00MC	saprolite, Cw horizon	3.9	7.7	0.60	-0.51	-0.64	-0.64	-0.67	-0.70	-0.74	-0.96	-0.83	-0.48	-0.67	-0.91	-0.31	0.72713	0.00006	n.a.	n.a.
CON 21	GFDUH00MD	saprolite, Cw horizon	4.4	7.3	0.58	-0.48	-0.65	-0.64	-0.68	-0.72	-0.74	-0.96	-0.83	-0.48	-0.68	-0.92	-0.34	0.72712	0.00017	n.a.	n.a.
CON 22	GFDUH00ME	saprolite, Cw horizon	5.0	7.1	0.56	-0.48	-0.62	-0.60	-0.64	-0.69	-0.71	-0.96	-0.81	-0.43	-0.65	-0.91	-0.29	0.72662	0.00006	n.a.	n.a.
CON 23	GFDUH00MF	saprolite, Cw horizon	5.7	7.1	0.46	-0.37	-0.51	-0.47	-0.50	-0.59	-0.60	-0.95	-0.72	-0.25	-0.59	-0.88	-0.04	0.72693	0.00010	n.a.	n.a.
CON 24	GFDUH00MG	saprolite, Cw horizon	6.5	7.1	0.62	-0.53	-0.68	-0.66	-0.68	-0.73	-0.74	-0.96	-0.83	-0.53	-0.70	-0.91	-0.44	0.72446	0.00017	n.a.	n.a.
CON 28	GFDUH00MT	weathered rock fragments	0.4	n.a.	0.20	-0.01	-0.39	-0.29	-0.36	-0.63	-0.48	-0.98	-0.76	0.08	-0.61	-0.91	0.11	n.a.	n.a.	n.a.	n.a.
CON 32	GFDUH00MX	weathered rock fragments	1.6	n.a.	0.36	-0.26	-0.42	-0.34	-0.40	-0.75	-0.52	-0.99	-0.89	0.16	-0.78	-0.94	-0.02	n.a.	n.a.	n.a.	n.a.
CON 36	GFDUH00N1	weathered rock fragments	2.8	n.a.	0.27	-0.01	-0.54	-0.51	-0.62	-0.81	-0.69	-0.95	-0.57	-0.31	-0.56	-0.84	-0.35	n.a.	n.a.	n.a.	n.a.
CON 45	GFDUH00N5	weathered paragneiss	7.6	n.a.	-2.26	3.28	-0.74	1.79	-0.61	-0.61	-0.85	-0.80	2.46	6.60	1.70	-0.51	0.08	0.70826	0.00005	n.a.	n.a.
CON 40.41	GFDUH00N7, GFDUH00N8	weathered paragneiss	10.5	n.a.	0.05	0.11	-0.41	-0.10	-0.42	-0.29	-0.48	-0.58	0.16	0.00	-0.06	-0.11	-0.32	0.71108	0.00012	n.a.	n.a.
CON 47	GFDUH00N9	weathered paragneiss	13.0	n.a.	0.22	-0.22	-0.23	-0.21	-0.22	-0.01	-0.30	-0.31	-0.21	-0.20	0.03	-0.08	0.01	0.70899	0.00016	n.a.	n.a.
CON 48	GFDUH00NA	unweathered paragneiss	15.2	n.a.	0.09	-0.09	0.01	-0.10	-0.03	-0.22	0.00	-0.11	-0.23	-0.07	0.04	-0.14	-0.18	0.70959	0.00019	n.a.	n.a.
CON 49	GFDUH00NB	unweathered paragneiss	16.3	n.a.	-0.15	0.11	0.21	0.17	0.31	0.17	0.22	0.20	0.15	0.00	-0.12	-0.09	0.10	0.70957	0.00016	n.a.	n.a.
CON 50	GFDUH00NC	unweathered paragneiss	18.4	n.a.	0.01	0.01	-0.05	-0.01	-0.11	0.13	-0.06	-0.08	0.04	-0.04	0.19	0.06	0.16	0.70942	0.00020	n.a.	n.a.
CON 51	GFDUH00ND	unweathered paragneiss	19.5	n.a.	0.02	0.00	-0.14	-0.03	-0.13	-0.04	-0.13	0.03	0.08	0.12	-0.13	0.17	-0.05	0.71087	0.00017	n.a.	n.a.
CON bedload sediment																					
CON 27	GFDUH00SK	bedload sediment	-	n.a.	n.d.	n.d.	n.d.	n.d.	n.d.	n.d.	n.d.	n.d.	n.d.	n.d.	n.d.	n.d.	n.d.	n.d.	n.d.	88	5.9

continued next page …

Supplementary Table 2-1c continued - Soil pH, weathering indices and isotopic composition of soil, saprolite and rock samples at CON and MIT (for colour coding see table caption).

sample ID	IGSN[†]	brief sample description	mean depth	soil pH	CDF	τ_{Zr}^{Si}	τ_{Zr}^{Ti}	τ_{Zr}^{Al}	τ_{Zr}^{Fe}	τ_{Zr}^{Mn}	τ_{Zr}^{Mg}	τ_{Zr}^{Ca}	τ_{Zr}^{Na}	τ_{Zr}^{K}	τ_{Zr}^{P}	τ_{Zr}^{Sr}	τ_{Zr}^{Zn}	MC-ICP-MS analyses		AMS analyses	
																		(^{87}Sr / ^{86}Sr)	SD	$^{10}Be_{in\ situ}$	uncertainty
			(m)																	(10^3 at/g_{Qtz})	(10^3 at/g_{Qtz})
MIT regolith - bedrock depth profile																					
MIT 14	GFDUH004A	soil, Bw horizon	0.2	3.6	0.18	-0.13	-0.18	-0.10	-0.22	-0.29	-0.36	-0.66	-0.55	-0.27	-0.67	-0.46	-0.22	0.71591	0.00011	n.a.	n.a.
MIT 13	GFDUH004B	soil, Bw horizon	0.4	4.1	0.01	0.11	0.05	-0.09	0.00	-0.36	-0.54	-0.54	-0.47	-0.20	-0.28	-0.26	-0.42	0.71647	0.00011	n.a.	n.a.
MIT 12	GFDUH004C	soil, Bw horizon	0.6	4.5	0.11	-0.05	-0.10	-0.09	-0.05	-0.30	-0.45	-0.62	-0.53	-0.28	-0.59	-0.39	-0.35	0.71690	0.00009	n.a.	n.a.
MIT 11	GFDUH0045	soil, Bw horizon	0.8	4.6	0.11	-0.05	-0.10	-0.04	-0.06	-0.28	-0.40	-0.63	-0.53	-0.27	-0.60	-0.40	-0.25	0.71771	0.00010	n.a.	n.a.
MIT 10	GFDUH0046	soil, Bw horizon	1.0	4.7	0.15	-0.10	-0.17	-0.08	-0.12	-0.25	-0.33	-0.65	-0.53	-0.25	-0.65	-0.44	-0.18	0.71810	0.00011	n.a.	n.a.
MIT 9	GFDUH0047	soil, Bw horizon	1.2	4.7	0.17	-0.15	-0.16	-0.08	-0.09	-0.23	-0.27	-0.66	-0.56	-0.16	-0.62	-0.46	-0.18	0.71952	0.00007	n.a.	n.a.
MIT 8	GFDUH0048	saprolite, Cw horizon	1.4	4.8	0.23	-0.21	-0.22	-0.14	-0.12	-0.18	-0.30	-0.67	-0.57	-0.14	-0.61	-0.50	-0.27	0.72168	0.00010	n.a.	n.a.
MIT 7	GFDUH0049	saprolite, Cw horizon	1.6	4.7	0.21	-0.21	-0.20	-0.09	-0.07	-0.07	-0.29	-0.65	-0.55	-0.18	-0.58	-0.49	-0.27	0.72135	0.00011	n.a.	n.a.
MIT 6	GFDUH004D	saprolite, Cw horizon	1.8	4.8	0.19	-0.24	-0.10	-0.02	0.09	0.13	-0.10	-0.68	-0.43	-0.08	-0.57	-0.45	-0.16	0.72295	0.00010	n.a.	n.a.
MIT 5	GFDUH004E	saprolite, Cw horizon	2.0	4.7	0.18	-0.18	-0.20	-0.01	-0.05	-0.04	-0.26	-0.62	-0.40	-0.26	-0.47	-0.34	-0.24	0.72178	0.00011	n.a.	n.a.
MIT 4	GFDUH004F	saprolite, Cw horizon	2.2	4.8	0.16	-0.15	-0.22	-0.03	-0.06	0.13	-0.27	-0.60	-0.42	-0.33	-0.48	-0.32	-0.23	0.72022	0.00010	n.a.	n.a.
MIT 3	GFDUH004G	saprolite, Cw horizon	2.4	4.9	0.23	-0.24	-0.15	-0.07	0.01	0.05	-0.14	-0.75	-0.63	-0.17	-0.64	-0.53	-0.10	0.72089	0.00011	n.a.	n.a.
MIT 2	GFDUH004H	saprolite, Cw horizon	2.6	5.1	0.18	-0.17	-0.19	-0.05	-0.07	-0.09	-0.16	-0.69	-0.53	-0.16	-0.64	-0.37	-0.20	0.72004	0.00011	n.a.	n.a.
MIT 1	GFDUH004J	saprolite, Cw horizon	2.8	5.3	0.11	-0.10	-0.16	-0.01	0.02	0.00	-0.12	-0.60	-0.40	-0.16	-0.50	-0.28	-0.14	0.71955	0.00012	n.a.	n.a.
MIT 19	GFDUH00AT	saprolite, Cw horizon	3.2	5.1	-0.73	0.76	0.60	0.86	0.94	1.48	1.71	0.36	-0.31	-0.10	0.98	0.09	1.11	0.71554	0.00009	n.a.	n.a.
MIT 20	GFDUH00AU	saprolite, Cw horizon	3.6	5.2	0.10	-0.31	-0.48	-0.29	1.00	4.83	1.76	1.36	-0.86	-0.35	5.31	0.15	0.45	0.71466	0.00007	n.a.	n.a.
MIT 21	GFDUH00AV	saprolite, Cw horizon	4.0	5.1	-1.09	1.21	0.59	1.17	1.36	2.15	1.88	-0.05	-0.39	0.75	0.45	-0.02	1.90	0.71836	0.00009	n.a.	n.a.
MIT 22	GFDUH00AW	saprolite, Cw horizon	4.7	5.7	-0.94	1.01	0.35	1.13	0.67	0.73	1.09	0.48	0.25	0.94	1.00	0.64	1.17	0.71621	0.00006	n.a.	n.a.
MIT 23	GFDUH00AX	saprolite, Cw horizon	5.3	5.6	0.15	-0.12	-0.24	0.01	-0.18	-0.34	-0.16	-0.67	-0.62	-0.16	-0.57	-0.53	0.10	0.71855	0.00006	n.a.	n.a.
MIT 24	GFDUH00AY	saprolite, Cw horizon	6.7	5.9	-0.19	0.42	-0.32	-0.03	-0.26	-0.37	-0.17	-0.62	-0.69	0.73	-0.58	-0.34	0.12	0.72066	0.00006	n.a.	n.a.
MIT 25	GFDUH00AZ	saprolite, Cw horizon	8.4	6.1	-0.17	0.10	0.23	0.31	0.67	0.63	0.67	-0.62	-0.50	1.63	-0.66	0.00	0.70	0.71970	0.00012	n.a.	n.a.
MIT 26	GFDUH00B0	saprolite, Cw horizon	9.5	6.0	0.46	-0.69	3.04	-0.32	0.71	0.83	-0.22	0.10	n.d.	-0.68	-0.26	-0.33	-0.20	0.71356	0.00005	n.a.	n.a.
MIT 27	GFDUH00B1	saprolite, Cw horizon	12.5	6.4	0.33	-0.39	1.03	-0.29	-0.01	0.24	0.06	-0.11	-0.81	-0.37	-0.27	-0.33	-0.09	0.71393	0.00006	n.a.	n.a.
MIT 28	GFDUH00B2	saprolite, Cw horizon	13.4	6.3	0.18	-0.22	1.48	-0.18	0.30	1.15	-0.04	-0.04	-0.86	-0.25	-0.26	-0.17	0.11	0.71402	0.00006	n.a.	n.a.
MIT 29	GFDUH00B3	saprolite, Cw horizon	16.3	6.4	0.12	-0.17	-0.01	0.00	0.15	0.00	0.27	-0.37	-0.19	0.09	-0.74	0.04	0.17	0.71515	0.00007	n.a.	n.a.
MIT 41	GFDUH00AG	weathered rock fragments	1.0	n.a.	n.d.	n.d.	n.d.	n.d.	n.d.	n.d.	n.d.	n.d.	n.d.	n.d.	n.d.	n.d.	n.d.	0.71462	0.00011	n.a.	n.a.
MIT 42	GFDUH00B7	weathered rock fragments	1.9	n.a.	n.d.	n.d.	n.d.	n.d.	n.d.	n.d.	n.d.	n.d.	n.d.	n.d.	n.d.	n.d.	n.d.	0.71358	0.00006	n.a.	n.a.
MIT 43	GFDUH00AH	weathered rock fragments	2.4	n.a.	n.d.	n.d.	n.d.	n.d.	n.d.	n.d.	n.d.	n.d.	n.d.	n.d.	n.d.	n.d.	n.d.	0.71415	0.00007	n.a.	n.a.
MIT 44	GFDUH00B9	weathered rock fragments	3.2	n.a.	n.d.	n.d.	n.d.	n.d.	n.d.	n.d.	n.d.	n.d.	n.d.	n.d.	n.d.	n.d.	n.d.	0.71424	0.00007	n.a.	n.a.
MIT 45	GFDUH00B8	weathered rock fragments	4.0	n.a.	n.d.	n.d.	n.d.	n.d.	n.d.	n.d.	n.d.	n.d.	n.d.	n.d.	n.d.	n.d.	n.d.	0.71151	0.00006	n.a.	n.a.
MIT 46	GFDUH00AJ	weathered rock fragments	4.6	n.a.	n.d.	n.d.	n.d.	n.d.	n.d.	n.d.	n.d.	n.d.	n.d.	n.d.	n.d.	n.d.	n.d.	0.71176	0.00007	n.a.	n.a.
MIT 47	GFDUH00B6	weathered rock fragments	5.3	n.a.	n.d.	n.d.	n.d.	n.d.	n.d.	n.d.	n.d.	n.d.	n.d.	n.d.	n.d.	n.d.	n.d.	0.71116	0.00006	n.a.	n.a.
MIT 48	GFDUH00BD	weathered rock fragments	7.9	n.a.	n.d.	n.d.	n.d.	n.d.	n.d.	n.d.	n.d.	n.d.	n.d.	n.d.	n.d.	n.d.	n.d.	0.72396	0.00005	n.a.	n.a.
MIT 49	GFDUH00BA	weathered rock fragments	8.1	n.a.	n.d.	n.d.	n.d.	n.d.	n.d.	n.d.	n.d.	n.d.	n.d.	n.d.	n.d.	n.d.	n.d.	0.71803	0.00006	n.a.	n.a.
MIT 31	GFDUH00BY	weathered gneiss	17.7	n.a.	-0.35	0.43	0.19	0.20	0.33	0.29	0.63	-0.52	-0.04	1.64	-0.53	0.33	0.14	0.72586	0.00005	n.a.	n.a.
MIT 32	GFDUH00BX	weathered gneiss	20.1	n.a.	-0.69	0.64	0.87	0.69	1.04	0.92	1.68	0.93	0.58	0.25	-0.20	0.78	0.75	0.71429	0.00005	n.a.	n.a.
MIT 33	GFDUH00BW	weathered gneiss	22.8	n.a.	-2.36	2.57	1.08	2.38	1.29	1.01	1.52	2.47	2.78	1.30	1.26	3.44	1.38	0.71438	0.00005	n.a.	n.a.
MIT 34	GFDUH00BV	weathered gneiss	25.9	n.a.	-0.07	0.19	-0.33	-0.05	-0.32	-0.36	-0.39	-0.18	-0.04	0.18	-0.59	0.01	-0.42	0.71675	0.00005	n.a.	n.a.

continued next page …

Supplementary Table 2-1c continued - Soil pH, weathering indices and isotopic composition of soil, saprolite and rock samples at CON and MIT (for colour coding see table caption).

																		MC-ICP-MS analyses		AMS analyses	
sample ID	**IGSN†**	**brief sample description**	**mean depth**	**soil pH**	**CDF**	τ_{Zr}^{Si}	τ_{Zr}^{Ti}	τ_{Zr}^{Al}	τ_{Zr}^{Fe}	τ_{Zr}^{Mn}	τ_{Zr}^{Mg}	τ_{Zr}^{Ca}	τ_{Zr}^{Na}	τ_{Zr}^{K}	τ_{Zr}^{P}	τ_{Zr}^{Sr}	τ_{Zr}^{Zn}	**(^{87}Sr / ^{86}Sr)**	**SD**	**$^{10}Be_{in\ situ}$**	**uncertainty**
MIT 35	GFDUH00BU	unweathered gneiss	26.3	n.a.	-0.06	0.17	-0.29	-0.06	-0.26	-0.39	-0.26	-0.11	-0.03	-0.02	-0.42	-0.03	-0.37	0.71701	0.00006	n.a.	n.a.
MIT 36	GFDUH00BT	unweathered gneiss	26.5	n.a.	0.01	0.06	-0.14	-0.06	-0.20	-0.17	-0.24	-0.17	-0.07	0.09	-0.67	-0.07	-0.29	0.71730	0.00006	n.a.	n.a.
MIT 37	GFDUH00BS	unweathered gneiss	27.9	n.a.	0.08	-0.01	-0.40	-0.13	-0.31	-0.25	-0.35	-0.16	-0.09	-0.29	-0.53	0.01	-0.26	0.71475	0.00006	n.a.	n.a.
MIT 38	GFDUH00BR	unweathered gneiss	28.6	n.a.	-0.06	-0.01	0.52	0.08	0.46	0.49	0.47	0.11	-0.03	0.19	0.36	-0.02	0.28	0.72048	0.00006	n.a.	n.a.
MIT 39	GFDUH00BQ	unweathered gneiss	29.0	n.a.	-0.41	0.29	0.56	0.53	0.62	0.91	0.63	0.58	0.56	0.47	1.25	0.50	1.19	0.71758	0.00010	n.a.	n.a.
MIT 40	GFDUH00BP	unweathered gneiss	29.6	n.a.	0.24	-0.31	-0.03	-0.15	-0.07	-0.23	-0.01	-0.05	-0.13	-0.21	0.32	-0.19	-0.14	0.71877	0.00006	n.a.	n.a.
MIT bedload sediment																					
MIT 30	GFDUH0077	bedload sediment	-	n.d.	n.d.	n.d.	n.d.	n.d.	n.d.	n.d.	n.d.	n.d.	n.d.	n.d.	n.d.	n.d.	n.d.	n.d.	n.d.	190	8.3
International reference materials for soil pH and isotope data quality control																					
IRMM-443-7 (a)				4.8																	
IRMM-443-7 (b)				4.7																	
IRMM-443-7 (c)				4.8																	
IRMM-443-7 (d)				4.7																	
IRMM-443-7 (e)				4.7																	
IRMM-443-7 (f)				4.8																	
IRMM-443-7 mean				**4.8**																	
IRMM-443-7 2SD				*0.1*																	
IRMM-443-7 certified value				4.3																	
IRMM-443-7 certified relative uncertainty				0.7																	
relative uncertainty (%)				**10%**																	
SRM 2709a San Joaquin Soil (a) N=8																		0.70819	0.00004		
SRM 2709a San Joaquin Soil (b) N=1																		0.70810	0.00012		
SRM 2709a San Joaquin Soil (c) N=1																		0.70816	0.00013		
SRM 2709a San Joaquin Soil mean, SD																		**0.70815**	**0.00005**		
TILL-1 (CCRMP) (a) N=1																		0.71151	0.00021		
TILL-1 (CCRMP) (b) N=1																		0.71146	0.00006		
TILL-1 (CCRMP) (b) N=1, SD																		**0.71149**	**0.00004**		
RGM-1 Rhyolite (USGS) N=9																		0.70425	0.00004		
RGM-1 Rhyolite (USGS) published data N=5																		*0.70421*	*0.00001*		
GA granite (CNRS) (a) N=1																		0.71386	0.00010		
GA granite (CNRS) (b) N=1																		0.71378	0.00004		
GA granite (CNRS) (a) N=1 mean, SD																		**0.71382**	**0.00006**		
SRM987 processed through column chemistry N=32																		0.71026	0.00011		
SRM987 not processed through column chemistry N=240																		0.71029	0.00001		
SRM987 published data (measured with MC-ICP-MS) N=247*																		*0.71029*	*0.00033*		

n.a. = not analysed; * data from: Jochum et al. (2005)

Grey labelled data indicate samples identified to stem from a non-representative source rock as indicated by Zr concentrations that are too low (see Section 2.3.4). These were excluded in metrics that rely on Zr data. Brown labelled data indicate samples that also stem from another source rock as indicated by Cr, Nb, Ni, Ti concentrations that are too high. The metrics derived from these samples that rely on Zr concentrations were excluded.

† IGSN (International Geo Sample Number). Metadata of samples are available under: www.igsn.org by adding the IGSN after igsn.org, e.g. igsn.org/GFDUH00LT

Supplementary Table 2-2a Chemical composition of the water-soluble fraction from sequential extractions of soil and saprolite at CON and MIT.

				ICP-OES analyses										
sample ID	**IGSN†**	**sample type**	**mean depth**	**Al**	**Ba**	**Ca**	**Fe**	**K**	**Mg**	**Mn**	**Na**	**S**	**Sr**	**Zn**
			(m)	(µg/g)	(µg/g)	(µg/g)	(µg/g)	(µg/g)	(µg/g)	(µg/g)	(µg/g)	(µg/g)	(µg/g)	(µg/g)
CON depth profile of water-soluble fractions														
CON 14	GFDUH00J0	soil, Ah horizon	0.2	20	0.79	14	4.8	12	11	17	8.8	18	0.11	0.49
CON 13	GFDUH00J1	soil, Ah + Bw horizon	0.4	13	0.74	9.4	4.6	7.7	8.4	10	7.3	12	0.09	<0.38
CON 12	GFDUH00J2	soil, Bw I horizon	0.6	4.2	0.60	7.1	<0.78	3.3	5.8	5.8	7.0	12	<0.08	<0.38
CON 11	GFDUH00J3	soil, Bw I horizon	0.8	2.6	0.50	7.1	<0.78	1.9	4.0	6.0	6.3	15	<0.08	<0.38
CON 10	GFDUH00J4	soil, Bw I horizon	1.0	2.4	0.63	7.2	<0.78	1.7	2.8	4.6	5.2	16	0.08	<0.38
CON 9	GFDUH00J5	soil, Bw I horizon	1.2	1.8	0.68	5.8	<0.78	2.5	3.5	3.5	6.2	16	0.08	<0.38
CON 8	GFDUH00J6	soil, Bw I horizon	1.4	1.9	0.67	6.2	<0.78	5.6	5.3	2.5	7.5	21	0.10	<0.38
CON 7	GFDUH00J7	soil, Bw I horizon	1.6	1.0	0.68	4.0	<0.78	6.4	4.5	1.9	6.8	17	0.08	<0.38
CON 6	GFDUH00J8	soil, Bw II horizon	1.8	0.38	0.48	3.5	<0.78	4.0	2.4	0.57	6.9	11	0.08	<0.38
CON 5	GFDUH00J9	soil, Bw II horizon	2.0	0.48	0.47	3.4	<0.78	3.6	2.3	0.33	7.5	11	<0.08	<0.38
CON 4	GFDUH00JA	soil, Bw II horizon	2.2	1.4	0.16	2.1	0.78	4.6	2.1	0.32	8.2	8.3	<0.08	<0.38
CON 3	GFDUH00JB	saprolite, Cw horizon	2.4	0.89	0.06	1.6	<0.78	3.7	1.1	0.07	6.8	6.7	<0.08	<0.38
CON 2	GFDUH00JC	saprolite, Cw horizon	2.6	1.7	0.06	2.0	1.0	3.2	1.3	0.09	6.7	5.8	<0.08	<0.38
CON 1	GFDUH00JD	saprolite, Cw horizon	2.8	1.7	0.04	1.8	0.81	3.2	1.2	0.03	6.5	5.9	<0.08	<0.38
CON 19	GFDUH00JJ	saprolite, Cw horizon	3.4	1.4	0.05	13	0.92	4.8	7.5	0.06	10	3.4	0.09	<0.38
CON 20	GFDUH00JK	saprolite, Cw horizon	3.9	0.57	0.07	33	<0.78	7.1	16	0.06	11	2.9	0.19	<0.38
CON 21	GFDUH00HZ	saprolite, Cw horizon	4.4	<0.37	0.09	57	<0.78	9.9	24	0.05	13	3.7	0.28	<0.38
CON 22	GFDUH00FB	saprolite, Cw horizon	5.0	7.2	0.06	3.8	6.0	5.3	3.4	0.17	12	5.2	<0.08	<0.38
CON 23	GFDUH00JM	saprolite, Cw horizon	5.7	4.7	0.04	5.7	3.7	4.7	4.1	0.13	9.5	3.5	<0.08	<0.38
CON 24	GFDUH00JN	saprolite, Cw horizon	6.5	5.3	0.05	6.1	4.0	6.4	4.5	0.16	11	4.2	<0.08	<0.38
MIT depth profile of water-soluble fractions														
MIT 14	GFDUH002Z	soil, Bw horizon	0.2	43	0.19	8.3	47	29	14	0.49	7.2	45	<0.08	<0.38
MIT 13	GFDUH0030	soil, Bw horizon	0.4	15	0.29	2.3	4.4	4.1	5.9	0.93	4.7	10	<0.08	<0.38
MIT 12	GFDUH000K	soil, Bw horizon	0.6	6.0	0.50	1.7	<0.78	1.9	4.2	0.91	4.2	7.1	<0.08	<0.38
MIT 11	GFDUH0000	soil, Bw horizon	0.8	3.0	1.7	1.8	<0.78	1.3	3.0	0.91	3.8	8.3	<0.08	<0.38
MIT 10	GFDUH002L	soil, Bw horizon	1.0	2.6	1.3	1.8	<0.78	1.5	2.3	1.0	3.7	8.4	<0.08	<0.38
MIT 9	GFDUH0002	soil, Bw horizon	1.2	1.6	1.8	2.7	<0.78	2.8	3.3	2.0	5.3	12	<0.08	<0.38
MIT 8	GFDUH002N	saprolite, Cw horizon	1.4	0.94	6.2	2.0	<0.78	4.1	3.0	2.3	3.8	13	0.11	<0.38
MIT 7	GFDUH0004	saprolite, Cw horizon	1.6	1.5	5.6	2.4	<0.78	4.0	3.4	2.6	3.8	13	0.12	<0.38
MIT 6	GFDUH0005	saprolite, Cw horizon	1.8	0.55	13	1.8	<0.78	4.1	1.5	2.1	3.7	12	0.12	<0.38
MIT 5	GFDUH003K	saprolite, Cw horizon	2.0	0.53	17	2.4	<0.78	3.7	0.46	1.2	3.6	12	0.09	<0.38
MIT 4	GFDUH003L	saprolite, Cw horizon	2.2	<0.37	16	1.0	<0.78	3.6	0.39	1.8	3.4	11	<0.08	<0.38
MIT 3	GFDUH003M	saprolite, Cw horizon	2.4	<0.37	9.2	0.63	<0.78	7.8	0.62	0.73	3.7	9.3	<0.08	<0.38
MIT 2	GFDUH0031	saprolite, Cw horizon	2.6	<0.37	9.9	0.93	<0.78	8.8	1.2	0.83	3.7	11	<0.08	<0.38
MIT 1	GFDUH0032	saprolite, Cw horizon	2.8	<0.37	3.7	1.1	<0.78	9.4	1.8	1.1	3.4	9.7	<0.08	<0.38
MIT 19	GFDUH008R	saprolite, Cw horizon	3.2	<0.37	18	4.0	<0.78	3.9	2.4	0.87	4.1	15	0.25	<0.38
MIT 20	GFDUH008S	saprolite, Cw horizon	3.6	<0.37	2.5	4.1	<0.78	7.2	2.0	0.63	6.2	12	0.13	<0.38
MIT 21	GFDUH008T	saprolite, Cw horizon	4.0	<0.37	3.6	2.8	<0.78	4.9	1.6	0.58	6.0	10	0.12	<0.38
MIT 22	GFDUH008U	saprolite, Cw horizon	4.7	<0.37	0.76	3.6	<0.78	3.3	1.6	0.21	8.9	10	0.12	<0.38
MIT 23	GFDUH008V	saprolite, Cw horizon	5.3	<0.37	0.43	0.92	<0.78	2.8	0.38	0.03	7.1	5.2	<0.08	<0.38
MIT 24	GFDUH008W	saprolite, Cw horizon	6.7	<0.37	0.08	0.83	<0.78	2.8	0.40	0.06	5.8	3.8	<0.08	<0.38
MIT 25	GFDUH008X	saprolite, Cw horizon	8.4	2.3	0.01	1.2	<0.78	1.8	0.26	0.02	5.5	2.2	<0.08	<0.38
MIT 26	GFDUH008K	saprolite, Cw horizon	9.5	6.4	0.03	2.1	2.7	3.6	0.51	0.11	8.8	3.5	<0.08	<0.38
MIT 27	GFDUH008L	saprolite, Cw horizon	12.5	6.2	0.04	3.1	2.7	3.0	0.92	0.21	7.7	3.8	<0.08	<0.38
MIT 28	GFDUH008Y	saprolite, Cw horizon	13.4	7.6	0.07	3.5	2.5	3.7	0.84	0.17	8.3	5.0	<0.08	<0.38
MIT 29	GFDUH008Z	saprolite, Cw horizon	16.3	4.8	0.06	1.9	4.9	3.0	0.98	0.15	5.6	2.1	<0.08	<0.38
water soluble fraction of international reference materials														
SRM 2709a San Joaquin Soil				0.93	0.36	69	0.72	68	40	0.05	121	59	0.95	<0.38
TILL-1 (CCRMP)				7.0	0.19	58	9.0	12	26	5.6	37	20	0.16	<0.38

n.d = not determined,
For uncertainties on water-soluble and exchangeable concentration data see Supplementary Table 2-2b caption.
† IGSN (International Geo Sample Number). Metadata of samples are available under: www.igsn.org by adding the IGSN after igsn.org, e.g.igsn.org/GFDUH00LT

Supplementary Table 2-2b Chemical composition of the exchangeable fraction from sequential extractions of soil and saprolite at CON and MIT.

				ICP-OES analyses										
sample ID	**IGSN**[†]	**sample type**	**mean depth**	**Al**	**Ba**	**Ca**	**Fe**	**K**	**Mg**	**Mn**	**Na**	**S**	**Sr**	**Zn**
			(m)	(µg/g)	(µg/g)	(µg/g)	(µg/g)	(µg/g)	(µg/g)	(µg/g)	(µg/g)	(µg/g)	(µg/g)	(µg/g)
CON depth profile of exchangeable fractions														
CON 14	GFDUH00J0	soil, Ah horizon	0.2	16	13	77	4.0	53	35	73	3.9	24	0.58	0.50
CON 13	GFDUH00J1	soil, Ah + Bw horizon	0.4	17	19	51	2.2	42	21	57	3.4	34	0.50	<0.38
CON 12	GFDUH00J2	soil, Bw I horizon	0.6	38	15	35	1.0	29	12	15.1	3.8	88	0.30	<0.38
CON 11	GFDUH00J3	soil, Bw I horizon	0.8	41	12	21	<0.78	22	4.7	8.9	3.5	185	0.20	<0.38
CON 10	GFDUH00J4	soil, Bw I horizon	1.0	30	13	12	<0.78	19	2.4	5.4	5.1	187	0.15	<0.38
CON 9	GFDUH00J5	soil, Bw I horizon	1.2	19	11	11	<0.78	22	3.1	3.0	3.0	169	0.12	<0.38
CON 8	GFDUH00J6	soil, Bw I horizon	1.4	28	17	16	<0.78	29	8.7	3.4	2.9	96	0.24	<0.38
CON 7	GFDUH00J7	soil, Bw I horizon	1.6	24	16	17	<0.78	34	13	4.8	3.1	54	0.30	<0.38
CON 6	GFDUH00J8	soil, Bw II horizon	1.8	19	17	43	<0.78	32	22	5.0	3.6	14	0.88	<0.38
CON 5	GFDUH00J9	soil, Bw II horizon	2.0	17	23	56	<0.78	31	30	3.9	3.8	9.4	1.03	<0.38
CON 4	GFDUH00JA	soil, Bw II horizon	2.2	11	28	83	<0.78	45	54	8.4	4.6	6.3	1.5	<0.38
CON 3	GFDUH00JB	saprolite, Cw horizon	2.4	3.6	37	217	<0.78	53	78	6.1	5.3	3.5	2.9	<0.38
CON 2	GFDUH00JC	saprolite, Cw horizon	2.6	0.39	45	368	<0.78	52	101	4.5	5.7	2.5	4.2	<0.38
CON 1	GFDUH00JD	saprolite, Cw horizon	2.8	<0.37	46	452	<0.78	51	164	2.2	5.7	2.2	5.2	<0.38
CON 19	GFDUH00JJ	saprolite, Cw horizon	3.4	<0.37	48	719	<0.78	52	222	3.0	6.1	1.1	5.7	<0.38
CON 20	GFDUH00JK	saprolite, Cw horizon	3.9	<0.37	45	1487	<0.78	55	410	2.6	5.2	1.0	6.4	<0.38
CON 21	GFDUH00HZ	saprolite, Cw horizon	4.4	<0.37	43	1257	<0.78	61	244	3.9	5.6	1.4	6.0	<0.38
CON 22	GFDUH00JL	saprolite, Cw horizon	5.0	<0.37	38	743	<0.78	70	258	5.9	8.6	0.94	6.2	<0.38
CON 23	GFDUH00JM	saprolite, Cw horizon	5.7	<0.37	34	763	<0.78	60	240	4.6	7.2	0.86	5.8	<0.38
CON 24	GFDUH00JN	saprolite, Cw horizon	6.5	<0.37	34	804	<0.78	68	316	6.0	7.3	0.93	6.1	<0.38
MIT depth profile of exchangeable fractions														
MIT 14	GFDUH002Z	soil, Bw horizon	0.2	24	1.3	26	36	45	28	0.92	3.6	41	0.214	<0.38
MIT 13	GFDUH0030	soil, Bw horizon	0.4	35	3.5	6.4	5.3	19	7.1	1.3	2.5	46	<0.08	<0.38
MIT 12	GFDUH000K	soil, Bw horizon	0.6	55	4.5	4.7	1.4	15	3.8	0.98	2.5	57	<0.08	<0.38
MIT 11	GFDUH0000	soil, Bw horizon	0.8	33	14	4.2	<0.78	14	2.2	0.48	2.3	96	<0.08	<0.38
MIT 10	GFDUH002L	soil, Bw horizon	1.0	24	4.7	3.6	<0.78	14	1.5	0.50	2.3	88	<0.08	<0.38
MIT 9	GFDUH0002	soil, Bw horizon	1.2	15	6.1	3.8	<0.78	20	1.9	1.1	2.4	91	<0.08	<0.38
MIT 8	GFDUH002N	saprolite, Cw horizon	1.4	4.1	21	2.8	<0.78	18	2.0	1.5	2.1	62	<0.08	<0.38
MIT 7	GFDUH0004	saprolite, Cw horizon	1.6	9.0	9.2	3.7	<0.78	19	2.5	2.1	2.2	62	<0.08	<0.38
MIT 6	GFDUH0005	saprolite, Cw horizon	1.8	3.1	28	3.8	<0.78	16	2.0	2.5	2.2	54	0.12	<0.38
MIT 5	GFDUH003K	saprolite, Cw horizon	2.0	1.4	43	3.3	<0.78	14	0.91	1.4	2.7	92	0.15	<0.38
MIT 4	GFDUH003L	saprolite, Cw horizon	2.2	0.50	38	2.7	<0.78	11	0.85	2.8	1.8	64	0.11	<0.38
MIT 3	GFDUH003M	saprolite, Cw horizon	2.4	0.64	86	5.3	<0.78	33	4.9	4.3	2.1	34	0.16	<0.38
MIT 2	GFDUH0031	saprolite, Cw horizon	2.6	0.62	80	7.4	<0.78	37	8.5	5.3	2.3	30	0.17	<0.38
MIT 1	GFDUH0032	saprolite, Cw horizon	2.8	0.38	58	8.0	<0.78	37	10	5.6	2.1	29	0.17	<0.38
MIT 19	GFDUH008R	saprolite, Cw horizon	3.2	1.1	66	11.3	<0.78	18	4.6	1.8	2.5	26	0.64	<0.38
MIT 20	GFDUH008S	saprolite, Cw horizon	3.6	0.41	54	53	<0.78	24	17	7.5	3.0	26	1.9	<0.38
MIT 21	GFDUH008T	saprolite, Cw horizon	4.0	2.6	99	34	<0.78	37	14	4.5	3.6	21	1.5	<0.38
MIT 22	GFDUH008U	saprolite, Cw horizon	4.7	<0.37	80	72	<0.78	41	23	3.3	5.7	11	2.7	<0.38
MIT 23	GFDUH008V	saprolite, Cw horizon	5.3	1.1	159	95	<0.78	57	30	2.2	6.6	8.3	3.6	<0.38
MIT 24	GFDUH008W	saprolite, Cw horizon	6.7	<0.37	40	91	<0.78	41	30	5.0	4.3	3.2	2.5	<0.38
MIT 25	GFDUH008X	saprolite, Cw horizon	8.4	<0.37	29	1199	<0.78	58	71	2.3	7.7	2.8	9.9	<0.38
MIT 26	GFDUH008K	saprolite, Cw horizon	9.5	<0.37	46	4809	<0.78	82	86	0.6	16	6.8	19	<0.38
MIT 27	GFDUH008L	saprolite, Cw horizon	12.5	<0.37	49	1065	<0.78	55	75	23	9.4	5.1	13	<0.38
MIT 28	GFDUH008Y	saprolite, Cw horizon	13.4	<0.37	85	1368	<0.78	79	91	12	12	7.3	23	<0.38
MIT 29	GFDUH008Z	saprolite, Cw horizon	16.3	<0.37	49	943	<0.78	64	59	4.1	7.2	1.7	5.4	<0.38
exchangeable fraction of international reference materials														
SRM 2709a San Joaquin Soil				0.12	46	3269	<0.01	451	563	5.4	91	12	22	<0.38
TILL-1 (CCRMP)				0.7	18	876	0.19	57	108	86	11	7	2.2	<0.38

continued next page …

Supplementary Table 2-2b continued - Chemical composition of the exchangeable fraction from sequential extractions of soil and saprolite at CON and MIT.

	ICP-OES analyses										
sample ID	**Al**	**Ba**	**Ca**	**Fe**	**K**	**Mg**	**Mn**	**Na**	**S**	**Sr**	**Zn**
	(µg/g)	(µg/g)	(µg/g)	(µg/g)	(µg/g)	(µg/g)	(µg/g)	(µg/g)	(µg/g)	(µg/g)	(µg/g)
international reference material for concentration data quality control											
SLRS-5 (NRC CNRS) (a)	<lod	<lod	9.9	0.10	0.85	2.9	<lod	5.2	2.4	<lod	<lod
SLRS-5 (NRC CNRS) (b)	<lod	<lod	11	0.09	0.78	2.8	<lod	5.2	2.4	<lod	<lod
SLRS-5 (NRC CNRS) (c)	<lod	<lod	11	0.09	0.79	2.6	<lod	6.5	2.5	<lod	<lod
SLRS-5 (NRC CNRS) (d)	<lod	<lod	12	0.09	0.84	2.6	<lod	5.5	2.2	<lod	<lod
SLRS-5 (NRC CNRS) (e)	<lod	<lod	9.9	0.09	0.77	2.7	<lod	5.6	2.2	<lod	<lod
SLRS-5 (NRC CNRS) (f)	<lod	<lod	12	0.10	0.82	2.7	<lod	5.2	2.2	<lod	<lod
SLRS-5 (NRC CNRS) (g)	<lod	<lod	10	0.09	0.77	2.5	<lod	4.9	2.1	<lod	<lod
SLRS-5 (NRC CNRS) mean	**n.d.**	**n.d.**	**11**	**0.09**	**0.80**	**2.7**	**n.d.**	**5.4**	**2.3**	**n.d.**	**n.d.**
SLRS-5 (NRC CNRS) SD	*n.d.*	*n.d.*	*0.88*	*0.00*	*0.03*	*0.12*	*n.d.*	*0.51*	*0.14*	*n.d.*	*n.d.*
SLRS-5 (NRC CNRS) RSD (%)	*n.d.*	*n.d.*	*0.08*	*0.05*	*0.04*	*0.04*	*n.d.*	*0.09*	*0.06*	*n.d.*	*n.d.*
SLRS-5 (NRC CNRC) certified value*	0.05	0.01	11	0.09	0.84	2.5	0.00	5.4	2.4	0.05	0.85
SLRS-5 (NRC CNRC) certified absolute uncertainty*	0.01	0.00	0.40	0.01	0.04	0.16	0.00	0.10	0.24	0.00	0.10
relative uncertainty on the water soluble and exchangeable fraction (%)	n.d.	n.d.	3%	2%	-4%	6%	n.d.	1%	-3%	n.d.	n.d.
SRM 1640a (a)	<lod	0.15	5.7	<lod	0.58	1.2	<lod	3.1	1.6	0.13	<lod
SRM 1640a (b)	<lod	0.14	5.6	<lod	0.49	1.2	<lod	3.1	1.5	0.11	<lod
SRM 1640a mean	**n.d.**	**0.14**	**5.6**	**n.d.**	**0.54**	**1.2**	**n.d.**	**3.1**	**1.5**	**0.12**	**n.d.**
SRM 1640a SD	*n.d.*	*0.00*	*0.11*	*n.d.*	*0.06*	*0.01*	*n.d.*	*0.03*	*0.02*	*0.01*	*n.d.*
SRM 1640a RSD (%)	*n.d.*	*2%*	*2%*	*n.d.*	*12%*	*0%*	*n.d.*	*1%*	*1%*	*7%*	*n.d.*
SRM 1640a certified value	0.05	0.15	5.57	0.04	0.58	1.05	0.04	3.11	n.r.	0.13	0.06
SRM 1640a certified absolute uncertainty	0.00	0.00	0.02	0.00	0.00	0.00	0.00	0.03	n.r.	0.00	0.00
relative uncertainty on the water soluble and exchangeable fraction (%)	n.d.	-4%	1%	n.d.	-7%	12%	n.d.	0%	n.d.	-3%	-3%
M212 (USGS) (a)	<lod	<lod	5.7	<lod	0.51	2.3	<lod	8.4	2.0	<lod	<lod
M212 (USGS) (b)	<lod	<lod	6.1	<lod	0.53	2.1	<lod	10	2.1	<lod	<lod
M212 (USGS) (c)	<lod	<lod	5.7	<lod	0.53	2.2	<lod	9.3	1.8	<lod	<lod
M212 (USGS) (d)	<lod	<lod	6.6	<lod	0.55	2.2	<lod	9.0	1.8	<lod	<lod
M212 (USGS) (e)	<lod	<lod	5.6	<lod	0.52	2.1	<lod	8.3	1.7	<lod	<lod
M212 (USGS) mean	**n.d.**	**n.d.**	**5.9**	**n.d.**	**0.53**	**2.2**	**n.d.**	**9.0**	**1.9**	**n.d.**	**n.d.**
M212 (USGS) SD	*n.d.*	*n.d.*	*0.42*	*n.d.*	*0.01*	*0.08*	*n.d.*	*0.70*	*0.13*	*n.d.*	*n.d.*
M212 (USGS) RSD (%)	*n.d.*	*n.d.*	*7%*	*n.d.*	*3%*	*4%*	*n.d.*	*8%*	*7%*	*n.d.*	*n.d.*
M212 (USGS) certified value	n.r.	n.r.	5.6	n.r.	0.59	2.0	n.r.	8.7	1.9	0.02	n.r.
M212 (USGS) certified absolute uncertainty	n.r.	n.r.	0.29	n.r.	0.03	0.10	n.r.	0.46	0.10	0.00	n.r.
relative uncertainty on the water soluble and exchangeable fraction (%)	n.d.	n.d.	7%	n.d.	-10%	8%	n.d.	3%	-2%	n.d.	n.d.

n.d = not determined, n.r. = not reported, <lod = below limit of detection, * S concentration and uncertainty from Jochum et al. (2005)
Uncertainties on the water-soluble and exchangeable concentration data are estimated to be ±5% relative for Ba, Ca, Fe, Na, S, Sr based on accuracy of repeat analyses of reference materials, ±10% relative for K, Mg based on accuracy of repeat analyses of reference materials, ±5% relative for Al, Mn based on accuracy of repeat analyses of synthetic in-house standards.

Supplementary Table 2-2c Chemical composition of the carbonate fraction from sequential extractions of soil and saprolite at CON and MIT.

				ICP-OES analyses										
sample ID	**IGSN**[†]	**sample type**	**mean depth**	**Al**	**Ba**	**Ca**	**Fe**	**K**	**Mg**	**Mn**	**Na**	**S**	**Sr**	**Zn**
			(m)	(µg/g)	(µg/g)	(µg/g)	(µg/g)	(µg/g)	(µg/g)	(µg/g)	(µg/g)	(µg/g)	(µg/g)	(µg/g)
CON depth profile of carbonate fractions														
CON 14	GFDUH00J0	soil, Ah horizon	0.2	99	6.3	31	9.4	2.7	6.3	35	2.8	3.2	0.20	1.5
CON 13	GFDUH00J1	soil, Ah + Bw horizon	0.4	171	8.8	33	17	1.7	4.8	40	2.8	2.9	0.22	1.5
CON 12	GFDUH00J2	soil, Bw I horizon	0.6	274	9.7	33	4.3	1.2	3.4	16	3.0	2.8	0.22	0.59
CON 11	GFDUH00J3	soil, Bw I horizon	0.8	365	8.7	31	4.1	1.1	2.2	14	2.9	2.9	0.20	0.57
CON 10	GFDUH00J4	soil, Bw I horizon	1.0	435	7.9	26	3.5	0.9	1.4	8.6	3.1	2.6	0.17	0.43
CON 9	GFDUH00J5	soil, Bw I horizon	1.2	434	6.5	18	3.3	1.1	1.1	6.0	2.7	2.1	0.12	<0.38
CON 8	GFDUH00J6	soil, Bw I horizon	1.4	314	4.7	12	3.6	1.0	0.8	2.4	2.9	2.4	<0.08	<0.38
CON 7	GFDUH00J7	soil, Bw I horizon	1.6	312	3.9	10	3.6	1.3	1.0	2.4	3.0	2.4	<0.08	<0.38
CON 6	GFDUH00J8	soil, Bw II horizon	1.8	262	4.6	13	2.9	1.7	1.9	2.6	3.0	2.1	0.10	<0.38
CON 5	GFDUH00J9	soil, Bw II horizon	2.0	223	4.9	14	2.5	1.6	2.2	1.9	2.8	2.1	0.09	<0.38
CON 4	GFDUH00JA	soil, Bw II horizon	2.2	141	4.6	15	2.6	2.0	3.1	2.8	3.8	2.8	0.12	<0.38
CON 3	GFDUH00JB	saprolite, Cw horizon	2.4	62	3.4	22	<0.78	1.8	2.8	1.7	2.7	1.9	0.12	<0.38
CON 2	GFDUH00JC	saprolite, Cw horizon	2.6	21	2.4	65	<0.78	1.7	3.5	2.2	3.1	2.3	0.21	<0.38
CON 1	GFDUH00JD	saprolite, Cw horizon	2.8	12	1.5	76	<0.78	1.9	3.8	1.9	3.6	2.5	0.23	<0.38
CON 19	GFDUH00JJ	saprolite, Cw horizon	3.4	14	1.2	98	<0.78	3.2	13	9.0	4.2	2.3	0.33	0.96
CON 20	GFDUH00JK	saprolite, Cw horizon	3.9	13	1.1	100	0.96	3.5	24	12	3.8	2.4	0.37	0.83
CON 21	GFDUH00HZ	saprolite, Cw horizon	4.4	27	2.3	147	4.9	5.9	47	25	4.8	2.7	0.46	1.50
CON 22	GFDUH00JL	saprolite, Cw horizon	5.0	18	1.1	86	2.2	4.4	15	16	4.6	2.6	0.35	0.89
CON 23	GFDUH00JM	saprolite, Cw horizon	5.7	14	0.9	76	1.3	3.6	13	13	4.4	2.5	0.29	0.89
CON 24	GFDUH00JN	saprolite, Cw horizon	6.5	18	1.3	91	1.9	4.2	16	15	4.1	2.1	0.36	0.77
MIT depth profile of carbonate fractions														
MIT 14	GFDUH002Z	soil, Bw horizon	0.2	49	0.33	11	62	3.9	5.5	0.49	3.2	10	<0.08	0.40
MIT 13	GFDUH0030	soil, Bw horizon	0.4	260	2.4	13	29	0.93	7.1	2.6	3.2	3.7	<0.08	0.52
MIT 12	GFDUH000K	soil, Bw horizon	0.6	565	4.6	14	11	0.85	5.3	2.6	3.1	3.5	<0.08	0.50
MIT 11	GFDUH0000	soil, Bw horizon	0.8	578	6.3	17	6.5	0.75	2.8	1.2	3.1	3.1	<0.08	0.66
MIT 10	GFDUH002L	soil, Bw horizon	1.0	463	5.1	13	3.8	<0.51	1.5	1.1	3.1	2.7	<0.08	0.55
MIT 9	GFDUH0002	soil, Bw horizon	1.2	422	5.2	15	3.2	<0.51	1.2	1.9	3.0	2.5	<0.08	0.56
MIT 8	GFDUH002N	saprolite, Cw horizon	1.4	304	6.4	11	3.7	1.2	1.7	2.6	2.5	1.9	<0.08	<0.38
MIT 7	GFDUH0004	saprolite, Cw horizon	1.6	391	7.5	11	4.3	1.4	2.3	3.8	3.3	2.7	<0.08	<0.38
MIT 6	GFDUH0005	saprolite, Cw horizon	1.8	205	17	8.1	2.0	1.0	1.1	4.2	2.8	2.1	<0.08	<0.38
MIT 5	GFDUH003K	saprolite, Cw horizon	2.0	128	17	5.6	1.7	<0.51	0.39	3.1	2.7	2.2	<0.08	<0.38
MIT 4	GFDUH003L	saprolite, Cw horizon	2.2	107	22	42	1.6	0.8	1.3	5.5	3.1	2.1	<0.08	<0.38
MIT 3	GFDUH003M	saprolite, Cw horizon	2.4	100	31	5.2	3.6	1.8	1.1	4.7	2.9	2.3	<0.08	<0.38
MIT 2	GFDUH0031	saprolite, Cw horizon	2.6	104	11	6.8	8.2	2.1	2.0	4.2	3.2	2.4	<0.08	<0.38
MIT 1	GFDUH0032	saprolite, Cw horizon	2.8	112	5.6	6.1	9.3	2.1	2.1	5.5	2.9	2.3	<0.08	<0.38
MIT 19	GFDUH008R	saprolite, Cw horizon	3.2	225	23	36	1.1	1.3	1.0	3.4	3.0	2.5	0.08	<0.38
MIT 20	GFDUH008S	saprolite, Cw horizon	3.6	237	11	92	1.1	1.2	1.2	31	3.1	2.4	0.35	0.48
MIT 21	GFDUH008T	saprolite, Cw horizon	4.0	181	18	32	1.6	2.3	1.8	3.6	3.3	2.4	0.11	0.59
MIT 22	GFDUH008U	saprolite, Cw horizon	4.7	230	7.1	51	12	3.3	5.4	6.3	4.0	2.2	0.25	0.81
MIT 23	GFDUH008V	saprolite, Cw horizon	5.3	172	8.4	28	1.7	3.3	2.4	2.7	3.5	2.3	0.15	0.33
MIT 24	GFDUH008W	saprolite, Cw horizon	6.7	78	2.4	82	3.0	2.1	2.8	3.0	3.5	2.5	0.20	0.66
MIT 25	GFDUH008X	saprolite, Cw horizon	8.4	14	1.9	86	0.79	4.0	4.4	6.8	4.7	2.9	0.47	<0.38
MIT 26	GFDUH008K	saprolite, Cw horizon	9.5	6.2	2.4	61	<0.78	3.5	4.9	2.9	3.7	2.5	0.75	0.40
MIT 27	GFDUH008L	saprolite, Cw horizon	12.5	16	3.0	91	<0.78	1.8	3.4	12	2.5	1.7	0.62	0.55
MIT 28	GFDUH008Y	saprolite, Cw horizon	13.4	18	6.3	92	<0.78	3.0	4.5	14	3.6	2.2	1.23	1.1
MIT 29	GFDUH008Z	saprolite, Cw horizon	16.3	9.6	3.1	62	1.7	3.9	4.4	14	4.3	2.3	0.24	<0.38
carbonate fraction of international reference materials														
SRM 2709a San Joaquin Soil				2.6	0.60	4.7	<0.78	2.0	6.7	1.5	0.63	0.56	0.46	<0.38
TILL-1 (CCRMP)				94	7.8	141	91	4.3	27	176	6.2	2.9	0.84	0.93

Supplementary Table 2-2d Chemical composition of the organic-bound fraction from sequential extractions of soil and saprolite at CON and MIT.

				ICP-OES analyses										
sample ID	**IGSN**[†]	**sample type**	**mean depth**	**Al**	**Ba**	**Ca**	**Fe**	**K**	**Mg**	**Mn**	**Na**	**S**	**Sr**	**Zn**
			(m)	(µg/g)	(µg/g)	(µg/g)	(µg/g)	(µg/g)	(µg/g)	(µg/g)	(µg/g)	(µg/g)	(µg/g)	(µg/g)
CON depth profile of organic fractions														
CON 14	GFDUH00J0	soil, Ah horizon	0.2	2292	9.1	37	1149	5.3	26	159	6.7	176	0.30	4.9
CON 13	GFDUH00J1	soil, Ah + Bw horizon	0.4	2149	7.1	31	504	3.6	17	114	7.5	89	0.24	2.9
CON 12	GFDUH00J2	soil, Bw I horizon	0.6	1333	5.0	22	65	3.3	9.3	106	6.1	18	0.19	1.4
CON 11	GFDUH00J3	soil, Bw I horizon	0.8	1163	3.2	20	22	2.8	8.6	141	5.7	11	0.15	0.68
CON 10	GFDUH00J4	soil, Bw I horizon	1.0	823	3.0	23	10	5.6	13	125	6.3	10	0.19	<0.38
CON 9	GFDUH00J5	soil, Bw I horizon	1.2	454	3.0	28	3.6	11	18	63	5.8	6.4	0.21	<0.38
CON 8	GFDUH00J6	soil, Bw I horizon	1.4	350	3.9	30	2.0	15	24	27	6.8	3.6	0.20	0.46
CON 7	GFDUH00J7	soil, Bw I horizon	1.6	239	4.6	26	1.0	18	21	33	6.4	3.2	0.19	0.76
CON 6	GFDUH00J8	soil, Bw II horizon	1.8	276	4.8	25	1.5	16	20	40	6.7	3.5	0.19	0.78
CON 5	GFDUH00J9	soil, Bw II horizon	2.0	275	5.5	26	1.7	15	21	42	7.0	3.3	0.21	0.91
CON 4	GFDUH00JA	soil, Bw II horizon	2.2	246	5.5	25	3.4	17	24	47	7.7	3.7	0.23	1.1
CON 3	GFDUH00JB	saprolite, Cw horizon	2.4	138	6.4	43	1.2	18	29	80	7.9	2.7	0.29	1.5
CON 2	GFDUH00JC	saprolite, Cw horizon	2.6	93	7.7	89	1.7	19	40	106	8.9	3.3	0.46	1.7
CON 1	GFDUH00JD	saprolite, Cw horizon	2.8	46	7.3	122	1.0	19	41	108	8.9	3.3	0.55	1.6
CON 19	GFDUH00JJ	saprolite, Cw horizon	3.4	36	8.9	92	1.8	25	55	76	11	2.5	0.51	3.3
CON 20	GFDUH00JK	saprolite, Cw horizon	3.9	27	7.6	115	1.4	25	59	94	10	3.2	0.56	2.1
CON 21	GFDUH00HZ	saprolite, Cw horizon	4.4	31	7.8	115	1.7	25	65	66	10	2.6	0.47	2.6
CON 22	GFDUH00JL	saprolite, Cw horizon	5.0	42	7.7	90	1.7	30	70	69	12	2.4	0.59	2.4
CON 23	GFDUH00JM	saprolite, Cw horizon	5.7	19	5.3	78	<0.78	25	56	67	10	2.2	0.48	2.2
CON 24	GFDUH00JN	saprolite, Cw horizon	6.5	45	7.4	102	1.6	25	69	77	12	2.8	0.55	2.6
MIT depth profile of organic fractions														
MIT 14	GFDUH002Z	soil, Bw horizon	0.2	2178	3.9	32	6331	10	205	15	5.4	424	0.24	5.2
MIT 13	GFDUH0030	soil, Bw horizon	0.4	3207	3.3	15	606	7.1	25	4.6	5.0	58	0.12	1.5
MIT 12	GFDUH000K	soil, Bw horizon	0.6	3020	2.5	29	61	10	37	6.7	7.1	23	0.10	1.2
MIT 11	GFDUH0000	soil, Bw horizon	0.8	723	1.8	22	5.0	17	26	5.6	4.8	8.2	0.11	0.38
MIT 10	GFDUH002L	soil, Bw horizon	1.0	540	2.0	24	3.2	23	26	7.5	4.6	6.8	0.13	0.44
MIT 9	GFDUH0002	soil, Bw horizon	1.2	299	3.8	34	0.88	46	33	14	5.2	4.7	0.17	0.63
MIT 8	GFDUH002N	saprolite, Cw horizon	1.4	195	6.3	39	<0.78	79	37	21	5.2	3.0	0.18	0.76
MIT 7	GFDUH0004	saprolite, Cw horizon	1.6	442	3.6	31	3.3	59	30	20	5.0	5.9	0.15	0.54
MIT 6	GFDUH0005	saprolite, Cw horizon	1.8	180	10	44	0.80	97	35	66	7.2	3.0	0.24	1.0
MIT 5	GFDUH003K	saprolite, Cw horizon	2.0	127	11	26	<0.78	97	27	109	5.8	2.5	0.17	0.90
MIT 4	GFDUH003L	saprolite, Cw horizon	2.2	117	12	20	<0.78	86	23	185	6.2	2.8	0.13	1.2
MIT 3	GFDUH003M	saprolite, Cw horizon	2.4	104	14	34	<0.78	91	26	79	5.4	2.2	0.21	1.4
MIT 2	GFDUH0031	saprolite, Cw horizon	2.6	118	12	42	0.94	117	35	50	6.6	2.5	0.29	1.4
MIT 1	GFDUH0032	saprolite, Cw horizon	2.8	112	10	37	<0.78	113	33	56	6.5	2.4	0.24	1.3
MIT 19	GFDUH008R	saprolite, Cw horizon	3.2	143	11	82	<0.78	52	22	27	4.5	2.3	0.32	1.1
MIT 20	GFDUH008S	saprolite, Cw horizon	3.6	104	7.7	21	<0.78	2.5	4.2	485	5.9	4.5	0.14	1.2
MIT 21	GFDUH008T	saprolite, Cw horizon	4.0	124	8.8	71	<0.78	52	24	38	5.9	2.5	0.37	1.7
MIT 22	GFDUH008U	saprolite, Cw horizon	4.7	130	7.3	72	<0.78	62	27	16	7.5	2.3	0.43	2.0
MIT 23	GFDUH008V	saprolite, Cw horizon	5.3	128	7.8	75	<0.78	70	27	23	6.8	2.3	0.49	1.4
MIT 24	GFDUH008W	saprolite, Cw horizon	6.7	128	4.5	53	1.0	39	19	13	5.2	2.0	0.38	2.0
MIT 25	GFDUH008X	saprolite, Cw horizon	8.4	28	7.9	142	<0.78	80	42	62	7.8	2.3	1.0	2.1
MIT 26	GFDUH008K	saprolite, Cw horizon	9.5	2.5	4.6	91	<0.78	4.0	8.6	182	4.7	3.0	0.80	0.77
MIT 27	GFDUH008L	saprolite, Cw horizon	12.5	27	8.3	209	<0.78	23	19	152	7.7	2.6	1.2	1.5
MIT 28	GFDUH008Y	saprolite, Cw horizon	13.4	6.6	6.9	112	<0.78	8.4	11	227	6.7	3.1	1.2	0.88
MIT 29	GFDUH008Z	saprolite, Cw horizon	16.3	14	15	157	<0.78	127	55	110	11	2.5	0.88	2.0
organic fraction of international reference materials														
SRM 2709a San Joaquin Soil				5.7	2.0	317	<0.78	22	91	16	20	74	1.6	<0.38
TILL-1 (CCRMP)				1094	4.6	137	48	12	33	103	18	59	0.45	1.2

Supplementary Table 2-2e Phosphorus concentrations of leachates from sequential extractions of soil and saprolite at CON and MIT.

				ICP-OES analyses & UV-spectrometry*											
sample ID	**IGSN†**	**brief sample description**	**mean depth**	**Σ**	**Pi resin**	**Po resin**	**Pi HCO_3**	**Po HCO_3**	**Pi NaOH**	**Po NaOH**	**Pi 1M HCl**	**Po 1M HCl**	**Pi + Po 14M HCl**	**Pi + Po residual**
			(m)	(µg/g)	(µg/g)	(µg/g)	(µg/g)	(µg/g)	(µg/g)	(µg/g)	(µg/g)	(µg/g)	(µg/g)	(µg/g)
CON depth profile of Hedley fractionation														
CON 14	GFDUH00LT	soil, Ah horizon	0.2	789	11	3.3	21	49	72	328	35	46	192	31
CON 13	GFDUH00LU	soil, Ah + Bw horizon	0.4	763	3.1	1.9	15	39	89	318	36	20	205	36
CON 12	GFDUH00LV	soil, Bw I horizon	0.6	762	0.44	1.9	11	33	83	324	42	17	218	31
CON 11	GFDUH00LW	soil, Bw I horizon	0.8	825	0.23	1.3	19	30	193	247	67	14	220	33
CON 10	GFDUH00LX	soil, Bw I horizon	1.0	800	0.68	1.2	23	23	196	222	61	19	227	29
CON 9	GFDUH00LY	soil, Bw I horizon	1.2	590	0.42	1.6	19	10	153	93	73	16	197	26
CON 8	GFDUH00LZ	soil, Bw I horizon	1.4	487	0.72	3.1	23	5.3	143	43	37	15	186	33
CON 7	GFDUH00M0	soil, Bw I horizon	1.6	651	4.8	0.77	8.9	0.46	25	1.1	381	n.d.	196	32
CON 6	GFDUH00M1	soil, Bw II horizon	1.8	534	8.7	1.5	29	5.6	153	24	42	8.9	235	27
CON 5	GFDUH00M2	soil, Bw II horizon	2.0	501	15	n.d.	23	6.2	126	41	37	10	208	36
CON 4	GFDUH00M3	soil, Bw II horizon	2.2	478	16	n.d.	22	8.2	121	22	49	12	201	27
CON 3	GFDUH00M4	saprolite, Cw horizon	2.4	526	18	2.7	24	2.6	88	16	139	n.d.	211	26
CON 2	GFDUH00M5	saprolite, Cw horizon	2.6	581	19	n.d.	21	1.4	85	17	196	5.7	214	22
CON 1	GFDUH00M6	saprolite, Cw horizon	2.8	639	14	n.d.	23	0.45	75	13	227	12	248	27
CON 19	GFDUH00MB	saprolite, Cw horizon	3.4	617	4.4	1.9	8.6	n.d.	17	13	321	n.d.	228	23
CON 21	GFDUH00MD	saprolite, Cw horizon	4.4	786	8.2	0.60	8.5	1.4	29	11	376	72	252	26
CON 22	GFDUH00ME	saprolite, Cw horizon	5.0	714	8.2	0.60	10	0.49	37	2.9	385	25	221	23
CON 23	GFDUH00MF	saprolite, Cw horizon	5.7	603	3.4	3.5	7.7	n.d.	16	12	307	n.d.	234	19
CON 24	GFDUH00MG	saprolite, Cw horizon	6.5	661	6.6	3.4	11	0.28	25	7.1	323	34	219	31

continued next page …

Supplementary Table 2-2e continued - Phosphorus concentrations of leachates from sequential extractions of soil and saprolite at CON and MIT.

				ICP-OES analyses & UV-spectrometry*										
sample ID	**IGSN†**	**brief sample description**	**mean depth**	**Σ**	**Pi resin**	**Po resin**	**Pi HCO_3**	**Po HCO_3**	**Pi NaOH**	**Po NaOH**	**Pi 1M HCl**	**Po 1M HCl**	**Pi + Po 14M HCl**	**Pi + Po residual**
			(m)	(µg/g)	(µg/g)	(µg/g)	(µg/g)	(µg/g)	(µg/g)	(µg/g)	(µg/g)	(µg/g)	(µg/g)	(µg/g)
MIT depth profile of Hedley fractionation														
MIT 14	GFDUH004A	soil, Bw horizon	0.2	733	22	5.1	28	178	65	230	26	16	130	34
MIT 13	GFDUH004B	soil, Bw horizon	0.4	667	2.2	2.8	14	93	56	253	40	23	151	33
MIT 12	GFDUH004C	soil, Bw horizon	0.6	718	0.40	2.0	12	67	102	202	76	19	149	89
MIT 11	GFDUH0045	soil, Bw horizon	0.8	694	0.34	0.84	16	27	202	107	54	23	173	92
MIT 10	GFDUH0046	soil, Bw horizon	1.0	653	1.1	1.1	22	28	219	85	58	26	182	30
MIT 9	GFDUH0047	soil, Bw horizon	1.2	706	3.0	0.93	38	15	246	79	87	15	186	38
MIT 8	GFDUH0048	saprolite, Cw horizon	1.4	1311	8.9	1.6	66	18	767	n.d.	117	37	265	30
MIT 7	GFDUH0049	saprolite, Cw horizon	1.6	1165	4.5	0.56	44	26	626	n.d.	131	15	296	22
MIT 6	GFDUH004D	saprolite, Cw horizon	1.8	746	2.9	0.56	26	6.9	214	n.d.	77	28	362	29
MIT 5	GFDUH004E	saprolite, Cw horizon	2.0	946	7.1	n.d.	22	2.1	198	1.7	61	20	606	29
MIT 4	GFDUH004F	saprolite, Cw horizon	2.2	820	5.3	n.d.	19	6.1	148	n.d.	61	11	543	28
MIT 3	GFDUH004G	saprolite, Cw horizon	2.4	619	4.1	0.28	12	3.3	94	1.8	36	13	414	40
MIT 2	GFDUH004H	saprolite, Cw horizon	2.6	587	4.1	0.60	12	4.7	106	1.5	38	8.0	372	40
MIT 1	GFDUH004J	saprolite, Cw horizon	2.8	911	6.3	0.56	30	9.9	329	65	110	22	311	27
MIT 19	GFDUH00AT	saprolite, Cw horizon	3.2	2563	18	n.d.	84	n.d.	513	5.8	802	639	467	33
MIT 20	GFDUH00AU	saprolite, Cw horizon	3.6	16131	40	n.d.	124	n.d.	376	492	1500	11268	2309	21
MIT 21	GFDUH00AV	saprolite, Cw horizon	4.0	1217	14	n.d.	44	n.d.	230	16	539	7.1	341	27
MIT 22	GFDUH00AW	saprolite, Cw horizon	4.7	2870	28	0.9	73	n.d.	433	n.d.	1162	428	724	21
MIT 23	GFDUH00AX	saprolite, Cw horizon	5.3	882	20	2.3	51	n.d.	222	0.21	298	13	245	30
MIT 24	GFDUH00AY	saprolite, Cw horizon	6.7	443	8.8	0.04	19	n.d.	67	0.33	180	13	133	21
MIT 25	GFDUH00AZ	saprolite, Cw horizon	8.4	487	11	n.d.	24	n.d.	59	2.6	41	13	296	39
MIT 26	GFDUH00B0	saprolite, Cw horizon	9.5	2480	29	n.d.	88	n.d.	265	6.8	201	20	1696	175
MIT 27	GFDUH00B1	saprolite, Cw horizon	12.5	2245	26	n.d.	58	n.d.	196	3.1	750	533	616	62
MIT 28	GFDUH00B2	saprolite, Cw horizon	13.4	2000	22	n.d.	76	n.d.	243	4.8	534	211	847	62
MIT 29	GFDUH00B3	saprolite, Cw horizon	16.3	413	5.5	2.2	13	n.d.	39	4.8	27	36	239	47

n.d. = not detected

* ICP-OES analyses was performed to analyse total P. UV-spectrometry was performed to analyse inorganic carbon.

† IGSN (International Geo Sample Number). Metadata of samples are available under: www.igsn.org by adding the IGSN after igsn.org, e.g. igsn.org/GFDUH00LT

Supplementary Table 2-3 Chemical composition of plant samples at CON and MIT.

sample ID	IGSN†	sampling date (month year)	brief sample description	ICP-OES analyses Al (µg/g)	Ba (µg/g)	Ca (µg/g)	Cu (µg/g)	Fe (µg/g)	K (µg/g)	Mg (µg/g)	Mn (µg/g)	Na (µg/g)	P (µg/g)	S (µg/g)	Sr (µg/g)	Zn (µg/g)
living foliage																
CON-V-3	GFDUH00Q7	Sept. 2014	Fagus sylvatica - leaves	85	164	8552	6.8	86	10743	1338	629	80	1458	1400	47	40
MIT-V-9	GFDUH006W	Sept. 2014	Fagus sylvatica - leaves	80	5.3	2674	11	111	8928	745	130	283	1554	1748	5.2	33
MIT-V-10	GFDUH006R	Sept. 2014	Fagus sylvatica - leaves	76	12	3291	10	97	7880	777	236	124	1488	1884	14	34
CON-V-4	GFDUH00Q8	Sept. 2014	Picea abies - needles	384	54	15734	2.8	36	7275	1118	1073	57	1437	1203	52	76
CON-V-5	GFDUH00Q9	Sept. 2014	Picea abies - needles	407	50	15165	2.9	52	7802	1137	1075	54	1496	1227	50	74
MIT-V 3	GFDUH006Q	July 2014	Picea abies - needles	223	1.8	2699	4.7	36	7315	855	271	10	n.d.	n.d.	1.4	21
MIT-V-11	GFDUH006S	Sept. 2014	Picea abies - needles	375	3.7	3693	3.8	42	5201	1081	213	35	1209	1391	4.1	24
MIT-V-12	GFDUH006T	Sept. 2014	Picea abies - needles	367	3.6	3270	4.1	50	5451	1117	221	21	1221	1374	3.6	24
living wood																
CON-V 1	GFDUH00NE	July 2014	Fagus sylvatica - heartwood	4.4	65	1205	1.1	24	1273	141	40	<4.0	n.d.	n.d.	9.4	3.0
CON-V-10	GFDUH00T9	Sept. 2014	Fagus sylvatica - heartwood	2.3	25	987	0.45	56	1579	183	39	8.5	47	87	7.0	1.4
MIT-V-17	GFDUH00TB	Sept. 2014	Fagus sylvatica - heartwood	4.9	19	1015	1.1	42	721	201	44	11	63	104	6.8	5.0
MIT-V-5,6	GFDUH00TJ	July 2014	Fagus sylvatica - heartwood	9.4	46	2111	2.5	58	661	313	121	<4.0	n.d.	n.d.	17	12
CON-V-10	GFDUH00TA	Sept. 2014	Fagus sylvatica - sapwood	2.5	27	741	0.90	96	1384	159	60	13	82	151	6.3	2.7
MIT-V 5	GFDUH00T3	July 2014	Fagus sylvatica - sapwood	6.4	18	584	2.1	58	560	138	28	14	n.d.	n.d.	5.6	8.0
MIT-V-17	GFDUH00T2	Sept. 2014	Fagus sylvatica - sapwood	8.4	13	582	1.5	57	519	114	24	26	58	100	4.3	4.3
MIT-V 6	GFDUH00T4	July 2014	Fagus sylvatica - sapwood	4.4	12	691	1.6	29	639	116	44	8	n.d.	n.d.	4.3	4.3
CON-V 6,7	GFDUH00TG	Sept. 2014	Fagus sylvatica - bulk wood	n.d.	n.d.	n.d.	n.d.	n.d.	n.d.	n.d.	n.d.	n.d.	n.d.	n.d.	n.d.	n.d.
MIT-V-14,15,16	GFDUH00TL	Sept. 2014	Fagus sylvatica - bulk wood	n.d.	n.d.	n.d.	n.d.	n.d.	n.d.	n.d.	n.d.	n.d.	n.d.	n.d.	n.d.	n.d.
CON-V 2	GFDUH00NF	July 2014	Picea abies - heartwood	6.9	5.3	412	1.1	39	2534	87	12	16	n.d.	n.d.	3.1	3.8
CON-V-18	GFDUH00TD	Sept. 2014	Picea abies - heartwood	7.0	5.4	392	0.58	23	1510	86	12	12	5.9	46	2.8	4.0
MIT-V 7	GFDUH00TF	July 2014	Picea abies - heartwood	4.1	9.7	516	1.3	48	434	101	33	<4.0	n.d.	n.d.	2.7	21
MIT-V-24	GFDUH00T7	Sept. 2014	Picea abies - heartwood	7.1	3.5	217	1.4	38	2546	43	10	13	15	78	2.4	6.1
MIT-V 8	GFDUH00T5	July 2014	Picea abies - heartwood	10	3.5	306	2.2	63	2825	94	20	10	n.d.	n.d.	2.4	7.5
CON-V-18	GFDUH00TE	Sept. 2014	Picea abies - sapwood	5.6	7.0	675	1.3	41	1043	67	20	10	99	78	3.3	4.8
MIT-V 7	GFDUH00TC	July 2014	Picea abies - sapwood	9.9	6.3	311	1.6	69	392	89	20	4.3	n.d.	n.d.	1.4	15
MIT-V-24	GFDUH00T8	Sept. 2014	Picea abies - sapwood	5.1	2.4	486	1.4	37	634	77	17	16	81	108	1.8	6.4
MIT-V 8	GFDUH00T6	July 2014	Picea abies - sapwood	7.2	3.4	536	1.4	21	556	85	23	<4.0	n.d.	n.d.	2.3	7.6
CON-V-14.15	GFDUH00TH	Sept. 2014	Picea abies - bulk wood	n.d.	n.d.	n.d.	n.d.	n.d.	n.d.	n.d.	n.d.	n.d.	n.d.	n.d.	n.d.	n.d.
MIT-V-23.25	GFDUH00TK	Sept. 2014	Picea abies - bulk wood	n.d.	n.d.	n.d.	n.d.	n.d.	n.d.	n.d.	n.d.	n.d.	n.d.	n.d.	n.d.	n.d.

continued next page …

Supplementary Table 2-3 continued - Chemical composition of plant samples at CON and MIT.

sample ID	IGSN†	sampling date (month year)	brief sample description	ICP-OES analyses Al (µg/g)	Ba (µg/g)	Ca (µg/g)	Cu (µg/g)	Fe (µg/g)	K (µg/g)	Mg (µg/g)	Mn (µg/g)	Na (µg/g)	P (µg/g)	S (µg/g)	Sr (µg/g)	Zn (µg/g)
organic layer on forest floor																
CON-QP1-1	GFDUH00TN	May 2014	forest floor - L horizon	454	5.2	4243	6.0	271	2727	852	458	143	515	870	16	35
CON-QP1-2	GFDUH00TS	May 2014	forest floor - Of horizon	2784	50	2001	9.4	1442	1304	618	168	303	762	1833	16	36
CON-QP1-3	GFDUH00TP	May 2014	forest floor - Oh horizon	36894	169	801	17	16209	8454	3481	94	4007	516	1951	32	59
MIT-QP-1	GFDUH00TQ	Febr. 2014	forest floor - L horizon	476	14	4401	8.8	337	2252	725	528	101	1005	1146	13	52
MIT-QP-2	GFDUH00TR	Febr. 2014	forest floor - Of horizon	4539	25	2456	13	2175	1306	741	304	400	1032	2240	16	50
MIT-QP-3	GFDUH00TM	Febr. 2014	forest floor - Oh horizon	30552	148	2324	22	15485	5403	3574	165	4233	1038	2269	42	65
international reference materials for concentration data quality control																
SRM 1515 Apple leaves (a)				n.d.	n.d.	n.d.	n.d.	n.d.	n.d.	n.d.	n.d.	n.d.	n.d.	n.d.	n.d.	n.d.
SRM 1515 Apple leaves (a)*				n.d.	n.d.	n.d.	n.d.	n.d.	n.d.	n.d.	n.d.	n.d.	n.d.	n.d.	n.d.	n.d.
SRM 1515 Apple leaves (b)				219	36	10485	5.0	57	11752	2061	39	29	n.d.	n.d.	19	9.3
SRM 1515 Apple leaves (c)				284	48	12399	6.0	74	14896	2472	53	30	n.d.	n.d.	27	9.3
SRM 1515 Apple leaves (d)				288	48	15455	5.2	78	15485	2684	54	36	1633	1848	26	12
SRM 1515 Apple leaves (e)				327	49	17489	4.4	85	16976	2898	58	47	1788	2032	26	12
SRM 1515 Apple leaves (f)				n.d.	n.d.	n.d.	n.d.	n.d.	n.d.	n.d.	n.d.	n.d.	n.d.	n.d.	n.d.	n.d.
SRM 1515 Apple leaves (g)				n.d.	n.d.	n.d.	n.d.	n.d.	n.d.	n.d.	n.d.	n.d.	n.d.	n.d.	n.d.	n.d.
SRM 1515 Apple leaves (h)				n.d.	n.d.	n.d.	n.d.	n.d.	n.d.	n.d.	n.d.	n.d.	n.d.	n.d.	n.d.	n.d.
SRM 1515 Apple leaves mean				**280**	**45**	**13957**	**5.1**	**73**	**14777**	**2529**	**51**	**35**	**1710**	**1940**	**24**	**10.7**
SRM 1515 Apple leaves SD				*44*	*6.3*	*3120*	*0.6*	*12*	*2199*	*357*	*8.1*	*8.4*	*110*	*130*	*3.6*	*1.6*
SRM 1515 Apple leaves RSD (%)				*16%*	*14%*	*22%*	*13%*	*16%*	*15%*	*14%*	*16%*	*24%*	*6%*	*7%*	*15%*	*15%*
*SRM 1515 Apple leaves certified value***				*286*	*49*	*15260*	*5.64*	*83*	*16100*	*2710*	*54*	*24*	*1590*	*1800*	*25*	*13*
SRM 1515 Apple leaves certified absolute uncertainty				*9.0*	*2.0*	*150*	*0.24*	*5.0*	*200*	*80*	*3.0*	*1.2*	*110*		*2.0*	*0.30*
SRM 1515 Apple leaves certified relative uncertainty (%)				*3%*	*4%*	*1%*	*4%*	*6%*	*1%*	*3%*	*6%*	*5%*	*7%*		*8%*	*2%*
relative difference (%)				**-2%**	**-8%**	**-9%**	**-9%**	**-12%**	**-8%**	**-7%**	**-6%**	**45%**	**8%**	**8%**	**-3%**	**-14%**

Uncertainties on ICP-OES concentration data are estimated to be 5% (Al, Sr), 10% (Ba, Ca, Cu, K, Mg, Mn, P), 15% (Fe, Zn), 45% (Na) relative, based on repeat analyses of reference materials

* replicate analyses, n.d. = not determined

** The concentration of S is not certified in the certificate from NIST, but an indictive number is given in this certificate.

† IGSN (International Geo Sample Number). Metadata of samples are available under: www.igsn.org by adding the IGSN after igsn.org, e.g. igsn.org/GFDUH00LT

3 Phosphorus supply by deep rock weathering sustains temperate forest ecosystem functioning

Abstract

Primary productivity of forest ecosystems depends on the availability of the essential mineral nutrient phosphorus. Because phosphorus demand of trees exceeds phosphorus supply from rock, tree nutrition is sustained by multiple utilisation of organic-bound phosphorus, which is continuously returned from trees to the forest floor. However, where soil phosphorus is permanently lost by drainage and erosion, phosphorus limitation may develop over millennia. It has been suggested that the development of such a deficit is prevented if, in eroding landscapes, advection of unweathered bedrock continuously supplies mineral nutrients. However, observations of the mechanisms and the depth range for this advective model are missing. Here we show that in two montane temperate forest ecosystems phosphorus originates from several meters depth, beneath which minor primary phosphate minerals have not yet been weathered. As evidence we use the depth distribution of calcium-bound phosphorus, and the concordance of the isotope ratios $^{87}Sr/^{86}Sr$ and $^{10}Be(meteoric)/^{9}Be$ between plant tissue and the regolith. We conclude that nutrient supply from deep regolith is critical for forest ecosystem functioning, and should be considered in global carbon models assessing, for instance, the contribution of forest ecosystems as natural sinks for anthropogenic carbon dioxide emissions.

3.1 Introduction

Among the essential mineral nutrient elements, phosphorus (P) frequently limits plant-growth (Vance et al. 2003; Augusto et al. 2017) because P fulfils diverse life-sustaining functions in all living organisms. Yet P is present in only trace amounts in host rock (Taylor and McLennan 1995) and, over millennial timescales, the inventory of mineral P is reduced by dissolved loss into drainage during chemical weathering that converts bedrock into regolith (Graham et al. 2010) (regolith is defined here to comprise soil, saprolite and weathered bedrock). Weathering also reduces the availability of P for trees by the transformation of plant-available P (e.g. dissolved P and P adsorbed onto soil minerals) into P forms that are not readily plant-available (e.g. P occluded within sesquioxides) (Walker and Syers 1976). According to the classical Walker and Syers model (Walker and Syers 1976), the inventory and plant-availability of P depends on soil age. Consequently, on mature soils the P demand of trees (e.g. up to 3000 mg m^{-2} yr^{-1} (Brady and Weil 2002)) exceeds P supply from mineral sources (e.g. 5-100 mg m^{-2} yr^{-1} (Newman 1995)). In this "static" model, primary productivity of forest ecosystems on mature soils is sustained by tight turnover of P contained in plant litter (Vitousek and Farrington 1997; Jobbagy and Jackson 2000; Turner et al. 2013) and soil organic matter, returned from trees to soil in previous years, from the forest floor and shallow organic soil horizons (Lang et al. 2016).

The paradox emerging from this static turnover model is that the tight recycling loop of P between soil and forest biomass prevents P limitation only as long as P is prevented from complete loss from soil, a criterion not met at geographic settings identified as experiencing P limitation (Vitousek et al. 2010). For example, half of the terrestrial surface has slopes exceeding 5° (Larsen et al. 2014), and experiences permanent loss of P through erosion or drainage. The dissolved (Bol et al. 2016) or colloidal (Missong et al. 2016) loss of P caused by weathering of minerals or by litter leaching (Cleveland et al. 2006) typically amounts to 1-60 mg m^{-2} yr^{-1} but can reach up to 242 mg m^{-2} yr^{-1} (Bol et al. 2016). However, due to the tight binding of P to organic matter and soil minerals 90 % of total P loss actually occurs as particulate export (Tiessen 1995), where fine particulate export amounts to up to 807 mg m^{-2} yr^{-1} (Meyer and Likens 1979). Finally, P loss can also occur directly by erosion of plant litter (Uhlig et al. 2017). These P losses are too small to affect annual tree nutrition, i.e. they do not invalidate the static turnover model when budgeted over the timescales of tree growth. Over longer (millennial) timescales, however, the permanent leakage of P should inevitably result in a P deficit. To balance this permanent loss of P, external wet and dry atmospheric deposition input fluxes have been suggested to sustain primary productivity (Chadwick et al. 1999). However, typical atmospheric P deposition rates (Aciego et al. 2017) are mostly much smaller than P losses (Uhlig et al. 2017). Another hypothesis thus suggests that the development of P limitation is countered over these timescales by a continuous transfer of P in primary minerals across the weathering front (Porder et al. 2007). In such eroding settings, in contrast to the Walker and Syers model, P availability in the weathering zone varies

vertically rather than temporally (Porder et al. 2007) (Figure 3-1). However, this weathering front usually occurs below a typical soil profile depth, which is frequently considered to encompass all possible sources of plant nutrition. Here we demonstrate that mineral P uptake by trees from the deep but potentially plant-available calcium phosphate-rich regolith continuously provides P that is tightly cycled through forest biomass at the forest floor, and that this uptake compensates for the otherwise declining P availability with soil development and thus sustains forest growth.

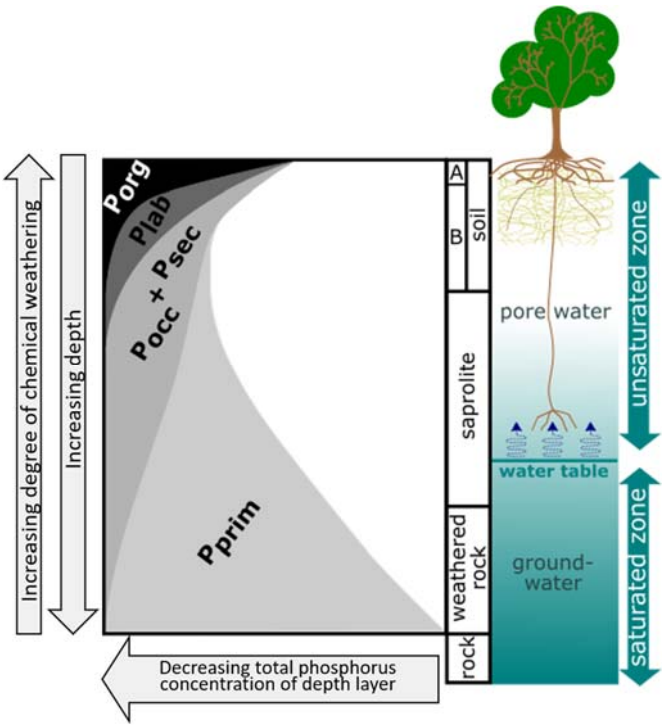

Figure 3-1 The depth distribution of extractable phosphorus (re-drawn and rotated by 90° from (Walker and Syers 1976) and nutrient uptake mechanisms. Phosphorus uptake mechanisms shown here are: deep rooting, dimorphic root systems, capillary rise (blue arrows), symbiotic relationship between roots and mycorrhizal fungi (yellow network). P_{org}: organic-bound phosphorus, P_{lab}: labile phosphorus, P_{occ}: occluded phosphorus, P_{sec}: secondary mineral-bound phosphorus, P_{prim}: primary mineral-bound phosphorus. A, B: soil horizons.

3.2 Study area

Phosphorus sources and fluxes were determined in two southern German upland forest ecosystems, which are monitored by the International Co-operative Program on assessment and monitoring of air pollution effects on forests (ICP Forests). Neither site was glaciated during the last glacial maximum (LGM). The Black Forest (Conventwald, site CON) is characterised by mean annual precipitation (MAP) of 1749 mm, mean annual temperature (MAT) of 6.8 °C, and by a Hyperdystric skeletic folic Cambisol (Baxter 2007) with a fragment rock content of about 70 % within the top 100 cm of soil (Lang et al. 2017). The Bavarian Forest (Mitterfels, site MIT) is characterised by MAP of 1300 mm, MAT of 4.5 °C and by a Hyperdystric chromic folic Cambisol (Baxter 2007) with a fragment rock content of about 25 % within the top 100 cm of soil (Lang et al. 2017). European beech (*Fagus sylvatica)* and Norway spruce (*Picea abies)* of about 130 years age (Lang et al. 2017) dominate site CON and site MIT. Both study sites are underlain by paragneiss, while the Cambisols developed on periglacial slope deposits. Total

denudation rates from *in situ* cosmogenic nuclides (see Methods), which integrate physical erosion and chemical weathering losses over several thousands of years, are 125 t km^{-2} yr^{-1} at site CON and 57 t km^{-2} yr^{-1} at site MIT. We determined the degree of chemical weathering, the depth distribution and bonding forms of P, and tree P sources using radiogenic strontium (Sr) and meteoric cosmogenic beryllium (Be) isotopes in up to 30 m deep drill cores through the regolith into unweathered bedrock.

3.3 RESULTS

3.3.1 Degree of chemical weathering

The degree of chemical weathering was quantified by the chemical depletion fraction (CDF, see Methods, Figure 3-2, Supplementary Table 2-1c), where relative changes in the concentrations of zirconium, an element hosted by the insoluble mineral zircon, are used to quantify the loss of more soluble elements in regolith relative to bedrock. The CDF is high at site CON, where the CDF of 0.57 is close to the maximum CDF observed in mountain belts (~0.60) (Dixon and von Blanckenburg 2012). At site MIT, the CDF is 0.14. The lower depletion at MIT is consistent with bedrock containing albite-rich plagioclase minerals of slower dissolution kinetics and site CON containing faster dissolving anorthite-rich plagioclase. As an independent proxy for the weathering intensity we have used radiogenic Sr ($^{87}Sr/^{86}Sr$, (Blum and Erel 1995); see Methods), which is a bulk regolith proxy for the rock weathering intensity if bedrock mineralogy comprises minerals that differ in its dissolution kinetics, Sr contents and $^{87}Sr/^{86}Sr$ ratio (Blum and Erel 1995). For example, the $^{87}Sr/^{86}Sr$ of bulk regolith shifts from low ratios in unweathered rock to high ratios in soil regolith as plagioclase with low $^{87}Sr/^{86}Sr$ and high Sr concentrations is lost and some biotite with high (radiogenic) $^{87}Sr/^{86}Sr$ and low Sr concentrations remains. $^{87}Sr/^{86}Sr$ thus confirms

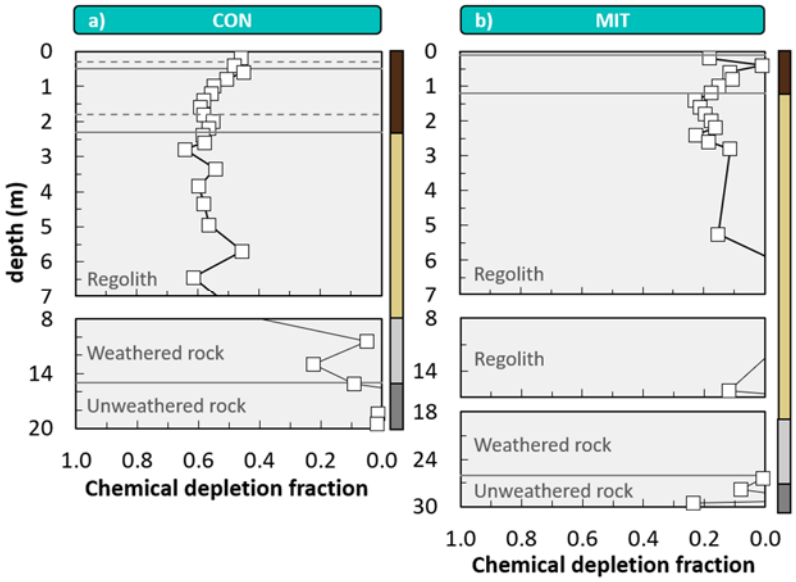

Figure 3-2 Depth distribution of the chemical depletion fraction (CDF, see Methods) of bulk regolith and bulk weathered and unweathered rock. Dashed lines indicate soil horizon subdivision (see Figure 2-2). Coloured bars at the right site of panel a and b refer to colour coding of drill core sections from Figure 2-2.

the difference in the degree of weathering between the sites as the radiogenic Sr of bulk regolith is more radiogenic than bedrock at site CON, but not at site MIT (Figure 3-3, Supplementary Table 2-1c).

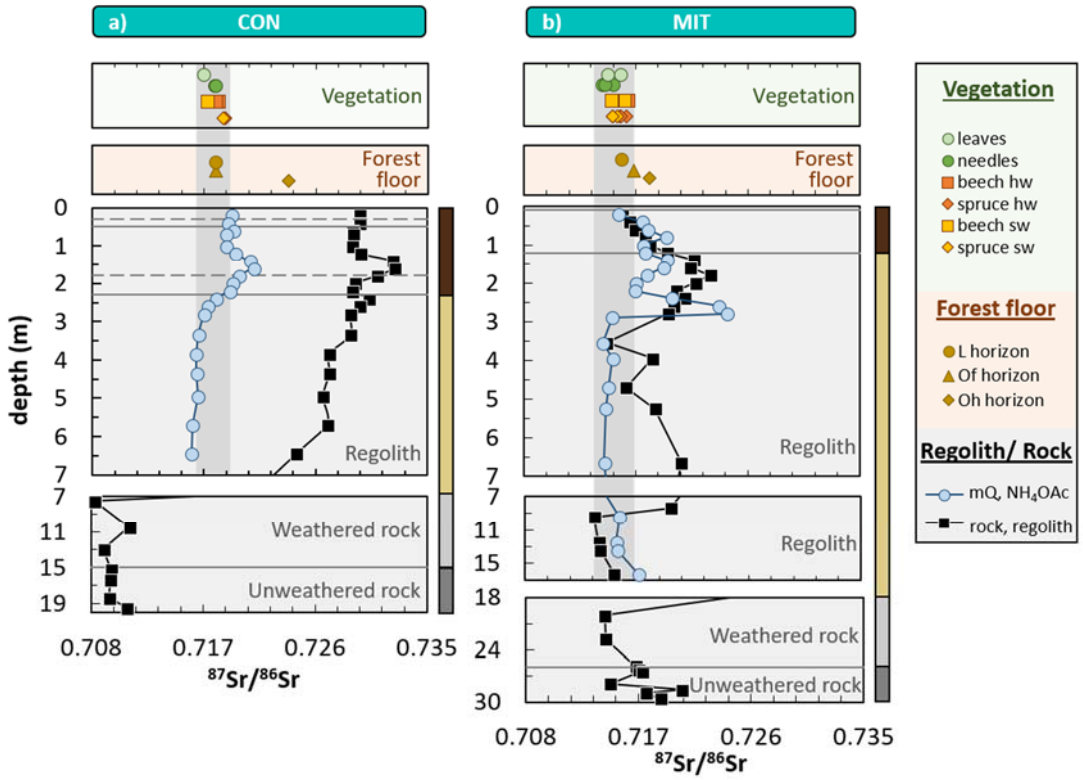

Figure 3-3 Depth distribution of $^{87}Sr/^{86}Sr$ in plants, regolith, and rock. hw: heartwood, sw: sapwood. L: litter layer, Of: organic fermented layer, Oh: organic humic layer. mQ, NH_4OAc: sequentially extracted plant-available fraction comprising the water soluble (deionised water, pH 5) and 1 M NH_4OAc extractable fraction. Dashed lines indicate soil horizon subdivision (see Figure 2-2). Coloured bars at the right site of panel a and b refer to colour coding of drill core sections from Figure 2-2. Grey bar: range of vegetation $^{87}Sr/^{86}Sr$.

3.3.2 Phosphorus availability and fluxes

The degree of P depletion of the regolith was quantified by the mass transfer coefficient (τ^{P}_{Zr}, see Methods) of P, which measures the fractional loss of P by chemical weathering or gain of P by e.g. atmospheric dust inputs. Negative τ^{P}_{Zr}-values denote P loss, while positive τ^{P}_{Zr}-values denote P gain. Despite different degrees of weathering, the depletion of P in soil and saprolite relative to parent rock is astonishingly similar at both sites and amounts to 60-70 % (Figure 3-4; Supplementary Table 2-1c). We infer that the mechanism mobilising P does not depend on the complete transformation of rock into saprolite, but rather is an early process linked directly to the advance of the weathering front. Weathered rock fragments found at site CON within the soil matrix of the uppermost 100 cm are as strongly P depleted as the <2 mm fraction of soil and saprolite, with τ^{P}_{Zr} of 65 % (Supplementary Table 2-1c). To evaluate the plant-availability of P, we performed Hedley fractionation of the P forms (see Methods, Supplementary Table 3-1), which shows that at both sites the 35 % remaining P in soil regolith consists of P in the occluded and recalcitrant (soil organic-bound P) form (Figure 3-4,

Supplementary Table 3-2) that are essentially unavailable to plants. A plant-available form of P (calcium-bound Pi-HCl_{dil}) is the dominant extractable P form only in deep saprolite regolith and weathered bedrock at 7 m and 17 m depth at site CON and site MIT. Thus, considerable fractions of potentially plant-available calcium-bound P are present only in the deep saprolite regolith and weathered rock at both study sites.

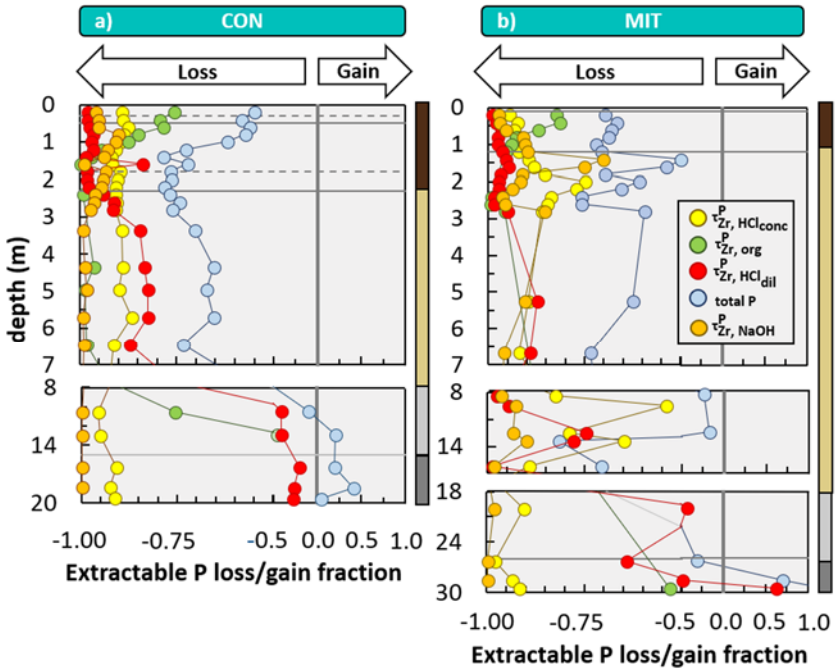

Figure 3-4 Depth distributions of the mass transfer coefficient (τ^{P}_{Zr}, see Methods, here termed "P loss/ gain fraction") of total phosphorus and selected extractable P. $\tau^{P}_{Zr,org}$: resin-P_o + NaOH-P_o + HCO_3-P_o + HCl_{conc}-P_o extractable phosphorus fractions; $\tau^{P}_{Zr,HCl_{conc}}$: HCl_{conc}-P_i extractable phosphorus; $\tau^{P}_{Zr,HCl_{dil}}$: HCl_{dil}-P_i extractable phosphorus; $\tau^{P}_{Zr,NaHO}$: NaOH-P_i extractable phosphorus; $\tau^{P}_{Zr,total}$: total phosphorus. Dashed lines indicate soil horizon subdivision (see Figure 2-2). Coloured bars at the right site of panel a and b refer to colour coding of drill core sections from Figure 2-2. Note changing scaling of x-axis (from -1.00 to -0.50 in 0.05 increments, but from -0.50 to 1.0 in 0.25 increments).

The P uptake flux into the forest biomass (U^{P}_{total}, see Methods) amounts to circa 1000 mg m^{-2} yr^{-1} (Table 2-3). The P reservoir supplying this uptake flux is the forest floor and the A and Bw horizon beneath it, which contain organically-bound P. The wet and dry deposition fluxes (Dep^{P}_{wet}, Dep^{P}_{dry}, see Methods, (Table 2-3, Supplementary Table 3-4) are 8 mg m^{-2} yr^{-1} at site CON and 50 mg m^{-2} yr^{-1} at site MIT. These atmospheric deposition fluxes cannot balance the annual total loss of P, shown above to typically amount to a few hundred mg m^{-2} yr^{-1} (Meyer and Likens 1979; Tiessen 1995; Bol et al. 2016; Missong et al. 2016). Thus, a P deficit must develop over millennial timescales unless P loss is balanced by P supply from deep P-rich reservoirs. We have calculated the net P solubilisation fluxes in deep regolith ($W^{P}_{regolith}$, see Methods), that is P release from primary minerals minus P sequestration into secondary minerals. $W^{P}_{regolith}$ is about 80 mg m^{-2} yr^{-1} at site CON and about 62 mg m^{-2} yr^{-1} at site MIT. Comparison with U^{P}_{total} means that after solubilisation, P is utilised on average 20 times by forest trees

before being lost by drainage or plant debris erosion (Uhlig et al. 2017). That some or all of this P is lifted up from depth to topsoil is reflected by the enrichment of total P from the Bw horizon to topsoil at site CON, which then also results in an enrichment of organically-bound P. However, these patterns alone do not represent unequivocal evidence that the dominant tree species possess the ability to directly tap into this deep nutrient compartment.

3.3.3 $^{87}Sr/^{86}Sr$ and $^{10}Be_{(meteoric)}/^{9}Be_{(stable)}$ as depth tracer for nutrient uptake

We thus used isotope ratios that vary with depth as proxies for the potential nutrient uptake depth. We compared the isotope ratio $^{87}Sr/^{86}Sr$ (see Methods) of living wood and foliage with the plant-available – comprising the water-soluble and NH_4OAc extractable – fractions of Sr in the drill-cores (Blum et al. 2002; Pett-Ridge et al. 2009a). Although Sr is a non-nutritive element, plant roots nevertheless take up Sr via non-selective cation channels as the charge of Sr and calcium (Ca) are identical and the ionic radii are comparable, making $^{87}Sr/^{86}Sr$ a promising tracer for the Ca source of plants (e.g. (Schmitt et al. 2017)). In contrast to Ca and Sr, P is taken up as inorganic PO_4^{3-} through a H^+-coupled high affinity transporter. Although the membrane transporters differ between Sr and P, we can use $^{87}Sr/^{86}Sr$ as an indicator of P uptake depth provided that tree roots take up Sr and P from the same dissolved pool. $^{87}Sr/^{86}Sr$ of leaf foliage is identical to wood, the forest floor (L and Of horizon), and bulk topsoil (Figure 3-3, Supplementary Table 3-3) at both sites. This isotopic matching confirms the tight turnover of organic-bound P through forest biomass. The second important finding is that $^{87}Sr/^{86}Sr$ of living plant matter is identical to $^{87}Sr/^{86}Sr$ of the plant-available fraction over the entire weathering zone at site CON (Figure 3-3, Supplementary Table 3-3, Supplementary Table 3-5) and to that from 3 to 17 m depth at site MIT (Figure 3-3, Supplementary Table 3-3, Supplementary Table 3-5). Thus, the Sr found in the forest floor and organic soil layers originates from these deep regolith layers.

We further explored the capability of trees for deep elemental uptake with the $^{10}Be_{(meteoric)}/^{9}Be_{(stable)}$ ratio (see Methods), applying the same approach and assumptions as for $^{87}Sr/^{86}Sr$. Although Be is not a nutrient, Be can be as passively taken up by plants as Mg by transporters of the MGT family (Maathuis 2009) and can substitute for Mg (Kabata-Pendias 2011). Due to its geologically short half-life of 1.4 Myr, meteoric ^{10}Be is not an original constituent of rocks, and instead is produced in the atmosphere, scavenged with rainwater and infiltrates into the soil. Conversely, the stable isotope ^{9}Be occurs in trace amounts in rock (von Blanckenburg et al. 2012) and is released by chemical weathering. Both isotopes mix in soil water and co-precipitate as amorphous oxides (am-ox). Because of the reactive nature of Be and the distinct sources of these two isotopes, the $^{10}Be_{(meteoric)}/^{9}Be_{(stable)}$ ratio follows a bulge shaped depth profile and decreases strongly with regolith depth (Maher and von Blanckenburg 2016). $^{10}Be_{(meteoric)}/^{9}Be_{(stable)}$ ratios in foliage exceed those found in wood (Figure 3-5, Supplementary Table 3-3), due to the direct uptake of wet deposition rich in ^{10}Be through leaf stomata.

This effect is more pronounced for coniferous than for deciduous species due to the higher relative surface area and the longer life time of its foliage. We thus compare the wood $^{10}Be_{(meteoric)}/^{9}Be_{(stable)}$ with the am-ox ratio to fingerprint the P uptake depth. The $^{10}Be_{(meteoric)}/^{9}Be_{(stable)}$ of *Fagus sylvatica* matches the am-ox ratio at 1.5 to 2.0 m depth at site CON and at 0.0 to 1.5 m depth at site MIT, and *Picea abies* at 2.0 to 7.0 m depth at site CON and 2.0 to 2.5 m depth at site MIT (Figure 3-5, Supplementary Table 3-3, Supplementary Table 3-6). Thus, the uptake depth of Be is species-dependent.

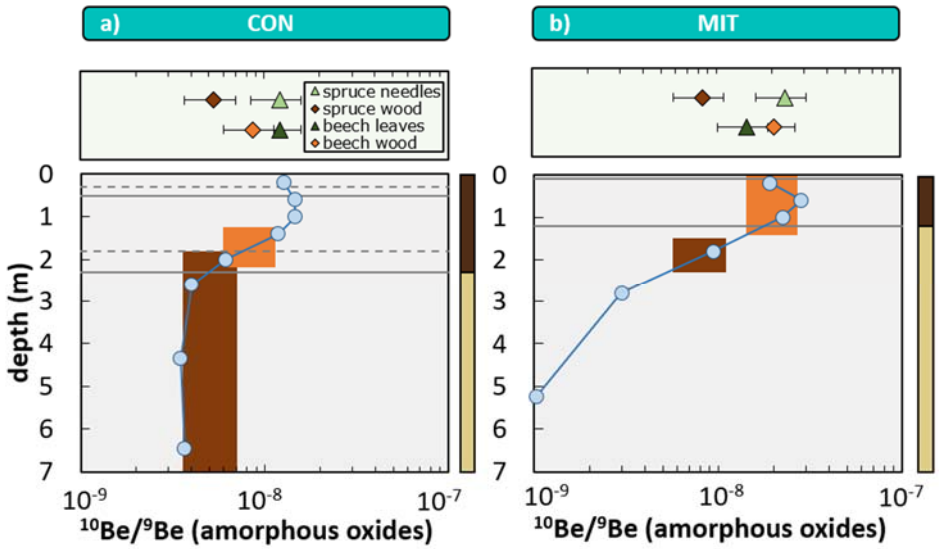

Figure 3-5 Depth distributions of $^{10}Be_{(meteoric)}/^{9}Be_{(stable)}$ as a fingerprint of the phosphorus uptake depth. Vertical bars: range of $^{10}Be_{(meteoric)}/^{9}Be_{(stable)}$ of stem wood from Fagus sylvatica (dark brown) and Picea abies (light brown) scales to depth. Dashed lines indicate soil horizon subdivision (see Figure 2-2). Coloured bars at the right site of panel a and b refer to colour coding of drill core sections from Figure 2-2.

A likely cause for the Be uptake depth differing from that of Sr is the depth-dependence of these elements' mobility, and the same likely holds for P uptake depth too. Whereas Be is highly surface reactive at soil pH above four (in the presence of humic acid) (Willenbring and von Blanckenburg 2010) or above six (in the absence of humic acid) (Willenbring and von Blanckenburg 2010), Sr is mobile at acidic to neutral soil pH. A pH of 6 to 7 provides the highest solubility of the potentially plant-available calcium phosphate in the regolith (Brady and Weil 2002). We find conditions favourable to mobilisation of both P and Sr deep in the profiles. The soil pH (see Methods) is between 6 and pH 7 at ~3 m and 5-7 m at site CON, and at 7-17 m at site MIT (Figure 3-6, Supplementary Table 2-1c). The lower soil pH favourable to solubilising Be is found at a depth <3 m. Thus, the uptake depth of Be at site MIT and for *Picea abies* at site CON is shallower than that of Sr since Be is strongly bound to soil particles at greater depth (Figure 3-6). Regardless, we find evidence for the upward translocation of mineral-sourced elements from 2-17 m depth, and it is likely that P is amongst them.

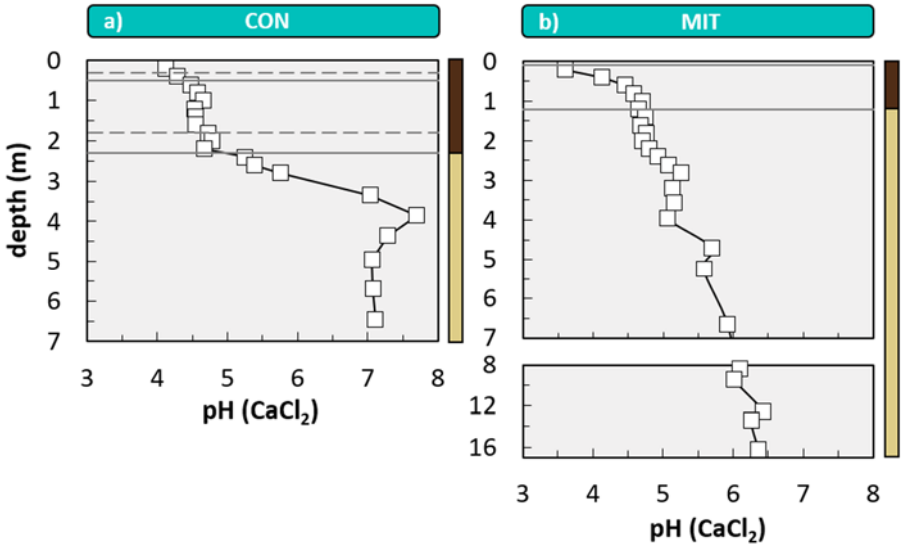

Figure 3-6 Depth distributions of soil pH (see Methods). Dashed lines indicate soil horizon subdivision (see Figure 2-2). Coloured bars at the right site of panel a and b refer to colour coding of drill core sections from Figure 2-2.

3.3.4 Phosphorus uplift mechanisms

We have shown that to balance the permanent loss of P in eroding landscapes over the timescale of the soil particle´s residence time, P uptake from depth, i.e. nutrient uplift (Jobbagy and Jackson 2000; Bullen and Chadwick 2016), is the long-term nutrition strategy at play. The differences in the uptake depth of the elements Sr and Be (interpreted to constrain the uptake depth range of P), provide insight into the uplift pathways that we infer to be several meters. The most obvious mechanism is direct uptake by roots. *Picea abies* is known to root shallow, particularly in mixed stands with *Fagus sylvatica* (Schmid and Kazda 2002), where *Fagus sylvatica* acts as a Ca-pump for *Picea abies* (Berger et al. 2006). However, our results suggest uptake from a depth beyond the main rooting depth of either *Picea abies* or *Fagus sylvatica*, both of which are reported as being constrained to less than two meters (Canadell et al. 1996). In surveys of rooting depth, deep roots are likely undersampled (Fan et al. 2017). Importantly, plant rooting depth is regulated hydrologically (Fan et al. 2017). It has been shown that groundwater water table and rooting depth correlate linearly by a 1:1 line (Fan et al. 2017). Dimorphic root systems (comprising shallow horizontal roots and deep taproots), allow trees to tap into the capillary fringe near the water table (Fan et al. 2017). In that case they simultaneously take up water, e.g. during summer droughts, and mobilised nutrients. Although varying seasonally, the water table lies at 7.5 m depth at site CON and at 8 m depth at site MIT, which is consistent with the uptake depth inferred from $^{87}Sr/^{86}Sr$ (Figure 3-3) as well as with the most significant increase of potentially plant-available calcium-phosphate with depth (Figure 3-4). From that depth hydraulic redistribution by roots (McCulley et al. 2004; Lambers et al. 2006) re-allocates deep water carrying dissolved P from deep calcium phosphate-rich layers to shallow roots due to a water potential gradient. Since we still lack visual evidence for the presence of roots at depths of ~8 m, we suggest capillary rise and diffusion as

additional P uplift mechanisms. However, the presence of an acidic soil pH – ranging between pH 4 and pH 5 – in the uppermost 3 m of regolith at both sites should reduce the P mobility required for this uplift mechanism, as at this pH P is fixed mainly by hydrous Al, Fe or Mn oxides (Brady and Weil 2002). Yet, low amounts of P remain in soil solution: The P concentration of interflow water in the Bw horizon ranges from 0.02 to 0.2 mg/kg (unpublished data) at site CON. Thus, P may be slowly, but permanently, lifted up over millennial timescales. This abiotic lift may further be supported by hyphae of endomycorrhiza fungi that can bridge deep nutrient sources and shallow tree roots by more than a meter (Graham et al. 2010). Such hyphae have been found in oak woodland down to four meters depth (Bornyasz et al. 2005). At that depth, they take up nutrient-rich pore waters, or penetrate directly into mineral grains, such as apatite, for nutrient uptake (Jongmans et al. 1997; Blum et al. 2002). We suggest that a combination of root-mycorrhiza symbiosis, dimorphic root systems and capillary rise (Figure 3-1) explains the nutrient uplift from depth that is required by P mass-balance and demonstrated with our $^{87}Sr/^{86}Sr$ and $^{10}Be/^{9}Be$ data.

3.4 Implications for global forest carbon balances

To mitigate the rise of industrial CO_2 emissions long-term storage of plant-derived carbon into soil has been suggested (Lal 2008). The Carbon Use Efficiency (CUE) metric quantifies the partitioning of atmospheric carbon into biomass and ultimately into soil. CUE approaches maximum values when soil nutrient availability is high (Fernández-Martínez et al. 2014). Nutrient availability has thus been suggested to be a key regulator of global carbon balances (Fernández-Martínez et al. 2014). In terrestrial biosphere models the availability of plant growth limiting nutrients, such as phosphorus should be thus taken into account. Implementation of the conventional hypothesis - namely that forests are nourished solely from the shallow organic or mineral soil horizons - in such terrestrial biosphere models, might underestimate the potential of forests as a sink in the global carbon balance. Instead, considering the presence of nutrient-rich reservoirs of several meters depth that are accessible to trees as shown in this study would allow a more accurate prediction of the global carbon forest balance.

3.5 METHODS

3.5.1 Determination of the total denudation rate

The catchment wide denudation rate (D) was estimated from concentrations of the *in situ*-produced cosmogenic nuclide ^{10}Be (Supplementary Table 2-1c) following Equation 3-1 (von Blanckenburg 2005). In Equation 3-1 PROD is the production rate (at g^{-1} yr^{-1}) of cosmogenic ^{10}Be at the Earth surface in quartz, $[^{10}Be]_{in\ situ}$ the measured cosmogenic nuclide concentration (at g^{-1}), λ is the decay constant (yr^{-1}) of ^{10}Be and Λ the cosmic ray absorption mean free path (150 g cm^{-2}) in rock. To calculate D we used

a PROD of 4.01 at g^{-1} yr^{-1} at sea-level high latitude (SLHL) (Lal 1991; Stone 2000) and scaled for altitude and latitude following Stone (2000).

$$D = \left(\frac{PROD}{[^{10}Be]_{in\ situ}} - \lambda\right)\Lambda \qquad \textbf{Equation 3-1}$$

3.5.2 Determining the chemical depletion fraction

The chemical depletion fraction (CDF) quantifies the degree of chemical alteration of the regolith (r) relative to unweathered parent bedrock (p) by using the concentration ratio of an immobile element (X_i) such as Zr, which as justified in Section 2.3.4.2 was used in this study (Brimhall and Dietrich 1987; Riebe et al. 2003) following Equation 3-2. A CDF value of 0 indicates the absence of chemical depletion, and a CDF value of 0.5 means that 50 % of the parent rock's mass has been dissolved. CDF values and corresponding Zr concentrations from XRF analyses are reported in Supplementary Table 2-1b and 2-1c. Each site's CDF value was estimated by averaging Zr concentration through the weathering profile from below the topsoil enrichment horizons (located at 1.4 m depth at both sites) down to the saprolite-weathered bedrock interface (located at 7 m depth at site CON and at 17 m depth at MIT). The bedrock's Zr concentration was determined by averaging the least weathered samples beneath the weathering front.

$$CDF = 1 - \frac{[X_i]_p}{[X_i]_r} \qquad \textbf{Equation 3-2}$$

3.5.3 Determining elemental loss/gain fractions of extractable phosphorus

The mass transfer coefficient, hereafter termed elemental loss and gain fractions ($\tau^{X}_{X_i}$) quantify the depletion (negative $\tau^{X}_{X_i}$) or enrichment (positive $\tau^{X}_{X_i}$) of an element X in regolith (r) relative to parent bedrock (p) (Brimhall and Dietrich 1987; Anderson et al. 2002). To determine $\tau^{X}_{X_i}$ the concentrations of an immobile element (X_i), Zr used here, and the element of interest, here P, from unweathered parent bedrock and regolith as well as the respective extractable fraction of P from regolith (e) are normalised following Equation 3-3 and reported in Supplementary Table 3-2.

$$\tau^{X}_{X_{i,(e)}} = \frac{[X_i]_p}{[X_i]_r} \cdot \frac{[X]_{r,(e)}}{[X]_p} - 1 \qquad \textbf{Equation 3-3}$$

We used the Zr and P concentrations from XRF analyses of bulk bedrock and regolith to determine τ^{P}_{Zr}. We used the Hedley fraction method (see below) to determine $\tau^{P}_{Zr,(e)}$ for each P operationally defined P pool. The individual organic fractions (resin-P_o + NaOH-P_o + HCO_3-P_o + HCl_{conc}-P_o) were grouped together (Supplementary Table 3-1). We note that τ^{P}_{Zr} derived from XRF analyses differs from $\tau^{P}_{Zr,total}$ derived from Hedley fractionation by on average ~10 %. The disparities may arise from the low sensitivity of XRF for P, or the possibility of non-quantitative Hedley extraction steps (e.g. Lauer et al. (2013) and unpublished data). Nevertheless, we used both methods for the assessment of weathering depth.

3.5.4 Determining the net P solubilisation flux

The net solubilisation flux of P ($W^{P}_{regolith}$) is defined as the chemical release flux minus the uptake flux by secondary mineral formation. $W^{P}_{regolith}$ is derived from the total denudation rate (D, Equation 3-1), the P concentration of parent bedrock ($[P]_{rock}$) and the elemental loss and gain fraction of P (τ^{P}_{Zr}, Equation 3-3) by Equation 3-4 and is reported in Table 2-3. At site CON, we used τ^{P}_{Zr} from between the base of the enrichment horizons and the saprolite - weathered bedrock interface (from 1.4 m to 7.0 m depth) and at site MIT, which shows no enrichment horizons, we used the most negative τ^{P}_{Zr} values from the mineral soil at 0.4 m depth.

$$W^{P}_{regolith} = D \cdot [P]_{rock} \cdot \left(-\tau^{P}_{Zr}\right) \qquad \textbf{Equation 3-4}$$

3.5.5 Determining external atmospheric wet and dry deposition fluxes

Wet atmospheric deposition fluxes (Dep^{P}_{wet}) were monitored by the long-term monitoring program ICP Level II. For site CON, we used data from the Forest Research Institute Baden-Wuerttemberg (FVA) and for site MIT we used data from the State Institute of Bavaria for Forestry and Silviculture (LWF). As dry deposition fluxes were not monitored, we estimated elemental dry deposition fluxes (Dep^{P}_{dry}, Supplementary Table 3-4). We estimated Dep^{P}_{dry} by using the global dry deposition flux map of Jickells et al. (2005) and multiplying the total dust mass flux with the upper continental crust (UCC) concentration of P from Taylor and McLennan (1995) (data reported in Supplementary Table 3-4). Since UCC concentrations refer to unweathered bedrock, while the dust particles might be altered prior to or during eolian transport, this estimate is likely an upper limit.

3.5.6 Determining the P ecosystem uptake

The P ecosystem uptake flux (U^{P}_{total}) was determined from ecosystem gross primary productivity (GPP in gC m^{-2} yr^{-1}) and the bulk tree phosphorus concentration. As GPP includes the energy utilised for

respiration (Chapin et al. 2012), we converted GPP into net primary productivity (NPP) by dividing GPP by a factor of two. To convert the carbon based NPP flux into a total annual biomass production flux we divided NPP through the bulk tree carbon concentration of ~50 wt. %. Next, we multiplied total biomass production with the nutrient concentration of bulk tree and report the data used to infer U^{P}_{total} in Table 2-4. Since GPP is not available for our study sites, we used mean annual (1982−2008) GPP data from a global empirical upscaling model based on FLUXNET data (Jung et al. 2011) instead. To determine a bulk tree P concentration, we calculated a mean concentration from the compartments trunk wood and non-woody foliage (for more detail see Section 2.3.4.4). Thus, we used the entire dataset in Supplementary Table 2-3 for wood and non-woody foliage.

3.5.7 Analysing the bulk chemical composition of bedrock, regolith and plant samples

The chemical composition of bedrock, regolith and reference materials including SRM 2709a (San Joaquin soil, NIST), TILL-1 (soil, CCRMP), GM (granite, ZGI) and TB (clay shale, ZGI) was analysed by X-ray fluorescence spectroscopy (XRF, PANalytical Axios Advanced) at GFZ-Potsdam with relative uncertainties better than 10 %. Bedrock and regolith mineral identification was performed by X-ray diffraction analyses (XRD, Siemens D5000, Cu-Kα radiation) with a relative identification limit of detection of 5 %.

Vegetation samples and the reference material SRM 1515 (apple leaves, NIST) were digested using a microwave method (MLS start) with ultrapure acid mixtures (H_2O_2, HNO_3, HCl, HF) in PFA vials and their chemical compositions were analysed by Inductively Coupled Plasma Optical Emission Spectrometry (ICP-OES, Varian 720ES) with relative uncertainties better than 10 %. Beryllium concentrations were determined by Inductively Coupled Plasma Quadrupole Mass Spectrometry (Q-ICP-MS, Thermo iCAP-Q), with a relative precision better than 16 % based on repeat digestion and analyses.

3.5.8 Analysing the soil pH

The pH of soil and saprolite was assessed on a suspension of 1 g oven dried (60 °C, 24 h) bulk soil (<2 mm fraction) and 5 ml 0.01 M $CaCl_2$ with a WTW pH meter. Prior to soil pH measurements the suspension was dispersed for 10 min in an ultrasonic bath and shaken for 20 min on a Stuart rocker & roller mixer. For quality control, the Merck pH 4 buffer solution and the international reference material IRMM-443-7 (Cambisol, BCR/IRMM representing the same soil type as those at our study sites) were analysed after every tenth sample. The soil pH analyses were stable, accurate and the reproducibility was better than ± 1.5 %.

3.5.9 Extracting the plant-available fraction of strontium

The plant-available fraction of Sr comprises the water-soluble fraction and the exchangeable fraction, which forms weak electrostatic bounds to the negative surfaces of phyllosilicates and clay minerals or organic matter. Each extraction was performed on a suspension of 2 g of bulk soil (dried, sieved to <2 mm) in 14 ml of reactant, where deionised water (Milli-Q, 18 MΩ) was used for the water-soluble extraction and 1 M NH_4OAc at neutral pH for the exchangeable fraction. The suspension was first dispersed in an ultrasonic bath for 1 h and then gently shaken on a hotdog roller at 7 rpm for 24 h (water-soluble extraction) and 2 h (exchangeable extraction). After shaking the suspension was centrifuged at 4200 rpm for 30 min and the supernatant was pipetted off into a syringe and filtered through a 0.2 µm acetate filter. The entire sequential extraction method was repeated for each sample.

Both individual supernatants were combined, treated as one sample with concentrated acid mixtures (HF, HCl, HNO_3) and re-dissolved prior to radiogenic Sr analyses.

3.5.10 Determining the P forms by the Hedley fractionation method

Sieved and ground aliquots from the cores were extracted sequentially in duplicate according to a modified Hedley procedure (Moir and Tiessen 1993). This method assesses P availability in a stepwise extraction of 0.5 g soil at a 1:60 soil:solution ratio (w/v) using anion exchange resin (resin P), 0.5 M $NaHCO_3$ (P-$NaHCO_3$), 0.1 M NaOH (P-NaOH) and 1 M HCl (P-HCl) at an extraction time of 16 hours on an over-head shaker, followed by centrifugation and filtration through ashless quantitative paper filters (Albet LabScience, Dassel, Germany). Subsequently, the P-HCl_{conc} fraction was extracted with hot concentrated HCl (80 °C, 20 minutes). For the final extraction of residual P, we used *aqua regia* (following Lauer et al. 2013). For each fraction, we determined inorganic P (P_i) by the molybdenum-blue method (Murphy and Riley 1962) and total P by ICP-OES (Ultima 2, HORIBA Jobin Yvon, Longjumeau, France); organic P (P_o) was calculated as the difference of total P and P_i. A detailed description of the sequential extraction scheme of P and the fraction properties is provided in Supplementary Table 3-1.

3.5.11 Analysing the radiogenic Sr ($^{87}Sr/^{86}Sr$) ratios

Radiogenic Sr analyses were performed at GFZ-Potsdam, Helmholtz Laboratory for the Geochemistry of the Earth Surface (HELGES). Prior to radiogenic Sr analyses samples were dissolved by a silicate digestion method for rock and regolith samples using ultrapure concentrated acid mixtures (HCl, HNO_3, HF, H_2O_2) in PFA vials. After sample digestion Sr was separated from matrix elements using inverted disposable pipettes packed with 200 µl Sr Spec resin (TrisKem SR-B50-S (50-100 µm)). Matrix elements were removed by elution with 5.5 ml 7.5 M HNO_3 and Sr was eluted with 2 ml deionised water (Milli-

Q water, 18 MΩ). To destroy any organic crown-ether released from the Sr Spec resin, the Sr fraction was dried, re-dissolved and treated in closed PFA vials for more than 12 h in a concentrated acid mixture (H_2O_2, HNO_3) at 85 °C and then in concentrated HNO_3 at 170 °C. The purity of the Sr fraction was monitored by ICP-OES analyses. Impurities were significant only for Ba and were kept below a Ba/Sr ratio of less than 5. Doping tests (not shown here) with SRM 987 demonstrate the absence of analytical bias below this threshold. $^{87}Sr/^{86}Sr$ was measured as 40 ppb pure Sr solutions in 0.3 M HNO_3 on a multi collector inductively coupled plasma mass spectrometer (MC-ICP-MS, Thermo Neptune) in low resolution using an APEX-Q (ESI), and a nickel sampler cone. $^{87}Sr/^{86}Sr$ ratios were determined over 8 blocks of 10 cycles with an integration time of 4.194 seconds. The sequence of a sample run consisted of 5-12 blocks where each block comprised a blank, four samples or reference materials and SRM 987 (not processed through chemistry). Blank correction of samples and reference material during the sequence was less than 0.4 % of sample signal. Simultaneously to the signals of ^{84}Sr (L2), ^{86}Sr (central Faraday Cup), ^{87}Sr (H1) and ^{88}Sr (H2) the signals of ^{82}Kr (L4) and ^{83}Kr (L3) and ^{85}Rb (L1) were monitored to correct for Kr and Rb interferences on the masses 84 and 87 with the Kr and Rb isotope ratios measured prior to the sequence run. The measured $^{87}Sr/^{86}Sr$ ratio was normalised to the $^{88}Sr/^{86}Sr$ ratio of 8.375209 by using an exponential law to correct for natural and instrumental isotope fractionation. Repeat analyses of SRM 987 both processed the same way as samples and without chemistry was used to determine the long-term accuracy of the method. Averages and two standard deviations are SRM 987 = 0.71029 ± 0.00001 (N=240, without chemistry) and SRM 987 = 0.71026 ± 0.00011 (N=32, including chemistry) and are identical to published values for SRM 987 = 0.71029 ± 0.00033 (N=247, Jochum et al. 2005) measured with MC-ICP-MS.

3.5.12 Extraction and analyses of amorphous oxides

The amorphous oxides (am-ox) were separated following the procedure described in (Wittmann et al. 2012). Although not analysed, we separated the adsorbed exchangeable fraction prior to the am-ox extraction step to allow optimal comparison of the chemical composition of leachates from the Be extraction and Sr extraction procedure. We added 10 ml 1 M $MgCl_2$ to 0.5 g bulk soil (dried, sieved to <63 µm), shook the suspension for more than 12 h, centrifuged for 20 min at 4200 rpm and pipetted off the supernatant. Then, we washed the sample three times using 10 ml deionised water at pH 9 (Milli-Q, 18 MΩ, pH adjusted with ammonia) and discarded the wash solutions. Finally, the amorphous oxides were separated by adding 10 ml 0.5 M HCl and by mild shaking for 24 h. The supernatant was pipetted off as the exchangeable fraction and treated with concentrated acid mixtures (HF, HCl, HNO_3). Next, two aliquots were taken for separate analyses of ^{9}Be and ^{10}Be.

The ^{9}Be concentration of amorphous oxides was measured at GFZ-Potsdam with ICP-OES in 0.3 M HNO_3 with a relative uncertainty of 5 % based on accuracy of repeat analyses of the international

reference materials GA (granite, CNRS) and RGM-1 (rhyolite, USGS) and reported in Supplementary Table 3-6.

3.5.13 Analysing in situ ^{10}Be in quartz

To determine the measured $[^{10}Be]_{in\ situ}$ concentrations we sieved bedload sediment to 125-250 µm and purified 10 g quartz from matrix minerals. Then we added 400 µg of an in-house ^{9}Be "phenakite" carrier with a ^{9}Be concentration of 372.5 ppm to each sample, digested the pure quartz sample with 14 M HF and separated Be from matrix elements by cation chromatography following the method described in (von Blanckenburg et al. 2004). Finally, Be was further purified by alkaline precipitation described in detail in (von Blanckenburg et al. 1996), oxidised, pressed into accelerator mass spectrometer (AMS) cathodes and analysed at the University of Cologne - Centre for Accelerator Mass Spectrometry (AMS). Procedure blanks were run in each sample batch and subtracted from the samples.

3.5.14 Analysing the $^{10}Be_{(meteoric)}/^{9}Be_{(stable)}$ ratio

We split the ^{9}Be aliquot to separately measure major and trace element concentrations in a low and a high dilution run, where the calibration standards of the low dilution run were matrix matched.
^{9}Be of plant matter was measured on an iCAP-Q with fast pump system (ESI Fast DX, 1 ml loop) with uncertainties better than 30 % relative based on repeat digestion and analyses of SRM 1515 (apple leaves, NIST). Prior to ^{9}Be analyses of plant matter the sample matrix was reduced by several orders of magnitudes by cation chromatography using inverted disposable pipettes packed with 3 ml AG50W-X12 resin (200-400 mesh). P and S were rinsed with 7.5 ml deionised water (Milli-Q, 18 MΩ) and the Be fraction was eluted with 4.5 ml 0.3 M HF, dried and re-dissolved in 0.3 M HNO_3. After cation chromatography, the ^{9}Be aliquot was sufficiently purified to avoid matrix effects during iCAP-Q analyses.

^{10}Be aliquots were spiked depending on the natural ^{9}Be concentration with 400 to 550 µg of our in-house ^{9}Be "phenakite" carrier (^{9}Be: 372.5 ppm). The matrix elements were separated from the spiked ^{10}Be aliquot using anion and cation chromatography methods and alkaline precipitation described in detail in (von Blanckenburg et al. 2004) and (von Blanckenburg et al. 1996). ^{10}Be/^{9}Be analyses were performed at the University of Cologne - Centre for Accelerator Mass Spectrometry (AMS). Procedure blanks were subtracted from the samples.

3.6 Acknowledgements

We are grateful for funding by the German National Science Foundation Priority Program 1685 "Ecosystem nutrition: forest strategies for limited phosphorus resources" and Fritzi Lang for its

coordination and discussions. We also thank the State Institute of Bavaria for Forestry and Silviculture (LWF) and the Forest Research Institute Baden-Wuerttemberg (FVA) for providing wet deposition data. R. Naumann (GFZ) and A. Gottsche (GFZ) are acknowledged for X-ray fluorescence and X-ray diffraction analyses. We thank J. Schuessler (GFZ), H. Wittmann (GFZ) and G. Floor (GFZ) for analytical support. R. Kapannusch (GFZ) as well as A. Rodionov and S. Bauke (University of Bonn, INRES) are acknowledged for field work, sample preparation and analyses. We also thank Patrick Frings for discussions.

3.7 SUPPLEMENTS

Supplementary Table 3-1 Sequential fractionation scheme with resultant P fractions and fraction properties (slightly modified from (Barej et al. 2014))

Fraction	Extraction procedure[a]	Fraction properties[b]
Resin-P_i	Anion exchange resin, 16 h	Labile P_i, biologically most available P form
$NaHCO_3$-P_i	0.5 M NaHCO3 pH 8.5, 16 h	Labile P_i, likely to be plant-available, associated with Fe and Al oxides
$NaHCO_3$-P_o		Easily mineralizable P_o
NaOH-P_i	0.1 M NaOH, 16 h	Moderately labile P_i, associated with secondary Fe and Al oxides
NaOH-P_o		Stable P_o, involved in long term transformation of P
HCl_{dil}-P_i	1 M HCl, 16 h	Moderately stable P_i, Ca-bound P, associated with primary minerals (e.g. apatite), considered as potentially bioavailable
HCl_{conc}-P_i	HCl_{conc}, 80°C 10 min.	Very stable P_i, covers recalcitrant P_i occluded in sesquioxides
HCl_{conc}-P_o		P_o in very stable residual pools, eventually also derived from particulate organic matter that is not alkali extractable, but potentially bioavailable
Residual P	*Aqua regia* digestion	Highly resistant and occluded P forms
Sum of organic P	Sum of P_o: $NaHCO_3$-P_o, NaOH-P_o, HCl_{conc}-P_o, resin-P_o	
Total P (P_t)	Sum of all fractions	

[a] according to Tiessen and Moir (1993) and Hedley et al. (1982)
[b] based on Tiessen and Moir (1993) and Cross and Schlesinger (1995)

Supplementary Table 3-2 Phosphorus Hedley loss / gain fractions of soil and saprolite at site CON and site MIT (for colour coding see table caption)

sample ID	IGSN†	brief sample description	$\tau^{P}_{Zr,resin}$	τ^{P}_{Zr,HCO_3}	$\tau^{P}_{Zr,NaOH}$	$\tau^{P}_{Zr,HCl_{dil}}$	$\tau^{P}_{Zr,HCl_{conc}}$	$\tau^{P}_{Zr,residual}$	$\tau^{P}_{Zr,org}$
CON regolith depth profile									
CON 14	GFDUH00LT	soil, Ah horizon	-0.99	-0.99	-0.96	-0.98	-0.89	-0.98	-0.76
CON 13	GFDUH00LU	soil, Ah + Bw horizon	-1.00	-0.99	-0.95	-0.98	-0.89	-0.98	-0.79
CON 12	GFDUH00LV	soil, Bw I horizon	-1.00	-0.99	-0.95	-0.98	-0.87	-0.98	-0.78
CON 11	GFDUH00LW	soil, Bw I horizon	-1.00	-0.99	-0.90	-0.97	-0.89	-0.98	-0.85
CON 10	GFDUH00LX	soil, Bw I horizon	-1.00	-0.99	-0.91	-0.97	-0.89	-0.99	-0.87
CON 9	GFDUH00LY	soil, Bw I horizon	-1.00	-0.99	-0.93	-0.97	-0.91	-0.99	-0.94
CON 8	GFDUH00LZ	soil, Bw I horizon	-1.00	-0.99	-0.94	-0.98	-0.92	-0.99	-0.97
CON 7	GFDUH00M0	soil, Bw I horizon	-1.00	-1.00	-0.99	-0.84	-0.92	-0.99	-1.00
CON 6	GFDUH00M1	soil, Bw II horizon	-1.00	-0.99	-0.93	-0.98	-0.90	-0.99	-0.98
CON 5	GFDUH00M2	soil, Bw II horizon	-0.99	-0.99	-0.94	-0.98	-0.90	-0.98	n.d.
CON 4	GFDUH00M3	soil, Bw II horizon	-0.99	-0.99	-0.94	-0.98	-0.91	-0.99	n.d.
CON 3	GFDUH00M4	saprolite, Cw horizon	-0.99	-0.99	-0.96	-0.94	-0.91	-0.99	-0.99
CON 2	GFDUH00M5	saprolite, Cw horizon	-0.99	-0.99	-0.96	-0.91	-0.91	-0.99	n.d.
CON 1	GFDUH00M6	saprolite, Cw horizon	-0.99	-0.99	-0.97	-0.92	-0.91	-0.99	n.d.
CON 19	GFDUH00MB	saprolite, Cw horizon	-1.00	-1.00	-0.99	-0.85	-0.89	-0.99	n.d.
CON 21	GFDUH00MD	saprolite, Cw horizon	-1.00	-1.00	-0.99	-0.83	-0.89	-0.99	-0.96
CON 22	GFDUH00ME	saprolite, Cw horizon	-1.00	-1.00	-0.98	-0.82	-0.90	-0.99	-0.99
CON 23	GFDUH00MF	saprolite, Cw horizon	-1.00	-1.00	-0.99	-0.82	-0.87	-0.99	n.d.
CON 24	GFDUH00MG	saprolite, Cw horizon	-1.00	-1.00	-0.99	-0.87	-0.91	-0.99	-0.98
CON 41	GFDUH00N7	weathered paragneiss	-1.00	n.d.	-1.00	-0.41	-0.95	-0.98	-0.76
CON 47	GFDUH00N9	weathered paragneiss	-1.0	n.d.	-1.0	-0.4	-0.95	-0.99	-0.46
CON 49	GFDUH00NB	unweathered paragneiss	-1.00	n.d.	-1.00	-0.20	-0.91	-0.97	n.d.
CON 50	GFDUH00NC	unweathered paragneiss	-1.00	n.d.	-1.00	-0.27	-0.93	-0.98	n.d.
CON 51	GFDUH00ND	unweathered paragneiss	n.d.	n.d.	n.d.	-0.27	-0.91	-0.99	n.d.
MIT regolith depth profile									
MIT 14	GFDUH004A	soil, Bw horizon	-0.99	-0.99	-0.97	-0.99	-0.95	-0.99	-0.82
MIT 13	GFDUH004B	soil, Bw horizon	-1.00	-0.99	-0.97	-0.98	-0.92	-0.98	-0.81
MIT 12	GFDUH004C	soil, Bw horizon	-1.00	-0.99	-0.95	-0.97	-0.93	-0.96	-0.87
MIT 11	GFDUH0045	soil, Bw horizon	-1.00	-0.99	-0.91	-0.98	-0.92	-0.96	-0.93
MIT 10	GFDUH0046	soil, Bw horizon	-1.00	-0.99	-0.91	-0.98	-0.92	-0.99	-0.94
MIT 9	GFDUH0047	soil, Bw horizon	-1.00	-0.98	-0.90	-0.96	-0.92	-0.98	-0.95
MIT 8	GFDUH0048	saprolite, Cw horizon	-1.00	-0.97	-0.70	-0.95	-0.90	-0.99	n.d.
MIT 7	GFDUH0049	saprolite, Cw horizon	-1.00	-0.98	-0.75	-0.95	-0.88	-0.99	n.d.
MIT 6	GFDUH004D	saprolite, Cw horizon	-1.00	-0.99	-0.91	-0.97	-0.85	-0.99	n.d.
MIT 5	GFDUH004E	saprolite, Cw horizon	-1.00	-0.99	-0.92	-0.97	-0.75	-0.99	n.d.
MIT 4	GFDUH004F	saprolite, Cw horizon	-1.00	-0.99	-0.94	-0.97	-0.77	-0.99	n.d.
MIT 3	GFDUH004G	saprolite, Cw horizon	-1.00	-1.00	-0.96	-0.99	-0.84	-0.98	-0.99
MIT 2	GFDUH004H	saprolite, Cw horizon	-1.00	-0.99	-0.96	-0.98	-0.85	-0.98	-0.99
MIT 1	GFDUH004J	saprolite, Cw horizon	-1.00	-0.99	-0.85	-0.95	-0.86	-0.99	-0.96
MIT 19	GFDUH00AT	saprolite, Cw horizon	-0.98	-0.93	-0.55	-0.30	-0.59	-0.97	n.d.
MIT 20	GFDUH00AU	saprolite, Cw horizon	-0.98	-0.94	-0.83	-0.32	0.05	-0.99	n.d.
MIT 21	GFDUH00AV	saprolite, Cw horizon	-0.99	-0.95	-0.76	-0.43	-0.64	-0.97	n.d.
MIT 22	GFDUH00AW	saprolite, Cw horizon	-0.97	-0.93	-0.58	0.14	-0.29	-0.98	n.d.
MIT 23	GFDUH00AX	saprolite, Cw horizon	-0.99	-0.98	-0.91	-0.87	-0.90	-0.99	n.d.
MIT 24	GFDUH00AY	saprolite, Cw horizon	-0.99	-0.99	-0.96	-0.89	-0.92	-0.99	n.d.
MIT 25	GFDUH00AZ	saprolite, Cw horizon	-0.99	-0.99	-0.97	-0.98	-0.83	-0.98	n.d.
MIT 26	GFDUH00B0	saprolite, Cw horizon	-0.99	-0.98	-0.93	-0.95	-0.54	-0.95	n.d.
MIT 27	GFDUH00B1	saprolite, Cw horizon	-0.99	-0.98	-0.93	-0.75	-0.79	-0.98	n.d.
MIT 28	GFDUH00B2	saprolite, Cw horizon	-0.99	-0.97	-0.90	-0.78	-0.65	-0.97	n.d.
MIT 29	GFDUH00B3	saprolite, Cw horizon	-1.00	-0.99	-0.98	-0.99	-0.89	-0.98	n.d.
MIT 31	GFDUH00BY	weathered gneiss	-1.00	n.d.	-0.99	-0.78	-0.96	-0.99	n.d.
MIT 32	GFDUH00BX	weathered gneiss	-0.99	-1.00	-0.98	-0.43	-0.91	-0.99	n.d.
MIT 35	GFDUH00BU	unweathered gneiss	-1.00	n.d.	-1.00	-0.64	-0.98	-1.00	n.d.
MIT 38	GFDUH00BR	unweathered gneiss	-0.99	n.d.	-1.00	-0.48	-0.93	-1.00	n.d.
MIT 40	GFDUH00BP	unweathered gneiss	-0.99	-1.00	n.d.	0.63	-0.92	-1.00	-0.53

n.d. = not determined

Grey labelled data indicate samples identified to stem from a non-representative source rock as indicated by Zr concentrations that are too low (see Section 2.3.4). These were excluded in metrics that rely on Zr data. Brown labelled data indicate samples that also stem from another source rock as indicated by Cr, Nb, Ni, Ti concentrations that are too high. The metrics derived from these samples that rely on Zr concentrations were excluded.

† IGSN (International Geo Sample Number). Metadata of samples are available under: www.igsn.org by adding the IGSN after igsn.org, e.g. igsn.org/GFDUH00LT

Supplementary Table 3-3 Isotopic composition of plant samples at site CON and site MIT

sample ID	IGSN†	sampling date (month year)	brief sample description	MC-ICP-MS analyses (^{87}Sr / ^{86}Sr)	SD	Q-ICP-MS analyses ^{9}Be (ng/g)	AMS analyses $^{10}Be_{meteoric}$ (10^6 at/g)	uncertainty (10^6 at/g)	(^{10}Be / ^{9}Be) (10^{-9})	uncertainty (10^{-9})
living foliage										
CON-V-3	GFDUH00Q7	Sept. 2014	Fagus sylvatica - leaves	0.71695	0.00005	28	15	0.48	12	3.7
MIT-V-9	GFDUH006W	Sept. 2014	Fagus sylvatica - leaves	0.71473	0.00005	13	9.0	0.29	15	4.4
MIT-V-10	GFDUH006R	Sept. 2014	Fagus sylvatica - leaves	0.71576	0.00005	n.d.	n.d.	n.d.	n.d.	n.d.
CON-V-4	GFDUH00Q8	Sept. 2014	Picea abies - needles	0.71781	0.00005	14	8.1	0.26	12	3.7
CON-V-5	GFDUH00Q9	Sept. 2014	Picea abies - needles	0.71788	0.00005	n.d.	n.d.	n.d.	n.d.	n.d.
MIT-V 3	GFDUH006Q	July 2014	Picea abies - needles	0.71448	0.00013	n.d.	n.d.	n.d.	n.d.	n.d.
MIT-V-11	GFDUH006S	Sept. 2014	Picea abies - needles	0.71424	0.00004	7.8	8.6	0.28	24	7.1
MIT-V-12	GFDUH006T	Sept. 2014	Picea abies - needles	0.71513	0.00005	n.d.	n.d.	n.d.	n.d.	n.d.
living wood										
CON-V 1	GFDUH00NE	July 2014	Fagus sylvatica - heartwood	0.71808	0.00011	n.d.	n.d.	n.d.	n.d.	n.d.
CON-V-10	GFDUH00T9	Sept. 2014	Fagus sylvatica - heartwood	0.71791	0.00004	n.d.	n.d.	n.d.	n.d.	n.d.
MIT-V-17	GFDUH00TB	Sept. 2014	Fagus sylvatica - heartwood	0.71529	0.00005	n.d.	n.d.	n.d.	n.d.	n.d.
MIT-V-5,6	GFDUH00TJ	July 2014	Fagus sylvatica - heartwood	0.71633	0.00011	n.d.	n.d.	n.d.	n.d.	n.d.
CON-V-10	GFDUH00TA	Sept. 2014	Fagus sylvatica - sapwood	0.71725	0.00004	n.d.	n.d.	n.d.	n.d.	n.d.
MIT-V 5	GFDUH00T3	July 2014	Fagus sylvatica - sapwood	0.71604	0.00012	n.d.	n.d.	n.d.	n.d.	n.d.
MIT-V-17	GFDUH00T2	Sept. 2014	Fagus sylvatica - sapwood	0.71505	0.00004	n.d.	n.d.	n.d.	n.d.	n.d.
MIT-V 6	GFDUH00T4	July 2014	Fagus sylvatica - sapwood	0.71499	0.00010	n.d.	n.d.	n.d.	n.d.	n.d.
CON-V 6,7	GFDUH00TG	Sept. 2014	Fagus sylvatica - bulk wood	n.d.	n.d.	2.4	0.95	0.03	8.6	2.6
MIT-V-14,15,16	GFDUH00TL	Sept. 2014	Fagus sylvatica - bulk wood	n.d.	n.d.	1.2	1.1	0.04	20	6.2
CON-V 2	GFDUH00NF	July 2014	Picea abies - heartwood	0.71860	0.00011	n.d.	n.d.	n.d.	n.d.	n.d.
CON-V-18	GFDUH00TD	Sept. 2014	Picea abies - heartwood	0.71863	0.00004	n.d.	n.d.	n.d.	n.d.	n.d.
MIT-V 7	GFDUH00TF	July 2014	Picea abies - heartwood	0.71563	0.00011	n.d.	n.d.	n.d.	n.d.	n.d.
MIT-V-24	GFDUH00T7	Sept. 2014	Picea abies - heartwood	0.71622	0.00004	n.d.	n.d.	n.d.	n.d.	n.d.
MIT-V 8	GFDUH00T5	July 2014	Picea abies - heartwood	0.71573	0.00009	n.d.	n.d.	n.d.	n.d.	n.d.
CON-V-18	GFDUH00TE	Sept. 2014	Picea abies - sapwood	0.71849	0.00004	n.d.	n.d.	n.d.	n.d.	n.d.
MIT-V 7	GFDUH00TC	July 2014	Picea abies - sapwood	0.71510	0.00009	n.d.	n.d.	n.d.	n.d.	n.d.
MIT-V-24	GFDUH00T8	Sept. 2014	Picea abies - sapwood	0.71541	0.00004	n.d.	n.d.	n.d.	n.d.	n.d.
MIT-V 8	GFDUH00T6	July 2014	Picea abies - sapwood	0.71506	0.00011	n.d.	n.d.	n.d.	n.d.	n.d.
CON-V-14.15	GFDUH00TH	Sept. 2014	Picea abies - bulk wood	n.d.	n.d.	0.48	0.12	0.01	5.3	1.6
MIT-V-23.25	GFDUH00TK	Sept. 2014	Picea abies - bulk wood	n.d.	n.d.	0.51	0.20	0.01	8.4	2.6

continued next page …

Supplementary Table 3-3 continued - Isotopic composition of plant samples at site CON and site MIT

sample ID	IGSN†	sampling date (month year)	brief sample description	MC-ICP-MS analyses (^{87}Sr / ^{86}Sr)	SD	Q-ICP-MS analyses ^{9}Be (ng/g)	AMS analyses ^{10}Be (10^6 at/g)	uncertainty (10^6 at/g)	(^{10}Be / ^{9}Be) (10^{-9})	uncertainty (10^{-9})
organic layer on forest floor										
CON-QP1-1	GFDUH00TN	May 2014	forest floor - L horizon	0.71792	0.00004	n.d.	n.d.	n.d.	n.d.	n.d.
CON-QP1-2	GFDUH00TS	May 2014	forest floor - Of horizon	0.71792	0.00003	n.d.	n.d.	n.d.	n.d.	n.d.
CON-QP1-3	GFDUH00TP	May 2014	forest floor - Oh horizon	0.72371	0.00002	n.d.	n.d.	n.d.	n.d.	n.d.
MIT-QP-1	GFDUH00TQ	Febr. 2014	forest floor - L horizon	0.71580	0.00001	n.d.	n.d.	n.d.	n.d.	n.d.
MIT-QP-2	GFDUH00TR	Febr. 2014	forest floor - Of horizon	0.71678	0.00002	n.d.	n.d.	n.d.	n.d.	n.d.
MIT-QP-3	GFDUH00TM	Febr. 2014	forest floor - Oh horizon	0.71802	0.00001	n.d.	n.d.	n.d.	n.d.	n.d.
international reference materials for concentration data quality control										
SRM 1515 Apple leaves (a)				0.71400	0.00010	n.d.	n.d.	n.d.	n.d.	n.d.
SRM 1515 Apple leaves (a)*				0.71398	0.00006	n.d.	n.d.	n.d.	n.d.	n.d.
SRM 1515 Apple leaves (b)**				0.71403	0.00005	24	2.6	0.09	1.1	0.62
SRM 1515 Apple leaves (c)				0.71401	0.00003	n.d.	n.d.	n.d.	n.d.	n.d.
SRM 1515 Apple leaves (d)**				n.d.	n.d.	28	2.6	0.09	1.1	0.62
SRM 1515 Apple leaves (e)				n.d.	n.d.	19	n.d.	n.d.	n.d.	n.d.
SRM 1515 Apple leaves (f)				n.d.	n.d.	24	n.d.	n.d.	n.d.	n.d.
SRM 1515 Apple leaves mean				**0.71400**	**0.00002**	**24**				
SRM 1515 Apple leaves SD						*3.7*				
SRM 1515 Apple leaves RSD (%)						*16%*				

AMS analyses are performed at the University of Cologne - Centre for Accelerator Mass Spectrometry (AMS).
n.d. = not determined
* replicate analyses
** For ^{10}Be analyses aliquots from two different digestion batches d and f were combined.
† IGSN (International Geo Sample Number). Metadata of samples are available under: www.igsn.org by adding the IGSN after igsn.org, e.g. igsn.org/GFDUH00LT

Supplementary Table 3-4 Atmospheric dry deposition fluxes and phosphorus concentration of UCC

Dep_{dry} min.	Dep_{dry} max.	UCC^P	Dep^P_{dry} min.	Dep^P_{dry} max.
(mg m^{-2} yr^{-1})	(mg m^{-2} yr^{-1})	(µg/g)	(mg m^{-2} yr^{-1})	(mg m^{-2} yr^{-1})
2000	5000	700	1.4	3.5

UCC: Upper Continental Crust; UCC data from Taylor and McLennan (1995)
Dep_{dry}: atmospheric dry deposition; Dep_{dry}; data from Jickells et al. (2005)
min: minimum estimate, max: maximum estimate

Supplementary Table 3-5 Isotopic composition of leachates from sequential extractions of soil and saprolite at site CON and site MIT

			MC-ICP-MS analyses			
sample ID	**IGSN†**	**brief sample description**	**(^{87}Sr / ^{86}Sr)**	**SD**	**(^{87}Sr / ^{86}Sr)**	**SD**
CON depth profile			***water soluble (mQ-H_2O)***		***exchangeable (NH_4OAc)***	
CON 14	GFDUH00J0	soil, Ah horizon	0.71938	0.00007	0.71924	0.00004
CON 13	GFDUH00J1	soil, Ah + Bw horizon	0.71905	0.00005	0.71895	0.00005
CON 12	GFDUH00J2	soil, Bw I horizon	0.71947	0.00006	0.71932	0.00005
CON 11	GFDUH00J3	soil, Bw I horizon	0.71877	0.00007	0.71883	0.00005
CON 10	GFDUH00J4	soil, Bw I horizon	0.71878	0.00006	0.71879	0.00005
CON 9	GFDUH00J5	soil, Bw I horizon	0.71971	0.00006	0.71935	0.00008
CON 8	GFDUH00J6	soil, Bw I horizon	0.72078	0.00006	0.72064	0.00005
CON 7	GFDUH00J7	soil, Bw I horizon	0.72119	0.00006	0.72093	0.00004
CON 6	GFDUH00J8	soil, Bw II horizon	0.71982	0.00006	0.71980	0.00005
CON 5	GFDUH00J9	soil, Bw II horizon	0.71924	0.00007	0.71927	0.00005
CON 4	GFDUH00JA	soil, Bw II horizon	0.71896	0.00006	0.71905	0.00005
CON 3	GFDUH00JB	saprolite, Cw horizon	0.71789	0.00006	0.71795	0.00004
CON 2	GFDUH00JC	saprolite, Cw horizon	0.71742	0.00006	0.71726	0.00005
CON 1	GFDUH00JD	saprolite, Cw horizon	0.71721	0.00006	0.71697	0.00004
CON 19	GFDUH00JJ	saprolite, Cw horizon	0.71656	0.00006	0.71653	0.00004
CON 20	GFDUH00JK	saprolite, Cw horizon	0.71638	0.00006	0.71633	0.00004
CON 21	GFDUH00HZ	saprolite, Cw horizon	0.71656	0.00005	0.71639	0.00007
CON 22	GFDUH00JL	saprolite, Cw horizon	0.71790	0.00005	0.71650	0.00005
CON 23	GFDUH00JM	saprolite, Cw horizon	0.71668	0.00005	0.71604	0.00005
CON 24	GFDUH00JN	saprolite, Cw horizon	0.71648	0.00006	0.71597	0.00005
MIT depth profile						
MIT 14	GFDUH002Z	soil, Bw horizon	0.71556	0.00005	0.71557	0.00005
MIT 13	GFDUH0030	soil, Bw horizon	0.71698	0.00005	0.71765	0.00004
MIT 12	GFDUH000K	soil, Bw horizon	0.71783	0.00005	0.71798	0.00004
MIT 11	GFDUH0000	soil, Bw horizon	0.71926	0.00005	0.71955	0.00004
MIT 10	GFDUH002L	soil, Bw horizon	0.71741	0.00005	0.71777	0.00004
MIT 9	GFDUH0002	soil, Bw horizon	0.71963	0.00005	0.71094	0.00004
MIT 8	GFDUH002N	saprolite, Cw horizon	0.71916	0.00006	0.72002	0.00004
MIT 7	GFDUH0004	saprolite, Cw horizon	0.71878	0.00007	0.71998	0.00007
MIT 6	GFDUH0005	saprolite, Cw horizon	0.71762	0.00006	0.71813	0.00004
MIT 5	GFDUH003K	saprolite, Cw horizon	0.71664	0.00006	0.71725	0.00005
MIT 4	GFDUH003L	saprolite, Cw horizon	0.71656	0.00006	0.71706	0.00003
MIT 3	GFDUH003M	saprolite, Cw horizon	0.71927	0.00006	0.72000	0.00004
MIT 2	GFDUH0031	saprolite, Cw horizon	0.72237	0.00006	0.72382	0.00005
MIT 1	GFDUH0032	saprolite, Cw horizon	0.72440	0.00005	0.72430	0.00005
MIT 19	GFDUH008R	saprolite, Cw horizon	0.71509	0.00009	0.71507	0.00007
MIT 20	GFDUH008S	saprolite, Cw horizon	0.71447	0.00009	0.71433	0.00009
MIT 21	GFDUH008T	saprolite, Cw horizon	0.71518	0.00009	0.71513	0.00009
MIT 22	GFDUH008U	saprolite, Cw horizon	0.71472	0.00011	0.71480	0.00006
MIT 23	GFDUH008V	saprolite, Cw horizon	0.71456	0.00009	0.71457	0.00006
MIT 24	GFDUH008W	saprolite, Cw horizon	0.71442	0.00029	0.71444	0.00005
MIT 25	GFDUH008X	saprolite, Cw horizon	n.d.	n.d.	0.71576	0.00004
MIT 26	GFDUH008K	saprolite, Cw horizon	0.71550	0.00038	0.71557	0.00005
MIT 27	GFDUH008L	saprolite, Cw horizon	0.71536	0.00007	0.71532	0.00006
MIT 28	GFDUH008Y	saprolite, Cw horizon	0.71539	0.00009	0.71539	0.00005
MIT 29	GFDUH008Z	saprolite, Cw horizon	0.71772	0.00007	0.71711	0.00005
International reference materials						
SRM 2709a San Joaquin Soil			0.70776	0.00008	0.70774	0.00005
TILL-1 (CCRMP)			0.71033	0.00008	0.71020	0.00004

n.d = not determined, mQ-H_2O = deionised water (Milli-Q water, 18 MΩ).
† IGSN (International Geo Sample Number). Metadata of samples are available under: www.igsn.org by adding the IGSN after igsn.org, e.g. igsn.org/GFDUH00LT

Supplementary Table 3-6 Beryllium concentration and isotopic ratio of leachates from sequential extractions of soil and saprolite at site CON and site MIT

					ICP-OES	AMS analyses			
sample ID	**IGSN†**	**brief sample description**	**extractant**	**mean depth**	**Be**	**$^{10}Be_{meteoric}$**	**uncertainty**	**(^{10}Be / ^{9}Be)**	**uncertainty**
				(m)	(µg/g)	(10^6 at/g)	(10^6 at/g)	(10^{-9})	(10^{-9})
CON depth profile of amorphous oxide fractions									
CON 14	GFDUH00KX	soil, Ah horizon	0.5M HCl	0.2	0.47	236	7.6	13	1.6
CON 12	GFDUH00KZ	soil, Bw I horizon	0.5M HCl	0.6	0.61	351	11	15	1.8
CON 10	GFDUH00L1	soil, Bw I horizon	0.5M HCl	1.0	0.83	481	15	15	1.8
CON 8	GFDUH00L3	soil, Bw I horizon	0.5M HCl	1.4	0.47	216	7.0	12	1.5
CON 5	GFDUH00L6	soil, Bw II horizon	0.5M HCl	2.0	0.35	86	2.8	6.2	0.76
CON 2	GFDUH00L9	saprolite, Cw horizon	0.5M HCl	2.6	0.36	57	1.9	4.0	0.49
CON 21	GFDUH00LH	saprolite, Cw horizon	0.5M HCl	4.4	0.38	53	1.8	3.5	0.43
CON 24	GFDUH00LL	saprolite, Cw horizon	0.5M HCl	6.5	0.37	55	1.8	3.7	0.45
MIT depth profile of amorphous oxide fractions									
MIT 14	GFDUH003R	soil, Bw horizon	0.5M HCl	0.2	0.05	36	1.2	19	2.4
MIT 12	GFDUH003S	soil, Bw horizon	0.5M HCl	0.6	0.42	459	15	28	3.5
MIT 10	GFDUH003T	soil, Bw horizon	0.5M HCl	1.0	0.39	339	11	22	2.8
MIT 6	GFDUH0040	saprolite, Cw horizon	0.5M HCl	1.8	0.38	138	4.5	9.4	1.2
MIT 1	GFDUH0043	saprolite, Cw horizon	0.5M HCl	2.8	0.81	95	3.1	3.0	0.38
MIT 23	GFDUH009L	saprolite, Cw horizon	0.5M HCl	5.3	1.17	47	1.6	1.0	0.13
MIT 29	GFDUH009R	saprolite, Cw horizon	0.5M HCl	16.3	0.15	0.13	0.03	0.02	0.01
international reference material used to determine the reproducibility of the method									
SRM 2709a San Joaquin Soil (a)*			0.5M HCl		0.32	9.5	0.39	0.61	0.03
SRM 2709a San Joaquin Soil (b)*			0.5M HCl		0.31	10	0.37	0.67	0.05
SRM 2709a San Joaquin Soil mean*					**0.32**	**10**	**0.38**	**0.64**	**0.04**
SRM 2709a San Joaquin Soil SD					*0.01*	*0.59*	-	*0.04*	-
SRM 2709a San Joaquin Soil RSD (%)					*2%*	*6%*	-	*7%*	-
international reference material for concentration data quality control									
RGM-1 Rhyolite (USGS) (a)					2.3				
RGM-1 Rhyolite (USGS) (a)**					2.2				
RGM-1 Rhyolite (USGS) (a)**					2.3				
RGM-1 Rhyolite (USGS) (a)**					2.3				
RGM-1 Rhyolite (USGS) (a)**					2.2				
RGM-1 Rhyolite (USGS) (a)**					2.4				
RGM-1 Rhyolite (USGS) (a)**					2.4				
RGM-1 Rhyolite (USGS) mean					**2.3**				
RGM-1 Rhyolite (USGS) SD					*0.07*				
RGM-1 Rhyolite (USGS) RSD (%)					*3%*				
RGM-1 Rhyolite (USGS) certified value					2.4				
RGM-1 Rhyolite (USGS) certified absolute uncertainty					0.20				
relative uncertainty on the amorphous oxide (%)					**-4%**				
GA Granite (CNRS) (a)					3.4				
GA Granite (CNRS) (a)**					3.5				
GA Granite (CNRS) mean					**3.4**				
GA Granite (CNRS) SD					*0.05*				
GA Granite (CNRS) RSD (%)					*1%*				
GA Granite (CNRS) certified value					3.6				
GA Granite (CNRS) certified absolute uncertainty					0.30				
relative uncertainty on the amorphous oxides (%)					**-5%**				

* The reported ^{10}Be concentrations and the $^{10}Be/^{9}Be$ ratios refer to a mixed sample comprising the amorphous oxide and the crystalline oxide leachates. The crystalline oxides were extracted with 1M hydroxylamine-hydrochloride (NH_2OH*HCl) following the method described elsewhere (Wittmann et al. 2012).
** Repeat analyses of reference material in different sample batches. Uncertainties on amorphous oxide concentration data are estimated to be ±5% relative for Be based on accuracy of repeat analyses of reference materials.
(a), (b) = letters indicate different sample digestions
† IGSN (International Geo Sample Number). Metadata of samples are available under: www.igsn.org by adding the IGSN after igsn.org, e.g. igsn.org/GFDUH00LT

4 Quantifying nutrient uptake as driver of rock weathering in forest ecosystems by magnesium stable isotopes

Abstract

Plants and soil microbiota play an active role in rock weathering and potentially couple weathering at depth with erosion at the soil surface. The nature of this coupling is still unresolved because we lacked means to quantify the passage of chemical elements from rock through higher plants. In a temperate forested landscape characterised by relatively fast (~220 t km^{-2} yr^{-1}) denudation and a kinetically limited weathering regime of the Southern Sierra Critical Zone Observatory (SSCZO), California, we measured magnesium (Mg) stable isotopes that are sensitive indicators of Mg utilisation by biota. We find that Mg is highly bio-utilised: 50-100 % of the Mg released by chemical weathering is taken up by forest trees. To estimate the tree uptake of other bio-utilised elements (K, Ca, P and Si) we compared the dissolved fluxes of these elements and Mg in rivers with their solubilisation fluxes from rock (rock dissolution flux minus secondary mineral formation flux). We find a deficit in the dissolved fluxes throughout, which we attribute to the nutrient uptake by forest trees. Therefore both the Mg isotopes and the flux comparison suggest that a substantial part of the major element weathering flux is consumed by the tree biomass. The enrichment of ^{26}Mg over ^{24}Mg in tree trunks relative to leaves suggests that tree trunks account for a substantial fraction of the net uptake of Mg. This isotopic and elemental compartment separation is prevented from obliteration (which would occur by Mg redissolution) by two potential effects. Either the mineral nutrients accumulate today in regrowing forest biomass after clear cutting, or they are exported in litter and coarse woody debris (CWD) such that they remain in “solid” biomass. Over pre-forest management weathering timescales, this removal flux might have been in operation in the form of natural erosion of CWD. Regardless of the removal mechanism, our approach provides entirely novel means towards the direct quantification of biogenic uptake following weathering. We find that Mg and other nutrients and the plant-beneficial element Si ("bio-elements") are taken up by trees at up to 6 m depth, and surface recycling of all bio-elements but P is minimal. Thus, in the watersheds of the SSCZO, the coupling between erosion and weathering might be established by bio-elements that are taken up by trees, are not recycled and are missing in the dissolved river flux due to erosion as CWD and as leaf-derived bio-opal for Si. We suggest that the partitioning of a biogenic weathering flux into eroded plant debris might represent a significant global contribution to element export after weathering in eroding mountain catchments that are characterised by a continuous supply of fresh mineral nutrients.

This chapter is published in:

Biogeosciences Vol. 14, Pages 3111-3128

David Uhlig, Jan A. Schuessler, Julien Bouchez, Jean L. Dixon, Friedhelm von Blanckenburg (2017); https://doi.org/10.5194/bg-14-3111-2017

4.1 Introduction

In continuously eroding landscapes, the mass loss of particles by erosion and solutes by drainage needs to be balanced over a ~ kilo year timescale by the conversion of rock into regolith, where we define regolith as the entire weathering zone above bedrock, including topsoil. The advance of the weathering front at depth is thus coupled to surface denudation (Brantley and Lebedeva 2011). It has been hypothesised that biotic processes contribute towards this coupling (Brantley et al. 2011). If the nutrient demand of plants and soil microbes is linked to the advance of the weathering front, investigating the dependence of nutrient fluxes on the weathering regime allows for a test of this "biogenic weathering" hypothesis.

The way weathering systems operate can be characterised by two endmembers, each associated with a specific pattern of nutrient dynamics. In the supply-limited regime, the transfer of nutrient-bearing mineral grains from rock into the regolith is so slow that their complete dissolution makes the mineral nutrient status of the regolith very low, such that plants and soil microbes are rather nourished by recycling of nutrients extracted from plant litter (Vitousek and Farrington 1997; Lang et al. 2016) and by atmospheric inputs (Vitousek and Farrington 1997). In the kinetically limited regime, erosion rejuvenates the regolith (Porder et al. 2007), such that the rate of supply outpaces the weathering of minerals (West et al. 2005). In the kinetically limited system, the supply of solutes by chemical weathering into soil solutions ensures that nutrients are readily available for plant uptake from regolith water, and a fraction of these nutrients is lost after bio-utilisation in plant debris such as leaf litter and coarse woody debris (CWD). The plant litter can also be "re-mineralised" (meaning oxidation of plant litter), so that nutrients are lost by drainage in the dissolved form. If erosion of plant debris outpaces nutrient leaching, nutrients are eroded in leaf litter by erosion or stochastically as woody matter in landslides. To replace either loss, nutrients should be uplifted from subsoil layers (Jobbágy and Jackson 2001; Bullen and Chadwick 2016). To facilitate the uplift from subsoil in the kinetically limited regime, plants and soil microbes could stimulate chemical weathering rates by decreasing the rhizospheric pH through respiration and excretion of weathering agents (Brantley et al. 2011). Moreover, the symbiosis of roots with mycorrhiza fungi (Landeweert et al. 2001) could enable plants to directly assimilate nutrients from primary minerals (Jongmans et al. 1997). Here we explore this set of hypotheses in a kinetically limited mountain setting using isotopic and geochemical techniques.

The stable isotopes of magnesium (Mg) – a macronutrient for plants (Marschner 2011) and a major constituent of the bulk silicate Earth – are suited to trace these cycles. Unless the formation of secondary minerals is significant (Wimpenny et al. 2014), the main shift affecting the $^{26}Mg/^{24}Mg$ ratio in weathering systems is the isotopic fractionation towards high ratios during nutrient uptake by plants (Black et al. 2008; Bolou-Bi et al. 2012; Mavromatis et al. 2014), such that the residual dissolved Mg is shifted towards the complementary low ratio. These two isotopically distinct compartments will

remain separated if a fraction of the Mg accumulates in wood of a regrowing forest after clear cutting or if a fraction of the Mg is eroded after utilisation and is not released back into solution. In that case the isotope ratio serves as a proxy for the catchment-wide net nutrient uptake flux, where “net” excludes dissolution from biomass and recycling. Here we use an isotope mass balance model (Bouchez et al. 2013) to quantify the relative fluxes of Mg transfer in the ecosystem after Mg release by rock weathering: uptake into plants, export as solute or erosion in particles including minerals and a substantial CWD fraction at three forested headwater catchments.

4.2 Methods

4.2.1 Study site

Our study sites comprise three catchments at Providence Creek, Sierra Nevada, USA, and are part of two monitoring programs: Kings River Experimental Watersheds (KREW) and Southern Sierra Critical Zone Observatory (SSCZO). The extensive monitoring dataset is highly suited for nutrient cycling studies in forest ecosystems and provides evidence that rock phosphorus (P) might be growth limiting (Hahm et al. 2014). Our study sites are underlain by granodiorite bedrock (Bateman and Wones 1972) and mantled by weakly developed soils comprising entisols and inceptisols (Bales et al. 2011). The main vegetation cover is Sierran mixed conifer comprising *Pinus ponderosa*, *Pinus lambertiana, Abies concolor* and *Libocedrus decurrens* (McCorkle et al. 2016).

Soil water and stream water pH ranges from 5.5 to 7. We estimate the soil production rate from the total denudation rate from cosmogenic nuclides, which is ~220 t km^{-2} yr^{-1} (Dixon et al. 2009). This weathering regime is kinetically limited and soils are only partially depleted in mineral nutrients. Concerning dust inputs, Aciego et al. (2017) recently suggested that P supply by dust deposition outpaces local bedrock-derived P supply at the SSCZO for ecosystems developed over P-poor bedrock. However, estimates of the influence of dust inputs on nutrient dynamics are minor compared to the total denudation rate at our sites, with inputs of 3 to 36 t km^{-2} yr^{-1} (Aciego et al. 2017). Importantly, the total denudation rate of 220 t km^{-2} yr^{-1} (Dixon et al. 2009) measured at this site is higher than the range of denudation rates of 103 - 175 t km^{-2} yr^{-1} used in Aciego et al. (2017), and the P bedrock concentrations are higher in the Providence catchments studied here. We excluded the catchment comprising P-poor bedrock at site D102 ("Duff Creek"). The ratio of elemental dust deposition to the local, bedrock-derived elemental supply flux (referred to as RP^X in the following) amounts to less than 4 % for K, Ca and Mg and to 5.3 % for P at our sites and agrees with data shown in Aciego et al. (2017) for the P-rich bedrock. Therefore, the atmospheric supply flux of mineral nutrients can be considered to be insignificant relative to the local long-term supply fluxes from weathering.

4.2.2 Analytical methods

The chemical composition of soil, saprolite and rock samples were analysed by X-ray fluorescence spectrometry (XRF, Panalytical Axios Advanced) on fused tablets at GFZ Potsdam or by Acme Labs, Canada, with uncertainties better than 10 % relative. Additional concentration data were compiled from Hahm et al. (2014) and Riebe and Granger (2013). Element concentrations in plant material were analysed by an inductively coupled plasma optical emission spectrometer (ICP-OES, Varian 720ES) with uncertainties better than 15 %, after complete dissolution in HNO_3/H_2O_2 in PFA vials on a hotplate or using a microwave digestion system as successfully applied in previous Mg isotope studies (e.g. Bolou-Bi et al. (2012)). Dissolved element concentrations in water samples were analysed by ICP-OES following the procedure described in (Schuessler et al. 2016), inductively coupled plasma quadrupole mass spectrometry (Q-ICP-MS, Thermo iCAP-Q) and ion chromatography (Thermo Dionex DX-120) with uncertainties better than 10 %, respectively. All data of samples and reference materials (for assessment of analytical uncertainties) are reported in Supplementary Table 4-1, Supplementary Table 4-2, Supplementary Table 4-3a and Supplementary Table 4-3c.

4.2.3 Mg isotope analyses by MC-ICP-MS

Mg stable isotope analyses have been performed at GFZ Potsdam, Helmholtz Laboratory for the Geochemistry of the Earth Surface (HELGES). Samples and reference materials were digested in PFA vials using ultra-pure acid mixtures (HF, HCl, HNO_3, H_2O_2). The exchangeable Mg fraction of soil and saprolite samples was obtained by a 1 M NH_4OAc extraction (Arunachalam et al. 1996). This procedure was specifically tested for Mg isotope measurements (Bolou-Bi et al. 2012). After extraction, the residual solids were analysed after HF/HNO_3 total digestion. Before isotope analysis, Mg was separated from other matrix elements by column chromatography (AG50W-X12 resin) following the procedure described in (Pogge von Strandmann et al. 2011). Matrix elements were eluted with 1 M HNO_3, and then Mg was collected by elution with 2 M HNO_3. Purity of the Mg solutions as well as Mg yields were verified by analyses of final Mg-containing solutions using ICP-OES or Q-ICP-MS. Mg isotope ratios were measured with a multi collector inductively coupled plasma mass spectrometer (MC-ICP-MS, Thermo Neptune). All sample solutions were diluted in 0.3 M HNO_3, where the sample Mg concentration was closely matched to those of the bracketing standard DSM-3. Results are expressed as the ‰ difference of the Mg isotope ratio of the sample relative to the DSM-3 isotope reference material (Galy et al. 2001) using the delta notation: $\delta^{26}Mg = [(^{26}Mg/^{24}Mg)_{sample}/(^{26}Mg/^{24}Mg)_{DSM3} - 1] \times 1000$. The uncertainty is estimated to be ±0.10 ‰ (2SD) for $\delta^{26}Mg$, respectively, based on repeat measurements on reference materials (Supplementary Table 4-1, Supplementary Table 4-2, Supplementary Table 4-3c).

4.2.4 Mg isotope analyses by fsLA-MC-ICP-MS

The micro-scale Mg isotope composition of individual minerals (amphibole and biotite) was determined on a thin section of sample BP-0c (from the bedrock-saprolite interface) by UV femtosecond laser ablation coupled to a Thermo Neptune MC-ICP-MS (fsLA-MC-ICP-MS, *Fem2*) at GFZ Potsdam. Instrumentation, data acquisition and evaluation procedures are described in detail in Schuessler and von Blanckenburg (2014). Laser ablation was performed on individual mineral grains with a spatial resolution of less than 200 x 200 µm surface area with less than 10 µm crater depth. The laser beam with a diameter of about 25 µm was scanned across the mineral surface to adapt to the irregular shape of the grains and cracks with repetition rates between 13 to 20 Hz. The high mass resolution mode of the MC-ICP-MS was used for Mg isotope ratio measurements. With high-mass resolution, isobaric interferences ($^{52}Cr^{2+}$ on $^{26}Mg^{+}$, $^{50}Ti^{2+}$ and $^{50}Cr^{2+}$ on $^{25}Mg^{+}$, or $^{48}Ca^{2+}$ and $^{48}Ti^{2+}$ on $^{24}Mg^{+}$) can be resolved from Mg isotopes (Oeser et al. 2014; Dai et al. 2016). Mass bias correction was performed using the komatiite glass GOR132-G as bracketing standard. Using a $\delta^{26}Mg$ value for GOR132-G of -0.17 ‰ relative to DSM-3 (Oeser et al. 2014), we converted results to δ-values relative to DSM-3. Based on our current experience, we conservatively estimate the uncertainty of the fsLA-MC-ICP-MS method for Mg isotope ratios to be better than ±0.25 ‰ (2SD) for $\delta^{26}Mg$. Repeat measurements on reference material BHVO-2G (basaltic glass) (average $\delta^{26}Mg$ = −0.07 ± 0.18 ‰, 2SD, n=18) agree within uncertainties to published values (Figure 4-1) for this reference material (−0.20 ± 0.07 ‰; Dai et al. 2016). Results of biotite and amphibole analyses are presented in Figure 4-1. Photomicrographs (Figure 4-2) show representative analysis locations in amphibole and biotite before and after laser ablation.

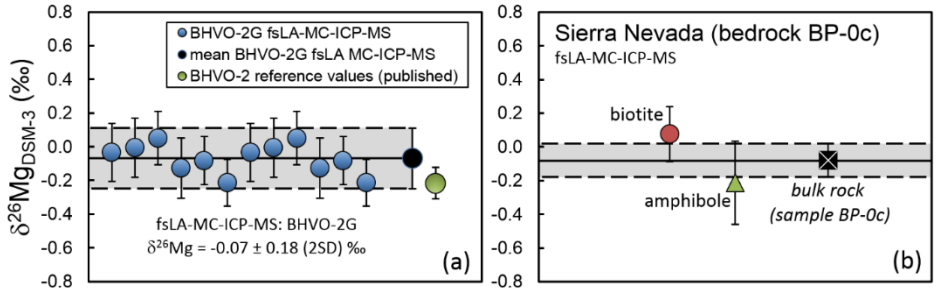

Figure 4-1 Mg isotopic composition measured by fsLA-MC-ICP-MS. (a): Repeat measurements of BHVO-2G. Solid black circle and solid line represent the mean value of all BHVO-2G measurements with the 2SD range represented by dashed lines. Published literature data (Dai et al. 2016) is shown for comparison. (b): Biotite and amphibole of sample BP-0c measured by fsLA-MC-ICP-MS. Bulk rock was measured by solution MC-ICP-MS.

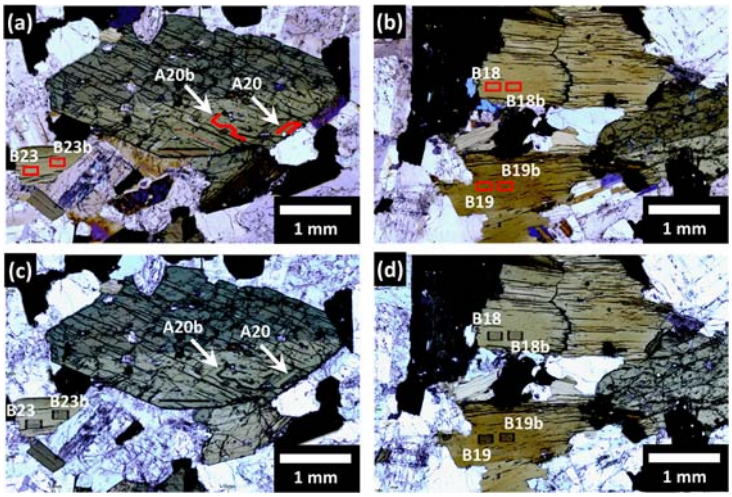

Figure 4-2 Photomicrographs before and after fsLA-MC-ICP-MS. Red rectangles and lines indicate laser ablation locations. Amphibole before (a) and after (c) fsLA-MC-ICP-MS. Biotite before (b) and after (d) fsLA-MC-ICP-MS

4.3 Results

4.3.1 Mg isotopic composition of ecosystem compartments

The Mg isotopic composition (Figure 4-3, Supplementary Table 4-1, Supplementary Table 4-2, Supplementary Table 4-3c) of mean bulk rock ($\delta^{26}Mg_{rock}$ = -0.22 ‰ ± 0.10 ‰, 2SD) is identical within uncertainties to mean bulk regolith ($\delta^{26}Mg_{reg}$ = -0.15 ‰ ± 0.13 ‰, 2SD) and mean suspended sediment ($\delta^{26}Mg_{susp.sed}$ = -0.30 ‰ ± 0.16 ‰, 2SD). Results of analyses on biotite and amphibole on a thin section of rock sample BP-0c indicate that Mg-bearing minerals in the bedrock are not distinguishable in $\delta^{26}Mg$ within analytical uncertainties and are also identical to the bulk bedrock value of sample BP-0c (Figure 4-1). $\delta^{26}Mg$ in wood from growing trees ranges from -0.21 to +0.16 ‰, and $\delta^{26}Mg$ in growing foliage is lower than wood, i.e. -0.72 to -0.10 ‰. $\delta^{26}Mg$ of foliage, twigs, bark and needles sampled from the forest floor and from the gauged creek sediment pond is within the range found in living foliage (Figure 4-3). The intra-plant differences are consistent with previous studies that have shown that during translocation ^{24}Mg is preferred by the foliage whereas ^{26}Mg is preferred by wood (Black et al. 2008; Bolou-Bi et al. 2012). Despite the low $\delta^{26}Mg$ in foliage, bulk tree ($\delta^{26}Mg_{tree} \approx$ -0.07 ‰; see mass balance calculation in Section 4.7.1) is not distinguishable from bulk soil and rock. Only Mg in creek water ($\delta^{26}Mg_{diss}$ = -0.76 ‰ ± 0.11 ‰, 2SD) and exchangeable Mg from soil and saprolite ($\delta^{26}Mg_{exch}$ = -0.68 ‰ ± 0.36‰, 2SD) differ from the solid compartments. $\delta^{26}Mg_{diss}$ is remarkably constant throughout one hydrological water year and is in the range of global rivers draining silicate catchments (Tipper et al. 2012, and references therein). Results of element concentration measurements in rock, saprolite, soil, vegetation, water and sediment samples are reported together with field measurement data (pH, temperature, conductivity, discharge, alkalinity) in Supplementary Table 4-1, Supplementary Table 4-2, Supplementary Table 4-3a and Supplementary Table 4-3c.

4.4 Discussion

4.4.1 Mg isotope fractionation by clay formation

Neoformation of Mg clays is a mechanism that preferentially removes ^{26}Mg from soil solution and enriches this heavy isotope in Mg clays such as smectite, illite or vermiculite (Wimpenny et al. 2014; Ryu et al. 2016).Clay formation is thus a potential cause for the low $\delta^{26}Mg_{diss}$ observed in the Providence Creek streams. Three independent lines of evidence all suggest that this effect is insignificant at our site. First, Mg clay abundances are beneath the 5 % detection limit of X-ray analysis. Second, their absence was confirmed by thermodynamic modelling (PhreeqC). Third, we use an isotope mass balance based on bulk soil Mg isotope composition to evaluate whether the low $\delta^{26}Mg$ of dissolved Mg could nevertheless be due to preferential incorporation of ^{26}Mg into small amounts of Mg clay. In an isotope mass balance (Equation 4-1) we assign $\delta^{26}Mg_{bulk\ soil}$ the value of the isotopically heaviest soil sample (-0.05 ‰, see Supplementary Table 4-3c), which has the potential to be most affected by Mg clay formation; for primary minerals $\delta^{26}Mg_{prim}$ we use the rock mean $\delta^{26}Mg_{rock}$ (-0.22 ‰, Supplementary Table 4-3c).

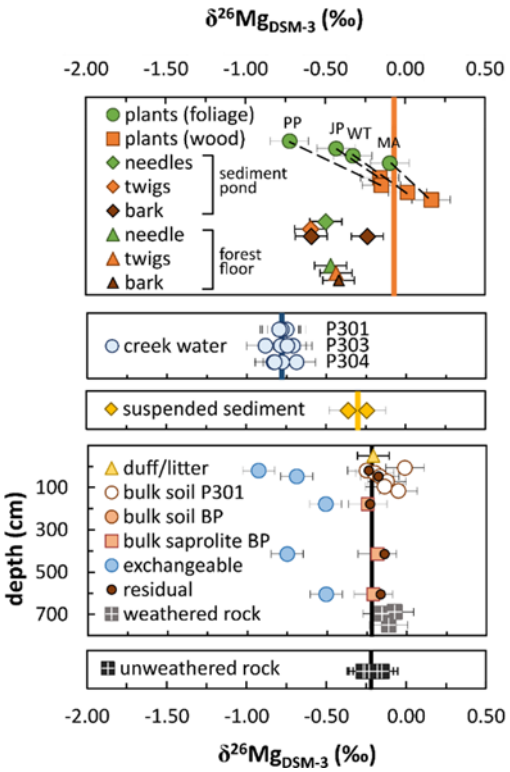

Figure 4-3 Magnesium isotopic composition of the compartments at Providence Creek, Southern Sierra Nevada, USA. Vertical lines represent mean $\delta^{26}Mg$ values of bulk unweathered rock (black), bulk suspended sediment (yellow), bulk tree (orange; mass balance see Section 4.7.1), and creek water (blue). The diagonal dashed lines connect woody with non-woody plant material of the same sample. Exchangeable and residual refer to sequentially extracted soil phases. P301, P303 and P304 refer to headwater catchments at Providence Creek. BP refers to the soil-saprolite profile (Balsam Profile). PP refers to ponderosa pine [Pinus ponderosa], JP refers to jeffrey pine [Pinus jeffreyi], WT refers to whitethorn [Ceanothus cordulatus] and MA refers to manzanita [Arctostaphylos manzanita]. Error bars amount to 0.10 ‰ (2SD).

$$\delta^{26}\mathrm{Mg}_{\mathrm{bulk\,soil}} = \delta^{26}\mathrm{Mg}_{\mathrm{sec}} \cdot \mathrm{f}_{\mathrm{sec}}^{\mathrm{Mg}} + \delta^{26}\mathrm{Mg}_{\mathrm{prim}} \cdot \left(1 - \mathrm{f}_{\mathrm{sec}}^{\mathrm{Mg}}\right) \qquad \textbf{Equation 4-1}$$

We first solve Equation 4-1 for $\delta^{26}Mg_{sec}$ with f_{sec}^{Mg}; the fraction of Mg borne by secondary minerals is estimated to be 4 %, which is contained in an upper possible limit of 5 % Mg clay (XRD detection limit) relative to 20 % amphibole/biotite in bulk soil (Section 4.7.2). Soil Mg isotopes can only be explained if $\delta^{26}Mg$ in secondary minerals ($\delta^{26}Mg_{sec}$) ≥ 4 ‰. To our knowledge, such high clay $\delta^{26}Mg$ values have

never been reported to date (Wimpenny et al. 2014). These clay $\delta^{26}Mg$ values would require that Mg clays precipitate from dissolved Mg with a $\delta^{26}Mg$ of ~3.5 ‰, which has never been observed either (Tipper et al. (2012), and references therein). Second, we solve Equation 4-1 for f_{sec}^{Mg} by using the maximum published $\delta^{26}Mg_{sec}$ of 0.5 ‰ (Ryu et al. (2016) and references therein). This clay value is also consistent with a Rayleigh-type mass balance constrained by the $\delta^{26}Mg$ of measured stream water and bulk rock as source Mg using $\alpha_{solid\text{-}solution}$ = 1.00054 (Ryu et al., 2016). In this case the bulk soil Mg clay content was 30 %, far in excess of our XRD analyses (Section 4.7.2).

Therefore, incorporation of Mg into clays does not drive the low $\delta^{26}Mg$ of dissolved Mg. The remaining process that depletes soil water in ^{26}Mg is the preferential uptake of ^{26}Mg by plants (Black et al. 2008; Bolou-Bi et al. 2012) associated with an isotope fractionation factor between plant Mg and dissolved Mg in the soil solution, expressed as $\Delta^{26}Mg_{plant\text{-}diss}$.

4.4.2 Mg tree uptake fractions from an isotope mass balance

We quantify the fraction of Mg uptake by higher plants (f_{uptake}^{Mg}) by an equation frequently used in stable isotope geochemistry (e.g. Beard et al. (2004), Black et al. (2008)) to calculate the partitioning of an element between two distinct compartments (Equation 4-2). This equation is derived from a simple "closed system" mass balance model, where the element can freely exchange between the two compartments (which are in turn isolated from any other compartment) and fractionate isotopically between these compartments. $\Delta^{26}Mg_{plant\text{-}diss}$ is the isotopic difference between Mg in plants and dissolved Mg in soil water.

$$f_{uptake}^{Mg} = \frac{\delta^{26}Mg_{rock} - \delta^{26}Mg_{diss}}{\Delta^{26}Mg_{plant-diss}} \qquad \textbf{Equation 4-2}$$

In Equation 4-2 we use the isotopic difference between the "initial" $\delta^{26}Mg_{diss}$ and $\delta^{26}Mg_{diss}$ that has been modified from the initial soil solution by Mg uptake into plants. Since we do not know the initial $\delta^{26}Mg_{diss}$ we use $\delta^{26}Mg_{rock}$ as a proxy for this weathering solution, assuming congruent rock dissolution (Bouchez et al. 2013). It can be excluded that differences in primary mineral $\delta^{26}Mg$ lead to preferential release of specific $\delta^{26}Mg$, based on fs-laser ablation data of biotite and amphibole, the main Mg carriers, which are similar to $\delta^{26}Mg$ of bulk bedrock (Section 4.2.4 and Figure 4-1). The f_{uptake}^{Mg} calculated here presents a minimum estimate ("net") of the total uptake fraction, as it does not include a fraction of Mg that is potentially recycled back into solution after uptake through Mg release from plant litter. We note that f_{uptake}^{Mg} calculated by Equation 4-2 is mathematically equivalent to the results of the steady state flow-through reactor model of Bouchez et al. (2013) (see below) but here f_{uptake}^{Mg} reflects an

instantaneous mass balance and does not depend on a steady state of fluxes, but applies only to an idealised closed system where plants exchange Mg with regolith water.

We can also describe both uptake and removal of Mg by a flow-through reactor isotope model (Bouchez et al. 2013), where the isotope ratios are modelled as a function of elemental fluxes. Combining Equation 3c, Equation 3d and Equation 5e from Bouchez et al. (2013) and assuming that no Mg is incorporated into secondary minerals leads to Equation 4-3 and Equation 4-4:

$$\frac{\delta^{26}\mathrm{Mg}_{\mathrm{rock}} - \delta^{26}\mathrm{Mg}_{\mathrm{diss}}}{\Delta^{26}\mathrm{Mg}_{\mathrm{plant-diss}}} = \frac{\mathrm{U}^{\mathrm{Mg}} - \mathrm{S}_{\mathrm{org}}^{\mathrm{Mg}}}{\mathrm{S}_{\mathrm{rock}}^{\mathrm{Mg}} + \mathrm{S}_{\mathrm{prim}}^{\mathrm{Mg}}}, \qquad \textbf{Equation 4-3}$$

$$\frac{\delta^{26}\mathrm{Mg}_{\mathrm{rock}} - \delta^{26}\mathrm{Mg}_{\mathrm{diss}}}{\Delta^{26}\mathrm{Mg}_{\mathrm{plant-diss}}} = \frac{\mathrm{E}_{\mathrm{org}}^{\mathrm{Mg}}}{\mathrm{S}_{\mathrm{rock}}^{\mathrm{Mg}} + \mathrm{S}_{\mathrm{prim}}^{\mathrm{Mg}}}. \qquad \textbf{Equation 4-4}$$

The denominator in the right-hand terms of Equation 4-3 and Equation 4-4 represents the sum of the Mg supply fluxes from rock dissolution ($\mathrm{S}_{\mathrm{rock}}^{\mathrm{Mg}}$) at the weathering front and from primary minerals remaining in the regolith ($\mathrm{S}_{\mathrm{prim}}^{\mathrm{Mg}}$). In Equation 4-3 the flux term U^{Mg} quantifies the Mg uptake flux by trees. $\mathrm{S}_{\mathrm{org}}^{\mathrm{Mg}}$ represents the flux of Mg from leaching of plant litter that is either recycled back into the plants or discharged into the river. The difference U^{Mg}- $\mathrm{S}_{\mathrm{org}}^{\mathrm{Mg}}$ is therefore the net Mg accumulation in the "organic" compartment, combining living biomass and plant litter. The use of Equation 4-3 does not rely on any steady-state assumption regarding this organic compartment, meaning that the equation applies even if this pool grows, for example during forest growth after deforestation or climate change. If the organic Mg pool is at steady state, the difference U^{Mg}- $\mathrm{S}_{\mathrm{org}}^{\mathrm{Mg}}$ is equal to $\mathrm{E}_{\mathrm{org}}^{\mathrm{Mg}}$, where $\mathrm{E}_{\mathrm{org}}^{\mathrm{Mg}}$ refers to the particulate organic Mg export by erosion (Equation 4-4). The isotope ratios are thus set by the Mg uptake flux by trees relative to the solubilisation flux of Mg by chemical weathering. Note that the left-hand term of Equation 4-3 and Equation 4-4 is identical to the one used for the determination of the relative Mg uptake flux $\mathrm{f}_{\mathrm{uptake}}^{\mathrm{Mg}}$ by a closed system mass balance (Equation 4-2). As the formation of Mg clays and the dissolution of carbonates do not affect Mg fluxes at our study sites (Section 4.4.1, Bateman and Wones (1972)), an isotope difference between rock and dissolved Mg only emerges if a substantial fraction of isotopically fractionated Mg accumulates in wood of a regrowing forest after clear cutting or is exported in plant litter or CWD.

To estimate a range for $\mathrm{f}_{\mathrm{uptake}}^{\mathrm{Mg}}$ (Equation 4-2) or, at steady state, $\mathrm{E}_{\mathrm{org}}^{\mathrm{Mg}}$ (Equation 4-3), we applied Equation 4-2 and Equation 4-4 to all individual Providence Creek water samples by using a minimum and maximum $\Delta^{26}\mathrm{Mg}_{\mathrm{plant\text{-}diss}}$ of 0.50 ‰ (Opfergelt et al. 2014) and 0.68 ‰ (Black et al. 2008), respectively, and considered the analytical uncertainty on δ^{26}Mg of 0.10 ‰ (2SD). The difference of 0.50 ‰ we found between $\delta^{26}\mathrm{Mg}_{\mathrm{diss}}$ and $\delta^{26}\mathrm{Mg}_{\mathrm{rock}}$ shows that 50 % to 100 % of the Mg initially released

by chemical weathering is taken up by trees and accumulates in growing forest biomass, or it is eventually eroded in plant litter and CWD. Consequently, because of the high fraction of Mg uptake, the mean weighted $\delta^{26}Mg_{tree}$ is identical to bulk rock (Figure 4-3). Therefore, at Providence Creek Mg is strongly bio-utilised.

Mg isotopes are unevenly partitioned into the different tree compartments comprising roots, trunk wood and non-woody foliage. Even though bulk tree $\delta^{26}Mg$ is higher than $\delta^{26}Mg_{diss}$, its composition is close to that of the parent rock and soil (Figure 4-3). The reason is that during tree growth, the Mg taken up is partitioned into a high-$\delta^{26}Mg$ compartment in woody plant matter and a low-$\delta^{26}Mg$ compartment in leaves and needles. However, to explain the deficit in ^{26}Mg in dissolved stream Mg, a high-$\delta^{26}Mg$ compartment has to accumulate in wood or be eroded as plant debris present on the forest floor and then exported as river particulates. We analysed $\delta^{26}Mg$ of foliage, twigs and bark sampled from the forest floor and a sediment pond containing the erosion products of the ecosystem. Forest floor and sediment pond needles (Figure 4-3, Supplementary Table 4-2) are isotopically light as expected given that needles become isotopically lighter as they age (Bolou-Bi et al. 2012). Fine twigs (Figure 4-3, Supplementary Table 4-2) are isotopically light too. This finding is in contrast with the isotope composition we found in living wood (Figure 4-3) and isotopically heavy Mg published for wood (Black et al. 2008; Bolou-Bi et al. 2012). The low $\delta^{26}Mg$ of the fine twigs (diameter ~3 mm) is explained by their Mg isotopic composition being dominated by bark for which we also found low $\delta^{26}Mg$ (Figure 4-3), consistent with (Chapela Lara et al. 2017). Regardless, the compartment containing the required high-$\delta^{26}Mg$ fraction is not contained in fine plant matter present on the forest floor, making CWD a more likely vector of export for this high-$\delta^{26}Mg$ component. However, the high-$\delta^{26}Mg$ fraction is found in the wood of tree trunks (Figure 4-3, Supplementary Table 4-2). Our isotope mass balance allows for two explanations: transient growth of tree biomass following logging and mechanical removal of tree trunks (Equation 4-3); or natural erosion of coarse woody debris (CWD), at steady state with its uptake, with only minor leaching of Mg (Equation 4-4). We return to discussing these mechanisms in Section 4.4.8.

4.4.3 Mg weathering fluxes from an isotope mass balance

The fact that Mg is highly bio-utilised and most likely eroded as CWD dictates that the dissolved Mg export flux is low relative to other Mg fluxes in the ecosystem. We use the isotope mass balance model (Bouchez et al. 2013) to calculate the normalised dissolved Mg export flux ($w^{Mg}_{isotope}$, Table 4-1) by Equation 4-5 and report the data in Supplementary Table 4-4b:

$$w^{Mg}_{isotope} = \frac{\delta^{Mg}_{topsoil} - \delta^{Mg}_{rock}}{\delta^{Mg}_{topsoil} - \delta^{Mg}_{diss}}. \qquad \textbf{Equation 4-5}$$

This fraction reflects the Mg solute export from the whole system relative to the total Mg export of solutes and particulates as primary and secondary minerals plus organic material. Estimating $w_{isotope}^{Mg}$ does not depend on knowing isotope fractionation factors, but it assumes a steady state of fluxes.

Table 4-1 *Glossary of symbols used in Figure 4-4 and throughout this chapter.*

	Total mass fluxes (e.g. in t km^{-2} yr^{-1})
D	Denudation rate; i.e. the sum of chemical and physical denudation; Equation 4-7; Section 4.4.4
	Elemental fluxes F^X (e.g. in mg m^{-2} yr^{-1})
RP^X	Regolith production flux of element X; transfer of X from bedrock to regolith at the weathering front;Equation 4-7; Section 4.4.4
W_{river}^X	Dissolved river flux of element X; Equation 4-6; Section 4.4.4
$W_{regolith}^X$	Net solubilisation flux of element X; release flux of X from minerals minus the flux of incorporation of X into secondary minerals; Equation 4-9; Section 4.4.5
L^X	Litter fall flux of element X; sum of leaf, trunk and root litter flux of X from trees to topsoil through litter fall; Equation 4-14; Section 4.4.7
E_{org}^X	Erosion flux of element X in particulate organic matter or phytoliths; Equation 4-4; Section 4.4.2
	Normalised elemental fluxes f^X
$w_{isotope}^X$	Dissolved export flux of element X relative to the regolith production flux of element X, calculated from isotopes; Equation 4-5; Section 4.4.3
w_{river}^X	Dissolved export flux of element X relative to the regolith production flux of element X, calculated from river loads; W_{river}^X / RP^X; Equation 4-8, Section 4.4.4
$w_{regolith}^X$	Normalised net solubilisation flux of element X; $W_{regolith}^X$ / RP^X; Equation 4-11, Section 4.4.5
DEE^X	Dissolved export efficiency of element X; W_{river}^X / $W_{regolith}^X$; Equation 4-12, Section 4.4.6
DEE_{Na}^X	Dissolved export efficiency of element X; Na-normalised W_{river}^X / $W_{regolith}^X$; Equation 4-13, Section 4.4.6
Rec^X	Nutrient recycling factor; number of passages X takes through the vegetation after its initial release from rock; L^X/ $W_{regolith}^X$; Equation 4-14, Section 4.4.7
	Elemental mass fractions
f_{sec}^{Mg}	Fraction of Mg carried by secondary minerals relative to total soil Mg; Equation 4-1, Section 4.4.1
f_{uptake}^{Mg}	Fraction of Mg taken up by plants relative to Mg available in soil solution; Equation 4-2, Section 4.4.2
τ_{Zr}^X	Loss fraction of element X; elemental loss or gain relative to unweathered bedrock; Equation 4-10; Section 4.4.5
	Mg stable isotope properties (in ‰)
$\delta^{26}Mg_{comp.}$	Normalised $^{26}Mg/^{24}Mg$ isotope ratio in compartments (e.g. rock, sec, diss, reg, sed, topsoil, plant) relative to DSM-3
$\Delta^{26}Mg_{plant-diss}$	Isotopic difference between $\delta^{26}Mg_{plant}$ and $\delta^{26}Mg_{soil\ water}$

We use the mean δ^{26}Mg of unweathered rock, spatial- and time-integrated creek water of the individual Providence Creek sites (P301, P303, P304) and mean bulk soil and saprolite from the P301 soil profile and the soil-saprolite Balsam Profile (Figure 4-3). The mean δ^{26}Mg of bulk soil and saprolite was chosen as soil and saprolite samples vary insignificantly in their δ^{26}Mg (similar results would be obtained if we had used the topsoil signature only, where topsoil is the compartment that is

undergoing erosion at our sites). We consider the isotope composition of this soil-saprolite average to be more representative for exported particulate matter than samples from sediment ponds, because hydrodynamic sorting in the creek channel does not allow representative sampling of sediment from these ponds, where coarse, dense particles are enriched. δ^{26}Mg of topsoil, saprolite and bulk rock are identical within their analytical uncertainties. Therefore only a potential upper boundary of the relative Mg weathering flux $w^{Mg}_{isotope}$ can be estimated by propagating the analytical uncertainties as in Bouchez et al. (2013).

Our results show that according to Equation 4-5 only 11 ± 13 % of Mg is exported from the weathering zone in the dissolved form (Figure 4-5). Therefore, the complementary 89 % of Mg is exported predominantly in primary minerals and in a substantial proportion of CWD.

4.4.4 Elemental dissolved river fluxes

Next, we calculate an independent estimate of the relative dissolved Mg river flux (w^{Mg}_{river}) that allows comparison with the isotope-based dissolved Mg export ($w^{Mg}_{isotope}$). We also calculate the dissolved river flux w^{X}_{river} for the macronutrients (X) K, Ca, P and the plant beneficial element Si (hereafter we call these elements "bio-elements"). The absolute (non-normalised) dissolved annual river fluxes for these elements (W^{X}_{river}, Figure 4-4, Table 4-1) are derived from Equation 4-6, which is the sum of the catchment area (A) normalised products of daily dissolved creek water concentrations ($[X]_{river_i}$) and daily discharge (Q_i) of one hydrological water year:

$$W^{X}_{river} = \sum_{i=1}^{365} \frac{[X]_{river_i} \cdot Q_i}{A} . \qquad \textbf{Equation 4-6}$$

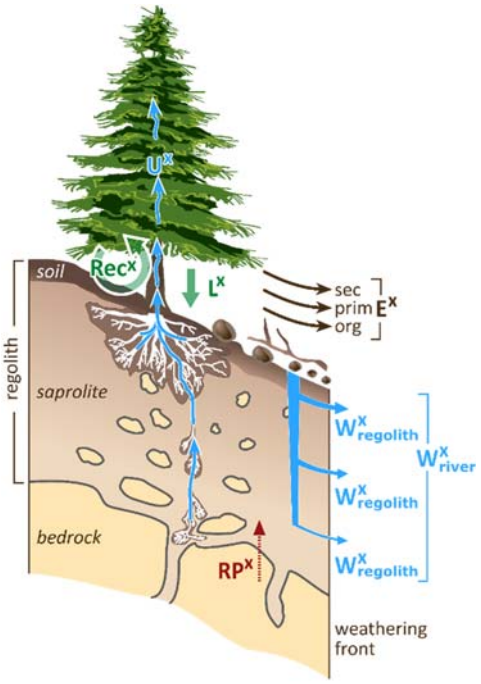

Figure 4-4 Schematic figure illustrating the metrics used in our flux model. "Org" refers to the sum of coarse woody debris (CWD), litter and trunk wood erosion. Rec^X refers to the nutrient recycling factor of element X, U^X refers to the nutrient uptake flux of element X, L^X refers to the litter flux of element X, RP^X refers to the regolith production flux of element X, W^X_{river} refers to the dissolved river flux of element X and $W^X_{regolith}$ refers to the net solubilisation flux of element X.

Since we lack daily resolution $[X]_{river}$ data and our sampling years (2010-2014) differ from the hydrological water years (2004-2010) for which daily discharge is available (http://criticalzone.org/sierra/data), we use the $[X]_{river}$-Q linear regression to determine daily $[X]_{river_i}$. We calculate mean discharge values from 15 days before to 15 days after each of our seven $[X]_{river}$ data points for all hydrological water years 2004-

2010 and calculate annual W^{X}_{river} for the individual hydrological water years 2004-2010 by applying Equation 4-6. We calculate an average of all hydrological water years 2004-2010 to derive W^{X}_{river} (Supplementary Table 4-4a). For example, catchment average W^{Mg}_{river} ranges from about 190 to 670 mg m^{-2} yr^{-1}.

To allow comparison between flux estimates of different elements, we normalise the measured fluxes using the elemental regolith production rate (RP^{X}, Figure 4-4, Table 4-1, Supplementary Table 4-4a), which quantifies the total transfer of an element X from bedrock to regolith at the weathering front, partitioned into secondary minerals, solutes and remaining primary minerals (Bouchez et al. 2013) by Equation 4-7:

$$RP^{X} = D \cdot [X]_{rock} . \qquad \textbf{Equation 4-7}$$

Here, we use the total denudation rate (D, Table 4-1) from cosmogenic *in situ* ^{10}Be concentration from Dixon et al. (2009). Using D of 220 t km^{-2} yr^{-1} for all catchments and $[Mg]_{rock}$ of 1.9 weight-%, RP^{Mg} is about 4300 mg m^{-2} yr^{-1}. The normalised dissolved river fluxes (w^{X}_{river}) are calculated by Equation 4-8 (Bouchez et al. 2013) and reported in Supplementary Table 4-4b:

$$w^{X}_{river} = \frac{W^{X}_{river}}{RP^{X}} . \qquad \textbf{Equation 4-8}$$

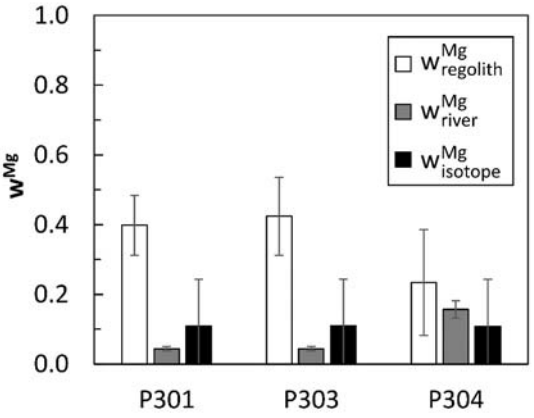

Figure 4-5 Comparison of the relative weathering flux derived from Mg isotopes ($w^{Mg}_{isotope}$, Supplementary Table 4-4b), dissolved river loads (w^{Mg}_{river}, Supplementary Table 4-4b), and net solubilisation fluxes ($w^{Mg}_{regolith}$, Supplementary Table 4-4b) for the individual Providence Creek sub-catchments. The ca. 4-fold higher w^{Mg}_{river} of the smallest watershed P304 compared to the larger watersheds P301 and P303 might be the result of the relatively high discharge record caused by higher baseflow (Eagan et al. 2007) for such a small watershed. For that reason, we consider this catchment to be unrepresentative.

w^{Mg}_{river} amounts to 4-16 % (Figure 4-5) of Mg fluxes and is similarly low as $w^{Mg}_{isotope}$ of ca. 11 %. Thus, in the absence of Mg-containing secondary minerals, Mg is exported predominantly in remaining primary minerals or, after uptake by plants, in the form of CWD or remains in the wood of a growing forest.

4.4.5 Net elemental solubilisation fluxes in the weathering zone

To test the interpretation that a substantial fraction of Mg and other bio-elements (X) initially solubilised from rock accumulate in wood (with or without subsequent export as plant litter and CWD), we compare the relative dissolved export fluxes of Mg w^{Mg}_{river} and $w^{Mg}_{isotope}$ to the normalised net

solubilisation flux ($w^{Mg}_{regolith}$, Supplementary Table 4-4b). The non-normalised net solubilisation flux ($W^{X}_{regolith}$, Figure 4-4, Table 4-1) is determined by Equation 4-9 and reported in Supplementary Table 4-4a:

$$W^{X}_{regolith} = RP^{X} \cdot \left(-\tau^{X}_{Zr}\right). \qquad \textbf{Equation 4-9}$$

$W^{X}_{regolith}$ is defined as the flux of release of X from minerals undergoing weathering minus the flux of incorporation of X into new minerals potentially formed during weathering reactions (e.g. clays) over the regolith profile. $W^{X}_{regolith}$ thus quantifies the net release of X from the bedrock-regolith system. $W^{X}_{regolith}$ is derived from the total denudation rate (D, Table 4-1) and bedrock concentrations ($[X]_{rock}$) following Equation 4-7, combined with the mass transfer coefficient (hereafter elemental loss fraction) (τ^{X}, Table 4-1). The loss fraction (τ^{X}) quantifies the depletion ($\tau^{X} < 0$) or enrichment ($\tau^{X} > 0$) of an element X relative to unweathered bedrock (Brimhall and Dietrich 1987; Anderson et al. 2002). τ^{X}_{Zr} is determined by Equation 4-10:

$$\tau^{X}_{Zr} = \frac{[Zr]_{unweathered\ bedrock}}{[Zr]_{weathered\ regolith}} \cdot \frac{[X]_{weathered\ regolith}}{[X]_{unweathered\ bedrock}} - 1. \qquad \textbf{Equation 4-10}$$

Zr is used as the immobile element. In addition to the data set of this study, published data (Riebe and Granger 2013; Hahm et al. 2014) was used to obtain the most representative bedrock concentrations and are reported with our data in Supplementary Table 4-3a - Supplementary Table 4-3c.

The net solubilisation flux $W^{X}_{regolith}$ is determined by Equation 4-9 for each of the Providence Creek catchments and ranges from 1000 to 1800 mg m^{-2} yr^{-1} for Mg. Since τ^{X}_{Zr} is relatively uniform across the sampled soil-saprolite profile (Figure 4-6) mean τ^{X}_{Zr}-values based on soil and saprolite data from Hahm et al. (2014) and Riebe and Granger (2013) (Supplementary Table 4-3) have been used. Only τ^{P}_{Zr} is strongly depth dependent (Figure 4-6). Hence we used the most negative τ^{P}_{Zr} from the dataset from Hahm et al. (2014) and Riebe and Granger (2013) (Supplementary Table 4-3). The normalised net solubilisation flux ($w^{X}_{regolith}$) is

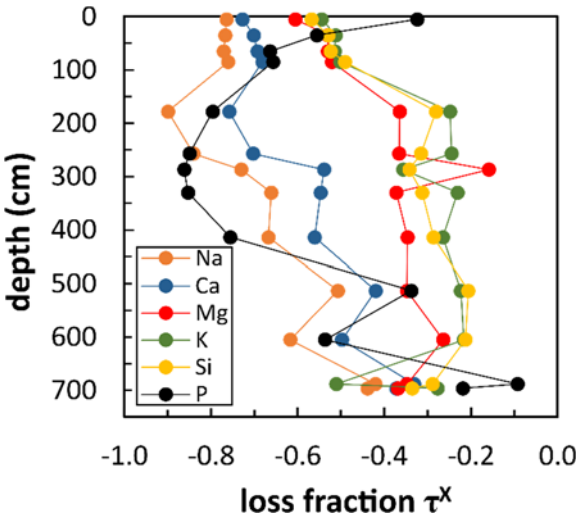

Figure 4-6 Elemental loss fraction (mass transfer coefficient) (τ^{X}_{Zr}) for macronutrients, the plant essential element Si and Na of the soil-saprolite depth profile BP. A τ^{X}_{Zr}-value < 0 indicates elemental loss in soil/saprolite relative to unweathered bedrock.

determined by Equation 4-11. The comparison to Equation 4-7 and Equation 4-9 shows that $w^{X}_{regolith}$ is actually equal to $-\tau^{X}_{Zr}$:

$$w^{X}_{regolith} = \frac{W^{X}_{regolith}}{RP^{X}} = -\tau^{X}_{Zr} . \quad \textbf{Equation 4-11}$$

$w^{Mg}_{regolith}$ amounts to ~40 % (Figure 4-5), meaning that in the regolith 40 % of the Mg supplied from rock is transferred into the dissolved form and is made available for plant uptake. Because $w^{Mg}_{regolith}$ is much higher than $w^{Mg}_{isotope}$ and w^{Mg}_{river} (Section 4.4.3 and Section 4.4.4), this calculation shows that a substantial fraction of Mg once released by chemical weathering is taken up into the biomass without subsequent redissolution.

4.4.6 Dissolved export efficiency

To confirm that Mg is not the only element that is strongly bio-utilised, we compared the dissolved river flux (W^{X}_{river}) with the net solubilisation flux ($W^{X}_{regolith}$) by its ratio $W^{X}_{river}/W^{X}_{regolith}$ for the other bio-elements (K, Ca, P, Si). Because this ratio quantifies the dissolved riverine loss of X from the ecosystem relative to its net release from the regolith we call the ratio the "dissolved export efficiency" (DEE^{X}, Equation 4-12, Figure 4-7, Table 4-1):

$$DEE^{X} = \frac{W^{X}_{river}}{W^{X}_{regolith}} . \quad \textbf{Equation 4-12}$$

If the DEE^{X} is larger than 1, input sources other than rock weathering are supplying X, such as atmospheric deposition (see Section 4.4.10). The DEE^{X} is less than 1 if some of the released element is partitioned into a plant uptake flux during forest growth or is eroded as plant litter or CWD (including eroded phytoliths in the case of Si). The DEE^{X} can also differ from 1, because W^{X}_{river} and $W^{X}_{regolith}$ integrate over entirely different timescales.

The inferred DEE^{X} (~ 0.40 for K, ~0.60 for Ca, ~0.30 for Mg, ~0.05 for P and ~0.10 for Si) of each nutritive element is less than 1 (Figure 4-7), suggesting that some fractions of bio-elements once released by chemical weathering are bio-utilised and remain in regrowing forest biomass after clear cutting or are eventually eroded as CWD. The DEE^{X} of the non-nutritive element Na is < 1 too and amounts to 0.68 (Supplementary Table 4-4d). Thus, DEE^{Na} suggests that 32 % of Na, which has been released by chemical weathering, is missing in the dissolved river flux. This result is unexpected because Na behaves conservatively, meaning Na is neither incorporated into secondary minerals nor

taken up as a nutrient by plants. Measured Na in pine tree wood amounts to 3 - 8 ppm (Supplementary Table 4-2) and in shrub wood to ~40 ppm (Supplementary Table 4-2). These low Na contents in plants translate into a plant uptake flux of about 2 % relative to the solubilisation flux, far lower than the ~1/3 of $W^{Na}_{regolith}$ estimated from DEE^{Na}. This observation agrees well with the fact that Na is only a plant beneficial element in halophilic and C4/CAM plants (Marschner 2011) and plays no significant nutritive role in pine trees representing the prevailing plant species at SSCZO. We argue that the supposed deficit in W^{X}_{river} relative to $W^{Na}_{regolith}$ is a timescale effect as W^{X}_{river} integrates over annual and $W^{X}_{regolith}$ over millennial timescales.

To obtain a metric that is independent of timescale effects, we normalised the fluxes W^{X}_{river} and $W^{X}_{regolith}$ over their respective Na fluxes (Equation 4-13) and rearrange the right-hand term of Equation 4-13:

$$DEE^{X}_{Na} = \frac{\frac{W^{X}_{river}}{W^{Na}_{river}}}{\frac{W^{X}_{regolith}}{W^{Na}_{regolith}}} = \frac{\left(\frac{[X]_{river}}{[Na]_{river}}\right) / \left(\frac{[X]_{rock}}{[Na]_{rock}}\right)}{\frac{(\tau^{X}_{Zr})}{(\tau^{Na}_{Zr})}}. \qquad \textbf{Equation 4-13}$$

This approach has a fundamental benefit, as knowing the denudation rate D (Equation 4-9) from cosmogenic nuclides and the discharge Q (Equation 4-6) from long-lasting gauging programs is not required. However, we note that the Na normalisation may also introduce bias into the DEE^{X}_{Na} (Table 4-1). This might be the case if, for example, changes in water flow during the development of the profile over a few thousand years result in a change in the stoichiometry of rock dissolution. Such changes in the congruency in the dissolution of rock might result from changes in the dissolution of Na-bearing primary minerals relative to other primary minerals or from a changing rate of secondary mineral formation relative to Na-bearing primary minerals. In that case the time-integrated denominator in Equation 4-13 does not reflect the present value.

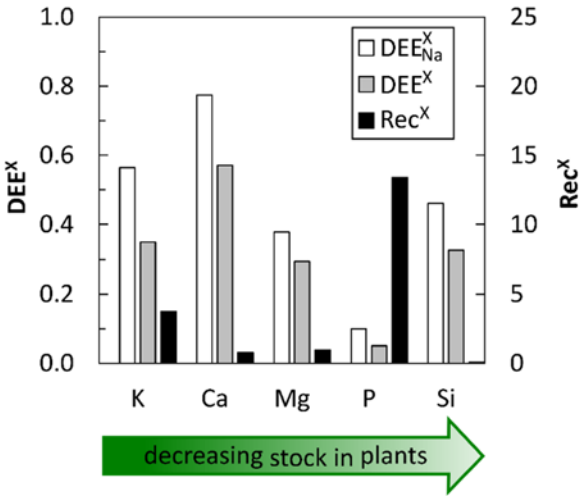

Figure 4-7 Dissolved export efficiency (DEE^{X}, left y-axis, Supplementary Table 4-4d - Supplementary Table 4-4e) and nutrient recycling factor (Rec^{X}, right y-axis, Supplementary Table 4-4f) for macronutrients and the plant beneficial element Si. The DEE^{X} quantifies the dissolved riverine loss of X from the ecosystem relative to its net release from the regolith. DEE^{X} refers to the pure ratio $W^{X}_{river}/W^{X}_{regolith}$ (Equation 4-12). DEE^{X}_{Na} refers to the ratio $W^{X}_{river}/W^{X}_{regolith}$ normalised over its corresponding Na fluxes (Equation 4-13). Rec^{X} (Equation 4-14) quantifies how often an element X is bio-utilised by plants after its release by chemical weathering.

The DEE_{Na}^{X} values obtained (Figure 4-7, Supplementary Table 4-4e) show that, of the elements solubilised from rock, ~80 % of Ca, ~60 % of K, ~50 % of Si, ~40 % of Mg and ~10 % of P appear in the streams dissolved load. The DEE_{Na}^{X} for Mg is in excellent agreement with the 50-100 % of Mg bio-utilisation calculated independently by isotope mass balances (Equation 4-2). The high DEE_{Na}^{X} for Ca can be attributed to its high concentrations in rock combined with its high degree of solubilisation by chemical weathering that results in excess availability compared to the nutrient demand of trees. In contrast, the low DEE_{Na}^{X} for P is most likely due to its high biological demand and low availability, resulting in high degree of plant uptake and subsequent export in plant litter and CWD.

4.4.7 Nutrient recycling factor

After uptake and return to the forest floor, nutrients are not directly discharged into the stream by litter dissolution or eroded as plant litter or CWD. Rather, they are subject to recycling - defined here as uptake of nutrients that are made bio-available again after their release from plant litter. The recycling flux can be hypothesised to depend on the ratio of nutrient demand to availability. We thus tested the hypothesis that in our kinetically limited setting, unlike in the supply-limited regime, intense nutrient recycling is not required as nutrient loss can be balanced by supply from mineral dissolution in the regolith (Jobbágy and Jackson 2001; Lucas 2001).In other words, if nutrient supply from regolith ($W_{regolith}^{X}$) is high, ecosystem nutrition can be satisfied even if recycling is low (Lang et al. 2016). We quantified nutrient recycling as the number of passages an element X takes through the vegetation after its initial release from rock (quantified by the net solubilisation flux $W_{regolith}^{X}$). We note that the nutrient uptake-release loop is distinct and formally independent of other fluxes such as regolith production, weathering and export fluxes calculated above (Figure 4-4). We call the number of passages in the loop the elemental recycling factor (Rec^{X}, Figure 4-4, Table 4-1). Rec^{X} is determined by Equation 4-14 and reported in Supplementary Table 4-4f:

$$Rec^{X} = \frac{L^{X}}{W_{regolith}^{X}}. \qquad \textbf{Equation 4-14}$$

The nutrient uptake flux is the product of net biomass productivity and biomass nutrient concentration (U^{X}, Figure 4-4). Since U^{X} is difficult to determine, we use the sum of litter fluxes (L^{X}; Table 4-1) comprising foliage litter fall ($L_{foliage}^{X}$, Supplementary Table 4-4c), root litter (L_{root}^{X}, Supplementary Table 4-4c) and trunk litter (L_{trunk}^{X}, Supplementary Table 4-4c) instead, assuming balanced uptake and litter fall fluxes (for input parameters see Section 4.7.3). L^{Mg} is 410, 240 to 490, and 680 mg m^{-2} yr^{-1} for foliage, stem and root, respectively. L^{X} represents a minimum estimate for U^{X} and hence Rec^{X} is likely underestimated because we did not consider return of growth-limiting nutrients from foliage via

phloem through roots back into soil during senescence and return of nutrients from throughfall or stem flow.

With an average Rec^P of 13, P is the only bio-element that is tightly recycled (Figure 4-7) and becomes enriched in topsoil (Figure 4-6). Aciego et al. (2017) also compared the sum of dust and bedrock-derived P supply fluxes with nutrient uptake fluxes at SSCZO, obtaining an order of magnitude higher uptake than supply fluxes, and concluded too that P is recycled. With Rec^K of ca. 4, K is also recycled. We note that Rec^K is likely underestimated due to the lack of throughfall data, which are generally highest for K compared to the other bio-elements (Boy and Wilcke 2008). The Rec^X for the macronutrients Ca and Mg is about unity (Figure 4-7) and thus these nutrients are not recycled by uptake after release from litter. This means that uptake from regolith is their only source. The Rec^{Si} of < 0.1 means that only a minor fraction of Si solubilised from rock is bio-utilised. The low Rec^X values for all bio-essential elements except P agree with our observation that after uptake the largest mass fraction of these bio-elements remains in wood or is disposed through export of plant litter and CWD. Altogether, the overall high $\mathrm{DEE}^{\mathrm{X}}_{\mathrm{Na}}$ (Section 4.4.6) and low Rec^X are consistent with the kinetically limited weathering regime of Providence Creek in which mineral nutrients are supplied in sufficient demand, the ecosystem is "acquiring" and thus the need for recycling is low (Lang et al. 2016).

Although Rec^X and $\mathrm{DEE}^{\mathrm{X}}_{\mathrm{Na}}$ rely on $\mathrm{W}^{\mathrm{X}}_{\mathrm{regolith}}$ we note that both metrics are independent from each other. This independency arises because ecologic stoichiometry enriches other mineral nutrients in plants than released from mineral dissolution kinetics. Thus, an element X can become recycled (meaning uptake of nutrients released from plant litter) many times compared to this element's weathering flux $\mathrm{W}^{\mathrm{X}}_{\mathrm{regolith}}$. This number of cycles as quantified by Rec^X can vary between 0 and a large number. In contrast, $\mathrm{DEE}^{\mathrm{X}}_{\mathrm{Na}}$ quantifies the fraction of an element that is exported in the dissolved river load rather than being contained in plant debris, relative to the fraction of X that was initially solubilised by chemical weathering, and can vary between 0 and 1 unless atmospheric input results in $\mathrm{DEE}^{\mathrm{X}}_{\mathrm{Na}}$ >1.

4.4.8 Accumulation of bio-elements during forest growth or export in coarse woody debris?

In the preceding sections, we have suggested two mechanisms that potentially explain the creek water being enriched in ^{24}Mg and the deficit in the dissolved river export fraction indicated by the $\mathrm{DEE}^{\mathrm{X}}_{\mathrm{Na}}$: (1) bio-utilisation and accumulation of bio-elements in wood of a regrowing forest after clear cutting on centennial timescales or (2) solid export of nutrients in CWD by natural erosion in pre-forest management times and over weathering (kyr) timescales. Concerning logging, in the late 19th century *Pinus ponderosa* forests became nearly wholesale clear-cut (Graham and Jain 2005) and our study sites underwent continuous logging of some form through the 1960s (Carolyn Hunsaker, personal communication, 2017). These logging activities triggered the growth of today's forest at Providence

Creek and might have shifted the ecosystem from some quasi-steady state – where elemental input fluxes equal elemental export fluxes, and where plant growth equals plant mortality – into an ecosystem being in a transient state characterised by the build-up of a pool of bio-elements (e.g. Sommer et al. (2013)). Concerning natural erosion, trunk wood that is enriched in ^{26}Mg is not contained in the sediment pond we sampled. Yet it is continuously removed from the ecosystem by stochastic events, such as tree turnover after tree death (Roering et al. 2010), wind throw, or wildfires – that are suppressed since the late 19th century – after which ash is fast eroded.

To estimate whether tree trunk growth satisfies the elemental and isotopic mass balance we estimated the budgets of bio-elements contained in *Pinus ponderosa* trunk wood (see Section 4.4.7 and Section 4.7.3). We find that the litter fall fluxes (L^X, Supplementary Table 4-4c) that we use to estimate uptake indeed are comparable with the deficit in the elemental dissolved export flux as indicated by 1-$\mathrm{DEE}^{\mathrm{X}}_{\mathrm{Na}}$ for Mg and Ca. Both the P and K trunk wood fluxes are higher than the deficit in the elemental dissolved export flux. This effect arises for strongly recycled elements, because the uptake flux contains the fraction added by nutrient recycling from the forest floor. However, for Si Rec^X amounts to <0.1 whereas the fraction not accounted for by dissolved loss (1-$\mathrm{DEE}^{\mathrm{X}}_{\mathrm{Na}}$) is 0.54. A possible reason is that pine needles can treble in Si concentrations as the needles age (Cornelis et al. 2010) and that Si is bio-utilised by shrubs whose leaves dispose phytoliths that are not accounted for in our budget. Thus, the Si concentrations used in our calculations might be unrepresentative of those in aged leaf litter (Section 4.7.3) and Rec^{Si} might be an underestimate. If true, the 1-$\mathrm{DEE}^{\mathrm{X}}_{\mathrm{Na}}$ of Si amounting to 50% is a better estimate for Si uptake.

Whether natural erosion of bio-elements by CWD is a feasible mechanism depends on whether the erosional timescale out-competes the leaching timescale from CWD. Trunk wood decomposition fluxes have been quantified for *Fagus grandifolia*, *Acer saccharum* and *Betula alleghaniensis.* About 25-50 % of Ca, 30-70 % of P, 5-20 % of K, 20-40 % of Mg (Johnson et al. 2014) and 25-60 % of Si (Clymans et al. 2016) remain in trunk wood after 16 years of decomposition. For comparison, after 2 years of *Pinus ponderosa* foliage litter decomposition ~90% of Ca, ~55 % of P, ~20 % of K and ~45 % of Mg (Klemmedson 1992) remain in foliage litter. The dissolution half-life of the bio-opal in phytoliths at the pH prevailing at Providence Creek amounts to a few hundred days (Fraysse et al. 2009). Therefore, bio-element leaching (except Ca) from foliage outpaces bio-element leaching from wood. Hence, after tree death and after litter fall (Si contained in phytoliths and Ca likely contained in oxalates) erosional removal must occur within this decomposition timescales for CWD to be a feasible mechanism.

Given the lack of information on the pre-logging fluxes and isotope ratios at Providence Creek we have no means to assess whether the natural CWD erosion mechanism has been in operation and caused the deficit in dissolved elemental export rather than forest growth today. We can speculate, however, that one effect has replaced the other with similar impact on fluxes. This is because the

natural erosion of mineral nutrients in tree trunks in the form of CWD is ultimately limited by tree growth too. One other study, using stable Sr isotopes in an unperturbed ecosystem in New Zealand, shows a similar partitioning of Sr between plants and the river dissolved flux (Andrews et al. 2016). Those data can be interpreted to imply natural erosion of Sr in plant litter and CWD. The same interpretation is possible for the data from the Shale Hills Critical Zone Observatory, where a similar deficit in heavy Mg isotopes was found in stream and soil water (Ma et al. 2015). In that study the bio-cycling hypothesis was dismissed on the grounds of missing accumulation of Mg in the organic-rich portions of the soil. The existence of a sub-micron pool enriched in ^{26}Mg was hypothesised instead. However, the Mg data at Shale Hills CZO are compatible with the CWD export hypothesis too.

4.4.9 Nutrient uplift from the deep saprolite

We determined the depth from which these nutrients are uplifted. A first indicator is the depth distribution of loss fractions τ^X (Brantley and Lebedeva 2011) that allows for the identification of so-called biogenic profiles that are characteristically depleted at depth and become enriched in topsoil, because nutrients are uplifted from depth (Jobbágy and Jackson 2001; Lucas 2001; Bullen and Chadwick 2016). Whereas P depletion amounts to 85 % at 3 m depth and increases towards the surface, indicating biogenic uplift of P, the loss fractions of Mg, K and Si amount to 20 to 40 % and show uniform depletion along the entire depth of the weathering zone down to 7 m depth. The traditional view is that this loss is induced by mineral dissolution and removal by infiltrating water (Brantley and Lebedeva 2011). We can use Mg isotopes to explore an alternative hypothesis: these bio-elements are taken up by tree roots or associated mycorrhiza fungi (Jongmans et al. 1997; Landeweert et al. 2001; Lucas 2001) at these deep levels. In the absence of Mg clays and carbonates the isotopically light composition of the exchangeable fraction throughout the regolith ($\delta^{26}Mg_{exch}$, Figure 4-3) can only be caused by the preferential uptake of heavy Mg isotopes by trees. We can exclude that the development of such an isotopically light exchangeable Mg compartment throughout the regolith is due to fractionation during adsorption (Opfergelt et al. 2014) as the associated fractionation factor is close to 0 ‰ (Wimpenny et al. 2014). Also, Bullen and Chadwick (2016) have shown that isotopic fractionation during adsorption onto clay minerals is absent for other bivalent cations. We can also exclude that low $\delta^{26}Mg_{soil\ water}$ infiltrates to depth from the surface as this $\delta^{26}Mg_{soil\ water}$ would be masked by the high Mg solubilisation flux from primary minerals at the considered depth (Figure 4-5). Deep water uptake from down to 6 m is supported by the rooting depth of *Pinus ponderosa*, which can reach up to 24 m (Stone and Kalisz 1991).

4.4.10 Atmospheric depositional fluxes

DEE^{X}_{Na}, Rec^{X} and the possible enrichment of nutrients from the deep saprolite to shallow soil might all be affected by external dust deposition. Aciego et al. (2017) recently suggested that P supply by dust deposition outpaces local bedrock P supply at the SSCZO in P-poor bedrock. We have argued in Section 4.2.1 that this observation does not hold for the P-rich bedrock at our sites nor when applied to the other mineral nutrients when long-term RP^{X} and $W^{X}_{regolith}$ are considered. Aciego et al. (2017) also compared dust P inputs to modern P export from sediment trapping, which averages erosion over the annual to decadal timescales of human observations. However, measurements of modern sediment fluxes in streams are known to systematically underestimate erosion rates (total denudation rate minus chemical weathering rate) due to the episodic nature of sediment transport (Kirchner et al. 2001; Schaller et al. 2001). In addition, P export also occurs as dissolved species, which needs to be taken into account when estimating bedrock-derived P supply using export fluxes. For example, at SSCZO both the total dissolved river export W^{P}_{river} and the total weathering flux $W^{P}_{regolith}$ that is calculated from cosmogenic nuclides, chemical depletion of regolith and bedrock P concentration exceed the P erosion flux from sediment trapping by 1 to 2 orders of magnitude. Because at these sites at most 58% of regolith production is partitioned into a dissolved flux (Dixon et al. 2009), the high recent dissolved flux needs to be associated with a complementary erosion flux. That this is not the case provides further evidence that the erosion flux determined by sediment trapping is a serious underestimate. Therefore from comparing our results with those of Aciego et al. (2017) we suggest that while dust input of P might be of significance to the local ecosystem on low-P substrate at SSCZO, it is insignificant for P and the other nutritive elements at our P-rich sites in the Providence Creek catchments.

4.5 Implications

To date the possible acceleration of weathering by plants has only been inferred indirectly by comparing the flux of watersheds of different vegetation cover over short timescales (Moulton et al. 2000). At Providence Creek a substantial fraction of bio-elements released by rock dissolution over typical weathering timescales (thousands of years) is directly utilised by the local forest trees – where nutrient uptake does not depend on the mechanism of export. Our data provide new insight into the role of biota in contributing to weathering fluxes in a given ecosystem. The partitioning of Sr stable isotopes in a mountain catchment in New Zealand (Andrews et al. 2016) can be interpreted in the same way. It is essential to both metal isotope-based observations that the elements taken up by plants are directly exported as particulate organic material. The low recycling factors observed support this notion of rapid nutrient uptake and disposal. Therefore, in this kinetically limited setting, this mechanism provides a possible tight coupling between weathering up to 6 m depth and nutrient

utilisation and erosion. We do not know whether this deep nutrient uptake is actively driven by nutrient demand (Landeweert et al. 2001; Lucas 2001; Brantley et al. 2011) or is coupled to deep water uptake during summer droughts. Regardless, either cause would deepen the weathering advance front and potentially facilitates the balance between erosion and weathering advance rate.

Considering that 30 % of the Earth's surface is covered by forests (Bonan 2008) the export of the bio-utilised elements in CWD and bio-opal might represent a more widespread phenomenon. Indeed, in active mountain belts the weathering intensity (total chemical weathering rate normalised by denudation rate) derived from river loads is far lower than that derived from regolith (Dixon and von Blanckenburg 2012). We suggest that one possible explanation for this discrepancy is the nutrient uptake by biota and its subsequent erosion as bio-opal, leaf litter and CWD in these predominantly kinetically limited weathering regimes. In contrast, in lowland supply-limited regimes and floodplains the low bio-element concentrations in plant debris, the low particulate organic matter sediment yield (0.1-1 % of total sediment yield) (Galy et al. 2015; Hilton 2017) and the low amorphous opal flux (0.6 % of total sediment yield) (Frings et al. 2016) result in nutrient export to occur predominantly in the dissolved form. The postulated fast weathering and rapid nutrient erosion coupling is significant only in geologically active mountains where CWD and bio-opal erosion are high (Galy et al. 2015; McCorkle et al. 2016), outpace nutrient recycling, and might constitute a significant solid export flux of elements released by weathering and hence not accounted for in weathering flux estimates based on dissolved river loads.

4.6 Conclusions

The Mg isotope composition of stream water in the Providence Creek watershed, Southern Sierra Nevada, requires a compartment separation between isotopically light Mg dissolved in water and isotopically heavy Mg accumulated in wood of a regrowing forest after clear cutting, or exported in tree wood, without substantial re-mineralisation and re-utilisation. A steady-state isotope mass balance supports the solid Mg export path in that the Mg export is dominated by particulates, and only a minor fraction of ca. 11 % of Mg is exported as solutes. Using Mg isotopes to quantify uptake, we found that 50-100 % of Mg that is released from primary minerals is utilised by trees. This high Mg bio-utilisation is confirmed by a deficit apparent in the Na-normalised dissolved river Mg export flux when compared to the Na-normalised net Mg solubilisation flux. The deficit of dissolved Mg (1-$\mathrm{DEE}_{\mathrm{Na}}^{\mathrm{Mg}}$), exported by creeks, amounts to 60 %, meaning that 60 % of Mg is bio-utilised. We find similar deficits (1-$\mathrm{DEE}_{\mathrm{Na}}^{\mathrm{X}}$) amounting to ~40 % for K, ~20 % for Ca, ~50 % for Si and ~90 % for P. These three lines of evidence show that weathering of rock and biogenic uptake are tightly coupled in this fast weathering, kinetically limited regime. In support of this rock-derived nutrient supply scenario we find that no bio-element except P and K becomes substantially recycled, i.e. re-mineralised from organic litter and then

bio-utilised again. Instead, we infer that Mg, other nutrients and the plant-beneficial element Si accumulate in a forest still growing after clear-cutting up to 50 years ago. As an alternative mechanism likely in operation in pre-forest-management times we suggest that bio-utilised elements were disposed from the forest ecosystem in CWD and Si in phytoliths eroded with leaf litter. CWD has potentially been eroded following tree death after wind throw or as ash after wildfires. We find that Mg is taken up from trees along the entire depth of the weathering profile down to 6 m depth as indicated by the light Mg isotopic composition of the easily exchangeable soil fraction. Therefore we provide entirely novel explanations how biota actively affects weathering fluxes. We suggest that in this kinetically limited regime weathering is tightly coupled to rapid nutrient utilisation and erosion. Finally, we speculate that rapid nutrient erosion might be coupled to fast weathering globally. This coupling then is significant in geologically active mountains where CWD and bio-opal erosion is high and might present a hitherto underestimated solid export flux of elements previously released by chemical weathering.

4.7 Appendix

4.7.1 Calculating δ^{26}Mg in bulk tree

We calculate the Mg isotopic composition of bulk tree ($\delta^{26}Mg_{tree}$) by a mass balance comprising the aboveground (needles, branches, stem) and belowground (roots) tree compartments. We measured δ^{26}Mg in foliage and stem wood. To estimate the isotopic composition of bulk *Pinus ponderosa* and *Pinus jeffrey* we combine these results with δ^{26}Mg and Mg concentration from (Bolou-Bi et al. 2012) and the biomass of different compartments of *Pinus ponderosa* from (Laclau 2003). We did not measure δ^{26}Mg in roots because of the challenges related to their purification from soil particles. Instead we use the published difference between δ^{26}Mg in roots and δ^{26}Mg in wood (Bolou-Bi et al. 2012) to infer δ^{26}Mg in roots from our measured value in wood. The isotopic composition of bulk tree is finally calculated by Equation 4-15, where $f^{Mg}_{compartment}$ is the fraction of Mg in a given tree compartment.

$$\delta^{26}\mathrm{Mg}_{\mathrm{bulk\,tree}} = f^{\mathrm{Mg}}_{\mathrm{needle}} \cdot \delta^{26}\mathrm{Mg}_{\mathrm{needle}} + f^{\mathrm{Mg}}_{\mathrm{stem}} \cdot \delta^{26}\mathrm{Mg}_{\mathrm{stem}} + f^{\mathrm{Mg}}_{\mathrm{root}} \cdot \delta^{26}\mathrm{Mg}_{\mathrm{root}} \qquad \textbf{Equation 4-15}$$

The inferred isotopic composition of roots is 0.43 ‰ for *Pinus ponderosa* and 0.34 ‰ for *Pinus jeffrey*. The $\delta^{26}Mg_{tree}$ plotted in Figure 4-3 represents a mean value of bulk *Pinus ponderosa* and *Pinus jeffrey*.

4.7.2 XRD analyses and the potential incorporation of Mg into secondary minerals

Powder XRD analyses (Siemens D5000, Cu-Kα radiation) were performed for mineral identification on selected soil, saprolite and bedrock samples. Figure 4-8 indicates characteristic reflections for some major and minor minerals. Kaolinite is the only secondary mineral identified. The limit of detection is 5 %.

The absence of Mg clays and the presence of kaolinite was confirmed by published clay contents of less than 10 % in the soils (Dahlgren et al. 1997) and by thermodynamic modelling (PhreeqC). Because kaolinite has a low Mg content (<0.03 wt%; (Wimpenny et al. 2014)) and a relatively low adsorption cation exchange capacity (CEC) of < 10 $cmol_c\ kg^{-1}$ (Wimpenny et al. 2014) it is unlikely to incorporate Mg in such amounts that the Mg mass balance in soil is affected. Therefore, neoformation of Mg clays is not the mechanism that preferentially removes ^{26}Mg from soil solution.

The fraction of Mg potentially contained in clay (f_{sec}^{Mg}) was calculated from the following mass balance. f_{sec}^{Mg} is governed by a mixture between Mg partitioned into Mg clays and Mg partitioned into primary minerals such as biotite and amphibole. While the abundances of Mg clays is at maximum 5 % (XRD limit of detection), primary minerals like biotite and amphibole are identified but not quantified by XRD. Hence, we estimate the relative abundances of biotite and amphibole from bedrock analysis (Bateman and Wones 1972), which we consider to be applicable to soil too given the kinetically limited weathering regime. We assume all mafic constituents to contain Mg. We use montmorillonite $(Al_{1.67}Mg_{0.33})[(OH)_2Si_4O_{10}]Na_{0.33}{\cdot}H_2O$ (Harder 1972) and biotite $K(Mg)_3[(OH,Fe)_2(Al,Fe,Ti)Si_3O_{10}]$ as model endmembers for Mg clays and Mg carrying primary minerals, respectively. Applying the mineral Mg stoichiometry to the abundances of Mg clays and biotite reveals that a Mg clay content of 5 % in the soil translates into 4 % Mg partitioned into Mg clays and 96 % Mg partitioned into biotite. This 4 % is used for f_{sec}^{Mg} in Equation 4-1, which is solved for $\delta^{26}Mg_{sec}$ (see Section 4.4.1).

This calculation confirms that the bulk soil sample with the highest measured $\delta^{26}Mg$ (-0.05 ‰), assuming it contains a maximum allowable Mg clay content of 5 %, can only be explained if $\delta^{26}Mg_{sec}$ is +4.0 ‰, which is highly unlikely (Wimpenny et al. (2014), and references therein). Alternatively, if we use the maximum $\delta^{26}Mg_{sec}$ value observed for Mg clay of 0.5 ‰ (Ryu et al., 2016 and references therein) in Equation 4-1, then the Mg fraction in the bulk soil carried by Mg clays (f_{sec}^{Mg}) were 24 %. This 24 % Mg partitioned into Mg clays can be converted into a 30 % Mg clay content in the bulk soil, which by far exceeds the XRD detection limit. Such high clay content was not observed by XRD (Figure 4-8).

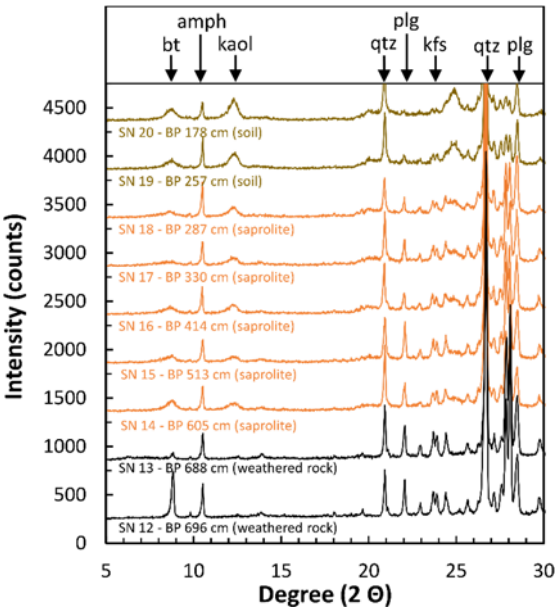

Figure 4-8 X-ray diffraction (XRD) patterns of bulk soil, bulk saprolite, and bulk bedrock stacked on top of each other. Major reflections of primary minerals (bt = biotite, amph = amphibole, qtz = quartz, kfs = K-feldspar, plg = plagioclase) and secondary minerals (kaol = kaolinite) are indicated.

Finally, we explore whether Mg isotope fractionation by Mg adsorption onto kaolinite and amorphous hydroxides might result in the negative $\delta^{26}Mg_{diss}$. The evidence for Mg isotope fractionation during adsorption/desorption is not conclusive and is discussed in Wimpenny et al. (2014) and references therein. Recent experimental evidence suggests that Mg adsorption is mostly associated with a slightly negative (-0.1 ‰) or complete absence of Mg isotope fractionation. Thus, our adsorbed Mg (termed 'exchangeable') likely reflects the isotopic composition of the fluid from which the exchange occurred. Indeed, our isotopically light exchangeable Mg isotope analyses is virtually identical to $\delta^{26}Mg_{diss}$.

Moreover, for such a process to shift $\delta^{26}Mg$ in the isotope mass balance (Equation 4-1), a substantial amount of Mg would need to be adsorbed. Our analyses of exchangeable Mg mass in regolith samples indicate that this compartment makes up less than 0.52 % of the bulk regolith sample (Supplementary Table 4-1). This low mass is consistent with the low cation exchange capacity measured in Providence Creek soils (e.g. $Mg^{2+} < 0.45$ $cmol_c$ kg^{-1}; Johnson et al. (2014)). Hence, neither clay formation nor adsorption is the mechanism that removes isotopically heavy Mg from soil solutions.

4.7.3 Determining foliage, stem and root litter fall fluxes

Since litter data for Providence Creek are not available we use total foliage litter fall fluxes of *Pinus ponderosa* from literature (Klemmedson et al. 1990; Law et al. 1999; Grady and Hart 2006) and multiply

its mean value (see Supplementary Table 4-4c) with the elemental foliage litter concentration of *Pinus ponderosa* (Klemmedson et al. 1990) to determine $L^{X}_{foliage}$ for K, Ca, Mg, P and Na. To determine $L^{X}_{foliage}$ for Si we used $L^{Si}_{foliage}$ data from Bartoli (1983) and simply converted the units. To determine L^{X}_{root} we used root litter production data from (Röderstein et al. 2005). Since roots were not sampled in this study we used Mg, Ca and K root concentrations from *Picea abies* (Bolou-Bi et al. 2012), P root concentration from *Pinus sylvestris* (George et al. 1997) and Na and Si needle concentration from *Pinus ponderosa* from this study. We used Na and Si needle concentrations instead its root concentrations as elemental needle and root concentrations are generally similar. Moreover, there is a lack of Na and Si root concentration for coniferous trees in the literature. To determine L^{X}_{trunk} we estimated the *Pinus ponderosa* minimum and maximum trunk wood biomass by using a logging calculator (www.burleyboys.com, for input parameters see below) and *Pinus ponderosa* Mg, Ca, K, Na and Si wood concentrations from this study and P wood concentration from *Pinus contorta* (Pearson et al. 1987).

To estimate a lower limit of *Pinus ponderosa* trunk wood biomass, we use a diameter at breast height (DBH) of 63 cm (Law et al. 1999), an upper diameter of 42 cm (by assuming that the diameter in the crown is reduced by one third compared to the DBH), a tree height of 34 m (Law et al. 1999) and a stand density of 40,000 trees per square kilometre. To convert the trunk wood biomass into an annual growing flux we used a living time of 250 years (Law et al. 1999). To estimate an upper limit of *Pinus ponderosa* trunk wood biomass we assume a younger forest (200 years) but denser (62,500 trees per square kilometre) forest stand.

4.8 Acknowledgements

We thank R. Naumann (GFZ) for X-ray diffraction and X-ray fluorescence analyses. A. Gottsche (GFZ) is acknowledged for anion quantification using ion chromatography and for assistance in X-ray fluorescence analyses. We also thank R. Meyer (GFZ) for trace element (P) water analyses by Q-ICP-MS (iCAP-Q). Logistical support and discharge data was provided by the NSF-supported Southern Sierra Critical Zone Observatory: time-series water sampling, sample pre-treatment in the field and shipping was done by M. Meadows (University of California, Merced); C. Hunsacker (US Forest Service, Fresno) is thanked for field support and daily Providence Creek discharge data (http://criticalzone.org/sierra/data). We thank M. Oelze (GFZ), F. Lang (University of Freiburg), W. Wilcke (KIT, Karlsruhe), and D. Calmels (UPSud, Orsay) for discussions. D.U. and F.v.B. are grateful for funding by the German National Science Foundation priority Program 1685 “Ecosystem nutrition: forest strategies for limited phosphorus resources”.

4.9 Supplementary Tables

Supplementary Table 4-1 Sierra Nevada (CA), analyses of water samples.

					field measurements					ICP-OES analyses							Q-ICP-MS	IC analyses				Mg isotope data (MC-ICP-MS)						
sample ID	**IGSN †**	**catchment**	**sampling date**	**sample type**	**pH**	**T**	**conductivity**	**discharge**	**alkalinity**	**K**	**Na**	**Mg**	**Ca**	**Si**	**Ba**	**Sr**	**P**	**Cl**	**NO_3**	**PO_4**	**SO_4**	**$d^{26}Mg$**	**2SD**	**$d^{25}Mg$**	**2SD**	**n**	**d**	**c**
			(year month day)			(ºC)	(µS/cm)	(liter/sec)	(mg/l)	(µg/g)	(µg/g)	(µg/g)	(µg/g)	(µg/g)	(µg/g)	(µg/g)	(µg/kg)	(µg/g)	(µg/g)	(µg/g)	(µg/g)	(‰)	(‰)	(‰)	(‰)			
P300 creek water																												
SNW34	GFFB1000X	P300	2012 June 6	creek water	7.4	11	55		n.d.	1.1	4.0	1.1	6.5	12	0.02	0.08	21	0.34	<0.1	<0.4	<0.2	-0.73	0.03	-0.39	0.04	3	1	1
SNW61	GFFB10010	P300	2014 April 15	creek water	6.4	7.9	64		n.d.	1.1	4.2	1.1	6.7	12	0.02	0.08	26	n.d.	<0.1	n.d.	n.d.							
SNW13	GFFB1000V	P300	2010 May 22	creek water	7.2	5.1	40		23	0.83	2.5	0.61	3.7	9.3	0.01	0.05	12	1.8	<0.1	n.d.	0.38	-0.71	0.04	-0.35	0.06	3	1	1
SNW56	GFFB1000Z	P300	2013 June 03	creek water	n.d.	11	n.d.		n.d.	1.2	4.4	1.1	7.0	13	0.02	0.09	28	0.59	<0.1	<0.1	0.25							
SNW44	GFFB1000Y	P300	2012 July 31	creek water	7.5	13	66		n.d.	1.2	4.5	1.2	7.4	13	0.02	0.09	33	0.40	<0.1	<0.4	<0.2	-0.66		-0.35		1	1	1
SNW24	GFFB1000U	P300	2011 November 7	creek water	7.1	3.5	65		n.d.	1.4	4.0	1.2	6.9	12	0.02	0.09	24	0.66	<0.1	<0.4	<0.2	-0.67	0.05	-0.34	0.01	2	1	1
SNW29	GFFB1000W	P300	2011 December 12	creek water	n.d.	n.d.	n.d.		n.d.	1.1	4.1	1.2	6.9	13	0.02	0.09	19	0.49	<0.1	<0.4	<0.2	-0.73	0.04	-0.36	0.04	3	1	1
P301 creek water																												
SNW58	GFFB1000H	P301	2014 April 15	creek water	5.3	6.3	36	2.2	n.d.	0.83	3.2	0.41	2.9	9.9	0.01	0.04	11	n.d.	<0.1	n.d.	n.d.							
SNW10	GFFB10007	P301	2010 May 22	creek water	6.5	4	37.8		18	0.72	2.2	0.36	2.5	7.8	0.01	0.04	4.5	0.42	<0.1	n.d.	0.16	-0.79	0.02	-0.40	0.03	3	1	1
SNW53	GFFB1000J	P301	2013 June 03	creek water	n.d.	11	n.d.		n.d.	0.98	3.4	0.58	4.4	11	0.02	0.06	17	0.65	<0.1	<0.1	0.19							
SNW31	GFFB1000G	P301	2012 June 6	creek water	7.2	9.2	40.3		n.d.	1.0	3.2	0.60	4.4	11	0.02	0.06	12	0.31	<0.1	<0.4	<0.2	-0.80	0.02	-0.41	0.04	3	1	1
SNW41	GFFB1000F	P301	2012 July 31	creek water	6.7	14	49		n.d.	1.1	3.5	0.69	5.2	12	0.02	0.07	18	0.44	<0.1	<0.4	<0.2	-0.78	0.05	-0.40	0.03	3	1	1
SNW21	GFFB1000D	P301	2011 November 7	creek water	7.2	3.8	44.7		n.d.	1.1	3.4	0.63	4.6	11	0.02	0.06	17	0.40	<0.1	<0.4	0.20	-0.75	0.03	-0.40	0.08	3	1	1
SNW26	GFFB10003	P301	2011 December 12	creek water	n.d.	n.d.	n.d.		n.d.	1.0	3.3	0.62	4.5	11	0.02	0.06	12	0.41	<0.1	<0.4	<0.2	-0.78	0.11	-0.41	0.04	2	1	1
P303 creek water																												
SNW59	GFFB1001E	P303	2014 April 15	creek water	4.9	6.5	65	1.2	n.d.	1.2	4.0	0.93	5.9	12	0.02	0.08	31	n.d.	<0.1	n.d.	n.d.							
SNW11	GFFB1001A	P303	2010 May 23	creek water	6.7	4.1	41		21	0.81	2.3	0.55	3.2	8.9	0.01	0.04	9.9	1.3	0.11	n.d.	0.29	-0.75	0.09	-0.38	0.01	3	1	1
SNW54	GFFB1001C	P303	2013 June 03	creek water	n.d.	10	n.d.		n.d.	1.2	4.0	0.91	5.7	12	0.02	0.08	25	0.71	<0.1	<0.1	0.16							
SNW32	GFFB1001D	P303	2012 June 6	creek water	6.7	9.5	51		n.d.	1.1	3.7	0.90	5.4	12	0.02	0.07	18	0.43	<0.1	<0.4	<0.2	-0.88	0.03	-0.44	0.02	2	1	1
SNW42	GFFB1001B	P303	2012 July 31	creek water	6.9	13	65		n.d.	1.2	4.1	0.94	5.8	13	0.02	0.08	25	0.43	<0.1	<0.4	<0.2	-0.74	0.02	-0.38	0.01	3	1	1
SNW22	GFFB10019	P303	2011 November 7	creek water	6.9	5.2	59		n.d.	1.2	3.9	1.1	6.4	10	0.03	0.08	n.d.	0.41	<0.1	<0.4	<0.2	-0.71		-0.35		1	1	1
SNW27	GFFB10018	P303	2011 December 12	creek water	n.d.	n.d.	n.d.		n.d.	1.1	3.6	0.88	5.3	12	0.02	0.07	20	0.46	<0.1	<0.4	<0.2	-0.79	0.05	-0.41	0.04	3	1	1
P304 creek water																												
SNW60	GFFB10017	P304	2014 April 15	creek water	6.0	7.4	73	1.8	n.d.	1.4	4.6	1.3	7.9	13	0.02	0.10	23	n.d.	<0.1	n.d.	n.d.							
SNW12	GFFB10013	P304	2010 May 23	creek water	7.3	5.6	52		32	1.1	3.4	0.88	5.4	11	0.02	0.07	12	4.55	0.28	n.d.	0.50	-0.78	0.08	-0.41	0.02	3	1	1
SNW55	GFFB10016	P304	2013 June 03	creek water	n.d.	12	n.d.		n.d.	0.80	4.7	1.2	7.9	13	0.02	0.10	20	0.62	0.23	<0.1	0.24							
SNW33	GFFB10014	P304	2012 June 6	creek water	7.7	12	61		n.d.	1.0	4.3	1.2	7.3	13	0.02	0.09	16	0.22	<0.1	<0.4	<0.2							
SNW43	GFFB10015	P304	2012 July 31	creek water	7.7	15	64		n.d.	1.0	4.6	1.1	7.6	13	0.02	0.10	25	0.30	<0.1	<0.4	<0.2	-0.82	0.10	-0.40	0.08	3	1	1
SNW23	GFFB10012	P304	2011 November 7	creek water	7.6	3.5	69		n.d.	2.1	4.2	1.2	7.3	13	0.02	0.09	22	0.96	<0.1	<0.4	<0.2	-0.69		-0.36		1	1	1
SNW28	GFFB10011	P304	2011 December 12	creek water	n.d.	n.d.	n.d.		n.d.	1.3	4.2	1.1	7.0	13	0.02	0.09	19	n.d.	<0.1	n.d.	n.d.	-0.83	0.05	-0.42	0.06	3	1	1
																						mean creek water of P300, P301, P303, P304 (n=19):		***-0.76***	***0.11***	***-0.39***	***0.06***		
international reference materials for isotope data quality control																												
Cambridge-1 (processed through column chemistry)																						-2.61	0.09	-1.35	0.05	6	1	1
Cambridge-1 (Apex)																						-2.61	0.10	-1.35	0.06	99	0	0
Cambridge-1 (SIS)																						-2.59	0.09	-1.34	0.05	99	0	0
Seawater (OSIL) (Apex)																						-0.81	0.05	-0.40	0.05	2	1	1
Seawater (OSIL) (SIS)																						-0.85	0.07	-0.43	0.07	4	1	1
SRM 1640a natural spring water (Apex)																						-0.69	0.20	-0.36	0.07	2	1	1
SRM 1640a natural spring water (SIS)																						-0.73	0.05	-0.39	0.06	6	3	3
SLRS-5 river water (Apex)																						-1.31	0.03	-0.67	0.03	2	1	1
SLRS-5 river water (SIS)																						-1.28	0.10	-0.67	0.07	10	3	3

continued next page …

Supplementary Table 4-1 continued - Sierra Nevada (CA), analyses of water samples.

	ICP-OES analyses							Q-ICP-MS	IC analyses				Mg isotope data (MC-ICP-MS)						
	K	**Na**	**Mg**	**Ca**	**Si**	**Ba**	**Sr**	**P**	**Cl**	**NO_3**	**PO_4**	**SO_4**	**$d^{26}Mg$**	**2SD**	**$d^{25}Mg$**	**2SD**	**n**	**d**	**c**
	(µg/g)	(µg/g)	(µg/g)	(µg/g)	(µg/g)	(µg/g)	(µg/g)	(µg/kg)	(µg/g)	(µg/g)	(µg/g)	(µg/g)	(‰)	(‰)	(‰)	(‰)			
international reference materials and in-house standards for concentration data quality control																			
SRM 1640a natural spring water mean (n=10 (ICP-OES); n=2 (iCAP-Q))	0.60	3.2	1.1	5.6	5.2	0.15	0.13	*7.9*											
SRM 1640a natural spring water SD (n=10 (ICP-OES); n=2 (iCAP-Q))	0.03	0.07	0.02	0.07	0.12	0.002	0.001	*0.04*											
SRM 1640a natural spring water certified value	*0.58*	*3.11*	*1.05*	*5.57*	*5.17*	*0.15*	*0.13*	*n.r.*											
SRM 1640a natural spring water certified uncertainty	*0.002*	*0.03*	*0.003*	*0.02*	*0.02*	*0.001*	*0.001*	*n.r.*											
relative difference (measured/certified) (%)	**4%**	**2%**	**1%**	**1%**	**0%**	**1%**	**2%**	**-**											
SLRS-5 mean (n=10 (ICP-OES); n=1 (iCAP-Q))	0.86	5.3	2.5	11	2.0	<0.06	0.05	16											
SLRS-5 SD (n=10 (ICP-OES); n=1 (iCAP-Q))	0.04	0.18	0.04	0.15	0.08	-	0.00	-											
SLRS-5 certified value	*0.84*	*5.4*	*2.5*	*11*	*1.9**	*0.01*	*0.05*	*13**											
SLRS-5 certified uncertainty	*0.04*	*0.10*	*0.16*	*0.40*	*0.08**	*0.001*	*0.001*	*2.2**											
relative difference (measured/certified) (%)	**2%**	**-2%**	**-1%**	**0%**	**1%**	**-**	**0%**	**19%**											
GFZ RW-1 (n=23)	0.59	3.2	1.0	5.6	5.3	<0.06	0.10												
GFZ RW-1 SD (n=23)	0.05	0.13	0.03	0.17	0.14		0.00												
GFZ RW-1b reference values	*0.56*	*3.2*	*1.0*	*5.5*	*5.3*	*n.d.*	*0.10*												
GFZ RW-1b reference uncertainty	*0.01*	*0.01*	*0.01*	*0.01*	*0.01*		*0.01*												
relative difference (measured/reference) (%)	**4%**	**0%**	**0%**	**1%**	**1%**	**-**	**0%**												
USGS M212 (n=3 (ICP-OES); n=2 (iCAP-Q))	0.61	8.9	2.0	5.7	2.9	0.01	0.02	31.95											
USGS M212 SD (n=3 (ICP-OES); n=2 (iCAP-Q))	0.003	0.11	0.01	0.05	0.003	0.001	0.001	0.24											
USGS M212 certified value	*0.59*	*8.7*	*2.0*	*5.6*	*2.8*		*0.02*	*30*											
USGS M212 certified uncertainty	*0.03*	*0.46*	*0.10*	*0.29*	*0.23*		*0.001*	*4.0*											
relative difference (measured/certified) (%)	**3%**	**2%**	**-1%**	**3%**	**4%**	**-**	**-3%**	**6%**											
USGS T187 (n=3)	9.1	17	12	4.0	3.1	0.1	0.0												
USGS T187 SD (n=3)	0.04	0.15	0.05	0.01	0.01	0.001	0.001												
USGS T187 certified value	*8.7*	*18*	*13*	*3.9*	*3.0*	*0.1*	*0.0*												
USGS T187 certified uncertainty	*0.28*	*0.78*	*0.39*	*0.13*	*0.36*	*0.002*	*0.001*												
relative difference (measured/certified) (%)	**4%**	**-3%**	**-4%**	**2%**	**3%**	**1%**	**-1%**												
international reference materials and in-house standards for concentration data quality control																			
USGS T213 (n=2)	9.2	>34	4.0	62	3.0	0.02	0.27												
USGS T213 SD (n=2)	0.02	0.05	0.01	0.09	0.02	0.001	0.001												
USGS T213 certified value	*8.9*	*38*	*4.1*	*63*	*2.9*	*0.02*	*0.28*												
USGS T213 uncertainty	*0.28*	*2.1*	*0.14*	*2.5*	*0.32*	*0.001*	*0.01*												
relative difference (measured/certified) (%)	**3%**	**-**	**-1%**	**-2%**	**4%**	**0%**	**-1%**												

Alkalinity was obtained by titration with 0.01M HCl to a pH of 4.3 and given as HCO_3^- in mg/l with an uncertainty estimate of 10% relative.
Uncertainties on ICP-OES concentration data are estimated to be <6% relative, based on repeat analyses of reference materials.
Uncertainties on Q-ICP-MS concentration data are estimated to be <19% (P) relative, based on analyses of reference materials.
Uncertainty on anions measured by Ion Chromatography (IC) are estimated at about 10% relative.
n.d. = not determined; n.r. = not reported
* not certified but reported in GeoReM
n = number of Mg isotope mass spectrometry analysis
d = number of individual sample dissolutions
c = number of independent processing through Mg column purification
† IGSN, International Geo Sample Number, www.igsn.org (syntax e.g. igsn.org/GFFB1000X)

Supplementary Table 4-2 Sierra Nevada (CA), analyses of plant samples.

sample ID	IGSN †	sampling date (year month day)	brief sample description	ICP-OES analyses Al (µg/g)	Ba (µg/g)	Ca (µg/g)	Cu (µg/g)	Fe (µg/g)	K (µg/g)	Mg (µg/g)	Mn (µg/g)	Na (µg/g)	Pb (µg/g)	Si (µg/g)	Sr (µg/g)	Zn (µg/g)	Mg isotope data (MC-ICP-MS) δ^{26}Mg (‰)	2SD (‰)	δ^{25}Mg (‰)	2SD (‰)	n	d	c
fresh foliage																							
MW1	GFFB1002Z	2010 May 23	Ponderosa Pine - needles	288	21	8880	2.3	123	4512	1445	376	22	< 0.3	387	33	34	-0.72	0.06	-0.36	0.10	2	1	1
MW2	GFFB10030	2010 May 23	Jeffrey Pine - needles	343	6.8	4031	2.5	66	1632	785	78	6.9	< 0.3	245	14	13	-0.43		-0.21		1	1	1
MW3	GFFB10031	2010 May 23	Manzanita - leaves	55	35	6710	4.0	44	2149	599	18	29	< 0.3	222	38	14	-0.33	0.06	-0.16	0.09	2	1	1
MW4	GFFB10032	2010 May 23	Whitethorn - leaves	1408	58	9539	5.4	737	3828	1150	151	53	0.9	611	64	14	-0.10	0.19	-0.05	0.08	2	1	1
fresh wood																							
MW6	GFFB10033	2010 May 23	Ponderosa Pine - wood	49	2.2	623	2.1	29	1882	287	18	2.8	< 0.3	43	4.6	12	-0.16	0.04	-0.06	0.03	2	1	1
MW5	GFFB10034	2010 May 23	Jeffrey Pine - wood	56	9.3	1575	1.2	27	1305	309	34	8.2	< 0.3	52	13	8.3	-0.15	0.02	-0.08	0.01	2	1	1
MW8	GFFB10035	2010 May 23	Manzanita - wood	33	53	5986	2.2	27	4606	1195	76	38	< 0.3	118	52	18	0.01	0.02	0.01	0.03	2	1	1
MW7	GFFB10036	2010 May 23	Whitethorn - wood	125	49	4223	3.2	76	3063	749	62	38	< 0.3	147	41	10	0.16	0.00	0.08	0.00	2	1	1
litter from forest floor																							
MW9	GFFB1003G	2010 May 23	mixed (soil + duff/litter) P303	24760	288	8268	8.3	9900	2406	3243	1789	243	10	245	69	57	-0.21		-0.11		1	1	1
SN63	GFFB1003F	2010 May 23	needles from duff/litter P303	n.d.	n.d.	n.d.	n.d.	n.d.	n.d.	>1305	n.d.	n.d.	n.d.	n.d.	n.d.	n.d.	-0.47	0.07	-0.23	0.03	5	1	1
SN63	GFFB1003E	2010 May 23	twigs from duff/litter P303	n.d.	n.d.	n.d.	n.d.	n.d.	n.d.	>891	n.d.	n.d.	n.d.	n.d.	n.d.	n.d.	-0.43	0.06	-0.22	0.04	4	1	1
SN63	GFFB1003D	2010 May 23	bark from litter P303	n.d.	n.d.	n.d.	n.d.	n.d.	n.d.	>680	n.d.	n.d.	n.d.	n.d.	n.d.	n.d.	-0.42	0.11	-0.20	0.07	4	1	1
plant debris from sediment pond																							
SN52	GFFB1003C	2013.00	needles from sediment pond P303	n.d.	n.d.	n.d.	n.d.	n.d.	n.d.	>470	n.d.	n.d.	n.d.	n.d.	n.d.	n.d.	-0.50	0.06	-0.25	0.06	3	1	1
SN52	GFFB1003B	2013.00	twigs from sediment pond P303	n.d.	n.d.	n.d.	n.d.	n.d.	n.d.	>605	n.d.	n.d.	n.d.	n.d.	n.d.	n.d.	-0.59	0.14	-0.31	0.11	3	1	1
SN47	GFFB1003A	2011.00	bark from sediment pond P303	n.d.	n.d.	n.d.	n.d.	n.d.	n.d.	>596	n.d.	n.d.	n.d.	n.d.	n.d.	n.d.	-0.24	0.05	-0.11	0.08	3	1	1
SN52	GFFB10039	2013.00	bark from sediment pond P303	n.d.	n.d.	n.d.	n.d.	n.d.	n.d.	>646	n.d.	n.d.	n.d.	n.d.	n.d.	n.d.	-0.59	0.07	-0.31	0.06	5	1	1
international reference materials for isotope data quality control																							
SRM 1515 Apple leaves (Apex)																	-1.26	0.07	-0.65	0.02	4	1	1
SRM 1515 Apple leaves (SIS)																	-1.20	0.10	-0.62	0.07	17	3	4
international reference materials for concentration data quality control																							
SRM 1515 Apple leaves				246	39	13004	4.6	65	12677	2250	45	32	0.52	204	17	8.9							
SRM 1515 Apple leaves*				n.d.	n.d.	n.d.	n.d.	n.d.	n.d.	> 2447	n.d.	n.d.	n.d.	n.d.	n.d.	n.d.							
SRM 1515 Apple leaves certified value				*286*	*49*	*15260*	*5.6*	*83*	*16100*	*2710*	*54*	*24*	*0.47*	*400*	*25*	*13*							
SRM 1515 Apple leaves certified absolute uncertainty				*9.0*	*2.0*	*150*	*0.24*	*5.0*	*200*	*80*	*3.0*	*1.2*	*0.02*	*0.04*	*2.0*	*0.30*							
SRM 1515 Apple leaves certified relative uncertainty				*0.03*	*0.04*	*0.01*	*0.04*	*0.06*	*0.01*	*0.03*	*0.06*	*0.05*	*0.05*	*0.00*	*0.08*	*0.02*							
relative difference (%)				**-0.14**	**-0.20**	**-0.15**	**-0.18**	**-0.21**	**-0.21**	**-0.17**	**-0.17**	**0.31**	**0.10**	**-0.49**	**-0.33**	**-0.29**							

Uncertainties on ICP-OES concentration data are estimated to be 20% (except Na, Sr, Zn: 30%) relative, based on repeat analyses of reference materials
* replicate dissolution; analysed within the same sample batch as samples SN47, SN52, SN63
n.d. = not determined
SRM 1515 reference value for Si from Barros et al. (2016)
n = number of Mg isotope mass spectrometry analysis
d = number of individual sample dissolutions
c = number of independent processing through Mg column purification
† IGSN, International Geo Sample Number, www.igsn.org (syntax e.g. igsn.org/GFFB1000X)

Supplementary Table 4-3a Sierra Nevada (CA), analyses of soil, saprolite, rock, bedload sediment and suspended load.

					Raw data (major oxides)													Raw data (trace elements)										
sample ID	**IGSN †**	**brief sample description**	**XRF lab**	**depth**	**SiO_2**	**TiO_2**	**Al_2O_3**	**Fe_2O_3**	**MnO**	**MgO**	**CaO**	**Na_2O**	**K_2O**	**P_2O_5**	**H_2O**	**CO_2**	**LOI**	**Sum**	**Ba**	**Cr**	**Ga**	**Nb**	**Ni**	**Rb**	**Sr**	**V**	**Y**	**Zn**	**Zr**
				(cm)	(wt%)	(wt%)	(wt%)	(wt%)	(wt%)	(wt%)	(wt%)	(wt%)	(wt%)	(wt%)	(wt%)	(wt%)	(wt%)	(wt%)	(µg/g)	(µg/g)	(µg/g)	(µg/g)	(µg/g)	(µg/g)	(µg/g)	(µg/g)	(µg/g)	(µg/g)	(µg/g)
P301 regolith depth profile																												
SN01	GFFB1002T	bulk soil	GFZ	7	36	0.55	11	3.9	0.42	1.6	4.5	1.3	1.9	0.36	n.d.	n.d.	38	99.66	1073	33	14	14	18	83	317	69	16	88	110
SN02	GFFB1002U	bulk soil	GFZ	20	49	0.71	15	4.8	0.17	1.9	3.2	1.9	2.2	0.26	n.d.	n.d.	20	99.69	781	30	16	13	16	93	286	87	20	80	149
SN02e	GFFB1002U	exchangeable soil*	-	20	n.d.	<lod	14	2.1	8.9	101	2700	72	206	n.d.	n.d.	n.d.	n.d.		64	<lod	<lod	n.d.	<lod	n.d.	19	n.d.	n.d.	<lod	n.d.
SN02r	GFFB1002U	residuum soil	-	20	n.d.	0.84	14	5.7	0.09	2.2	2.8	2.0	2.5	n.d.	n.d.	n.d.	n.d.		708	<lod	<lod	n.d.	<lod	n.d.	253	n.d.	n.d.	114	n.d.
SN03	GFFB1002V	bulk soil	GFZ	30	58	0.88	18	6.4	0.12	2.5	3.7	2.1	2.3	0.23	n.d.	n.d.	6.3	99.74	863	38	21	13	16	114	332	122	24	102	174
SN04	GFFB1002R	bulk soil	GFZ	39	57	0.93	18	6.9	0.11	2.7	3.7	1.9	2.3	0.22	n.d.	n.d.	6.8	99.67	825	39	20	15	19	114	313	130	24	96	175
SN04e	GFFB1002R	exchangeable soil*	-	39	n.d.	<lod	5	0.66	8.1	65	763	43	152	n.d.	n.d.	n.d.	n.d.		38	<lod	<lod	n.d.	<lod	n.d.	5.55	n.d.	n.d.	<lod	n.d.
SN04r	GFFB1002R	residuum soil	-	39	n.d.	0.91	15	7.0	0.11	2.9	3.7	1.8	2.2	n.d.	n.d.	n.d.	n.d.		891	<lod	<lod	n.d.	<lod	n.d.	289.7	n.d.	n.d.	121	n.d.
SN05	GFFB1002S	bulk soil	GFZ	53	57	0.97	18	7.0	0.11	2.7	3.6	1.8	2.3	0.19	n.d.	n.d.	6.1	99.71	835	44	19	16	18	108	311	141	25	97	179
SN06	GFFB1002P	bulk soil	GFZ	65	57	0.97	18	7.1	0.11	2.7	3.7	1.9	2.2	0.19	n.d.	n.d.	5.8	99.75	777	43	21	15	20	109	307	139	24	100	180
SN07	GFFB1002Q	bulk soil	GFZ	77	58	0.96	18	7.0	0.11	2.7	3.7	1.8	2.2	0.18	n.d.	n.d.	5.1	99.74	803	41	21	14	16	109	313	133	24	94	181
SN08	GFFB1002W	bulk soil	GFZ	89	56	1.0	19	7.7	0.12	2.9	3.7	1.7	2.2	0.18	n.d.	n.d.	5.3	99.72	773	44	22	15	21	111	300	151	26	101	205
SN09	GFFB1002X	bulk soil	GFZ	100	56	1.0	19	7.7	0.12	2.9	3.6	1.8	2.3	0.18	n.d.	n.d.	4.6	99.72	833	43	23	14	19	109	299	151	26	100	207
SN10	GFFB1002Y	bulk soil	GFZ	111	56	0.97	18	7.4	0.12	2.8	3.5	1.6	2.2	0.16	5.7	0.96	6.7	99.70	766	45	21	15	16	108	287	143	25	92	194
Balsam regolith depth profile																												
SN59	GFFB10022	bulk soil	GFZ	5	54	0.98	18	7.7	0.19	2.7	3.5	1.5	2.1	0.28	n.d.	n.d.	9.1	99.67	716	23	19	14	<10	101	222	137	29	115	268
SN60	GFFB10023	bulk soil	GFZ	35	54	1.1	20	8.6	0.14	2.9	3.6	1.4	2.1	0.17	n.d.	n.d.	5.6	99.65	677	23	23	14	<10	113	222	151	28	117	249
SN61	GFFB10024	bulk soil	GFZ	65	55	1.0	19	8.5	0.14	2.9	3.7	1.4	2.0	0.13	n.d.	n.d.	6.3	99.66	667	20	20	15	<10	105	221	155	27	109	249
SN62	GFFB10025	bulk soil	GFZ	85	57	1.0	18	8.6	0.14	2.9	3.7	1.4	2.0	0.13	n.d.	n.d.	4.8	99.67	636	26	20	12	<10	108	223	162	29	102	240
SN20	GFFB1002K	bulk soil	GFZ	178	56	1.0	19	9.3	0.10	2.7	1.9	0.41	2.1	0.05	7.6	0.37	7.9	99.74	651	33	23	15	12	103	109	172	25	82	167
SN20e	GFFB1002K	exchangeable soil*	-	178	n.d.	<lod	<lod	<lod	13	269	584	123	68	n.d.	n.d.	n.d.	n.d.		114	<lod	<lod	n.d.	<lod	n.d.	6	n.d.	n.d.	<lod	n.d.
SN20r	GFFB1002K	residuum soil	-	178	n.d.	0.14	15	9.6	0.08	2.0	1.8	0.59	1.7	n.d.	n.d.	n.d.	n.d.		484	<lod	<lod	n.d.	<lod	n.d.	<lod	n.d.	n.d.	<lod	n.d.
SN19	GFFB1002J	bulk soil	GFZ	257	56	1.0	19	8.3	0.10	2.8	2.5	0.69	2.3	0.04	6.6	0.25	6.9	99.76	744	31	20	14	12	102	167	143	26	86	178
SN18	GFFB1002N	bulk saprolite	GFZ	287	53	1.2	19	9.3	0.14	3.7	3.9	1.2	1.9	0.04	6.2	0.17	6.4	99.71	518	36	21	17	14	104	201	175	33	106	175
SN17	GFFB1002M	bulk saprolite	GFZ	330	57	0.94	19	7.3	0.14	2.8	3.9	1.5	2.3	0.04	5.3	0.30	5.6	99.75	753	28	21	14	11	103	267	134	25	85	178
SN16	GFFB1002H	bulk saprolite	GFZ	414	58	0.96	18	7.5	0.12	2.9	3.7	1.4	2.2	0.07	5.0	0.19	5.2	99.73	747	33	21	17	13	120	279	136	29	79	174
SN16e	GFFB1002H	exchangeable saprolite*	-	414	n.d.	<lod	<lod	<lod	10	219	395	117	45	n.d.	n.d.	n.d.	n.d.		109	<lod	<lod	n.d.	<lod	n.d.	11	n.d.	n.d.	<lod	n.d.
SN16r	GFFB1002H	residuum saprolite	-	414	n.d.	0.70	17	5.5	0.08	2.3	3.7	1.5	1.8	n.d.	n.d.	n.d.	n.d.		632	<lod	<lod	n.d.	<lod	n.d.	277	n.d.	n.d.	<lod	n.d.
SN15	GFFB1002G	bulk saprolite	GFZ	513	59	0.90	17	6.8	0.10	2.6	4.5	1.9	2.1	0.16	3.8	0.08	3.9	99.72	734	27	20	14	10	91	324	126	24	79	161
SN14	GFFB1002L	bulk saprolite	GFZ	605	59	1.0	17	7.6	0.12	3.0	3.9	1.5	2.1	0.11	4.5	0.11	4.6	99.75	613	28	21	14	11	111	262	141	25	85	161
SN14e	GFFB1002L	exchangeable saprolite*	-	605	n.d.	<lod	<lod	<lod	8	349	401	89	31	n.d.	n.d.	n.d.	n.d.		80	<lod	<lod	n.d.	<lod	n.d.	9	n.d.	n.d.	<lod	n.d.
SN14r	GFFB1002L	residuum saprolite	-	605	n.d.	0.96	19	7.2	0.11	2.8	4.9	2.2	1.9	n.d.	n.d.	n.d.	n.d.		547	<lod	<lod	n.d.	<lod	n.d.	331	n.d.	n.d.	<lod	n.d.
Creek sediment loads																												
SN46	GFFB10038	suspended load, P301 filter	-	-																								
SN47	GFFB10037	suspended load. P300 filter	-	-																								

continued next page …

Supplementary Table 4-3a continued - Sierra Nevada (CA), analyses of soil, saprolite, rock, bedload sediment and suspended load.

					Raw data (major oxides)													Raw data (trace elements)										
sample ID	**IGSN †**	**brief sample description**	**XRF lab**	**depth**	**SiO_2**	**TiO_2**	**Al_2O_3**	**Fe_2O_3**	**MnO**	**MgO**	**CaO**	**Na_2O**	**K_2O**	**P_2O_5**	**H_2O**	**CO_2**	**LOI**	**Sum**	**Ba**	**Cr**	**Ga**	**Nb**	**Ni**	**Rb**	**Sr**	**V**	**Y**	**Zn**	**Zr**
				(cm)	(wt%)	(wt%)	(wt%)	(wt%)	(wt%)	(wt%)	(wt%)	(wt%)	(wt%)	(wt%)	(wt%)	(wt%)	(wt%)	(wt%)	(µg/g)	(µg/g)	(µg/g)	(µg/g)	(µg/g)	(µg/g)	(µg/g)	(µg/g)	(µg/g)	(µg/g)	(µg/g)
Rocks																												
SN30	GFFB10004	Granodiorite	Acme	-	61	0.81	16	6.8	0.12	2.8	5.3	3.2	2.4	0.25	n.d.	n.d.	1.4	100.24	700	27	n.d.	n.d.	<10	n.d.	490	129	n.d.	130	130
SN31	GFFB1000B	Granodiorite	Acme	-	62	0.79	17	6.1	0.10	2.6	5.4	3.3	2.4	0.19	n.d.	n.d.	0.72	100.46	700	41	n.d.	n.d.	<10	n.d.	470	118	n.d.	110	100
SN32	GFFB10009	Granodiorite	Acme	-	68	0.53	15	4.9	0.08	1.6	3.3	3.0	3.6	0.14	n.d.	n.d.	0.49	100.19	1300	27	n.d.	n.d.	<10	n.d.	430	67	n.d.	100	100
SN33	GFFB1000A	Granodiorite	Acme	-	67	0.50	15	4.7	0.07	1.6	3.6	3.2	3.3	0.13	n.d.	n.d.	0.62	100.19	1200	34	n.d.	n.d.	<10	n.d.	410	62	n.d.	90	110
SN34	GFFB1000E	Granodiorite	Acme	-	68	0.53	14	5.2	0.08	1.6	3.3	2.9	3.4	0.14	n.d.	n.d.	0.45	100.05	1200	41	n.d.	n.d.	<10	n.d.	340	78	n.d.	90	100
SN35	GFFB1001W	Granodiorite/Tonalite -am-bt-rich	Acme	-	52	1.21	18	9.8	0.16	4.7	8.1	3.1	1.5	0.31	n.d.	n.d.	1.4	100.09	500	55	n.d.	n.d.	<10	n.d.	560	218	n.d.	140	70
SN36	GFFB1001X	Granodiorite/Tonalite -am-bt-rich	Acme	-	61	0.89	17	6.7	0.10	3.0	5.2	2.8	1.5	0.20	n.d.	n.d.	2.3	99.75	500	41	n.d.	n.d.	<10	n.d.	480	157	n.d.	100	80
SN37	GFFB1001Y	Granodiorite/Tonalite -am-bt-rich	Acme	-	57	1.11	17	8.6	0.14	3.7	6.2	3.1	1.9	0.26	n.d.	n.d.	1.1	99.87	600	21	n.d.	n.d.	<10	n.d.	470	162	n.d.	130	110
SN38	GFFB1001Z	Granodiorite/Tonalite -am-bt-rich	Acme	-	57	1.07	17	8.3	0.14	3.5	6.3	3.2	1.7	0.29	n.d.	n.d.	1.2	99.80	500	27	n.d.	n.d.	20	n.d.	510	179	n.d.	120	110
SN39	GFFB10020	Granodiorite/Tonalite -am-bt-rich	Acme	-	53	1.34	18	9.3	0.14	4.6	8.2	3.1	1.5	0.26	n.d.	n.d.	0.92	100.24	500	41	n.d.	n.d.	<10	n.d.	590	218	n.d.	140	70
SN40	GFFB1001T	Granodiorite/Tonalite -am-bt-rich	Acme	-	58	0.95	17	8.0	0.12	3.7	6.9	2.8	1.4	0.23	n.d.	n.d.	1.05	99.59	600	62	n.d.	n.d.	20	n.d.	590	185	n.d.	140	60
SN13	GFFB10021	weathered Granodiorite	GFZ	688	59	0.96	17	7.3	0.11	2.9	5.7	2.5	1.5	0.25	3.2	0.13	3.3	99.71	531	31	20	16	11	62	393	141	26	86	178
SN12	GFFB10027	weathered Granodiorite	GFZ	696	59	0.96	16	7.4	0.12	3.0	5.8	2.6	2.3	0.23	1.9	0.06	2.0	99.70	761	28	17	13	13	93	402	144	23	87	191
SN11	GFFB10026	weathered Granodiorite	GFZ	-	68	0.54	15	4.3	0.07	1.5	3.6	2.6	3.8	0.10	1.2	0.04	1.2	99.78	634	17	15	14	11	145	273	72	21	50	137
SN41	GFFB1001N	Granodiorite	Acme	-	60	0.92	17	7.2	0.11	3.0	6.0	3.1	2.2	0.18	n.d.	n.d.	0.63	99.79	600	14	n.d.	n.d.	<10	n.d.	410	157	n.d.	130	130
SN42	GFFB1001P	Granodiorite	Acme	-	60	0.88	17	6.8	0.11	2.9	6.0	3.2	2.2	0.19	n.d.	n.d.	0.56	99.85	700	21	n.d.	n.d.	<10	n.d.	370	151	n.d.	100	130
SN43	GFFB1001Q	Granodiorite	Acme	-	60	0.84	17	6.7	0.10	2.7	5.9	3.2	2.2	0.18	n.d.	n.d.	0.81	99.17	700	109	n.d.	n.d.	120	n.d.	410	134	n.d.	110	80
SN44	GFFB1001R	Granodiorite	Acme	-	60	0.89	17	6.7	0.11	2.8	5.8	3.1	2.2	0.18	n.d.	n.d.	0.89	99.35	700	27	n.d.	n.d.	<10	n.d.	400	146	n.d.	110	110
SN45	GFFB1001S	Granodiorite	Acme	-	60	0.86	17	7.0	0.11	2.9	6.1	3.2	2.2	0.18	n.d.	n.d.	0.68	100.16	600	27	n.d.	n.d.	<10	n.d.	420	134	n.d.	120	130
international reference materials and inter lab comparison for concentration data quality control																												
SY-4 Diorite (CCRMP) (a)			Acme		50	0.27	21	6.2	0.11	0.54	8.0	7.2	1.6	0.13	n.d.	n.d.	4.6	99.68	500	6.8	n.d.	n.d.	<10	n.d.	1190	n.d.	n.d.	130	540
SY-4 Diorite (CCRMP) (b)			Acme		50	0.28	21	6.2	0.11	0.53	8.0	7.2	1.6	0.13	n.d.	n.d.	4.6	99.41	400	<7	n.d.	n.d.	10.0	n.d.	1190	n.d.	n.d.	120	530
SY-4 Diorite (CCRMP) (c)			Acme		50	0.27	21	6.2	0.11	0.54	8.0	7.2	1.6	0.13	n.d.	n.d.	4.6	99.67	400	<7	n.d.	n.d.	<10	n.d.	1210	n.d.	n.d.	130	550
SY-4 Diorite (CCRMP) certified value			Certificate		50	0.29	21	6.2	0.11	0.54	8.1	7.1	1.7	0.13	n.r.	3.5	4.6	99.24	340	12	35	13	9.0	55	1191	8.0	119	93	517
SY-4 Diorite (CCRMP) certified relative uncertainty			Certificate		0.1%	0.003%	0.1%	0.03%	0.001%	0.01%	0.04%	0.1%	0.02%	0.004%	n.r.	0.01%	0.1%		1.5%	8.3%	2.9%	7.7%	11%	3%	1.0%	25%	2%	2.2%	3.1%
SRM 2709a San Joaquin Soil (a)			GFZ		63	0.53	14	4.6	0.07	2.3	2.6	1.4	2.4	0.15	6.0	3.0	9.1	99.52	921	129	16	13	83	94	233	108	21	89	146
SRM 2709a San Joaquin Soil (b)			GFZ		51	0.43	11	3.5	0.05	1.9	2.1	1.2	2.0	0.12	n.d.	n.d.	26	99.65	687	95	13	<10	57	68	185	85	15	78	126
SN11 (BP Rock, weathered Granodiorite)			GFZ		68	0.54	15	4.3	0.07	1.5	3.6	2.6	3.8	0.10	1.2	0.04	1.2	99.78	634	17	15	14	11	145	273	72	21	50	137
SN11 (BP Rock, weathered Granodiorite)			Acme		68	0.55	15	4.2	0.07	1.6	3.6	2.9	3.8	0.11	n.d.	n.d.	0.7	100.13	700	82	n.d.	n.d.	50	n.d.	260	84	n.d.	80	70

n.d. = not determined; n.r. = not reported; lod = limit of detection; am = amphibole; bt = biotite

ICP-OES analyses have been performed on soil/saprolite exchangeable and soil/saprolite residuum fractions. The limits of detection are: Al, Cu, Fe, Sr, Ti: <0.06µg/g, Ni: <0.11µg/g, Ga: <0.66µg/g, Zn: <2.8µg/g.

Uncertainties on XRF concentration data are estimated to be ±5% relative for major elements (wt%) and 10% relative for Na and for trace elements (based on accuracy of analysed reference materials) and inter lab comparison (Acme and GFZ for SN11).

* oxide concentrations in µg/g

† IGSN, International Geo Sample Number, www.igsn.org (syntax e.g. igsn.org/GFFB1000X)

Supplementary Table 4-3b Sierra Nevada (CA), Loss on ignition (LOI)-corrected analyses of soil, saprolite, rock, bedload sediment and suspended load.

				LOI corrected data (major oxides)										LOI corrected data (trace elements)									
sample ID	**IGSN †**	**brief sample description**	**depth**	**LOI**	**SiO_2**	**TiO_2**	**Al_2O_3**	**Fe_2O_3**	**MnO**	**MgO**	**CaO**	**Na_2O**	**K_2O**	**P_2O_5**	**Ba**	**Cr**	**Ga**	**Nb**	**Ni**	**Rb**	**Sr**	**V**	**Y**	**Zn**	**Zr**
			(cm)	(wt%)	(wt%)	(wt%)	(wt%)	(wt%)	(wt%)	(wt%)	(wt%)	(wt%)	(wt%)	(wt%)	(µg/g)	(µg/g)	(µg/g)	(µg/g)	(µg/g)	(µg/g)	(µg/g)	(µg/g)	(µg/g)	(µg/g)	(µg/g)
P301 regolith depth profile																									
SN01	GFFB1002T	bulk soil	7	38	58	0.88	18	6.2	0.67	2.5	7.3	2.1	3.1	0.58	1717	53	22	22	29	133	507	110	26	141	176
SN02	GFFB1002U	bulk soil	20	20	62	0.89	19	6.1	0.21	2.4	4.0	2.4	2.8	0.33	980	38	20	16	20	117	359	109	25	100	187
SN02e	GFFB1002U	exchangeable soil	20																						
SN02r	GFFB1002U	residuum soil	20																						
SN03	GFFB1002V	bulk soil	30	6.3	61	0.93	19	6.9	0.12	2.7	4.0	2.2	2.5	0.25	921	41	22	14	17	122	354	130	26	109	186
SN04	GFFB1002R	bulk soil	39	6.8	61	1.0	19	7.3	0.12	2.8	4.0	2.0	2.4	0.23	885	42	21	16	20	122	336	139	26	103	188
SN04e	GFFB1002R	exchangeable soil	39																						
SN04r	GFFB1002R	residuum soil	39																						
SN05	GFFB1002S	bulk soil	53	6.1	60	1.0	19	7.5	0.11	2.9	3.9	2.0	2.4	0.20	889	47	20	17	19	115	331	150	27	103	191
SN06	GFFB1002P	bulk soil	65	5.8	60	1.0	19	7.6	0.11	2.9	3.9	2.0	2.3	0.20	824	46	22	16	21	116	326	147	25	106	191
SN07	GFFB1002Q	bulk soil	77	5.1	61	1.0	19	7.4	0.11	2.9	3.9	1.9	2.4	0.19	846	43	22	15	17	115	330	140	25	99	191
SN08	GFFB1002W	bulk soil	89	5.3	59	1.1	20	8.1	0.13	3.1	3.9	1.8	2.3	0.19	816	46	23	16	22	117	317	159	27	107	216
SN09	GFFB1002X	bulk soil	100	4.6	59	1.1	20	8.1	0.13	3.0	3.8	1.8	2.4	0.19	873	45	24	15	20	114	313	158	27	105	217
SN10	GFFB1002Y	bulk soil	111	6.7	60	1.0	19	7.9	0.13	3.0	3.8	1.8	2.3	0.17	821	48	22	16	17	116	307	153	27	99	208
Balsam regolith depth profile																									
SN59	GFFB10022	bulk soil	5	9.1	59	1.1	20	8.5	0.21	2.9	3.9	1.7	2.3	0.30	788	25	21	15	<11	111	244	151	32	126	295
SN60	GFFB10023	bulk soil	35	5.6	58	1.1	21	9.1	0.15	3.1	3.8	1.5	2.2	0.18	717	24	24	15	<11	120	235	160	30	124	264
SN61	GFFB10024	bulk soil	65	6.3	59	1.1	20	9.1	0.15	3.1	3.9	1.5	2.2	0.14	712	21	21	16	<11	112	236	165	29	116	266
SN62	GFFB10025	bulk soil	85	4.8	60	1.1	19	9.0	0.15	3.0	3.9	1.5	2.1	0.13	668	27	21	13	<11	113	234	170	30	107	252
SN20	GFFB1002K	bulk soil	178	7.9	60	1.1	20	10	0.11	2.9	2.1	0.4	2.3	0.06	707	36	25	16	13	112	118	187	27	89	181
SN20e	GFFB1002K	exchangeable soil	178																						
SN20r	GFFB1002K	residuum soil	178																						
SN19	GFFB1002J	bulk soil	257	6.9	61	1.1	20	8.9	0.11	3.0	2.7	0.7	2.4	0.04	799	33	21	15	13	110	179	154	28	92	191
SN18	GFFB1002N	bulk saprolite	287	6.4	57	1.3	20	9.9	0.15	3.9	4.1	1.2	2.0	0.04	553	38	22	18	15	111	215	187	35	113	187
SN17	GFFB1002M	bulk saprolite	330	5.6	60	1.0	20	7.8	0.15	3.0	4.1	1.6	2.4	0.04	798	30	22	15	12	109	283	142	26	90	189
SN16	GFFB1002H	bulk saprolite	414	5.2	61	1.0	19	7.9	0.12	3.0	3.9	1.5	2.3	0.07	788	35	22	18	14	127	294	143	31	83	184
SN16e	GFFB1002H	exchangeable saprolite	414																						
SN16r	GFFB1002H	residuum saprolite	414																						
SN15	GFFB1002G	bulk saprolite	513	3.9	62	0.93	18	7.1	0.11	2.7	4.7	2.0	2.2	0.17	764	28	21	15	10	95	337	131	25	82	168
SN14	GFFB1002L	bulk saprolite	605	4.6	62	1.1	18	7.9	0.12	3.1	4.1	1.6	2.2	0.12	643	29	22	15	12	116	275	148	26	89	169
SN14e	GFFB1002L	exchangeable saprolite	605																						
SN14r	GFFB1002L	residuum saprolite	605																						
Creek sediment loads																									
SN46	GFFB10038	suspended load. P301 filter	-																						
SN47	GFFB10037	suspended load. P300 filter	-																						
Rocks																									
SN30	GFFB10004	Granodiorite	-	1.4	62	0.82	17	6.9	0.12	2.8	5.4	3.3	2.5	0.25	710	28	n.d.	n.d.	<10	n.d.	497	131	n.d.	132	132
SN31	GFFB1000B	Granodiorite	-	0.72	63	0.80	17	6.2	0.10	2.7	5.5	3.4	2.4	0.19	705	41	n.d.	n.d.	<10	n.d.	473	118	n.d.	111	101
SN32	GFFB10009	Granodiorite	-	0.49	68	0.53	15	5.0	0.08	1.6	3.3	3.0	3.6	0.14	1306	28	n.d.	n.d.	<10	n.d.	432	68	n.d.	100	100
SN33	GFFB1000A	Granodiorite	-	0.62	68	0.50	15	4.7	0.07	1.6	3.6	3.3	3.4	0.13	1207	34	n.d.	n.d.	<10	n.d.	413	62	n.d.	91	111
SN34	GFFB1000E	Granodiorite	-	0.45	68	0.53	14	5.2	0.08	1.6	3.3	3.0	3.4	0.14	1205	41	n.d.	n.d.	<10	n.d.	342	79	n.d.	90	100
SN35	GFFB1001W	Granodiorite/Tonalite -am-bt-rich	-	1.4	52	1.2	18	9.9	0.16	4.8	8.2	3.2	1.5	0.31	507	56	n.d.	n.d.	<10	n.d.	568	222	n.d.	142	71
SN36	GFFB1001X	Granodiorite/Tonalite -am-bt-rich	-	2.3	62	0.91	17	6.8	0.10	3.1	5.3	2.8	1.5	0.20	512	42	n.d.	n.d.	<10	n.d.	491	160	n.d.	102	82
SN37	GFFB1001Y	Granodiorite/Tonalite -am-bt-rich	-	1.1	58	1.1	17	8.7	0.14	3.7	6.3	3.1	1.9	0.26	607	21	n.d.	n.d.	<10	n.d.	475	164	n.d.	131	111
SN38	GFFB1001Z	Granodiorite/Tonalite -am-bt-rich	-	1.2	58	1.1	17	8.4	0.14	3.5	6.4	3.2	1.8	0.29	506	28	n.d.	n.d.	20	n.d.	516	181	n.d.	121	111

continued next page …

Supplementary Table 4-3b continued - Sierra Nevada (CA), Loss on ignition (LOI)-corrected analyses of soil, saprolite, rock, bedload sediment and suspended load.

				LOI corrected data (major oxides)										LOI corrected data (trace elements)										
sample ID	**IGSN †**	**brief sample description**	**depth**	**LOI**	**SiO_2**	**TiO_2**	**Al_2O_3**	**Fe_2O_3**	**MnO**	**MgO**	**CaO**	**Na_2O**	**K_2O**	**P_2O_5**	**Ba**	**Cr**	**Ga**	**Nb**	**Ni**	**Rb**	**Sr**	**V**	**Y**	**Zn**	**Zr**
			(cm)	(wt%)	(wt%)	(wt%)	(wt%)	(wt%)	(wt%)	(wt%)	(wt%)	(wt%)	(wt%)	(wt%)	(µg/g)	(µg/g)	(µg/g)	(µg/g)	(µg/g)	(µg/g)	(µg/g)	(µg/g)	(µg/g)	(µg/g)	(µg/g)
SN39	GFFB10020	Granodiorite/Tonalite -am-bt-rich	-	0.92	53	1.4	18	9.4	0.14	4.7	8.2	3.2	1.5	0.26	505	41	n.d.	n.d.	<10	n.d.	595	220	n.d.	141	71
SN40	GFFB1001T	Granodiorite/Tonalite -am-bt-rich	-	1.1	58	0.96	17	8.1	0.12	3.8	6.9	2.9	1.4	0.23	606	62	n.d.	n.d.	20	n.d.	596	187	n.d.	141	61
SN13	GFFB10021	weathered Granodiorite	688	3.3	61	0.99	17	7.5	0.12	3.0	5.9	2.6	1.5	0.26	549	32	21	17	11	64	406	146	27	89	184
SN12	GFFB10027	weathered Granodiorite	696	2.0	60	0.98	17	7.6	0.12	3.1	5.9	2.7	2.4	0.23	776	29	17	13	13	95	410	147	23	89	195
SN11	GFFB10026	weathered Granodiorite	-	1.2	68	0.54	15	4.3	0.07	1.6	3.6	2.6	3.8	0.11	642	17	15	14	11	147	276	73	21	51	139
SN41	GFFB1001N	Granodiorite	-	0.63	60	0.93	17	7.2	0.11	3.0	6.0	3.1	2.3	0.18	604	14	n.d.	n.d.	<10	n.d.	413	158	n.d.	131	131
SN42	GFFB1001P	Granodiorite	-	0.56	61	0.88	17	6.9	0.11	2.9	6.0	3.2	2.3	0.19	704	21	n.d.	n.d.	<10	n.d.	372	152	n.d.	101	131
SN43	GFFB1001Q	Granodiorite	-	0.81	60	0.85	17	6.8	0.10	2.8	5.9	3.2	2.2	0.18	706	110	n.d.	n.d.	121	n.d.	413	136	n.d.	111	81
SN44	GFFB1001R	Granodiorite	-	0.89	61	0.90	17	6.8	0.11	2.9	5.9	3.1	2.2	0.18	706	28	n.d.	n.d.	<10	n.d.	404	147	n.d.	111	111
SN45	GFFB1001S	Granodiorite	-	0.68	61	0.87	17	7.0	0.11	2.9	6.1	3.2	2.2	0.18	604	28	n.d.	n.d.	<10	n.d.	423	135	n.d.	121	131
Rocks, Data from Hahm et al. (2014) and Riebe and Granger (2013)																									
P301C01		Granodiorite, CZO Providence (Dinkey Creek)	-	n.r.	63	0.86	17	5.6	0.03	2.5	5.1	3.2	2.4	0.18	700	n.r.	n.r.	9.0	n.r.	n.r.	465	n.r.	16	n.r.	141
P301C02		Granodiorite, CZO Providence (Dinkey Creek)	-	n.r.	49	0.91	15	14	0.10	7.1	10	2.8	0.7	0.18	117	n.r.	n.r.	9.2	n.r.	n.r.	310	n.r.	46	n.r.	74
P301C03		Granodiorite, CZO Providence (Dinkey Creek)	-	n.r.	64	0.84	17	6.2	0.06	2.2	3.9	2.3	2.4	0.29	851	n.r.	n.r.	13	n.r.	n.r.	337	n.r.	20	n.r.	273
P301C08		Granodiorite, CZO Providence (Dinkey Creek)	-	n.r.	55	1.2	18	8.4	0.04	3.8	7.6	3.0	1.6	0.24	693	n.r.	n.r.	6.9	n.r.	n.r.	662	n.r.	19	n.r.	139
P301C11		Granodiorite, CZO Providence (Dinkey Creek)	-	n.r.	63	0.77	17	5.1	0.03	2.3	5.1	3.3	2.5	0.15	755	n.r.	n.r.	8.7	n.r.	n.r.	451	n.r.	18	n.r.	143
P301OS1		Granodiorite, CZO Providence (Dinkey Creek)	-	n.r.	61	0.94	17	6.6	0.04	3.0	5.5	3.1	2.3	0.21	n.r.	n.r.	n.r.	n.r.	n.r.	n.r.	n.r.	n.r.	n.r.	n.r.	n.r.
P301OS10me		Granodiorite, CZO Providence (Dinkey Creek)	-	n.r.	49	1.5	19	10	0.06	4.8	8.4	3.7	1.7	0.30	545	n.r.	n.r.	13	n.r.	n.r.	555	n.r.	29	n.r.	181
P301OS12		Granodiorite, CZO Providence (Dinkey Creek)	-	n.r.	63	0.82	17	5.6	0.03	2.4	5.2	3.2	2.5	0.17	744	n.r.	n.r.	8.8	n.r.	n.r.	481	n.r.	17	n.r.	148
P301OS12me1		Granodiorite, CZO Providence (Dinkey Creek)	-	n.r.	55	1.3	18	8.2	0.05	3.9	6.5	3.5	2.1	0.29	721	n.r.	n.r.	12	n.r.	n.r.	490	n.r.	21	n.r.	193
P301OS12me2		Granodiorite, CZO Providence (Dinkey Creek)	-	n.r.	56	1.3	17	9.8	0.05	3.8	5.8	3.0	2.7	0.28	843	n.r.	n.r.	13	n.r.	n.r.	419	n.r.	28	n.r.	230
P301OS20		Granodiorite, CZO Providence (Dinkey Creek)	-	n.r.	63	0.82	17	5.5	0.03	2.4	5.2	3.2	2.5	0.17	765	n.r.	n.r.	7.9	n.r.	n.r.	483	n.r.	15	n.r.	134
P301OS20m		Granodiorite, CZO Providence (Dinkey Creek)	-	n.r.	51	1.4	19	11	0.07	4.8	7.9	3.5	1.9	0.21	510	n.r.	n.r.	16	n.r.	n.r.	439	n.r.	37	n.r.	95
P301OS8		Granodiorite, CZO Providence (Dinkey Creek)	-	n.r.	63	0.77	18	5.1	0.03	2.2	5.2	3.2	2.4	0.17	762	n.r.	n.r.	6.8	n.r.	n.r.	496	n.r.	12	n.r.	126
P301OS9		Granodiorite, CZO Providence (Dinkey Creek)	-	n.r.	64	0.78	17	5.5	0.04	2.4	5.0	3.1	2.5	0.17	829	n.r.	n.r.	8.6	n.r.	n.r.	462	n.r.	17	n.r.	121
P301SV2		Granodiorite, CZO Providence (Dinkey Creek)	-	n.r.	61	0.90	17	6.3	0.04	2.7	5.5	3.2	2.3	0.20	729	n.r.	n.r.	8.3	n.r.	n.r.	477	n.r.	17	n.r.	134
P303C001		Granodiorite, CZO Providence (Dinkey Creek)	-	n.r.	61	0.98	17	6.7	0.04	3.0	5.8	3.1	2.2	0.20	774	n.r.	n.r.	9.7	n.r.	n.r.	509	n.r.	16	n.r.	149
P303C002		Granodiorite, CZO Providence (Dinkey Creek)	-	n.r.	61	0.94	17	6.7	0.04	2.9	5.9	3.2	2.1	0.20	764	n.r.	n.r.	9.0	n.r.	n.r.	512	n.r.	18	n.r.	143
P303C003		Granodiorite, CZO Providence (Dinkey Creek)	-	n.r.	60	0.97	17	7.0	0.04	3.1	6.1	3.2	2.2	0.21	788	n.r.	n.r.	8.5	n.r.	n.r.	502	n.r.	18	n.r.	142
P303C004		Granodiorite, CZO Providence (Dinkey Creek)	-	n.r.	61	0.99	17	6.8	0.04	3.0	5.8	3.1	2.2	0.20	699	n.r.	n.r.	8.6	n.r.	n.r.	499	n.r.	18	n.r.	130
P303C005		Granodiorite, CZO Providence (Dinkey Creek)	-	n.r.	57	1.0	17	7.5	0.04	4.2	7.5	2.9	1.8	0.20	473	n.r.	n.r.	5.7	n.r.	n.r.	562	n.r.	15	n.r.	123
P303C007-2		Granodiorite, CZO Providence (Dinkey Creek)	-	n.r.	60	0.94	18	6.7	0.04	2.9	6.1	3.3	2.3	0.20	915	n.r.	n.r.	8.4	n.r.	n.r.	538	n.r.	17	n.r.	154
P303C007-3		Granodiorite, CZO Providence (Dinkey Creek)	-	n.r.	61	0.90	17	6.4	0.04	2.9	6.1	3.3	2.0	0.19	777	n.r.	n.r.	7.9	n.r.	n.r.	535	n.r.	17	n.r.	126
P303C007part1		Granodiorite, CZO Providence (Dinkey Creek)	-	n.r.	61	0.85	17	6.1	0.03	2.8	6.2	3.4	1.9	0.18	748	n.r.	n.r.	7.7	n.r.	n.r.	543	n.r.	17	n.r.	139
P303C008-1		Granodiorite, CZO Providence (Dinkey Creek)	-	n.r.	60	0.97	17	7.3	0.04	3.3	6.1	3.0	1.7	0.19	530	n.r.	n.r.	7.7	n.r.	n.r.	499	n.r.	17	n.r.	111
P303C010		Granodiorite, CZO Providence (Dinkey Creek)	-	n.r.	60	1.0	17	7.1	0.04	3.4	6.1	3.0	2.2	0.21	710	n.r.	n.r.	9.0	n.r.	n.r.	486	n.r.	21	n.r.	174
P303C010A		Granodiorite, CZO Providence (Dinkey Creek)	-	n.r.	61	0.96	18	6.1	0.03	2.9	6.0	3.2	2.0	0.19	624	n.r.	n.r.	8.6	n.r.	n.r.	511	n.r.	15	n.r.	131
P303C011A		Granodiorite, CZO Providence (Dinkey Creek)	-	n.r.	58	1.1	18	8.1	0.04	3.8	6.5	2.8	1.8	0.21	631	n.r.	n.r.	8.0	n.r.	n.r.	510	n.r.	18	n.r.	137
P303C011B		Granodiorite, CZO Providence (Dinkey Creek)	-	n.r.	49	1.4	20	11	0.06	5.3	9.0	3.1	1.7	0.25	707	n.r.	n.r.	7.3	n.r.	n.r.	516	n.r.	16	n.r.	130
P303C012		Granodiorite, CZO Providence (Dinkey Creek)	-	n.r.	59	0.97	18	7.1	0.04	3.1	6.4	3.2	1.9	0.19	615	n.r.	n.r.	8.4	n.r.	n.r.	506	n.r.	19	n.r.	118
P303C013		Granodiorite, CZO Providence (Dinkey Creek)	-	n.r.	60	0.97	17	6.6	0.04	2.8	6.0	3.2	2.1	0.18	650	n.r.	n.r.	9.4	n.r.	n.r.	507	n.r.	17	n.r.	132
P303C014A		Granodiorite, CZO Providence (Dinkey Creek)	-	n.r.	61	0.94	17	6.7	0.04	2.9	6.0	3.1	2.0	0.19	683	n.r.	n.r.	7.6	n.r.	n.r.	499	n.r.	18	n.r.	137
P303C015		Granodiorite, CZO Providence (Dinkey Creek)	-	n.r.	59	1.1	16	8.1	0.05	3.6	6.0	2.9	2.5	0.23	842	n.r.	n.r.	11	n.r.	n.r.	439	n.r.	25	n.r.	179
P303C016		Granodiorite, CZO Providence (Dinkey Creek)	-	n.r.	61	0.89	17	6.5	0.03	2.7	5.4	3.1	2.4	0.19	777	n.r.	n.r.	8.9	n.r.	n.r.	472	n.r.	17	n.r.	138
P303C017		Granodiorite, CZO Providence (Dinkey Creek)	-	n.r.	61	0.90	17	6.4	0.03	2.8	5.7	3.2	2.3	0.20	813	n.r.	n.r.	8.7	n.r.	n.r.	509	n.r.	16	n.r.	146
P303C018		Granodiorite, CZO Providence (Dinkey Creek)	-	n.r.	60	0.96	17	7.1	0.04	3.1	6.4	3.1	1.6	0.20	529	n.r.	n.r.	8.1	n.r.	n.r.	540	n.r.	16	n.r.	115
P303C019		Granodiorite, CZO Providence (Dinkey Creek)	-	n.r.	59	1.1	18	7.5	0.04	3.3	6.5	3.1	1.8	0.21	548	n.r.	n.r.	8.3	n.r.	n.r.	512	n.r.	18	n.r.	127
P303C020		Granodiorite, CZO Providence (Dinkey Creek)	-	n.r.	51	1.4	19	10	0.06	4.7	8.5	3.2	1.7	0.24	512	n.r.	n.r.	8.1	n.r.	n.r.	569	n.r.	21	n.r.	110

continued next page …

Supplementary Table 4-3b continued - Sierra Nevada (CA), Loss on ignition (LOI)-corrected analyses of soil, saprolite, rock, bedload sediment and suspended load.

				LOI corrected data (major oxides)										LOI corrected data (trace elements)										
sample ID	† **brief sample description**	**depth**	**LOI**	**SiO_2**	**TiO_2**	**Al_2O_3**	**Fe_2O_3**	**MnO**	**MgO**	**CaO**	**Na_2O**	**K_2O**	**P_2O_5**	**Ba**	**Cr**	**Ga**	**Nb**	**Ni**	**Rb**	**Sr**	**V**	**Y**	**Zn**	**Zr**
		(cm)	(wt%)	(wt%)	(wt%)	(wt%)	(wt%)	(wt%)	(wt%)	(wt%)	(wt%)	(wt%)	(wt%)	(µg/g)	(µg/g)	(µg/g)	(µg/g)	(µg/g)	(µg/g)	(µg/g)	(µg/g)	(µg/g)	(µg/g)	(µg/g)
P303C020	Granodiorite, CZO Providence (Dinkey Creek)	-	n.r.	51	1.4	19	10	0.06	4.7	8.5	3.2	1.7	0.24	512	n.r.	n.r.	8.1	n.r.	n.r.	569	n.r.	21	n.r.	110
P303C021	Granodiorite, CZO Providence (Dinkey Creek)	-	n.r.	61	0.97	17	7.1	0.04	3.0	5.8	2.9	2.0	0.20	671	n.r.	n.r.	7.5	n.r.	n.r.	482	n.r.	18	n.r.	146
P303C022	Granodiorite, CZO Providence (Dinkey Creek)	-	n.r.	49	1.4	19	10	0.07	5.4	9.4	3.2	1.4	0.27	501	n.r.	n.r.	11	n.r.	n.r.	538	n.r.	28	n.r.	128
P303C023	Granodiorite, CZO Providence (Dinkey Creek)	-	n.r.	61	0.89	17	6.4	0.04	2.8	6.0	3.2	1.9	0.18	577	n.r.	n.r.	8.2	n.r.	n.r.	502	n.r.	17	n.r.	133
P303C024	Granodiorite, CZO Providence (Dinkey Creek)	-	n.r.	52	1.3	18	10	0.06	4.6	8.3	3.2	1.8	0.22	595	n.r.	n.r.	11	n.r.	n.r.	497	n.r.	26	n.r.	97
P303C025	Granodiorite, CZO Providence (Dinkey Creek)	-	n.r.	61	0.91	17	6.5	0.04	2.7	5.7	3.2	2.4	0.19	752	n.r.	n.r.	9.2	n.r.	n.r.	479	n.r.	19	n.r.	133
P303C026	Granodiorite, CZO Providence (Dinkey Creek)	-	n.r.	62	0.86	17	6.2	0.03	2.7	5.8	3.2	2.1	0.19	582	n.r.	n.r.	8.7	n.r.	n.r.	493	n.r.	17	n.r.	141
P303C027	Granodiorite, CZO Providence (Dinkey Creek)	-	n.r.	51	1.3	18	11	0.07	5.1	8.0	3.2	2.1	0.24	616	n.r.	n.r.	11	n.r.	n.r.	436	n.r.	29	n.r.	103
P303C028	Granodiorite, CZO Providence (Dinkey Creek)	-	n.r.	61	0.92	17	6.5	0.03	2.7	5.7	3.3	2.4	0.18	717	n.r.	n.r.	10.0	n.r.	n.r.	491	n.r.	18	n.r.	145
P303C029	Granodiorite, CZO Providence (Dinkey Creek)	-	n.r.	61	0.91	17	6.4	0.04	2.7	5.6	3.2	2.2	0.18	707	n.r.	n.r.	8.6	n.r.	n.r.	480	n.r.	18	n.r.	133
P303C030	Granodiorite, CZO Providence (Dinkey Creek)	-	n.r.	58	1.1	17	8.3	0.05	3.5	5.8	3.0	2.5	0.22	899	n.r.	n.r.	9.4	n.r.	n.r.	461	n.r.	20	n.r.	154
P303C031	Granodiorite, CZO Providence (Dinkey Creek)	-	n.r.	62	0.75	18	5.3	0.03	2.3	5.3	3.3	2.6	0.15	744	n.r.	n.r.	7.6	n.r.	n.r.	514	n.r.	12	n.r.	132
P303C032	Granodiorite, CZO Providence (Dinkey Creek)	-	n.r.	55	1.2	18	8.2	0.04	4.7	7.8	2.9	1.7	0.23	597	n.r.	n.r.	6.7	n.r.	n.r.	628	n.r.	15	n.r.	114
P303C033	Granodiorite, CZO Providence (Dinkey Creek)	-	n.r.	55	1.2	18	8.4	0.04	4.8	7.9	3.0	1.7	0.25	629	n.r.	n.r.	7.6	n.r.	n.r.	630	n.r.	17	n.r.	126
P303C035	Granodiorite, CZO Providence (Dinkey Creek)	-	n.r.	57	1.1	17	7.8	0.04	4.7	7.0	2.6	1.8	0.19	675	n.r.	n.r.	7.8	n.r.	n.r.	523	n.r.	15	n.r.	129
P303OS1	Granodiorite, CZO Providence (Dinkey Creek)	-	n.r.	61	1.0	17	6.8	0.04	2.9	5.7	3.1	2.2	0.21	635	n.r.	n.r.	8.5	n.r.	n.r.	464	n.r.	19	n.r.	128
P303OS1B	Granodiorite, CZO Providence (Dinkey Creek)	-	n.r.	51	1.3	19	9.7	0.06	4.5	8.3	3.3	1.8	0.24	520	n.r.	n.r.	11	n.r.	n.r.	514	n.r.	26	n.r.	114
P303OS3	Granodiorite, CZO Providence (Dinkey Creek)	-	n.r.	60	1.1	17	7.4	0.04	3.3	5.7	3.0	2.4	0.24	806	n.r.	n.r.	8.9	n.r.	n.r.	479	n.r.	19	n.r.	157
P303OS4A	Granodiorite, CZO Providence (Dinkey Creek)	-	n.r.	62	0.86	17	6.0	0.03	2.6	5.5	3.2	2.5	0.19	762	n.r.	n.r.	8.1	n.r.	n.r.	496	n.r.	17	n.r.	117
P303OS4B	Granodiorite, CZO Providence (Dinkey Creek)	-	n.r.	65	0.62	17	3.8	0.02	1.6	5.1	3.5	2.1	0.13	728	n.r.	n.r.	5.5	n.r.	n.r.	546	n.r.	10	n.r.	83
Rocks, Data from Hahm et al. (2014) and Riebe and Granger (2013)																								
P303OS4C	Granodiorite, CZO Providence (Dinkey Creek)	-	n.r.	53	1.3	18	10	0.06	4.9	7.4	3.1	2.1	0.24	629	n.r.	n.r.	11	n.r.	n.r.	416	n.r.	27	n.r.	123
P303OS6A	Granodiorite, CZO Providence (Dinkey Creek)	-	n.r.	59	0.98	17	7.1	0.04	3.2	5.8	3.2	2.4	0.19	734	n.r.	n.r.	8.3	n.r.	n.r.	485	n.r.	17	n.r.	126
P303OS6B	Granodiorite, CZO Providence (Dinkey Creek)	-	n.r.	54	1.1	18	9.3	0.06	4.8	7.6	3.2	1.9	0.21	585	n.r.	n.r.	8.7	n.r.	n.r.	458	n.r.	24	n.r.	120
P304C01	Granodiorite, CZO Providence (Dinkey Creek)	-	n.r.	52	1.3	18	9.8	0.05	5.2	9.1	2.4	1.3	0.17	333	n.r.	n.r.	4.8	n.r.	n.r.	568	n.r.	17	n.r.	57
P304C010	Granodiorite, CZO Providence (Dinkey Creek)	-	n.r.	62	0.79	17	5.8	0.04	2.6	5.2	3.2	2.8	0.17	682	n.r.	n.r.	8.6	n.r.	n.r.	476	n.r.	14	n.r.	132
P304C02	Granodiorite, CZO Providence (Dinkey Creek)	-	n.r.	52	1.3	18	10.0	0.05	5.3	9.2	2.2	1.5	0.19	342	n.r.	n.r.	5.8	n.r.	n.r.	577	n.r.	17	n.r.	62
P304C03	Granodiorite, CZO Providence (Dinkey Creek)	-	n.r.	56	1.2	17	8.4	0.04	4.3	7.7	2.7	1.6	0.19	469	n.r.	n.r.	7.4	n.r.	n.r.	533	n.r.	19	n.r.	84
P304C04	Granodiorite, CZO Providence (Dinkey Creek)	-	n.r.	55	1.1	18	8.8	0.05	4.3	7.6	2.8	1.9	0.18	438	n.r.	n.r.	7.5	n.r.	n.r.	538	n.r.	17	n.r.	64
P304C05	Granodiorite, CZO Providence (Dinkey Creek)	-	n.r.	62	0.91	17	6.2	0.03	2.6	5.8	3.1	1.9	0.17	571	n.r.	n.r.	7.4	n.r.	n.r.	509	n.r.	15	n.r.	121
P304C06	Granodiorite, CZO Providence (Dinkey Creek)	-	n.r.	60	1.0	17	6.9	0.04	2.9	5.9	3.1	2.1	0.20	602	n.r.	n.r.	8.1	n.r.	n.r.	504	n.r.	18	n.r.	142
P304C07	Granodiorite, CZO Providence (Dinkey Creek)	-	n.r.	60	0.97	17	6.9	0.03	3.1	6.2	3.1	1.9	0.19	579	n.r.	n.r.	8.0	n.r.	n.r.	510	n.r.	16	n.r.	113
P304C08	Granodiorite, CZO Providence (Dinkey Creek)	-	n.r.	63	0.88	17	6.0	0.03	2.5	5.4	3.3	1.9	0.17	558	n.r.	n.r.	8.2	n.r.	n.r.	469	n.r.	15	n.r.	123
P304C09	Granodiorite, CZO Providence (Dinkey Creek)	-	n.r.	59	1.1	18	7.3	0.04	3.2	6.2	3.1	1.9	0.20	548	n.r.	n.r.	8.8	n.r.	n.r.	494	n.r.	19	n.r.	111
P304C10	Granodiorite, CZO Providence (Dinkey Creek)	-	n.r.	61	0.91	17	6.4	0.03	2.7	5.9	3.1	2.1	0.18	648	n.r.	n.r.	8.2	n.r.	n.r.	495	n.r.	17	n.r.	124
P304C12	Granodiorite, CZO Providence (Dinkey Creek)	-	n.r.	62	0.91	17	6.0	0.03	2.6	5.2	3.2	2.5	0.17	694	n.r.	n.r.	10.2	n.r.	n.r.	466	n.r.	20	n.r.	151
P304C13B	Granodiorite, CZO Providence (Dinkey Creek)	-	n.r.	61	0.92	17	6.4	0.04	2.6	5.5	3.3	2.5	0.18	938	n.r.	n.r.	10.0	n.r.	n.r.	442	n.r.	20	n.r.	127
P304OS1	Granodiorite, CZO Providence (Dinkey Creek)	-	n.r.	62	0.92	17	6.2	0.03	2.4	5.4	3.3	2.3	0.18	645	n.r.	n.r.	8.6	n.r.	n.r.	463	n.r.	18	n.r.	121
P304OS1A	Granodiorite, CZO Providence (Dinkey Creek)	-	n.r.	59	1.1	18	7.3	0.04	3.1	5.6	3.3	2.6	0.24	705	n.r.	n.r.	9.1	n.r.	n.r.	442	n.r.	16	n.r.	130
P304OS2	Granodiorite, CZO Providence (Dinkey Creek)	-	n.r.	62	0.96	17	6.3	0.04	2.7	5.5	3.1	2.2	0.17	758	n.r.	n.r.	8.0	n.r.	n.r.	471	n.r.	16	n.r.	127
mean Rocks, data from Hahm et al. (2014) and Riebe and Granger (2013), and GFZ																								
mean bedrock after outlier removal				**60**	**0.97**	**17**	**7.2**	**0.05**	**3.2**	**6.2**	**3.1**	**2.2**	**0.20**	**685**	**35**	**18**	**8.9**	**39**	**102**	**484**	**119**	**19**	**102**	**128**
2 SD bedrock after outlier removal				8.7	0.39	1.8	3.4	0.05	2.0	2.5	0.39	0.9	0.06	325	48	6	3.9	109	83	121	71	11	43	46
2 SE bedrock after outlier removal				1.0	0.04	0.20	0.37	0.01	0.22	0.28	0.04	0.10	0.01	36	13	3	0.5	55	48	13	20	1	12	5
N bedrock after outlier removal				82	82	82	82	82	82	82	82	82	82	82	13	3	72	4	3	82	13	72	13	82

continued next page …

Supplementary Table 4-3b continued - Sierra Nevada (CA), Loss on ignition (LOI)-corrected analyses of soil, saprolite, rock, bedload sediment and suspended load.

				LOI corrected data (major oxides)										LOI corrected data (trace elements)									
sample ID	**brief sample description**	**depth**	**LOI**	**SiO_2**	**TiO_2**	**Al_2O_3**	**Fe_2O_3**	**MnO**	**MgO**	**CaO**	**Na_2O**	**K_2O**	**P_2O_5**	**Ba**	**Cr**	**Ga**	**Nb**	**Ni**	**Rb**	**Sr**	**V**	**Y**	**Zn**	**Zr**
		(cm)	(wt%)	(wt%)	(wt%)	(wt%)	(wt%)	(wt%)	(wt%)	(wt%)	(wt%)	(wt%)	(wt%)	(µg/g)	(µg/g)	(µg/g)	(µg/g)	(µg/g)	(µg/g)	(µg/g)	(µg/g)	(µg/g)	(µg/g)	(µg/g)
Soil/ Saprolite, data from Hahm et al. (2014) and Riebe and Granger (2013)																							
P301PF01M100cm	Soil Pit	100		62	0.94	19	6.6	0.03	2.7	3.9	2.2	2.3	0.13	781	45	23	n.r.	12	108	340	138	20	93	179
P301PF01M10cm	Soil Pit	10		63	0.87	18	6.1	0.05	2.4	3.8	2.4	2.4	0.36	858	28	20	n.r.	14	116	344	122	18	92	186
P301PF01M125cm	Soil Pit	125		62	0.95	19	6.8	0.03	2.7	3.6	2.1	2.3	0.11	n.r.	n.r.	n.r.	n.r.	n.r.	n.r.	n.r.	n.r.	n.r.	n.r.	n.r.
P301PF01M150cm	Soil Pit	150		61	1.0	18	7.2	0.04	3.0	4.3	2.4	2.4	0.15	790	29	21	n.r.	11	95	347	156	22	94	179
P301PF01M182cm	Saprolite	182		61	1.0	18	7.3	0.04	3.0	4.3	2.4	2.5	0.14	778	30	21	n.r.	10	101	346	154	22	95	184
P301PF01M25cm	Soil Pit	25		63	0.89	19	6.3	0.04	2.5	3.7	2.3	2.3	0.18	794	34	20	n.r.	11	114	331	126	19	93	174
P301PF01M50cm	Soil Pit	50		62	0.94	19	6.8	0.04	2.7	3.9	2.3	2.3	0.19	791	34	21	n.r.	13	118	339	140	20	95	176
P301PF01M75cm	Soil Pit	75		62	0.92	19	6.8	0.03	2.6	3.8	2.2	2.2	0.15	773	29	21	n.r.	12	112	335	135	20	90	170
P301PF01N100cm	Soil Pit	100		62	0.95	19	6.6	0.03	2.6	3.7	2.2	2.3	0.11	765	31	22	n.r.	12	105	319	137	20	89	180
P301PF01N10cm	Soil Pit	10		62	0.91	19	6.4	0.06	2.5	3.7	2.3	2.4	0.27	1028	34	22	n.r.	17	125	340	129	18	101	187
P301PF01N125cm	Soil Pit	125		61	1.0	20	7.1	0.04	2.9	3.8	2.1	2.4	0.10	816	33	23	n.r.	11	104	308	153	21	94	185
P301PF01N150cm	Soil Pit	150		60	1.1	19	7.9	0.04	3.2	4.0	2.1	2.4	0.12	845	36	23	n.r.	13	104	309	175	23	103	191
P301PF01N185cm	Saprolite	185		59	1.2	18	8.4	0.04	3.5	4.1	2.2	2.6	0.11	875	34	23	n.r.	11	115	319	188	23	113	206
P301PF01N25cm	Soil Pit	25		63	0.89	19	6.5	0.04	2.5	3.6	2.3	2.3	0.27	827	30	23	n.r.	13	119	323	136	19	96	175
P301PF01N50cm	Soil Pit	50		62	0.92	19	6.7	0.04	2.6	3.8	2.2	2.3	0.18	769	35	22	n.r.	12	117	327	137	19	94	182
P301PF01N75cm	Soil Pit	75		62	0.92	19	6.6	0.03	2.6	3.8	2.3	2.2	0.14	784	29	22	n.r.	12	108	332	131	20	90	169
P301PF01S100cm	Soil Pit	100		62	0.94	19	6.8	0.03	2.7	3.9	2.3	2.2	0.12	763	29	21	n.r.	12	103	336	145	20	90	180
P301PF01S10cm	Soil Pit	10		62	0.93	19	6.5	0.05	2.5	3.7	2.4	2.4	0.28	890	31	22	n.r.	16	120	333	135	20	98	183
P301PF01S125cm	Soil Pit	125		62	0.96	19	6.9	0.03	2.8	3.8	2.1	2.4	0.11	789	27	22	n.r.	11	102	318	143	21	90	166
P301PF01S150cm	Soil Pit	150		61	1.0	20	7.3	0.03	2.9	3.6	1.9	2.5	0.11	797	33	22	n.r.	11	103	298	153	22	94	200
P301PF01S177cm	Saprolite	177		62	0.94	18	6.8	0.03	2.8	4.1	2.4	2.5	0.15	783	27	21	n.r.	11	98	348	139	21	89	173
P301PF01S25cm	Soil Pit	25		62	0.88	19	6.3	0.04	2.5	3.8	2.4	2.4	0.18	848	26	21	n.r.	14	116	341	127	19	92	187
P301PF01S50cm	Soil Pit	50		62	0.95	19	6.7	0.04	2.6	3.9	2.3	2.3	0.20	797	47	21	n.r.	13	116	338	139	19	95	166
P301PF01S75cm	Soil Pit	75		62	0.92	19	6.6	0.04	2.6	3.8	2.3	2.3	0.15	755	28	23	n.r.	11	111	329	137	19	89	179
P301PF02M25cm	Soil Pit	10		63	0.91	19	6.3	0.04	2.5	3.7	2.2	2.3	0.17	n.r.	n.r.	n.r.	n.r.	n.r.	n.r.	n.r.	n.r.	n.r.	n.r.	n.r.
P301PF02NW10cm	Soil Pit	10		62	0.93	18	6.4	0.05	2.6	4.7	2.8	2.3	0.27	827	27	20	n.r.	11	101	416	132	19	93	189
P301PF02NW120cm_dpsp	Saprolite	120		62	0.85	18	5.9	0.03	2.5	5.0	3.1	2.1	0.16	723	25	20	n.r.	8.2	82	459	125	16	78	142
Soil/ Saprolite, data from Hahm et al. (2014) and Riebe and Granger (2013)																							
P301PF02NW25cm	Soil Pit	25		62	0.86	18	6.5	0.05	2.6	4.8	2.9	2.3	0.25	803	34	20	n.r.	12	100	418	132	19	92	185
P301PF02NW50cm	Soil Pit	50		62	0.93	18	6.5	0.04	2.7	4.8	2.9	2.2	0.21	772	26	20	n.r.	10	95	420	137	19	89	157
P301PF02NW75cm	Soil Pit	75		61	0.96	18	6.7	0.04	2.8	4.7	2.8	2.1	0.20	798	34	20	n.r.	11	95	413	147	19	92	173
P301PF02NW85cm	Saprolite	85		61	0.96	18	6.5	0.04	2.8	4.9	3.0	2.2	0.17	747	25	21	n.r.	10	91	432	128	18	95	172
P301PF02SE10cm	Soil Pit	10		62	0.91	18	6.4	0.05	2.6	4.6	2.9	2.3	0.31	882	28	21	n.r.	11	106	414	136	18	94	189
P301PF02SE25cm	Soil Pit	25		61	0.94	18	6.7	0.05	2.7	4.7	2.8	2.3	0.25	859	31	20	n.r.	13	105	416	144	19	100	193
P301PF02SE50cm	Soil Pit	50		61	0.91	18	6.9	0.04	2.8	4.7	2.8	2.2	0.20	779	37	20	n.r.	11	98	407	147	18	94	180
P301PF02SE85cmSap	Saprolite	75		60	1.1	17	7.6	0.04	3.3	5.0	2.8	2.5	0.18	936	30	20	n.r.	8.3	102	409	171	22	105	188
P301TP1A_20cm	Soil Pit	10		64	0.78	18	6.1	0.05	2.3	3.4	2.4	2.9	0.25	921	30	21	n.r.	13	114	306	108	19	95	179
P301TP1B_40cm	Soil Pit	30		n.r.	n.r.	n.r.	n.r.	n.r.	n.r.	n.r.	n.r.	n.r.	n.r.	902	31	21	n.r.	12	106	341	107	17	91	157
P301TP1BC_60cm	Soil Pit	50		63	0.81	18	6.1	0.04	2.4	3.8	2.5	2.7	0.19	846	28	20	n.r.	13	100	339	112	18	88	160
P301TP2A	Soil Pit	10		64	0.85	18	5.9	0.04	2.3	3.5	2.4	2.7	0.22	891	22	21	n.r.	11	111	318	104	17	91	158
P301TP2B	Soil Pit	30		64	0.76	18	5.6	0.03	2.2	3.7	2.5	2.6	0.20	899	21	20	n.r.	11	100	348	102	16	83	146
P301TP2BC	Soil Pit	50		64	0.75	18	5.4	0.03	2.1	3.7	2.5	2.7	0.19	913	26	20	n.r.	10	96	353	96	16	78	156
mean soil/ saprolite P301				**62**	**0.93**	**18**	**6.6**	**0.04**	**2.7**	**4.1**	**2.4**	**2.4**	**0.19**	**825**	**30**	**21**	**n.d.**	**12**	**106**	**354**	**136**	**19**	**93**	**176**
2 SD soil/ saprolite P301				2.2	0.16	1.2	1.1	0.01	0.56	0.93	0.58	0.37	0.12	127	10	2.1	n.d.	3.3	18	84	38	3	13	28
2 SE soil/ saprolite P301				0.34	0.03	0.19	0.18	0.00	0.09	0.15	0.09	0.06	0.02	20	1.7	0.34	n.d.	0.52	2.9	13	6.1	0.55	2.0	4.4
N soil/ saprolite P301				40	40	40	40	40	40	40	40	40	40	39	39	39	n.d.	39	39	39	39	39	39	39

continued next page …

Supplementary Table 4-3b continued - Sierra Nevada (CA), Loss on ignition (LOI)-corrected analyses of soil, saprolite, rock, bedload sediment and suspended load.

				LOI corrected data (major oxides)										LOI corrected data (trace elements)										
sample ID	**brief sample description**	**depth**	**LOI**	**SiO_2**	**TiO_2**	**Al_2O_3**	**Fe_2O_3**	**MnO**	**MgO**	**CaO**	**Na_2O**	**K_2O**	**P_2O_5**	**Ba**	**Cr**	**Ga**	**Nb**	**Ni**	**Rb**	**Sr**	**V**	**Y**	**Zn**	**Zr**
		(cm)	(wt%)	(wt%)	(wt%)	(wt%)	(wt%)	(wt%)	(wt%)	(wt%)	(wt%)	(wt%)	(wt%)	(µg/g)	(µg/g)	(µg/g)	(µg/g)	(µg/g)	(µg/g)	(µg/g)	(µg/g)	(µg/g)	(µg/g)	(µg/g)
P303P001ABHoriz	Soil Pit	20		61	1.0	19	7.5	0.06	2.7	4.2	2.3	1.8	0.24	891	33	21	n.r.	14	90	355	164	23	110	177
P303P001B-C	Soil Pit	50		62	1.0	18	6.8	0.04	2.9	4.7	2.2	1.9	0.12	774	30	21	n.r.	13	87	360	160	24	91	249
P303P001B-horiz	Soil Pit	84		59	1.1	19	9.2	0.05	2.8	4.1	2.0	1.6	0.31	893	37	22	n.r.	16	85	333	227	24	111	199
P303P2RF1	Soil Pit	60		59	1.0	18	6.6	0.04	2.8	5.6	3.3	2.5	0.21	868	20	22	n.r.	9.3	89	476	137	18	86	136
P303T003	Toe Slope	40		61	1.1	18	8.0	0.05	3.1	4.2	1.8	2.2	0.14	806	36	22	n.r.	11	93	303	186	25	101	289
P303T005	Toe Slope	37		65	1.1	15	7.6	0.05	3.1	4.6	1.7	1.9	0.14	664	39	18	n.r.	10	71	291	175	29	91	292
P303T008	Toe Slope	5		59	1.0	19	7.5	0.07	3.2	4.6	2.3	2.5	0.35	997	50	24	n.r.	18	115	368	171	23	117	228
P303T009	Toe Slope	5		59	1.1	18	7.9	0.05	3.3	5.6	2.2	2.0	0.28	946	54	22	n.r.	21	91	437	185	23	115	242
P303T010	Toe Slope	4		59	1.1	18	8.6	0.08	3.4	4.9	2.1	1.9	0.31	843	54	22	n.r.	18	86	360	203	25	118	231
P303T011	Toe Slope	12		58	1.1	18	8.7	0.07	3.9	5.7	2.2	1.9	0.33	759	82	22	n.r.	19	78	391	217	24	114	164
P303T017	Toe Slope	29		59	1.2	18	8.1	0.10	3.1	5.6	2.2	1.8	0.26	1003	44	21	n.r.	18	78	410	186	26	129	387
P303T031	Toe Slope	10		57	1.2	20	9.2	0.08	3.5	4.5	1.8	1.8	0.47	855	35	21	n.r.	15	106	298	167	25	96	234
P303T032	Toe Slope	12		59	1.1	19	8.2	0.06	3.1	4.8	2.1	1.6	0.48	793	34	24	n.r.	17	77	356	191	24	115	203
P303T033	Toe Slope	20		57	1.3	20	9.3	0.07	3.6	4.8	1.7	1.7	0.60	771	37	23	n.r.	17	87	332	224	25	128	185
P303T036	Toe Slope	5		56	1.2	20	9.0	0.08	3.4	5.3	2.2	1.7	0.64	861	43	21	n.r.	16	82	373	212	24	128	158
P303T037	Toe Slope	20		59	1.1	19	8.0	0.08	2.9	4.9	2.0	2.0	0.45	1055	33	22	n.r.	19	92	368	186	24	119	236
P303T038	Toe Slope	12		60	1.0	19	7.6	0.08	2.7	4.0	2.1	2.0	0.60	962	34	21	n.r.	18	87	309	170	25	121	247
P303T039	Toe Slope	20		59	1.0	19	7.5	0.13	2.7	5.1	2.5	2.1	0.89	1127	35	22	n.r.	17	94	420	162	25	145	195
P303T040	Toe Slope	20		59	1.1	19	8.0	0.07	2.9	4.6	2.2	2.0	0.37	783	35	22	n.r.	15	93	346	180	25	110	212
P303T041	Toe Slope	2		62	0.89	18	6.7	0.09	2.4	3.9	2.2	2.6	0.24	887	27	21	n.r.	15	117	296	152	23	102	197
P303T042	Toe Slope	9		62	0.97	18	7.2	0.06	2.6	4.0	2.1	2.2	0.19	852	30	22	n.r.	14	106	299	166	25	97	238
P303U01	Upper Slope	2		59	1.1	19	8.1	0.11	3.1	5.2	2.0	2.0	0.43	858	34	22	n.r.	16	94	356	188	22	152	218
mean soil/ saprolite P303				**60**	**1.1**	**19**	**8.0**	**0.07**	**3.1**	**4.8**	**2.1**	**2.0**	**0.37**	**875**	**39**	**22**	**n.d.**	**16**	**91**	**356**	**182**	**24**	**113**	**223**
2 SD soil/ saprolite P303				4.1	0.18	2.2	1.6	0.05	0.74	1.1	0.64	0.55	0.38	215	25	2.4	n.d.	5.8	23	98	47	3.9	33	106
2 SE soil/ saprolite P303				0.87	0.04	0.46	0.34	0.01	0.16	0.24	0.14	0.12	0.08	46	5.4	0.51	n.d.	1.2	5.0	21	10	0.83	7.1	23
N soil/ saprolite P303				22	22	22	22	22	22	22	22	22	22	22	22	22	n.d.	22	22	22	22	22	22	22
P304P01-1	Saprolite	135		63	1.0	19	6.4	0.03	2.6	3.7	1.8	2.2	0.05	729	19	22	n.r.	8.6	84	304	142	17	82	160
P304P01-2	Saprolite	135		63	1.0	19	6.7	0.03	2.6	3.4	1.6	2.1	0.05	746	17	22	n.r.	7.1	89	283	146	16	82	156
P304P01-3	Soil Pit	110		62	1.1	20	6.6	0.03	2.7	3.9	1.9	2.0	0.04	730	22	22	n.r.	8.6	95	317	159	18	76	151
P304P01-4	Soil Pit	90		60	1.1	19	7.8	0.03	3.0	5.1	2.4	1.4	0.08	550	19	23	n.r.	9.2	65	407	165	21	84	147
P304P01-5	Soil Pit	80		59	1.1	19	7.8	0.04	3.1	5.2	2.5	1.3	0.12	550	22	22	n.r.	8.8	66	420	166	24	95	153
P304P01-6	Soil Pit	65		59	1.1	20	7.8	0.04	3.1	4.8	2.3	1.3	0.27	595	23	23	n.r.	13	67	373	163	24	112	167
P304P01-7	Soil Pit	40		60	1.1	20	7.6	0.05	3.0	4.7	2.3	1.4	0.38	692	27	23	n.r.	14	73	367	182	23	105	171
P304P01-8	Soil Pit	40		59	1.1	20	7.7	0.05	3.0	4.7	2.3	1.5	0.51	691	27	21	n.r.	16	77	359	181	23	107	173
P304P01-9	Soil Pit	25		60	1.1	19	7.7	0.05	2.9	4.7	2.3	1.5	0.38	699	30	21	n.r.	13	71	358	172	22	104	175
P304P01RF1	Soil Pit	90		53	1.3	20	8.9	0.05	4.1	7.8	3.4	1.8	0.25	643	21	24	n.r.	11	64	556	194	24	107	126
P304P01RF2	Soil Pit	85		60	1.0	17	7.1	0.04	3.3	6.0	3.0	1.6	0.19	637	20	20	n.r.	9.4	65	489	165	18	89	101
P304P101RF1	Soil Pit	110		n.r.	n.r.	n.r.	n.r.	n.r.	n.r.	n.r.	n.r.	n.r.	n.r.	763	7	17	n.r.	4.3	109	141	13	8	14	92
P304P101RF2	Soil Pit	110		n.r.	n.r.	n.r.	n.r.	n.r.	n.r.	n.r.	n.r.	n.r.	n.r.	747	8	17	n.r.	4.2	97	146	11	9	15	97
P304P102BD1	Soil Pit	128		n.r.	n.r.	n.r.	n.r.	n.r.	n.r.	n.r.	n.r.	n.r.	n.r.	699	16	20	n.r.	8.2	79	420	121	17	82	138
P304T02	Toe Slope	20		60	1.1	19	7.4	0.10	2.9	4.6	1.9	2.0	0.44	758	n.r.	n.r.	n.r.	n.r.	n.r.	n.r.	n.r.	n.r.	n.r.	281
P304T05	Toe Slope	50		61	1.1	19	7.3	0.05	3.0	4.5	2.3	2.0	0.21	696	47	22	n.r.	14	80	338	173	23	117	247
mean soil/ saprolite P304				**60**	**1.1**	**19**	**7.4**	**0.04**	**3.0**	**4.9**	**2.3**	**1.7**	**0.23**	**683**	**22**	**21**	**n.d.**	**10**	**79**	**352**	**143**	**19**	**85**	**158**
2 SD soil/ saprolite P304				5.1	0.16	1.3	1.3	0.03	0.73	2.2	1.0	0.66	0.32	139	19	4.0	n.d.	6.9	28	220	112	10	63	99
2 SE soil/ saprolite P304				1.4	0.04	0.36	0.37	0.01	0.20	0.62	0.27	0.18	0.09	35	4.8	1.0	n.d.	1.8	7.1	57	29	2.7	16	25
N soil/ saprolite P304				13	13	13	13	13.00	13	13	13	13	13	16	15	15	n.d.	15	15	15	15	15	15	16

continued next page …

Supplementary Table 4-3b continued - Sierra Nevada (CA), Loss on ignition (LOI)-corrected analyses of soil, saprolite, rock, bedload sediment and suspended load.

			LOI corrected data (major oxides)										LOI corrected data (trace elements)										
sample ID	**brief sample description**	**LOI**	**SiO_2**	**TiO_2**	**Al_2O_3**	**Fe_2O_3**	**MnO**	**MgO**	**CaO**	**Na_2O**	**K_2O**	**P_2O_5**	**Ba**	**Cr**	**Ga**	**Nb**	**Ni**	**Rb**	**Sr**	**V**	**Y**	**Zn**	**Zr**
		(wt%)	(wt%)	(wt%)	(wt%)	(wt%)	(wt%)	(wt%)	(wt%)	(wt%)	(wt%)	(wt%)	(µg/g)	(µg/g)	(µg/g)	(µg/g)	(µg/g)	(µg/g)	(µg/g)	(µg/g)	(µg/g)	(µg/g)	(µg/g)
international reference materials and inter lab comparison for concentration data quality control																							
SY-4 Diorite (CCRMP) (a)		4.6	53	0.28	22	6.5	0.12	0.57	8.4	7.6	1.7	0.14	524	7.2	n.d.	n.d.	<10	n.d.	1247	n.d.	n.d.	136	566
SY-4 Diorite (CCRMP) (b)		4.6	52	0.29	22	6.5	0.12	0.56	8.4	7.6	1.7	0.14	419	<7	n.d.	n.d.	10	n.d.	1247	n.d.	n.d.	126	555
SY-4 Diorite (CCRMP) (c)		4.6	53	0.28	22	6.5	0.12	0.57	8.4	7.6	1.7	0.14	419	<7	n.d.	n.d.	<10	n.d.	1268	n.d.	n.d.	136	576
SY-4 Diorite (CCRMP) mean		**4.6**	**53**	**0.29**	**22**	**6.5**	**0.12**	**0.56**	**8.4**	**7.6**	**1.7**	**0.14**	**454**	**7.2**	**-**	**-**	**10**	**-**	**1254**	**-**	**-**	**133**	**566**
SY-4 Diorite (CCRMP) 2SD		*0.00*	*0.24*	*0.01*	*0.02*	*0.00*	*0.00*	*0.01*	*0.06*	*0.03*	*0.00*	*0.00*	*121*	-	-	-	-	-	*24*	-	-	*12*	*21*
SY-4 Diorite (CCRMP) 2SE		*0.00%*	*0.46%*	*4.2%*	*0.10%*	*0.00%*	*0.00%*	*2.2%*	*0.7%*	*0.42%*	*0.00%*	*0.00%*	*27%*	-	-	-	-	-	*1.9%*	-	-	*9.1%*	*3.7%*
SY-4 Diorite (CCRMP) certified value		4.6	52	0.30	22	6.5	0.11	0.57	8.4	7.4	1.7	0.14	356	13	37	14	9.4	58	1248	8.4	125	97	542
SY-4 Diorite (CCRMP) certified relative uncertainty		0.07%	0.10%	0.003%	0.08%	0.03%	0.001%	0.01%	0.04%	0.05%	0.02%	0.004%	1.5%	8.3%	2.9%	7.7%	11%	3%	1.0%	25%	1.7%	2.2%	3.1%
relative uncertainty on rock concentrations (%)			**0.5%**	**-5%**	**1%**	**0.0%**	**2%**	**-1%**	**-0.5%**	**2%**	**-4%**	**-1%**	**27%**	**-43%**	**-**	**-**	**11%**	**-**	**0.5%**	**-**	**-**	**36%**	**4.4%**
SRM 2709a San Joaquin Soil (a)		9.1	69	0.58	15	5.0	0.07	2.5	2.9	1.6	2.7	0.16	1013	142	18	14	91	103	256	119	23	98	161
SRM 2709a San Joaquin Soil (b)		26	69	0.59	15	4.7	0.07	2.5	2.9	1.6	2.7	0.17	933	129	18	<14	77	92	251	115	20	106	171
SRM 2709a San Joaquin Soil mean			**69**	**0.59**	**15**	**4.9**	**0.1**	**2.5**	**2.9**	**1.6**	**2.7**	**0.17**	**973**	**135**	**18**	**14**	**84**	**98**	**254**	**117**	**22**	**102**	**166**
SRM 2709a San Joaquin Soil 2SD			*0.48*	*0.004*	*0.19*	*0.51*	*0.00*	*0.04*	*0.03*	*0.03*	*0.00*	*0.00*	*113*	*18*	*0.09*	*14*	*20*	*16*	*7.0*	*4.7*	*3.8*	*11*	*15*
SRM 2709a San Joaquin Soil 2SE			*0.69%*	*0.69%*	*1.3%*	*11%*	*3.3%*	*1.5%*	*0.88%*	*1.9%*	*0.05%*	*0.65%*	*12%*	*13%*	*0.50%*	-	*23%*	*16%*	*3%*	*4%*	*18%*	*11%*	*9.0%*
SRM 2709a certified values			65	0.56	14	4.8	0.07	2.4	2.7	1.6	2.5	0.16	979	130	n.r.	n.r.	85	99	239	110	n.r.	103	195
SRM 2709a certified absolut uncertainty			*0.86*	*0.01*	*0.3*	*0.10*	*0.002*	*0.03*	*0.13*	*0.04*	*0.1*	*0.00*	*28*	*9.0*	*n.r.*	*n.r.*	*2.0*	*3.0*	*6.0*	*11*	*n.r.*	*4.0*	*46*
SRM 2709a RSD			*1.3%*	*2.1%*	*2.2%*	*2.1%*	*3.4%*	*1.4%*	*4.7%*	*2.5%*	*2.8%*	*1.9%*	*2.9%*	*6.9%*			*2.4%*	*3.0%*	*2.5%*	*10%*		*3.9%*	*24%*
relative uncertainty on soil and saprolite concentrations (%)			**7%**	**4%**	**7%**	**1%**	**7%**	**4%**	**7%**	**-4%**	**5%**	**5%**	**-1%**	**4%**	**-**	**-**	**-1%**	**-1%**	**6%**	**6%**	**-**	**-1%**	**-15%**
SN11 (BP Rock, weathered Granodiorite) (XRF lab: GFZ)		1.2	68	0.54	15	4.3	0.07	1.6	3.6	2.6	3.8	0.11	642	17	15	14	11	147	276	73	21	51	139
SN11 (BP Rock, weathered Granodiorite) (XRF lab: Acme)		0.65	68	0.55	15	4.2	0.07	1.7	3.6	2.9	3.9	0.11	705	83	n.d.	n.d.	50	n.d.	262	85	n.d.	81	70
SN11 (BP Rock, weathered Granodiorite) absolute difference			0.05	-0.01	-0.14	0.11	0.003	-0.09	-0.01	-0.28	-0.01	-0.01	-63	-65	-	-	-39	-	15	-12	-	-30	68
SN11 (BP Rock, weathered Granodiorite) relative difference			**0.1%**	**-2%**	**-1%**	**3%**	**5%**	**-6%**	**-0.3%**	**-10%**	**-0.3%**	**-5%**	**-9%**	**-79%**	**-**	**-**	**-78%**	**-**	**6%**	**-14%**	**-**	**-37%**	**97%**

n.d. = not determined; n.r. = not reported; lod = limit of detection; am = amphibole; bt = biotite

ICP-OES analyses have been performed on soil/saprolite exchangeable and soil/saprolite residuum fractions. The limits of detection are: Al, Cu, Fe, Sr, Ti: <0.06µg/g, Ni: <0.11µg/g, Ga: <0.66µg/g, Zn: <2.8µg/g.

Uncertainties on XRF concentration data are estimated to be ±5% relative for major elements (wt%) and 10% relative for Na and for trace elements (based on accuracy of analysed reference materials) and inter lab comparison (Acme & GFZ for SN11).

Data compiled from the literature is from Hahm et al. (2014) and Riebe and Granger (2013). Duplicates were removed, and soil samples reported as 0cm depth were removed.

Bedrock: An outlier test for zirconium concentrations was performed. Samples which failed the 2SD outlier test are labelled in grey and were not taken into account for the calculation of mean bedrock data (including Granodiorite/Tonalite).

† IGSN, International Geo Sample Number, www.igsn.org (syntax e.g. igsn.org/GFFB1000X)

Supplementary Table 4-3c Sierra Nevada (CA), Weathering indices and Mg isotope data.

				Chemical depletion fraction and mass transfer coefficients													Mg isotope data (MC-ICP-MS)						
sample ID	**IGSN †**	**brief sample description**	**depth**	**CDF**	τ_{Zr}^{Si}	τ_{Zr}^{Ti}	τ_{Zr}^{Al}	τ_{Zr}^{Fe}	τ_{Zr}^{Mn}	τ_{Zr}^{Mg}	τ_{Zr}^{Ca}	τ_{Zr}^{Na}	τ_{Zr}^{K}	τ_{Zr}^{P}	τ_{Zr}^{Sr}	τ_{Zr}^{Zn}	**δ^{26}Mg**	**2SD**	**δ^{25}Mg**	**2SD**	**n**	**d**	**c**
			(cm)														(‰)	(‰)	(‰)	(‰)			
P301 regolith depth profile																							
SN01	GFFB1002T	bulk soil	7	0.27	-0.29	-0.34	-0.23	-0.37	8.64	-0.44	-0.14	-0.50	0.03	1.17	-0.24	0.01	-0.13	0.13	-0.07	0.07	3	1	2
SN02	GFFB1002U	bulk soil	20	0.31	-0.29	-0.37	-0.25	-0.42	1.81	-0.49	-0.55	-0.47	-0.13	0.16	-0.49	-0.32	-0.26	0.04	-0.12	0.02	3	1	2
SN02e	GFFB1002U	exchangeable soil	20	n.d.	n.d.	n.d.	n.d.	n.d.	n.d.	n.d.	n.d.	n.d.	n.d.	n.d.	n.d.	n.d.	-0.93	0.06	-0.47	0.02	4	1	1
SN02r	GFFB1002U	residuum soil	20	n.d.	n.d.	n.d.	n.d.	n.d.	n.d.	n.d.	n.d.	n.d.	n.d.	n.d.	n.d.	n.d.	-0.24		-0.12		1	1	1
SN03	GFFB1002V	bulk soil	30	0.31	-0.29	-0.34	-0.24	-0.34	0.70	-0.43	-0.55	-0.51	-0.21	-0.12	-0.49	-0.26	-0.20	0.03	-0.10	0.05	3	1	2
SN04	GFFB1002R	bulk soil	39	0.32	-0.30	-0.30	-0.24	-0.30	0.57	-0.40	-0.56	-0.55	-0.23	-0.20	-0.53	-0.31	-0.17	0.06	-0.09	0.01	3	1	2
SN04e	GFFB1002R	exchangeable soil	39	n.d.	n.d.	n.d.	n.d.	n.d.	n.d.	n.d.	n.d.	n.d.	n.d.	n.d.	n.d.	n.d.	-0.69	0.05	-0.35	0.04	3	1	1
SN04r	GFFB1002R	residuum soil	39	n.d.	n.d.	n.d.	n.d.	n.d.	n.d.	n.d.	n.d.	n.d.	n.d.	n.d.	n.d.	n.d.	-0.18	0.11	-0.10	0.05	3	1	1
SN05	GFFB1002S	bulk soil	53	0.33	-0.32	-0.29	-0.25	-0.30	0.50	-0.39	-0.58	-0.58	-0.24	-0.31	-0.54	-0.32							
SN06	GFFB1002P	bulk soil	65	0.33	-0.32	-0.29	-0.24	-0.29	0.50	-0.39	-0.58	-0.58	-0.28	-0.32	-0.55	-0.30	-0.12	0.19	-0.09	0.07	3	1	2
SN07	GFFB1002Q	bulk soil	77	0.33	-0.31	-0.30	-0.26	-0.30	0.49	-0.40	-0.58	-0.59	-0.27	-0.34	-0.54	-0.35							
SN08	GFFB1002W	bulk soil	89	0.41	-0.41	-0.34	-0.30	-0.33	0.47	-0.43	-0.62	-0.65	-0.37	-0.42	-0.61	-0.38	-0.14	0.12	-0.07	0.06	5	1	2
SN09	GFFB1002X	bulk soil	100	0.41	-0.41	-0.35	-0.32	-0.33	0.51	-0.44	-0.63	-0.65	-0.34	-0.43	-0.62	-0.39							
SN10	GFFB1002Y	bulk soil	111	0.38	-0.38	-0.34	-0.30	-0.32	0.54	-0.42	-0.62	-0.65	-0.34	-0.47	-0.61	-0.40	-0.05	0.08	-0.03	0.04	4	1	2
Balsam regolith depth profile																							
SN59	GFFB10022	bulk soil	5	0.56	-0.57	-0.52	-0.50	-0.48	0.79	-0.61	-0.73	-0.76	-0.54	-0.32	-0.78	-0.46	-0.14	0.10	-0.06	0.05	5	1	1
SN60	GFFB10023	bulk soil	35	0.51	-0.53	-0.43	-0.41	-0.38	0.44	-0.53	-0.70	-0.77	-0.51	-0.56	-0.76	-0.41	-0.05	0.07	-0.04	0.04	4	1	1
SN61	GFFB10024	bulk soil	65	0.52	-0.52	-0.44	-0.44	-0.39	0.42	-0.53	-0.69	-0.77	-0.51	-0.66	-0.76	-0.45	-0.15	0.09	-0.09	0.09	4	1	1
SN62	GFFB10025	bulk soil	85	0.49	-0.49	-0.43	-0.43	-0.36	0.47	-0.52	-0.68	-0.76	-0.50	-0.66	-0.75	-0.47	-0.10	0.07	-0.06	0.03	3	1	1
SN20	GFFB1002K	bulk soil	178	0.29	-0.28	-0.18	-0.17	0.00	0.48	-0.36	-0.76	-0.90	-0.25	-0.80	-0.83	-0.38	-0.25	0.12	-0.12	0.06	4	1	2
SN20e	GFFB1002K	exchangeable soil	178	n.d.	n.d.	n.d.	n.d.	n.d.	n.d.	n.d.	n.d.	n.d.	n.d.	n.d.	n.d.	n.d.	-0.51	0.06	-0.25	0.03	2	1	2
SN20r	GFFB1002K	residuum soil	178	n.d.	n.d.	n.d.	n.d.	n.d.	n.d.	n.d.	n.d.	n.d.	n.d.	n.d.	n.d.	n.d.	-0.23	0.04	-0.13	0.03	2	1	1
SN19	GFFB1002J	bulk soil	257	0.33	-0.32	-0.24	-0.22	-0.16	0.46	-0.37	-0.70	-0.84	-0.24	-0.85	-0.75	-0.39							
SN18	GFFB1002N	bulk saprolite	287	0.31	-0.34	-0.12	-0.20	-0.05	1.03	-0.16	-0.54	-0.73	-0.36	-0.86	-0.70	-0.24							
SN17	GFFB1002M	bulk saprolite	330	0.32	-0.31	-0.30	-0.22	-0.26	0.94	-0.37	-0.55	-0.66	-0.23	-0.85	-0.60	-0.40							
SN16	GFFB1002H	bulk saprolite	414	0.30	-0.29	-0.27	-0.22	-0.23	0.67	-0.35	-0.56	-0.67	-0.26	-0.76	-0.57	-0.43	-0.15	0.10	-0.08	0.04	6	1	2
SN16e	GFFB1002H	exchangeable saprolite	414	n.d.	n.d.	n.d.	n.d.	n.d.	n.d.	n.d.	n.d.	n.d.	n.d.	n.d.	n.d.	n.d.	-0.75	0.10	-0.39	0.04	3	1	2
SN16r	GFFB1002H	residuum saprolite	414	n.d.	n.d.	n.d.	n.d.	n.d.	n.d.	n.d.	n.d.	n.d.	n.d.	n.d.	n.d.	n.d.	-0.14		-0.08		1	1	1
SN15	GFFB1002G	bulk saprolite	513	0.23	-0.21	-0.27	-0.19	-0.24	0.63	-0.35	-0.42	-0.51	-0.22	-0.34	-0.47	-0.38							
SN14	GFFB1002L	bulk saprolite	605	0.24	-0.21	-0.17	-0.21	-0.16	0.82	-0.26	-0.50	-0.62	-0.22	-0.54	-0.57	-0.34	-0.21	0.14	-0.08	0.07	2	1	2
SN14e	GFFB1002L	exchangeable saprolite	605	n.d.	n.d.	n.d.	n.d.	n.d.	n.d.	n.d.	n.d.	n.d.	n.d.	n.d.	n.d.	n.d.	-0.51	0.06	-0.28	0.06	3	1	3
SN14r	GFFB1002L	residuum saprolite	605	n.d.	n.d.	n.d.	n.d.	n.d.	n.d.	n.d.	n.d.	n.d.	n.d.	n.d.	n.d.	n.d.	-0.16		-0.08		1	1	1
																	-0.15	***0.13***	***-0.08***	***0.05***			
																	mean regolith of P301 and PB depth profiles (n=14):						
Creek sediment loads																							
SN46	GFFB10038	suspended load, P301 filter	-														-0.36	0.07	-0.18	0.02	2	1	1
SN47	GFFB10037	suspended load, P300 filter	-														-0.25	0.07	-0.11	0.02	2	1	1
Rocks																							
SN30	GFFB10004	Granodiorite	-	0.03	0.01	-0.18	-0.06	-0.06	1.33	-0.15	-0.14	0.01	0.11	0.26	0.00	0.26							
SN31	GFFB1000B	Granodiorite	-	-0.27	0.34	0.04	0.24	0.10	1.52	0.05	0.13	0.37	0.41	0.24	0.25	0.38	-0.15	0.11	-0.09	0.05	3	1	1

continued next page …

Supplementary Table 4-3c continued - Sierra Nevada (CA), Weathering indices and Mg isotope data.

				Chemical depletion fraction and mass transfer coefficients													Mg isotope data (MC-ICP-MS)						
sample ID	**IGSN †**	**brief sample description**	**depth**	**CDF**	τ_{Zr}^{Si}	τ_{Zr}^{Ti}	τ_{Zr}^{Al}	τ_{Zr}^{Fe}	τ_{Zr}^{Mn}	τ_{Zr}^{Mg}	τ_{Zr}^{Ca}	τ_{Zr}^{Na}	τ_{Zr}^{K}	τ_{Zr}^{P}	τ_{Zr}^{Sr}	τ_{Zr}^{Zn}	**δ^{26}Mg**	**2SD**	**δ^{25}Mg**	**2SD**	**n**	**d**	**c**
			(cm)														(‰)	(‰)	(‰)	(‰)			
SN32	GFFB10009	Granodiorite	-	-0.28	0.46	-0.30	0.11	-0.11	1.02	-0.36	-0.31	0.24	1.14	-0.08	0.14	0.26	-0.23	0.02	-0.13	0.02	2	1	1
SN33	GFFB1000A	Granodiorite	-	-0.16	0.32	-0.40	0.02	-0.24	0.61	-0.41	-0.33	0.21	0.79	-0.23	-0.01	0.03							
SN34	GFFB1000E	Granodiorite	-	-0.28	0.47	-0.30	0.07	-0.07	1.02	-0.35	-0.32	0.21	1.03	-0.08	-0.10	0.13							
SN35	GFFB1001W	Granodiorite/Tonalite -am-bt-rich	-	-0.81	0.59	1.28	0.94	1.51	4.77	1.69	1.40	0.82	0.28	1.90	1.12	1.52	-0.22		-0.14		1	1	1
SN36	GFFB1001X	Granodiorite/Tonalite -am-bt-rich	-	-0.57	0.63	0.47	0.55	0.50	2.16	0.52	0.36	0.42	0.12	0.64	0.59	0.57	-0.34	0.05	-0.18	0.09	2	1	1
SN37	GFFB1001Y	Granodiorite/Tonalite -am-bt-rich	-	-0.15	0.12	0.33	0.15	0.40	2.21	0.33	0.18	0.15	0.01	0.55	0.13	0.49							
SN38	GFFB1001Z	Granodiorite/Tonalite -am-bt-rich	-	-0.15	0.11	0.28	0.17	0.35	2.21	0.26	0.20	0.19	-0.07	0.73	0.23	0.37	-0.19	0.07	-0.09	0.05	1	1	1
SN39	GFFB10020	Granodiorite/Tonalite -am-bt-rich	-	-0.82	0.63	1.53	0.92	1.38	4.05	1.64	1.43	0.84	0.24	1.43	1.24	1.52							
SN40	GFFB1001T	Granodiorite/Tonalite -am-bt-rich	-	-1.12	1.08	1.09	1.07	1.38	4.05	1.48	1.38	0.94	0.39	1.51	1.61	1.94							
SN13	GFFB10021	weathered Granodiorite	688	0.30	-0.29	-0.29	-0.31	-0.27	0.59	-0.35	-0.33	-0.42	-0.51	-0.09	-0.41	-0.39	-0.11	0.11	-0.05	0.07	5	1	2
SN12	GFFB10027	weathered Granodiorite	696	0.34	-0.34	-0.34	-0.36	-0.30	0.56	-0.37	-0.37	-0.44	-0.28	-0.22	-0.44	-0.43	-0.08	0.13	-0.04	0.07	5	1	2
SN11	GFFB10026	weathered Granodiorite	-	0.07	0.06	-0.48	-0.21	-0.44	0.35	-0.55	-0.46	-0.23	0.64	-0.50	-0.47	-0.54	-0.06	0.07	-0.03	0.04	2	1	1
SN41	GFFB1001N	Granodiorite	-	0.02	0.00	-0.07	-0.05	-0.01	1.14	-0.09	-0.04	-0.01	0.02	-0.09	-0.16	0.26	-0.26	0.16	-0.14	0.10	4	1	1
SN42	GFFB1001P	Granodiorite	-	0.02	0.00	-0.11	-0.04	-0.06	1.14	-0.13	-0.04	0.01	0.02	-0.04	-0.24	-0.03							
SN43	GFFB1001Q	Granodiorite	-	-0.59	0.62	0.39	0.55	0.51	2.16	0.36	0.53	0.62	0.61	0.47	0.36	0.73	-0.27	0.16	-0.14	0.08	3	1	1
SN44	GFFB1001R	Granodiorite	-	-0.16	0.18	0.07	0.12	0.10	1.52	0.03	0.10	0.15	0.17	0.07	-0.03	0.26							
SN45	GFFB1001S	Granodiorite	-	0.02	0.00	-0.13	-0.04	-0.03	1.14	-0.11	-0.03	0.00	-0.01	-0.09	-0.14	0.16	-0.18	0.11	-0.09	0.09	8	1	1
Rocks, Data from Hahm et al. (2014) and Riebe and Granger (2013)																							
P301C01		CZO Providence (Dinkey Creek)	-	0.09	-0.03	-0.20	-0.12	-0.28	-0.40	-0.30	-0.25	-0.08	0.02	-0.18	-0.13	n.d.							
P301C02		CZO Providence (Dinkey Creek)	-	-0.74	0.43	0.63	0.50	2.39	2.53	2.84	1.89	0.56	-0.48	0.64	0.12	n.d.							
P301C03		CZO Providence (Dinkey Creek)	-	0.53	-0.49	-0.60	-0.54	-0.59	-0.40	-0.67	-0.70	-0.65	-0.48	-0.31	-0.67	n.d.							
P301C08		CZO Providence (Dinkey Creek)	-	0.07	-0.14	0.18	-0.01	0.09	-0.31	0.10	0.15	-0.10	-0.33	0.13	0.27	n.d.							
P301C11		CZO Providence (Dinkey Creek)	-	0.10	-0.04	-0.29	-0.11	-0.36	-0.46	-0.35	-0.25	-0.05	0.05	-0.29	-0.16	n.d.							
P301OS1		CZO Providence (Dinkey Creek)	-	n.d.	n.d.	n.d.	n.d.	n.d.	n.d.	n.d.	n.d.	n.d.	n.d.	n.d.	n.d.	n.d.							
P301OS10me		CZO Providence (Dinkey Creek)	-	0.29	-0.41	0.09	-0.19	0.03	-0.11	0.06	-0.03	-0.16	-0.44	0.09	-0.18	n.d.							
P301OS12		CZO Providence (Dinkey Creek)	-	0.13	-0.08	-0.27	-0.16	-0.32	-0.45	-0.35	-0.27	-0.10	-0.01	-0.25	-0.13	n.d.							
P301OS12me1		CZO Providence (Dinkey Creek)	-	0.34	-0.38	-0.08	-0.30	-0.24	-0.36	-0.19	-0.30	-0.26	-0.36	-0.01	-0.33	n.d.							
P301OS12me2		CZO Providence (Dinkey Creek)	-	0.44	-0.47	-0.27	-0.47	-0.24	-0.41	-0.34	-0.47	-0.46	-0.31	-0.21	-0.52	n.d.							
P301OS20		CZO Providence (Dinkey Creek)	-	0.04	0.01	-0.19	-0.05	-0.26	-0.43	-0.27	-0.18	-0.02	0.09	-0.16	-0.04	n.d.							
P301OS20m		CZO Providence (Dinkey Creek)	-	-0.35	0.15	0.91	0.45	1.01	0.77	1.02	0.72	0.50	0.21	0.42	0.22	n.d.							
P301OS8		CZO Providence (Dinkey Creek)	-	-0.02	0.08	-0.20	0.04	-0.28	-0.43	-0.29	-0.15	0.06	0.12	-0.14	0.05	n.d.							
P301OS9		CZO Providence (Dinkey Creek)	-	-0.07	0.14	-0.15	0.02	-0.18	-0.26	-0.20	-0.14	0.06	0.24	-0.10	0.02	n.d.							
P301SV2		CZO Providence (Dinkey Creek)	-	0.04	-0.01	-0.11	-0.04	-0.15	-0.33	-0.21	-0.15	-0.02	0.01	-0.04	-0.06	n.d.							
P303C001		CZO Providence (Dinkey Creek)	-	0.14	-0.12	-0.13	-0.16	-0.19	-0.38	-0.21	-0.19	-0.13	-0.13	-0.13	-0.09	n.d.							
P303C002		CZO Providence (Dinkey Creek)	-	0.10	-0.08	-0.14	-0.12	-0.16	-0.38	-0.18	-0.15	-0.10	-0.11	-0.09	-0.05	n.d.							
P303C003		CZO Providence (Dinkey Creek)	-	0.10	-0.09	-0.10	-0.10	-0.11	-0.33	-0.13	-0.11	-0.08	-0.07	-0.05	-0.06	n.d.							
P303C004		CZO Providence (Dinkey Creek)	-	0.01	0.01	0.00	-0.03	-0.07	-0.28	-0.08	-0.07	-0.01	0.01	0.00	0.02	n.d.							
P303C005		CZO Providence (Dinkey Creek)	-	-0.05	0.01	0.12	0.05	0.10	-0.22	0.37	0.27	-0.04	-0.13	0.05	0.22	n.d.							
P303C007-2		CZO Providence (Dinkey Creek)	-	0.17	-0.16	-0.19	-0.15	-0.22	-0.37	-0.24	-0.17	-0.13	-0.12	-0.16	-0.07	n.d.							
P303C007-3		CZO Providence (Dinkey Creek)	-	-0.02	0.04	-0.06	0.02	-0.09	-0.25	-0.10	0.00	0.07	-0.08	0.00	0.12	n.d.							
P303C007part1		CZO Providence (Dinkey Creek)	-	0.08	-0.06	-0.19	-0.07	-0.22	-0.37	-0.21	-0.08	-0.01	-0.17	-0.14	0.03	n.d.							

continued next page

Supplementary Table 4-3c continued - Sierra Nevada (CA), Weathering indices and Mg isotope data.

			Chemical depletion fraction and mass transfer coefficients													Mg isotope data (MC-ICP-MS)						
sample ID	**brief sample description**	**depth**	**CDF**	τ_{Zr}^{Si}	τ_{Zr}^{Ti}	τ_{Zr}^{Al}	τ_{Zr}^{Fe}	τ_{Zr}^{Mn}	τ_{Zr}^{Mg}	τ_{Zr}^{Ca}	τ_{Zr}^{Na}	τ_{Zr}^{K}	τ_{Zr}^{P}	τ_{Zr}^{Sr}	τ_{Zr}^{Zn}	**δ^{26}Mg**	**2SD**	**δ^{25}Mg**	**2SD**	**n**	**d**	**c**
		(cm)														(‰)	(‰)	(‰)	(‰)			
P303C008-1	CZO Providence (Dinkey Creek)	-	-0.16	0.16	0.15	0.17	0.17	-0.16	0.20	0.14	0.12	-0.11	0.12	0.19	n.d.							
P303C010	CZO Providence (Dinkey Creek)	-	0.26	-0.26	-0.24	-0.27	-0.27	-0.39	-0.23	-0.27	-0.29	-0.26	-0.21	-0.26	n.d.							
P303C010A	CZO Providence (Dinkey Creek)	-	0.02	0.00	-0.04	0.01	-0.16	-0.33	-0.11	-0.05	0.01	-0.09	-0.06	0.03	n.d.							
P303C011A	CZO Providence (Dinkey Creek)	-	0.06	-0.09	0.04	-0.04	0.06	-0.23	0.10	-0.02	-0.15	-0.20	0.00	-0.01	n.d.							
P303C011B	CZO Providence (Dinkey Creek)	-	0.01	-0.20	0.40	0.14	0.45	0.18	0.61	0.44	-0.02	-0.24	0.25	0.05	n.d.							
P303C012	CZO Providence (Dinkey Creek)	-	-0.09	0.08	0.08	0.13	0.08	-0.10	0.04	0.13	0.12	-0.02	0.06	0.14	n.d.							
P303C013	CZO Providence (Dinkey Creek)	-	0.03	-0.01	-0.03	-0.02	-0.10	-0.28	-0.15	-0.05	-0.02	-0.07	-0.09	0.02	n.d.							
P303C014A	CZO Providence (Dinkey Creek)	-	0.06	-0.04	-0.10	-0.07	-0.13	-0.32	-0.16	-0.09	-0.06	-0.12	-0.09	-0.03	n.d.							
P303C015	CZO Providence (Dinkey Creek)	-	0.28	-0.29	-0.17	-0.32	-0.18	-0.34	-0.20	-0.30	-0.34	-0.18	-0.16	-0.35	n.d.							
P303C016	CZO Providence (Dinkey Creek)	-	0.07	-0.04	-0.15	-0.08	-0.16	-0.37	-0.21	-0.18	-0.09	0.05	-0.12	-0.09	n.d.							
P303C017	CZO Providence (Dinkey Creek)	-	0.12	-0.10	-0.19	-0.12	-0.21	-0.43	-0.23	-0.18	-0.08	-0.06	-0.12	-0.07	n.d.							
P303C018	CZO Providence (Dinkey Creek)	-	-0.11	0.12	0.10	0.12	0.11	-0.15	0.09	0.16	0.09	-0.19	0.11	0.24	n.d.							
P303C019	CZO Providence (Dinkey Creek)	-	-0.01	-0.01	0.11	0.03	0.06	-0.18	0.05	0.06	-0.01	-0.16	0.07	0.07	n.d.							
P303C020	CZO Providence (Dinkey Creek)	-	-0.17	0.00	0.65	0.29	0.64	0.31	0.71	0.61	0.19	-0.07	0.45	0.37	n.d.							
P303C021	CZO Providence (Dinkey Creek)	-	0.12	-0.10	-0.13	-0.14	-0.12	-0.36	-0.18	-0.17	-0.18	-0.20	-0.11	-0.12	n.d.							
P303C022	CZO Providence (Dinkey Creek)	-	0.00	-0.17	0.42	0.08	0.47	0.41	0.69	0.52	0.03	-0.35	0.35	0.11	n.d.							
P303C023	CZO Providence (Dinkey Creek)	-	0.03	-0.01	-0.11	-0.03	-0.13	-0.30	-0.16	-0.05	0.00	-0.14	-0.10	0.01	n.d.							
P303C024	CZO Providence (Dinkey Creek)	-	-0.32	0.15	0.83	0.42	0.86	0.64	0.90	0.78	0.36	0.09	0.49	0.36	n.d.							
P303C025	CZO Providence (Dinkey Creek)	-	0.04	-0.01	-0.10	-0.04	-0.12	-0.31	-0.18	-0.11	-0.01	0.07	-0.08	-0.04	n.d.							
P303C026	CZO Providence (Dinkey Creek)	-	0.09	-0.06	-0.19	-0.10	-0.22	-0.40	-0.25	-0.15	-0.07	-0.12	-0.14	-0.07	n.d.							
P303C027	CZO Providence (Dinkey Creek)	-	-0.25	0.06	0.61	0.34	0.85	0.66	0.97	0.62	0.29	0.21	0.49	0.12	n.d.							
P303C028	CZO Providence (Dinkey Creek)	-	0.11	-0.09	-0.16	-0.11	-0.19	-0.40	-0.25	-0.19	-0.08	-0.02	-0.17	-0.10	n.d.							
P303C029	CZO Providence (Dinkey Creek)	-	0.04	-0.01	-0.10	-0.04	-0.13	-0.31	-0.18	-0.13	-0.02	-0.01	-0.10	-0.04	n.d.							
P303C030	CZO Providence (Dinkey Creek)	-	0.17	-0.18	-0.02	-0.18	-0.04	-0.24	-0.09	-0.22	-0.21	-0.04	-0.05	-0.20	n.d.							
P303C031	CZO Providence (Dinkey Creek)	-	0.03	0.02	-0.25	0.00	-0.28	-0.50	-0.30	-0.17	0.01	0.16	-0.23	0.03	n.d.							
P303C032	CZO Providence (Dinkey Creek)	-	-0.12	0.05	0.33	0.15	0.28	-0.10	0.65	0.42	0.06	-0.14	0.30	0.46	n.d.							
P303C033	CZO Providence (Dinkey Creek)	-	-0.02	-0.06	0.29	0.06	0.20	-0.12	0.51	0.31	-0.03	-0.20	0.29	0.33	n.d.							
P303C035	CZO Providence (Dinkey Creek)	-	0.01	-0.04	0.14	0.00	0.09	-0.22	0.45	0.13	-0.16	-0.17	-0.02	0.07	n.d.							
P303OS1	CZO Providence (Dinkey Creek)	-	0.00	0.02	0.03	-0.01	-0.05	-0.26	-0.10	-0.07	-0.01	0.02	0.07	-0.04	n.d.							
P303OS1B	CZO Providence (Dinkey Creek)	-	-0.12	-0.03	0.55	0.24	0.52	0.31	0.57	0.52	0.20	-0.08	0.39	0.19	n.d.							
P303OS3	CZO Providence (Dinkey Creek)	-	0.18	-0.18	-0.11	-0.20	-0.16	-0.35	-0.17	-0.24	-0.22	-0.11	0.00	-0.19	n.d.							
P303OS4A	CZO Providence (Dinkey Creek)	-	-0.09	0.13	-0.04	0.10	-0.08	-0.27	-0.12	-0.02	0.13	0.27	0.07	0.12	n.d.							
P303OS4B	CZO Providence (Dinkey Creek)	-	-0.54	0.70	-0.01	0.56	-0.17	-0.36	-0.22	0.29	0.72	0.49	0.03	0.74	n.d.							
Rocks, Data from Hahm et al. (2014) and Riebe and Granger (2013)																						
P303OS4C	CZO Providence (Dinkey Creek)	-	-0.04	-0.08	0.35	0.07	0.46	0.30	0.60	0.26	0.05	0.03	0.29	-0.10	n.d.							
P303OS6A	CZO Providence (Dinkey Creek)	-	-0.02	0.02	0.02	0.03	0.00	-0.23	0.01	-0.04	0.04	0.11	0.00	0.02	n.d.							
P303OS6B	CZO Providence (Dinkey Creek)	-	-0.07	-0.03	0.23	0.10	0.40	0.22	0.61	0.32	0.10	-0.06	0.14	0.01	n.d.							
P304C01	CZO Providence (Dinkey Creek)	-	-1.27	1.00	2.12	1.38	2.13	1.17	2.66	2.36	0.73	0.34	1.00	1.67	n.d.							
P304C010	CZO Providence (Dinkey Creek)	-	0.03	0.02	-0.21	-0.06	-0.21	-0.27	-0.22	-0.18	0.00	0.23	-0.18	-0.04	n.d.							
P304C02	CZO Providence (Dinkey Creek)	-	-1.08	0.82	1.87	1.16	1.89	0.95	2.42	2.09	0.49	0.42	1.01	1.48	n.d.							
P304C03	CZO Providence (Dinkey Creek)	-	-0.54	0.46	0.84	0.55	0.80	0.30	1.04	0.91	0.34	0.12	0.45	0.69	n.d.							

continued next page …

Supplementary Table 4-3c continued - Sierra Nevada (CA), Weathering indices and Mg isotope data.

			Chemical depletion fraction and mass transfer coefficients													Mg isotope data (MC-ICP-MS)						
sample ID	**brief sample description**	**depth**	**CDF**	τ_{Zr}^{Si}	τ_{Zr}^{Ti}	τ_{Zr}^{Al}	τ_{Zr}^{Fe}	τ_{Zr}^{Mn}	τ_{Zr}^{Mg}	τ_{Zr}^{Ca}	τ_{Zr}^{Na}	τ_{Zr}^{K}	τ_{Zr}^{P}	τ_{Zr}^{Sr}	τ_{Zr}^{Zn}	**δ^{26}Mg**	**2SD**	**δ^{25}Mg**	**2SD**	**n**	**d**	**c**
		(cm)														(‰)	(‰)	(‰)	(‰)			
P304C04	CZO Providence (Dinkey Creek)	-	-1.01	0.85	1.34	1.13	1.48	0.98	1.69	1.48	0.79	0.79	0.82	1.23	n.d.							
P304C05	CZO Providence (Dinkey Creek)	-	-0.06	0.11	0.00	0.05	-0.08	-0.33	-0.13	0.01	0.06	-0.04	-0.07	0.12	n.d.							
P304C06	CZO Providence (Dinkey Creek)	-	0.10	-0.08	-0.05	-0.10	-0.13	-0.37	-0.18	-0.13	-0.11	-0.12	-0.10	-0.06	n.d.							
P304C07	CZO Providence (Dinkey Creek)	-	-0.14	0.15	0.14	0.13	0.10	-0.22	0.11	0.15	0.12	-0.01	0.12	0.20	n.d.							
P304C08	CZO Providence (Dinkey Creek)	-	-0.05	0.10	-0.05	0.04	-0.13	-0.39	-0.20	-0.08	0.09	-0.06	-0.11	0.02	n.d.							
P304C09	CZO Providence (Dinkey Creek)	-	-0.16	0.15	0.25	0.19	0.18	-0.13	0.17	0.16	0.14	0.00	0.17	0.18	n.d.							
P304C10	CZO Providence (Dinkey Creek)	-	-0.03	0.06	-0.03	0.04	-0.08	-0.31	-0.12	-0.01	0.03	0.02	-0.05	0.06	n.d.							
P304C12	CZO Providence (Dinkey Creek)	-	0.15	-0.11	-0.20	-0.17	-0.28	-0.44	-0.32	-0.28	-0.14	-0.01	-0.26	-0.18	n.d.							
P304C13B	CZO Providence (Dinkey Creek)	-	-0.01	0.05	-0.04	0.00	-0.09	-0.26	-0.16	-0.10	0.06	0.15	-0.04	-0.07	n.d.							
P304OS1	CZO Providence (Dinkey Creek)	-	-0.06	0.10	0.00	0.04	-0.09	-0.28	-0.20	-0.07	0.12	0.10	-0.02	0.01	n.d.							
P304OS1A	CZO Providence (Dinkey Creek)	-	0.01	-0.03	0.10	0.02	0.01	-0.16	-0.06	-0.11	0.05	0.17	0.22	-0.10	n.d.							
P304OS2	CZO Providence (Dinkey Creek)	-	-0.01	0.06	0.00	-0.02	-0.11	-0.29	-0.15	-0.09	-0.01	0.01	-0.10	-0.01	n.d.							
mean Rocks, data from Hahm et al. (2014) and Riebe and Granger (2013), and GFZ																						
mean bedrock after outlier removal			**-0.04**	**0.03**	**0.04**	**0.04**	**0.05**	**0.05**	**0.05**	**0.05**	**0.04**	**0.03**	**0.03**	**0.03**	**0.08**							
2 SD bedrock after outlier removal			0.44	0.42	0.64	0.45	0.85	1.28	1.02	0.77	0.43	0.58	0.46	0.50	0.71							
2 SE bedrock after outlier removal			0.05	0.05	0.07	0.05	0.09	0.14	0.11	0.08	0.05	0.06	0.05	0.05	0.20							
N bedrock after outlier removal			82	82	82	82	82	82	82	82	82	82	82	82	13							
Soil/ Saprolite, data from Hahm et al. (2014) and Riebe and Granger (2013)																						
P301PF01M100cm	Soil Pit	100	0.28	-0.26	-0.31	-0.19	-0.33	-0.51	-0.41	-0.55	-0.49	-0.25	-0.54	-0.50	-0.35							
P301PF01M10cm	Soil Pit	10	0.31	-0.27	-0.38	-0.26	-0.41	-0.25	-0.49	-0.57	-0.46	-0.25	0.28	-0.51	-0.37							
P301PF01M125cm	Soil Pit	125	n.d.	n.d.	n.d.	n.d.	n.d.	n.d.	n.d.	n.d.	n.d.	n.d.	n.d.	n.d.	n.d.							
P301PF01M150cm	Soil Pit	150	0.28	-0.27	-0.25	-0.23	-0.28	-0.47	-0.33	-0.50	-0.45	-0.20	-0.47	-0.48	-0.34							
P301PF01M182cm	Saprolite	182	0.30	-0.29	-0.28	-0.27	-0.29	-0.49	-0.35	-0.52	-0.47	-0.19	-0.50	-0.50	-0.35							
P301PF01M25cm	Soil Pit	25	0.26	-0.22	-0.33	-0.20	-0.35	-0.46	-0.42	-0.56	-0.46	-0.22	-0.31	-0.50	-0.33							
P301PF01M50cm	Soil Pit	50	0.27	-0.24	-0.30	-0.20	-0.30	-0.42	-0.39	-0.53	-0.47	-0.22	-0.29	-0.49	-0.32							
P301PF01M75cm	Soil Pit	75	0.25	-0.22	-0.28	-0.16	-0.28	-0.51	-0.38	-0.53	-0.46	-0.23	-0.43	-0.48	-0.33							
P301PF01N100cm	Soil Pit	100	0.29	-0.26	-0.30	-0.20	-0.34	-0.56	-0.41	-0.57	-0.51	-0.26	-0.60	-0.53	-0.38							
P301PF01N10cm	Soil Pit	10	0.31	-0.28	-0.35	-0.26	-0.39	-0.14	-0.47	-0.59	-0.49	-0.24	-0.06	-0.52	-0.32							
P301PF01N125cm	Soil Pit	125	0.31	-0.29	-0.28	-0.21	-0.31	-0.50	-0.38	-0.58	-0.54	-0.25	-0.63	-0.56	-0.36							
P301PF01N150cm	Soil Pit	150	0.33	-0.32	-0.27	-0.26	-0.26	-0.49	-0.32	-0.56	-0.55	-0.25	-0.59	-0.57	-0.32							
P301PF01N185cm	Saprolite	185	0.38	-0.38	-0.25	-0.34	-0.27	-0.49	-0.32	-0.58	-0.57	-0.24	-0.65	-0.59	-0.31							
P301PF01N25cm	Soil Pit	25	0.27	-0.23	-0.32	-0.20	-0.33	-0.40	-0.42	-0.57	-0.46	-0.22	-0.01	-0.51	-0.31							
P301PF01N50cm	Soil Pit	50	0.29	-0.26	-0.33	-0.22	-0.34	-0.48	-0.43	-0.57	-0.51	-0.26	-0.34	-0.52	-0.35							
P301PF01N75cm	Soil Pit	75	0.24	-0.21	-0.28	-0.16	-0.30	-0.48	-0.38	-0.53	-0.44	-0.22	-0.45	-0.48	-0.33							
P301PF01S100cm	Soil Pit	100	0.29	-0.26	-0.31	-0.21	-0.32	-0.54	-0.40	-0.55	-0.49	-0.27	-0.55	-0.51	-0.37							
P301PF01S10cm	Soil Pit	10	0.30	-0.27	-0.33	-0.24	-0.37	-0.25	-0.45	-0.58	-0.47	-0.23	0.01	-0.52	-0.33							
P301PF01S125cm	Soil Pit	125	0.23	-0.20	-0.24	-0.14	-0.25	-0.49	-0.33	-0.53	-0.48	-0.16	-0.56	-0.49	-0.32							
P301PF01S150cm	Soil Pit	150	0.36	-0.34	-0.34	-0.27	-0.34	-0.57	-0.42	-0.62	-0.60	-0.27	-0.63	-0.60	-0.41							
P301PF01S177cm	Saprolite	177	0.26	-0.23	-0.28	-0.22	-0.30	-0.50	-0.36	-0.51	-0.44	-0.15	-0.44	-0.47	-0.35							

continued next page …

Supplementary Table 4-3c continued - Sierra Nevada (CA), Weathering indices and Mg isotope data.

			Chemical depletion fraction and mass transfer coefficients													Mg isotope data (MC-ICP-MS)						
sample ID	**brief sample description**	**depth**	**CDF**	τ_{Zr}^{Si}	τ_{Zr}^{Ti}	τ_{Zr}^{Al}	τ_{Zr}^{Fe}	τ_{Zr}^{Mn}	τ_{Zr}^{Mg}	τ_{Zr}^{Ca}	τ_{Zr}^{Na}	τ_{Zr}^{K}	τ_{Zr}^{P}	τ_{Zr}^{Sr}	τ_{Zr}^{Zn}	**δ^{26}Mg**	**2SD**	**δ^{25}Mg**	**2SD**	**n**	**d**	**c**
		(cm)														(‰)	(‰)	(‰)	(‰)			
P301PF01S25cm	Soil Pit	25	0.31	-0.28	-0.38	-0.25	-0.39	-0.43	-0.47	-0.58	-0.47	-0.25	-0.36	-0.52	-0.38							
P301PF01S50cm	Soil Pit	50	0.23	-0.20	-0.25	-0.15	-0.28	-0.39	-0.38	-0.51	-0.43	-0.18	-0.23	-0.46	-0.28							
P301PF01S75cm	Soil Pit	75	0.28	-0.25	-0.32	-0.21	-0.34	-0.49	-0.42	-0.56	-0.48	-0.25	-0.43	-0.51	-0.37							
P301PF02M25cm	Soil Pit	10	n.d.	n.d.	n.d.	n.d.	n.d.	n.d.	n.d.	n.d.	n.d.	n.d.	n.d.	n.d.	n.d.							
P301PF02NW10cm	Soil Pit	10	0.32	-0.29	-0.35	-0.29	-0.39	-0.39	-0.46	-0.49	-0.38	-0.29	-0.07	-0.42	-0.38							
P301PF02NW120cm_dpsp	Saprolite	120	0.09	-0.05	-0.21	-0.07	-0.25	-0.43	-0.29	-0.27	-0.09	-0.14	-0.25	-0.14	-0.31							
Soil/ Saprolite, data from Hahm et al. (2014) and Riebe and Granger (2013)																						
P301PF02NW25cm	Soil Pit	25	0.30	-0.28	-0.38	-0.27	-0.37	-0.34	-0.44	-0.46	-0.35	-0.27	-0.12	-0.40	-0.38							
P301PF02NW50cm	Soil Pit	50	0.18	-0.15	-0.22	-0.15	-0.25	-0.37	-0.32	-0.36	-0.25	-0.18	-0.11	-0.29	-0.28							
P301PF02NW75cm	Soil Pit	75	0.26	-0.23	-0.26	-0.23	-0.31	-0.42	-0.35	-0.43	-0.34	-0.26	-0.25	-0.37	-0.33							
P301PF02NW85cm	Saprolite	85	0.25	-0.23	-0.26	-0.23	-0.32	-0.48	-0.35	-0.40	-0.29	-0.25	-0.34	-0.33	-0.30							
P301PF02SE10cm	Soil Pit	10	0.32	-0.30	-0.36	-0.29	-0.39	-0.35	-0.45	-0.49	-0.37	-0.27	0.08	-0.42	-0.37							
P301PF02SE25cm	Soil Pit	25	0.34	-0.32	-0.36	-0.29	-0.38	-0.37	-0.44	-0.49	-0.40	-0.29	-0.14	-0.43	-0.35							
P301PF02SE50cm	Soil Pit	50	0.29	-0.27	-0.33	-0.25	-0.31	-0.43	-0.38	-0.45	-0.37	-0.28	-0.26	-0.40	-0.35							
P301PF02SE85cmSap	Saprolite	75	0.32	-0.31	-0.25	-0.32	-0.27	-0.43	-0.31	-0.45	-0.40	-0.21	-0.36	-0.42	-0.30							
P301TP1A_20cm	Soil Pit	10	0.28	-0.23	-0.42	-0.26	-0.39	-0.31	-0.49	-0.60	-0.45	-0.03	-0.08	-0.54	-0.33							
P301TP1B_40cm	Soil Pit	30	0.18	n.d.	n.d.	n.d.	n.d.	n.d.	n.d.	n.d.	n.d.	n.d.	n.d.	-0.42	-0.27							
P301TP1BC_60cm	Soil Pit	50	0.20	-0.15	-0.34	-0.16	-0.32	-0.45	-0.41	-0.50	-0.36	-0.01	-0.24	-0.44	-0.31							
P301TP2A	Soil Pit	10	0.19	-0.13	-0.29	-0.15	-0.33	-0.42	-0.43	-0.54	-0.37	0.03	-0.08	-0.46	-0.27							
P301TP2B	Soil Pit	30	0.12	-0.05	-0.32	-0.09	-0.31	-0.42	-0.40	-0.47	-0.30	0.07	-0.10	-0.37	-0.28							
P301TP2BC	Soil Pit	50	0.18	-0.11	-0.37	-0.14	-0.38	-0.52	-0.46	-0.50	-0.34	0.04	-0.22	-0.40	-0.37							
mean soil/ saprolite P301			**0.27**	**-0.24**	**-0.31**	**-0.22**	**-0.33**	**-0.43**	**-0.40**	**-0.52**	**-0.43**	**-0.20**	**-0.30**	**-0.46**	**-0.34**							
2 SD soil/ saprolite P301			0.12	0.14	0.10	0.12	0.09	0.18	0.11	0.14	0.19	0.19	0.45	0.17	0.07							
2 SE soil/ saprolite P301			0.02	0.02	0.02	0.02	0.01	0.03	0.02	0.02	0.03	0.03	0.07	0.03	0.01							
N soil/ saprolite P301			39	38	38	38	38	38	38	38	38	38	38	39	39							
P303P001ABHoriz	Soil Pit	20	0.28	-0.26	-0.25	-0.21	-0.25	-0.17	-0.39	-0.50	-0.48	-0.40	-0.11	-0.47	-0.22							
P303P001B-C	Soil Pit	50	0.49	-0.46	-0.45	-0.47	-0.51	-0.61	-0.53	-0.61	-0.63	-0.55	-0.69	-0.62	-0.54							
P303P001B-horiz	Soil Pit	84	0.35	-0.36	-0.29	-0.28	-0.17	-0.39	-0.43	-0.57	-0.58	-0.51	0.03	-0.55	-0.30							
P303P2RF1	Soil Pit	60	0.06	-0.06	-0.03	0.01	-0.13	-0.33	-0.17	-0.14	-0.01	0.07	0.02	-0.07	-0.20							
P303T003	Toe Slope	40	0.56	-0.54	-0.48	-0.54	-0.51	-0.57	-0.57	-0.70	-0.74	-0.56	-0.69	-0.72	-0.56							
P303T005	Toe Slope	37	0.56	-0.52	-0.51	-0.62	-0.53	-0.57	-0.57	-0.67	-0.76	-0.62	-0.68	-0.74	-0.61							
P303T008	Toe Slope	5	0.44	-0.44	-0.41	-0.39	-0.41	-0.25	-0.45	-0.58	-0.59	-0.34	0.00	-0.57	-0.36							
P303T009	Toe Slope	5	0.47	-0.48	-0.40	-0.43	-0.41	-0.43	-0.45	-0.52	-0.63	-0.52	-0.25	-0.52	-0.40							
P303T010	Toe Slope	4	0.44	-0.45	-0.36	-0.41	-0.33	-0.16	-0.42	-0.56	-0.62	-0.52	-0.11	-0.59	-0.35							
P303T011	Toe Slope	12	0.21	-0.24	-0.09	-0.17	-0.04	0.03	-0.05	-0.28	-0.45	-0.33	0.31	-0.37	-0.13							
P303T017	Toe Slope	29	0.67	-0.67	-0.60	-0.64	-0.62	-0.37	-0.68	-0.70	-0.77	-0.73	-0.56	-0.72	-0.58							
P303T031	Toe Slope	10	0.45	-0.48	-0.30	-0.36	-0.29	-0.15	-0.40	-0.59	-0.69	-0.55	0.33	-0.66	-0.48							
P303T032	Toe Slope	12	0.37	-0.37	-0.27	-0.29	-0.28	-0.24	-0.39	-0.50	-0.58	-0.53	0.54	-0.53	-0.29							
P303T033	Toe Slope	20	0.30	-0.34	-0.09	-0.19	-0.10	-0.02	-0.22	-0.45	-0.62	-0.47	1.13	-0.52	-0.13							

continued next page …

Supplementary Table 4-3c continued - Sierra Nevada (CA), Weathering indices and Mg isotope data.

			Chemical depletion fraction and mass transfer coefficients													Mg isotope data (MC-ICP-MS)						
sample ID	**brief sample description**	**depth**	**CDF**	τ_{Zr}^{Si}	τ_{Zr}^{Ti}	τ_{Zr}^{Al}	τ_{Zr}^{Fe}	τ_{Zr}^{Mn}	τ_{Zr}^{Mg}	τ_{Zr}^{Ca}	τ_{Zr}^{Na}	τ_{Zr}^{K}	τ_{Zr}^{P}	τ_{Zr}^{Sr}	τ_{Zr}^{Zn}	**δ^{26}Mg**	**2SD**	**δ^{25}Mg**	**2SD**	**n**	**d**	**c**
		(cm)														(‰)	(‰)	(‰)	(‰)			
P303T036	Toe Slope	5	0.19	-0.23	0.00	-0.07	0.02	0.30	-0.13	-0.30	-0.43	-0.38	1.64	-0.37	0.02							
P303T037	Toe Slope	20	0.46	-0.46	-0.40	-0.39	-0.39	-0.12	-0.51	-0.57	-0.65	-0.51	0.26	-0.59	-0.36							
P303T038	Toe Slope	12	0.48	-0.47	-0.45	-0.42	-0.45	-0.23	-0.57	-0.66	-0.66	-0.52	0.60	-0.67	-0.38							
P303T039	Toe Slope	20	0.34	-0.35	-0.32	-0.28	-0.31	0.70	-0.44	-0.45	-0.48	-0.37	1.99	-0.43	-0.07							
P303T040	Toe Slope	20	0.39	-0.39	-0.34	-0.33	-0.32	-0.21	-0.45	-0.55	-0.57	-0.45	0.14	-0.57	-0.35							
P303T041	Toe Slope	2	0.35	-0.32	-0.40	-0.31	-0.39	0.14	-0.52	-0.59	-0.55	-0.23	-0.21	-0.60	-0.35							
P303T042	Toe Slope	9	0.46	-0.44	-0.46	-0.43	-0.46	-0.33	-0.57	-0.65	-0.64	-0.44	-0.47	-0.67	-0.49							
P303U01	Upper Slope	2	0.41	-0.42	-0.32	-0.35	-0.33	0.27	-0.44	-0.51	-0.63	-0.47	0.28	-0.57	-0.12							
mean soil/ saprolite P303			**0.40**	**-0.40**	**-0.33**	**-0.34**	**-0.33**	**-0.17**	**-0.42**	**-0.53**	**-0.58**	**-0.45**	**0.16**	**-0.55**	**-0.33**							
2 SD soil/ saprolite P303			0.27	0.26	0.31	0.32	0.33	0.63	0.31	0.28	0.31	0.32	1.41	0.30	0.35							
2 SE soil/ saprolite P303			0.06	0.05	0.07	0.07	0.07	0.13	0.07	0.06	0.07	0.07	0.30	0.06	0.07							
N soil/ saprolite P303			22	22	22	22	22	22	22	22	22	22	22	22	22							
P304P01-1	Saprolite	135	0.20	-0.15	-0.17	-0.11	-0.28	-0.50	-0.35	-0.52	-0.54	-0.19	-0.80	-0.50	-0.36							
P304P01-2	Saprolite	135	0.18	-0.13	-0.15	-0.08	-0.24	-0.52	-0.33	-0.54	-0.58	-0.20	-0.77	-0.52	-0.34							
P304P01-3	Soil Pit	110	0.15	-0.12	-0.05	-0.03	-0.22	-0.49	-0.28	-0.47	-0.49	-0.21	-0.83	-0.44	-0.37							
P304P01-4	Soil Pit	90	0.12	-0.12	-0.02	-0.04	-0.04	-0.42	-0.17	-0.28	-0.34	-0.43	-0.65	-0.26	-0.28							
P304P01-5	Soil Pit	80	0.16	-0.16	-0.03	-0.05	-0.09	-0.38	-0.19	-0.29	-0.33	-0.49	-0.48	-0.27	-0.22							
P304P01-6	Soil Pit	65	0.23	-0.23	-0.11	-0.12	-0.16	-0.38	-0.26	-0.40	-0.43	-0.54	0.06	-0.41	-0.16							
P304P01-7	Soil Pit	40	0.25	-0.25	-0.15	-0.14	-0.20	-0.32	-0.31	-0.43	-0.44	-0.50	0.45	-0.43	-0.22							
P304P01-8	Soil Pit	40	0.26	-0.26	-0.16	-0.15	-0.20	-0.31	-0.31	-0.43	-0.45	-0.50	0.94	-0.45	-0.22							
P304P01-9	Soil Pit	25	0.27	-0.26	-0.17	-0.18	-0.21	-0.31	-0.33	-0.44	-0.46	-0.50	0.44	-0.46	-0.25							
P304P01RF1	Soil Pit	90	-0.02	-0.10	0.38	0.16	0.27	-0.01	0.29	0.30	0.10	-0.15	0.29	0.17	0.07							
P304P01RF2	Soil Pit	85	-0.27	0.28	0.31	0.28	0.27	-0.07	0.29	0.25	0.22	-0.04	0.23	0.29	0.11							
P304P101RF1	Soil Pit	110	-0.39	n.d.	n.d.	n.d.	n.d.	n.d.	n.d.	n.d.	n.d.	n.d.	n.d.	-0.59	-0.82							
P304P101RF2	Soil Pit	110	-0.32	n.d.	n.d.	n.d.	n.d.	n.d.	n.d.	n.d.	n.d.	n.d.	n.d.	-0.60	-0.80							
P304P102BD1	Soil Pit	128	0.07	n.d.	n.d.	n.d.	n.d.	n.d.	n.d.	n.d.	n.d.	n.d.	n.d.	-0.19	-0.25							
P304T02	Toe Slope	20	0.54	-0.54	-0.49	-0.50	-0.53	-0.13	-0.58	-0.66	-0.72	-0.57	0.04	n.d.	n.d.							
P304T05	Toe Slope	50	0.48	-0.47	-0.41	-0.43	-0.47	-0.54	-0.51	-0.62	-0.62	-0.53	-0.45	-0.64	-0.40							
mean soil/ saprolite P304			**0.12**	**-0.19**	**-0.10**	**-0.11**	**-0.16**	**-0.34**	**-0.23**	**-0.35**	**-0.39**	**-0.37**	**-0.12**	**-0.35**	**-0.30**							
2 SD soil/ saprolite P304			0.52	0.39	0.48	0.41	0.47	0.35	0.52	0.59	0.54	0.37	1.16	0.54	0.50							
2 SE soil/ saprolite P304			0.13	0.11	0.13	0.11	0.13	0.10	0.14	0.16	0.15	0.10	0.32	0.14	0.13							
N soil/ saprolite P304			16	13	13	13	13	13	13	13	13	13	13	15	15							
international reference materials for isotope data quality control																						
BHVO-2 (SIS)																-0.26	0.13	-0.13	0.08	12	5	5
SRM 2709a San Joaquin Soil (Apex)																-0.18	0.08	-0.09	0.08	7	1	2
SRM 2709a San Joaquin Soil (SIS)																-0.14	0.10	-0.08	0.06	19	2	6

n.d. = not determined; n.r. = not reported; lod = limit of detection; am = amphibole; bt = biotite

n = number of Mg isotope mass spectrometry analysis

d = number of individual sample dissolutions

c = number of independent processing through Mg column purification

[†] IGSN, International Geo Sample Number, www.igsn.org (syntax e.g. igsn.org/GFFB1000X)

Supplementary Table 4-4a Sierra Nevada (CA), regolith production fluxes, net solubilisation fluxes and dissolved river fluxes.

	K			Ca			Mg			P			Si			Na		
Flux	P301	P303	P304	P301	P303	P304	P301	P303	P304	P301	P303	P304	P301	P303	P304	P301	P303	P304
	(mg m^{-2} yr^{-1})			(mg m^{-2} yr^{-1})			(mg m^{-2} yr^{-1})			(mg m^{-2} yr^{-1})			(mg m^{-2} yr^{-1})			(mg m^{-2} yr^{-1})		
RP^X	4000	4000	4000	9700	9700	9700	4300	4300	4300	190	190	190	61000	61000	61000	5100	5100	5100
(uncertainty)	*560*	*560*	*560*	*1400*	*1400*	*1400*	*640*	*640*	*640*	*26*	*26*	*26*	*8200*	*8200*	*8200*	*680*	*680*	*680*
$W^{Mg}_{regolith}$	790	1800	1500	5000	5100	3400	1700	1800	1000	120	130	160	15000	24000	12000	2200	3000	2000
(uncertainty)	*170*	*370*	*460*	*740*	*920*	*1700*	*260*	*390*	*630*	*30*	*32*	*38*	*2400*	*4700*	*6900*	*330*	*520*	*810*
W^{Mg}_{river}	350	250	690	1300	1200	4100	190	190	670	4.2	6.1	11	4000	2600	7100	1200	800	2400
(SE)	*11*	*7.7*	*28*	*44*	*35*	*170*	*6.1*	*5.8*	*29*	*0.14*	*0.20*	*1.5*	*130*	*82*	*290*	*40*	*25*	*100*

Total denudation rates and uncertainties are from Dixon et al. (2009).

Supplementary Table 4-4b Sierra Nevada (CA), net solubilisation and dissolved river magnesium fluxes.

	net solubilisation fluxes		**river dissolved fluxes**		**fluxes based on δ^{26}Mg**	
catchment	$w^{Mg}_{regolith}$	*uncertainty*	w^{Mg}_{river}	*uncertainty*	$w^{Mg}_{isotope}$	*uncertainty*
P301	0.40	*0.09*	0.04	*0.01*	0.11	*0.13*
P303	0.42	*0.11*	0.04	*0.01*	0.11	*0.13*
P304	0.23	*0.15*	0.16	*0.02*	0.11	*0.13*

Supplementary Table 4-4c Elemental concentration (X) of foliage, stem and root litter fluxes (L^X), and estimates of foliage, stem and root litter fluxes (L^X).

	total L	**K**	*unc.*	**Ca**	*unc.*	**Mg**	*unc.*	**P**	*unc.*	**Si**	*unc.*	**Na**	*unc.*
Concentrations		(µg/g)		(µg/g)		(µg/g)		(µg/g)		(µg/g)		(µg/g)	
$(X)_{foliage}$	n.d.	1487 [(d)]		3133 [(d)]		1349 [(d)]		640 [(d)]		387 [(e)]		90 [(d)]	
$(X)_{stem}$ (min - max)	n.d.	1882 [(e)]		623 [(e)]		287 [(e)]		80 [(f)]		43 [(e)]		3 [(e)]	
$(X)_{root}$	n.d.	1970 [(g)]		1540 [(g)]		545 [(g)]		1300 [(h)]		-		22 [(e)]	
Fluxes	(g m^{-2} yr^{-1})	(mg m^{-2} yr^{-1})		(mg m^{-2} yr^{-1})		(mg m^{-2} yr^{-1})		(mg m^{-2} yr^{-1})		(mg m^{-2} yr^{-1})		(mg m^{-2} yr^{-1})	
foliage L^X	300 ± *36* [(a)]	430	*47*	920	*72*	410	*22*	190	*15*	510 [(i)]	*200*	23	*2.3*
stem L^X (min - max)	880 - 1720 [(b)]	1600 - 3100		560 - 1100		240 - 490		71 - 140		37 - 73		2.3 - 4.6	
root L^X	1226 ± *149* [(c)]	2400	*310*	1900	*240*	680	*73*	1500	*15*	480	*59*	28	*3.4*

(a) mean ± 1SD of total foliage L^X from data from Klemmedson et al. (1990) (foliage L^X: 279.5 t km^{-2} yr^{-1}), Grady and Hart (2006) (foliage L^X: 311 t km^{-2} yr^{-1}), Law et al. (1999) (foliage L^X: 310 t km^{-2} yr^{-1})
(b) for raw data see Appendix C
(c) data from Röderstein et al. (2005)
(d) data from Klemmedson et al. (1990)
(e) data from this study from Pinus ponderosa (table S2)
(f) data from Pearson et al. (1987)
(g) data from Bolou-Bi et al. (2012)
(h) data from George et al. (1997)
(i) mean ± 1 SD of foliage L^{Si} from data from Bartoli (1983) (single data: L^{Si} of deciduous Housseras: 6.7 ± 3.6 Kg ha^{-1} yr^{-1}; L^{Si} of coniferous Biffontaine: 3.8 ± 1.7 kg ha^{-1} yr^{-1})

Supplementary Table 4-4d Dissolved export efficiency (DEE^{X}).

catchment	DEE^{K}	DEE^{Ca}	DEE^{Mg}	DEE^{P}	DEE^{Si}	DEE^{Na}
P301	44%	27%	11%	3%	27%	55%
P303	14%	23%	10%	5%	5%	27%
P304	47%	122%	67%	7%	7%	122%
mean DEE^{X}	**35%**	**57%**	**29%**	**5%**	**13%**	**68%**

Supplementary Table 4-4e Na-normalised dissolved export effieciency (DEE^{X}_{Na}).

catchment	DEE^{K}_{Na}	DEE^{Ca}_{Na}	DEE^{Mg}_{Na}	DEE^{Mg}_{Na}	DEE^{Si}_{Na}
P301	79%	49%	20%	6%	49%
P303	51%	84%	39%	18%	40%
P304	38%	100%	55%	6%	49%
mean	**56%**	**77%**	**38%**	**10%**	**46%**

Supplementary Table 4-4f Recycling factor (Rec^{X}).

catchment	Rec^{K}	Rec^{Ca}	Rec^{Mg}	Rec^{P}	Rec^{Si}
P301	5.7	0.67	0.79	15	0.04
P303	2.5	0.66	0.74	14	0.02
P304	3.0	1.00	1.34	12	0.04
mean Rec^{X}	**3.7**	**0.78**	**0.95**	**13**	**0.03**

5 References

Åberg G (1995) The use of natural strontium isotopes as tracers in environmental studies. Water, Air, Soil Pollut 79:309–322. doi: 10.1007/BF01100444

Åberg G, Jacks G, Wickman T, Hamilton PJ (1990) Strontium isotopes in trees as an indicator for calcium availability. Catena 17:1–11. doi: 10.1016/0341-8162(90)90011-2

Aciego SM, Riebe CS, Hart SC, et al (2017) Dust outpaces bedrock in nutrient supply to montane forest ecosystems. Nat Commun 8:1–10. doi: 10.1038/ncomms14800

Aerts R (1996) Nutrient Resorption from Senescing Leaves of Perennials : Are there General Patterns ? Author (s): Rien Aerts Published by : British Ecological Society Stable URL : http://www.jstor.org/stable/2261481. J Ecol 84:597–608

Aerts R, Chapin FS (1999) The Mineral Nutrition of Wild Plants Revisited: A Re-evaluation of Processes and Patterns. Adv Ecol Res 30:1–67. doi: 10.1016/S0065-2504(08)60016-1

Ahnstrom ZS, Parker DR (1999) Development and assessment of a sequential extraction procedure for the fractionation of soil cadmium. Soil Sci Soc Am J 63:1650–1658

Albers D, Migge S, Schaefer M, Scheu S (2004) Decomposition of beech leaves (Fagus sylvatica) and spruce needles (Picea abies) in pure and mixed stands of beech and spruce. Soil Biol Biochem 36:155–164. doi: 10.1016/j.soilbio.2003.09.002

Amundson R, Richter DD, Humphreys GS, et al (2007) Coupling between biota and earth materials in the critical zone. Elements 3:327–332. doi: 10.2113/gselements.3.5.327

Anderson JU (1961) An Improved Pretreatment for Mineralogical Analysis of Samples Containing Organic Matter. Clays Clay Miner 10:380–388. doi: 10.1346/CCMN.1961.0100134

Anderson SP, Dietrich WE, Brimhall GH (2002) Weathering profiles, mass-balance analysis, and rates of solute loss: Linkages between weathering and erosion in a small, steep catchment. Bull Geol Soc Am 114:1143–1158. doi: 10.1130/0016-7606(2002)114<1143:WPMBAA>2.0.CO

Andrews MG, Jacobson AD, Lehn GO, et al (2016) Radiogenic and stable Sr isotope ratios (87Sr/86Sr, δ88/86Sr) as tracers of riverine cation sources and biogeochemical cycling in the Milford Sound region of Fiordland, New Zealand. Geochim Cosmochim Acta 173:284–303. doi: 10.1016/j.gca.2015.10.005

Arunachalam J, Emons H, Krasnodebska B, Mohl C (1996) Sequential extraction studies on homogenized forest soil samples. Sci Total Environ 181:147–159. doi: 10.1016/0048-9697(95)05005-1

Arvin LJ, Riebe CS, Aciego SM, Blakowski MA (2017) Global patterns of dust and bedrock nutrient supply to montane ecosystems. Sci Adv 3:1–11. doi: 10.1126/sciadv.aao1588

Attiwill PM, Adams MA (1993) Nutrient cycling in forests. New Phytol 124:561–582. doi: 10.1111/j.1469-8137.1993.tb03847.x

Audi G, Wapstra AH (1993) The 1993 atomic mass evaluation. (I) Atomic mass table. Nucl Physics, Sect A 565:1–65. doi: 10.1016/0375-9474(93)90024-R

Augusto L, Achat DL, Jonard M, et al (2017) Soil parent material—A major driver of plant nutrient limitations in terrestrial ecosystems. Glob Chang Biol 23:3808–3824. doi: 10.1111/gcb.13691

Bacon AR, Richter D de B, Bierman PR, Rood DH (2012) Coupling meteoric 10be with pedogenic losses of 9be to improve soil residence time estimates on an ancient North American interfluve. Geology 40:847–850. doi: 10.1130/G33449.1

Bailey SW, Hornbeck JW, Driscoll CT, Gaudette E (1996) Calcium inputs and transport in a base-poor forest ecosystem as interpreted by Sr isotopes Sample. Water Resour Res 32:707–719

Bain DC, Bacon JR (1994) Strontium isotopes as indicators of mineral weathering in catchments. Catena 22:201–214. doi: 10.1016/0341-8162(94)90002-7

Balco GA (2004) The sedimentary record of subglacial erosion beneath the Laurentide Ice Sheet. University of Washington

Bales RC, Hopmans JW, O'Geen AT, et al (2011) Soil Moisture Response to Snowmelt and Rainfall in a Sierra Nevada Mixed-Conifer Forest. Vadose Zo J 10:786–799. doi: 10.2136/vzj2011.0001

Balogh-Brunstad Z, Kent Keller C, Thomas Dickinson J, et al (2008) Biotite weathering and nutrient uptake by ectomycorrhizal fungus, Suillus tomentosus, in liquid-culture experiments. Geochim Cosmochim Acta 72:2601–2618. doi: 10.1016/j.gca.2008.04.003

Barej JAM, Pätzold S, Perkons U, Amelung W (2014) Phosphorus fractions in bulk subsoil and its biopore systems. Eur J Soil Sci 65:553–561. doi: 10.1111/ejss.12124

Barros JAVA, de Souza PF, Schiavo D, Nóbrega JA (2016) Microwave-assisted digestion using diluted acid and base solutions for plant analysis by ICP OES. J Anal At Spectrom 31:337–343. doi: 10.1039/C5JA00294J

Barth T (1961) Abundance of the elements, areal averages and geochemical cycles. Geochim Cosmochim Acta 23:1–8. doi: 10.1016/0016-7037(61)90086-2

Bartoli F (1983) The Biogeochemical Cycle of Silicon in Two Temperate Forest Ecosystems. Ecol Bull 35:469–476

Baruah BK, Das B, Haque A, et al (2011) Sequential extraction of common metals (Na, K, Ca and Mg) from surface soil. J Chem Pharm Res 3:565–573

Bateman PC, Wones DR (1972) Huntington Lake Quadrangle, Central Sierra Nevada, California Analytic Data

Baxter S (2007) World Reference Base for Soil Resources. World Soil Resources Report 103. Rome: Food and Agriculture Organization of the United Nations (2006), pp. 132

Beard BL, Johnson CM, Albarede F (2004) Geochemistry of non-traditional stable isotopes. Mineralogical Society of Amer

Bedel L, Poszwa A, van der Heijden G, et al (2016) Unexpected calcium sources in deep soil layers in low-fertility forest soils identified by strontium isotopes (Lorraine plateau, eastern France). Geoderma 264:103–116. doi: 10.1016/j.geoderma.2015.09.020

Bélanger N, Holmden C, Courchesne F, et al (2012) Constraining soil mineral weathering 87Sr/86Sr for calcium apportionment studies of a deciduous forest growing on soils developed from granitoid igneous rocks. Geoderma 185–186:84–96. doi: 10.1016/j.geoderma.2012.03.024

Berger TW, Swoboda S, Prohaska T, Glatzel G (2006) The role of calcium uptake from deep soils for spruce (Picea abies) and beech (Fagus sylvatica). For Ecol Manage 229:234–246. doi: 10.1016/j.foreco.2006.04.004

Bierman PR, Nichols KK (2004) Rock to Sediment - Slope to Sea with 10Be - Rates of Landscape Change. Annu Rev Earth Planet Sci 32:215–255. doi: 10.1146/annurev.earth.32.101802.120539

Binnie SA, Phillips WM, Summerfield MA, Fifield LK (2007) Tectonic uplift, threshold hillslopes, and denudation rates in a developing mountain range. Geology 35:743–746. doi: 10.1130/G23641A.1

Birks HJB, Birks HH (2004) The rise and fall of forests. Science (80-.). 305:484–485

Black JR, Epstein E, Rains WD, et al (2008) Magnesium-isotope fractionation during plant growth. Environ Sci Technol 42:7831–7836. doi: 10.1021/es8012722

Black JR, Yin Q zhu, Casey WH (2006) An experimental study of magnesium-isotope fractionation in chlorophyll-a photosynthesis. Geochim Cosmochim Acta 70:4072–4079. doi: 10.1016/j.gca.2006.06.010

Black JR, Yin QZ, Rustad JR, Casey WH (2007) Magnesium isotopic equilibrium in chlorophylls. J Am Chem Soc 129:8690–8691. doi: 10.1021/ja072573i

Blum JD, Erel Y (1995) A silicate weathering mechanism linking increases in marine 87Sr/86Sr with global glaciation. Nature 373:415–418. doi: 10.1038/373415a0

Blum JD, Klaue A, Nezat CA, et al (2002) Mycorrhizal weathering of apatite as an important calcium source in base-poor forest ecosystems. Nature 417:729–731. doi: 10.1038/nature00793

Bol R, Julich D, Brödlin D, et al (2016) Dissolved and colloidal phosphorus fluxes in forest ecosystems—an almost blind spot in ecosystem research. J Plant Nutr Soil Sci 179:425–438. doi: 10.1002/jpln.201600079

Bolou-Bi EB, Poszwa A, Leyval C, Vigier N (2010) Experimental determination of magnesium isotope fractionation during higher plant growth. Geochim Cosmochim Acta 74:2523–2537. doi: 10.1016/j.gca.2010.02.010

Bolou-Bi EB, Vigier N, Poszwa A, et al (2012) Effects of biogeochemical processes on magnesium isotope variations in a forested catchment in the Vosges Mountains (France). Geochim Cosmochim Acta 87:341–355. doi: 10.1016/j.gca.2012.04.005

Bonan GB (2008) Forests and climate change: Forcings, feedbacks, and the climate benefits of forests. Science (80-.). 320:1444–1449

Bonneville S, Smits MM, Brown A, et al (2009) Plant-driven fungal weathering: Early stages of mineral alteration at the nanometer scale. Geology 37:615–618. doi: 10.1130/G25699A.1

Bormann FH, Likens GE, Eaton JS (1969) Biotic Regulation of Particulate and Solution Losses from a Forest Ecosystem. Bioscience 19:600–610. doi: 10.2307/1294934

Bornyasz MA, Graham RC, Allen MF (2005) Ectomycorrhizae in a soil-weathered granitic bedrock regolith: Linking matrix resources to plants. Geoderma 126:141–160. doi: 10.1016/j.geoderma.2004.11.023

Bouchez J, Von Blanckenburg F, Schuessler JA (2013) Modeling novel stable isotope ratios in the weathering zone. Am J Sci 313:267–308. doi: 10.2475/04.2013.01

Bowen R (1994) Rubidium-Strontium Dating. In: Isotopes in the Earth Sciences. Springer Netherlands, Dordrecht, pp 162–200

Box GEP, Muller ME (1958) A Note on the Generation of Random Normal Deviates. Ann Math Stat

29:610–611. doi: 10.1214/aoms/1177706645

Boy J, Wilcke W (2008) Tropical Andean forest derives calcium and magnesium from Saharan dust. Global Biogeochem Cycles 22:1–11. doi: 10.1029/2007GB002960

Brady NC, Weil RR (2002) The nature and properties of soils, 13th. Pearson Educ Pte Ltd Indian Branch 482:621–624

Brantley SL, Eissenstat DM, Marshall JA, et al (2017a) Reviews and syntheses: On the roles trees play in building and plumbing the critical zone. Biogeosciences 14:5115–5142. doi: 10.5194/bg-14-5115-2017

Brantley SL, Goldhaber MB, Vala Ragnarsdottir K (2007) Crossing disciplines and scales to understand the critical zone. Elements 3:307–314. doi: 10.2113/gselements.3.5.307

Brantley SL, Lebedeva M (2011) Learning to Read the Chemistry of Regolith to Understand the Critical Zone. Annu Rev Earth Planet Sci 39:387–416. doi: 10.1146/annurev-earth-040809-152321

Brantley SL, Lebedeva MI, Balashov VN, et al (2017b) Toward a conceptual model relating chemical reaction fronts to water flow paths in hills. Geomorphology 277:100–117. doi: 10.1016/j.geomorph.2016.09.027

Brantley SL, Megonigal JP, Scatena FN, et al (2011) Twelve testable hypotheses on the geobiology of weathering. Geobiology 9:140–165. doi: 10.1111/j.1472-4669.2010.00264.x

Brenot A, Cloquet C, Vigier N, et al (2008) Magnesium isotope systematics of the lithologically varied Moselle river basin, France. Geochim Cosmochim Acta 72:5070–5089. doi: 10.1016/j.gca.2008.07.027

Brimhall GH, Dietrich WE (1987) Constitutive mass balance relations between chemical composition, volume, density, porosity, and strain in metasomatic hydrochemical systems: Results on weathering and pedogenesis. Geochim Cosmochim Acta 51:567–587. doi: 10.1016/0016-7037(87)90070-6

Buendía C, Kleidon A, Porporato A (2010) The role of tectonic uplift, climate, and vegetation in the long-term terrestrial phosphorous cycle. Biogeosciences 7:2025–2038. doi: 10.5194/bg-7-2025-2010

Bullen T, Chadwick O (2016) Ca, Sr and Ba stable isotopes reveal the fate of soil nutrients along a tropical climosequence in Hawaii. Chem Geol 422:25–45. doi: 10.1016/j.chemgeo.2015.12.008

Bullen TD (2014) Metal stable isotopes in weathering and hydrology: Chapter 10. In: US Geological Survey. pp 329–359

Bullen TD, Bailey SW (2005) Identifying calcium sources at an acid deposition-impacted spruce forest: A strontium isotope, alkaline earth element multi-tracer approach. Biogeochemistry 74:63–99. doi: 10.1007/s10533-004-2619-z

Cadisch G, Giller KE (1997) Driven by natureplant litter quality and decomposition

Canadell J, Jackson RB, Ehleringer JB, et al (1996) Maximum rooting depth of vegetation types at the global scale. Oecologia 108:583–595. doi: 10.1007/BF00329030

Capo RC, Stewart BW, Chadwick OA (1998) Strontium isotopes as tracers of ecosystem processes : theory and methods. Geoderma 82:197–225

Chadwick OA, Derry LA, Vitousek PM, et al (1999) Changing sources of nutrients during four million

years of ecosystem development. Nature 397:491–497. doi: 10.1038/17276

Chao TT (1984) Use of partial dissolution techniques in geochemical exploration. J Geochemical Explor 20:101–135. doi: 10.1016/0375-6742(84)90078-5

Chapela Lara M, Buss HL, Pogge von Strandmann PAE, et al (2017) The influence of critical zone processes on the Mg isotope budget in a tropical, highly weathered andesitic catchment. Geochim Cosmochim Acta 202:77–100. doi: 10.1016/j.gca.2016.12.032

Chapin SF, Matson PA, Vitousek PM (2012) Principles of terrestrial ecosystem ecology, Second. Springer New York Dordrecht Heidelberg London

Chaudhuri S, Clauer N, Semhi K (2007) Plant decay as a major control of river dissolved potassium: A first estimate. Chem Geol 243:178–190. doi: 10.1016/j.chemgeo.2007.05.023

Chen J, Li G, Yang J, et al (2007) Nd and Sr isotopic characteristics of Chinese deserts: Implications for the provenances of Asian dust. Geochim Cosmochim Acta 71:3904–3914. doi: 10.1016/j.gca.2007.04.033

Chmeleff J, von Blanckenburg F, Kossert K, Jakob D (2010) Determination of the10Be half-life by multicollector ICP-MS and liquid scintillation counting. Nucl Instruments Methods Phys Res Sect B Beam Interact with Mater Atoms 268:192–199. doi: 10.1016/j.nimb.2009.09.012

Chorover J, Kretzschmar R, Garica-Pichel F, Sparks DL (2007) Soil biogeochemicial processes within the critical zone. Elements 3:321–326. doi: 10.2113/gselements.3.5.321

Cleveland CC, Houlton BZ, Smith WK, et al (2013) Patterns of new versus recycled primary production in the terrestrial biosphere. Proc Natl Acad Sci 110:12733–12737. doi: 10.1073/pnas.1302768110

Cleveland CC, Reed SC, Townsend AR (2006) Nutrient Regulation of Organic Matter Decomposition in a Tropical Rain Forest. Ecology 87:492–503

Clymans W, Conley DJ, Battles JJ, et al (2016) Silica uptake and release in live and decaying biomass in a northern hardwood forest. Ecology 97:3044–3057. doi: 10.1002/ecy.1542

Cole DW, Rapp M (1981) Elemental cycling in forest ecosystems. In: Reichle DE (ed) Dynamic properties of forest ecosystems. Cambridge, NY: Cambridge University Press, pp 341–410

Colinvaux P (1987) Amazon diversity in light of the paleoecological record. Quat Sci Rev 6:93–114

Colinvaux P (1997) The ice-age Amazon and the problem of diversity. Nederlandse Organisatie voor Wetenschappelijk Onderzoek

Colinvaux PA, Oliveira PE De, Moreno JE, et al (1996) A Long Pollen Record from Lowland Amazonia: Forest and Cooling in Glacial Times. Science (80-) 274:85–89

Cornelis JT, Ranger J, Iserentant A, Delvaux B (2010) Tree species impact the terrestrial cycle of silicon through various uptakes. Biogeochemistry 97:231–245. doi: 10.1007/s10533-009-9369-x

Crews TE, Kitayama K, Fownes JH, et al (1995) Changes in Soil Phosphorus Fractions and Ecosystem Dynamics across a Long Chronosequence in Hawaii. Ecology 76:1407–1424

Cross AF, Schlesinger WH (1995) A literature review and evaluation of the. Hedley fractionation: Applications to the biogeochemical cycle of soil phosphorus in natural ecosystems. Geoderma 64:197–214. doi: 10.1016/0016-7061(94)00023-4

Cuevas E, Medina E (1986) Nutrient flux in fine litter fall and efficiency of nutrient utilization. Oecologia 68:466–472

Dahlgren RA, Boettinger JL, Huntington GL, Amundson RG (1997) Soil development along an elevational transect in the western Sierra Nevada, California. Geoderma 78:207–236. doi: 10.1016/S0016-7061(97)00034-7

Dai MN, Bao ZA, Chen KY, Yuan HL (2016) In situ Analysis of Mg Isotopic Compositions of Basalt Glasses by Femtosecond Laser Ablation Multi-collector Inductively Coupled Plasma Mass Spectrometry. Chinese J Anal Chem 44:173–178. doi: 10.1016/S1872-2040(16)60901-5

Dannhaus N, Wittmann H, Krám P, et al (2018) Catchment-wide weathering and erosion rates of mafic, ultramafic, and granitic rock from cosmogenic meteoric 10Be/9Be ratios. Geochim Cosmochim Acta 222:618–641. doi: 10.1016/j.gca.2017.11.005

De Biévre P, Taylor PDP (1993) Table of the isotopic compositions of the elements. Int J Mass Spectrom Ion Process 123:149–166. doi: 10.1016/0168-1176(93)87009-H

Dessert C, Lajeunesse E, Lloret E, et al (2015) Controls on chemical weathering on a mountainous volcanic tropical island: Guadeloupe (French West Indies). Geochim Cosmochim Acta 171:216–237. doi: 10.1016/j.gca.2015.09.009

Dixon JL, Heimsath AM, Amundson R (2009) The critical role of climate and saprolite weathering in landscape evolution. Earth Surf Process Landforms 34:1507–1521. doi: 10.1002/esp.1836

Dixon JL, Riebe CS (2014) Tracing and pacing soil across slopes. Elements 10:363–368. doi: 10.2113/gselements.10.5.363

Dixon JL, von Blanckenburg F (2012) Soils as pacemakers and limiters of global silicate weathering. Comptes Rendus - Geosci 344:597–609. doi: 10.1016/j.crte.2012.10.012

Drouet T, Herbauts J, Demaiffe D (2005a) Long-term records of strontium isotopic composition in tree rings suggest changes in forest calcium sources in the early 20th century. Glob Chang Biol 11:1926–1940. doi: 10.1111/j.1365-2486.2005.01034.x

Drouet T, Herbauts J, Gruber W, Demaiffe D (2005b) Strontium isotope composition as a tracer of calcium sources in two forest ecosystems in Belgium. Geoderma 126:203–223. doi: 10.1016/j.geoderma.2004.09.010

Dunai TJ (2000) Scaling factors for production rates of in situ produced cosmogenic nuclides: A critical reevaluation. Earth Planet Sci Lett 176:157–169. doi: 10.1016/S0012-821X(99)00310-6

Eagan SM, Hunsaker CT, Dolanc CR, et al (2007) Discharge and Sediment Loads at the Kings River Experimental Forest in the Southern Sierra Nevada of California. In: Advancing the fundamental sciences: proceedings of the Forest Service National Earth Sciences Conference, edited by: Furniss, M., Clifton, C., and Ronnenberg, K., Gen. Tech. Rep. PNW-GTR-689, Forest Service, Pacific Northwest Research Station, 18–22 O. pp 217–224

Elser JJ, Bracken MES, Cleland EE, et al (2007) Global analysis of nitrogen and phosphorus limitation of primary producers in freshwater, marine and terrestrial ecosystems. Ecol Lett 10:1135–1142. doi: 10.1111/j.1461-0248.2007.01113.x

Elser JJ, Fagan WF, Denno RF, et al (2000) Nutritional constraints in terrestrial and freshwater food webs. Nature 408:578–580. doi: 10.1038/nature02517.1.

Elser JJ, Fagan WF, Kerkhoff AJ, et al (2010) Biological stoichiometry of plant production: Metabolism, scaling and ecological response to global change. New Phytol 186:593–608. doi:

10.1111/j.1469-8137.2010.03214.x

Epstein E, Bloom AJ (2005) Mineral nutrition of plants: principles and perspectives, 2nd edn. Sinauer Assoc. Inc, Sunderland, UK 400

Erel Y, Torrent J (2010) Contribution of Saharan dust to Mediterranean soils assessed by sequential extraction and Pb and Sr isotopes. Chem Geol 275:19–25. doi: 10.1016/j.chemgeo.2010.04.007

Fan Y, Miguez-Macho G, Jobbágy EG, et al (2017) Hydrologic regulation of plant rooting depth. Proc Natl Acad Sci 1–6. doi: 10.1073/pnas.1712381114

Farooqui A, Ray JG, Farooqui SA, et al (2010) Tropical rainforest vegetation , climate and sea level during the Pleistocene in Kerala, India. Quat Int 213:2–11. doi: 10.1016/j.quaint.2009.09.024

Faure G, Mensing TM (2005) Isotopes: principles and applications. John Wiley & Sons Inc

Fernández-Martínez M, Vicca S, Janssens IA, et al (2014) Nutrient availability as the key regulator of global forest carbon balance. Nat Clim Chang 4:471–476. doi: 10.1038/nclimate2177

Field C V., Schmidt GA, Koch D, Salyk C (2006) Modeling production and climate-related impacts on ^{10}Be concentration in ice cores. J Geophys Res Atmos 111:1–13. doi: 10.1029/2005JD006410

Filgueiras A V., Lavilla I, Bendicho C (2002) Chemical sequential extraction for metal partitioning in environmental solid samples. J Environ Monit 4:823–857. doi: 10.1039/b207574c

Förstner U (1993) Metal speciation-general concepts and applications. Int J Environ Anal Chem 51:5–23. doi: 10.1080/03067319308027608

Fraysse F, Pokrovsky OS, Schott J, Meunier JD (2009) Surface chemistry and reactivity of plant phytoliths in aqueous solutions. Chem Geol 258:197–206. doi: 10.1016/j.chemgeo.2008.10.003

Frings PJ, Clymans W, Fontorbe G, et al (2016) The continental Si cycle and its impact on the ocean Si isotope budget. Chem Geol 425:12–36. doi: 10.1016/j.chemgeo.2016.01.020

Galy A, Bar-Matthews M, Halicz L, O'Nions RK (2002) Mg isotopic composition of carbonate: Insight from speleothem formation. Earth Planet Sci Lett 201:105–115. doi: 10.1016/S0012-821X(02)00675-1

Galy A, Belshaw NS, Halicz L, O'Nions RK (2001) High-precision measurement of magnesium isotopes by multiple- collector inductively coupled plasma mass spectrometry. Int J Mass Spectrom 208:89–98. doi: 10.1016/S1387-3806(01)00380-3

Galy A, Yoffe O, Janney PE, et al (2003) Magnesium isotope heterogeneity of the isotopic standard SRM980 and new reference materials for magnesium-isotope-ratio measurements. J Anal At Spectrom 18:1352–1356. doi: 10.1039/b309273a

Galy V, Peucker-Ehrenbrink B, Eglinton T (2015) Global carbon export from the terrestrial biosphere controlled by erosion. Nature 521:204–207. doi: 10.1038/nature14400

George E, Seith B, Schaeffer C, Marschner H (1997) Responses of Picea, Pinus and Pseudotsuga roots to heterogeneous nutrient distribution in soil. Tree Physiol 17:39–45. doi: 10.1093/treephys/17.1.39

George TS, Fransson A, Hammond JP, White PJ (2011) Phosphorus Nutrition: Rhizosphere Processes Plant Response and Adaptations. In: Phosphorus in Action. pp 245–271

Gibson MJ, Farmer JG (1986) Multi-step sequential chemical extraction of heavy metals from urban

soils. Environ Pollution Ser B, Chem Phys 11:117–135. doi: 10.1016/0143-148X(86)90039-X

Gosse JC, Phillips FM (2001) Terrestrial in situ cosmogenic nuclides:theory and application. Quat Sci Rev 20:1475–1560. doi: 10.1016/S0277-3791(00)00171-2

Göttlein A, Baier R, Mellert KH (2011) Neue Ernährungskennwerte für die forstlichen Hauptbaumarten in Mitteleuropa - Eine statistische Herleitung aus VAN DEN BURG'S Literaturzusammenstellung. Allg Forst- und Jagdzeitung 182:173–186

Grady KC, Hart SC (2006) Influences of thinning, prescribed burning, and wildfire on soil processes and properties in southwestern ponderosa pine forests: A retrospective study. For Ecol Manage 234:123–135. doi: 10.1016/j.foreco.2006.06.031

Graham RC, Rossi AM, Hubbert KR (2010) Rock to regolith conversion: Producing hospitable substrates for terrestrial ecosystems. GSA Today 20:4–9. doi: 10.1130/GSAT57A.1

Graham RT, Jain TB (2005) Ponderosa pine ecosystems

Graly JA, Bierman PR, Reusser LJ, Pavich MJ (2010) Meteoric 10Be in soil profiles - A global meta-analysis. Geochim Cosmochim Acta 74:6814–6829. doi: 10.1016/j.gca.2010.08.036

Granger DE, Kirchner JW, Finkel R (1996) Spatially averaged long-term erosion rates measured from in situ-produced cosmogenic nuclides in alluvial sediments. J Geol 104:249–257

Granger DE, Schaller M (2014) Cosmogenic nuclides and erosion at the watershed scale. Elements 10:369–373. doi: 10.2113/gselements.10.5.369

Graustein WC, Armstrong RL (1983) The use of strontium-87/strontium-86 ratios to measure atmospheric transport into forested watersheds. Science (80-) 219:289–292. doi: 10.1126/science.219.4582.289

Gross A, Palchan D, Krom MD, Angert A (2016) Elemental and isotopic composition of surface soils from key Saharan dust sources. Chem Geol 442:54–61. doi: 10.1016/j.chemgeo.2016.09.001

Grousset FE, Biscaye PE (2005) Tracing dust sources and transport patterns using Sr, Nd and Pb isotopes. Chem Geol 222:149–167. doi: 10.1016/j.chemgeo.2005.05.006

Grousset FE, Rognon P, Coudé-Gaussen G, Pédemay P (1992) Origins of peri-Saharan dust deposits traced by their Nd and Sr isotopic composition. Palaeogeogr Palaeoclimatol Palaeoecol 93:203–212. doi: 10.1016/0031-0182(92)90097-O

Grubb PJ (1995) Mineral Nutrition and Soil Fertility in Tropical Rain Forests. In: Lugo AE et al. (ed) Tropical Forests: Management and Ecology. Springer-Verlag New York, Inc., pp 308–330

Hahm WJ, Riebe CS, Lukens CE, Araki S (2014) Bedrock composition regulates mountain ecosystems and landscape evolution. Proc Natl Acad Sci 111:3338–3343. doi: 10.1073/pnas.1315667111

Hahn O, Strassman F, Mattauch J, Ewald H (1943) Geologische Altersbestimmungen mit der strontiummethode. Chem Zeitung 67:55–56

Hall GEM, Gauthier G, Pelchat J-C, et al (1996) Application of a sequential extraction scheme to ten geological certified reference materials for the determination of 20 elements. J Anal At Spectrom 11:787–796. doi: 10.1039/ja9961100787

Harder H (1972) The role of magnesium in the formation of smectite minerals. Chem Geol 10:31–39. doi: 10.1016/0009-2541(72)90075-7

Hättenschwiler S, Coq S, Barantal S, Handa IT (2011) Leaf traits and decomposition in tropical rainforests: Revisiting some commonly held views and towards a new hypothesis. New Phytol 189:950–965. doi: 10.1111/j.1469-8137.2010.03483.x

He X-T, Logan TJ, Traina SJ (1995) Physical and chemical characteristics of selected US municipal solid waste composts. J Environ Qual 24:543–552

Heartsill Scalley T, Scatena FN, Moya S, Lugo AE (2012) Long-term dynamics of organic matter and elements exported as coarse particulates from two Caribbean montane watersheds. J Trop Ecol 28:127–139. doi: 10.1017/S0266467411000733

Hedley MJ, Stewart JWB, Chauhan BS (1982) Changes in Inorganic and Organic Soil Phosphorus Fractions Induced by Cultivation Practices and by Laboratory Incubations1. Soil Sci Soc Am J 46:970–976. doi: 10.2136/sssaj1982.03615995004600050017x

Heikkilä U, von Blanckenburg F (2015) The global distribution of Holocene meteoric 10Be fluxes from atmospheric models. Distrib maps Terr Earths Surf Appl GFZ Data Serv GFZ Potsdam, Ger doi 10:

Heimsath AM, Chappel J, Finkel RC, et al (2006) Escarpment erosion and landscape evolution in southeastern Australia. Geol Soc Am 398:173–190. doi: 10.1130/2006.2398(10).

Heimsath AM, Dietrich WE, Nishiizumi K, Finkel RC (1999) Cosmogenic nuclides, topography, and the spatial variation of soil depth. Geomorphology 27:151–172. doi: 10.1016/S0169-555X(98)00095-6

Heimsath AM, Dietrich WE, Nishiizumi K, Finkel RC (1997) The soil production function and landscape equilibrium. Nature 388:358–361

Hellsten S, Helmisaari HS, Melin Y, et al (2013) Nutrient concentrations in stumps and coarse roots of Norway spruce, Scots pine and silver birch in Sweden, Finland and Denmark. For Ecol Manage 290:40–48. doi: 10.1016/j.foreco.2012.09.017

Hewawasam T, von Blanckenburg F, Bouchez J, et al (2013) Slow advance of the weathering front during deep, supply-limited saprolite formation in the tropical Highlands of Sri Lanka. Geochim Cosmochim Acta 118:202–230. doi: 10.1016/j.gca.2013.05.006

Hillis WE (2006) Heartwood and Tree Exudates. Springer-Verlag

Hilton RG (2017) Climate regulates the erosional carbon export from the terrestrial biosphere. Geomorphology 277:118–132. doi: 10.1016/j.geomorph.2016.03.028

Hinsinger P, Brauman A, Devau N, et al (2011) Acquisition of phosphorus and other poorly mobile nutrients by roots. Where do plant nutrition models fail? Plant Soil 348:29–61. doi: 10.1007/s11104-011-0903-y

Hogan JF, Blum JD (2003) Tracing hydrologic flow paths in a small forested watershed using variations in $^{87}Sr/^{86}Sr$, [Ca]/[Sr], [Ba]/[Sr] and $\delta^{18}O$. Water Resour Res 39:1–12. doi: 10.1029/2002WR001856

Holden NE (1990) Total half-lives for selected nuclides. Int Union Pure Appl Chem 62:941–958. doi: 10.1351/pac199062050941

Hooghiemstra H (1997) Tropical rain forest versus savanna: two sides of a precious medal? A comment. Broch NWO/Huygenslezing 31–43

Houlton BZ, Morford SL, Dahlgren RA (2018) Convergent evidence for widespread rock nitrogen sources in Earth ' s surface environment. Science (80-) 360:58–62

Huang KJ, Teng FZ, Wei GJ, et al (2012) Adsorption- and desorption-controlled magnesium isotope fractionation during extreme weathering of basalt in Hainan Island, China. Earth Planet Sci Lett 359–360:73–83. doi: 10.1016/j.epsl.2012.10.007

Hursthouse AS (2001) The relevance of speciation in the remediation of soils and sediments contaminated by metallic elements - An overview and examples from Central Scotland, UK. J Environ Monit 3:49–60. doi: 10.1039/b006132h

Jacobsen C, Rademacher P, Meesenburg H, Meiwes KJ (2002) Gehalte chemischer Elemente in Baumkompartimenten. Niedersächsische Forstl Versuchsanstalt Göttingen

Jacobson AD, Jacobson AD, Blum JD (2000) Ca / Sr and 87Sr / 86Sr geochemistry of disseminated calcite in Himalayan silicate rocks from Nanga Parbat ... Ca / Sr and 87 Sr / 86 Sr geochemistry of disseminated calcite in Himalayan silicate rocks from Nanga Parbat : Influence on river-water chemistr. Geology 28:463–466. doi: 10.1130/0091-7613(2000)28<463

Jansa J, Finlay R, Smith FA, Smith SE (2011) Role of Mycorrhizal Symbioses in Phosphorus Cycling. In: Phosphorus in Action. pp 137–168

Jickells TD, An ZS, Andersen KK, et al (2005) Global iron connections between desert dust, ocean biogeochemistry, and climate. Science (80-) 308:67–71. doi: 10.1126/science.1105959

Jobbagy EG, Jackson RB (2000) The Vertical Distribution of Soil Organic Carbon and Its Relation to Climate and Vegetation. Ecol Appl 10:423–436. doi: 10.2307/2641104

Jobbágy EG, Jackson RB (2001) The distribution of soil nutrients with depth: Global patterns and the imprint of plants. Biogeochemistry 53:51–77. doi: 10.1023/A:1010760720215

Jobbágy EG, Jackson RB (2004) The uplift of soil nutrients by plants: Biogeochemical consequences across scales. Ecology 85:2380–2389. doi: 10.1890/03-0245

Jochum KP, Nohl U, Herwig K, et al (2005) GeoReM: A New Geochemical Database for Reference Materials and Isotopic Standards. Geostand Geoanalytical Res 29:333–338. doi: 10.1111/j.1751-908X.2005.tb00904.x

Johnson CE, Siccama TG, Denny EG, et al (2014) In situ decomposition of northern hardwood tree boles: decay rates and nutrient dynamics in wood and bark. Can J For Res 44:1515–1524. doi: 10.1139/cjfr-2014-0221

Jongmans AG, Van Breemen N, Lundström U, et al (1997) Rock-eating fungi. Nature 389:682–683. doi: 10.1038/39493

Jordan C, Golley F, Hall J, Hall J (1980) Nutrient Scavenging of Rainfall by the Canopy of an Amazonian Rain Forest. Biotropica 12:61–66

Jordan CF (1982) The Nutrient Balance of an Amazonian Rain Forest. Ecology 63:647–654

Jung M, Reichstein M, Margolis HA, et al (2011) Global patterns of land-atmosphere fluxes of carbon dioxide, latent heat, and sensible heat derived from eddy covariance, satellite, and meteorological observations. J Geophys Res Biogeosciences 116:1–16. doi: 10.1029/2010JG001566

Kabata-Pendias A (2011) Trace elements in soils and plants

Kauffman S, Sombroek W, Mantel S (1998) Soils of rainforests Characterization and major constraints of dominant forest soils in the humid tropics BT - Soils of Tropical Forest Ecosystems. In: Schulte A, Ruhiyat D (eds). Springer Berlin Heidelberg, Berlin, Heidelberg, pp 9–20

Kennedy MJ, Chadwick OA, Vitousek PM, et al (1998) Changing sources of base cations during ecosystem development, Hawaiian Islands. Geology 26:1015–1018

Kennedy MJ, Hedin LO, Derry LA (2002) Decoupling of unpolluted temperate forests from rock nutrient sources revealed by natural 87Sr/86Sr and 84Sr tracer addition. Proc Natl Acad Sci 99:9639–9644. doi: 10.1073/pnas.152045499

Killingbeck KT (1996) Nutrients in Senesced Leaves : Keys to the Search for Potential Resorption and Resorption Proficiency. Ecology 77:1716–1727

Kimmig SR, Holmden C, Bélanger N (2018) Biogeochemical cycling of Mg and its isotopes in a sugar maple forest in Québec. Geochim Cosmochim Acta. doi: 10.1016/j.gca.2018.03.020

Kirchner JW, Finkel RC, Riebe CS, et al (2001) Mountain erosion over 10 yr, 10 k.y., and 10 m.y. time scales. Geology 29:591–594. doi: 10.1130/0091-7613(2001)029<0591:MEOYKY>2.0.CO;2

Klemmedson JO (1992) Decomposition and nutrient release from mixtures of Gambel oak and ponderosa pine leaf litter. For Ecol Manage 47:349–361. doi: 10.1016/0378-1127(92)90284-G

Klemmedson JO, Meier CE, Campbell RE (1990) Litter fall transfers of dry matter and nutrients in ponderosa pine stands. Can J For Res 20:1105–1115

Korschinek G, Bergmaier A, Faestermann T, et al (2010) A new value for the half-life of 10Be by Heavy-Ion Elastic Recoil Detection and liquid scintillation counting. Nucl Instruments Methods Phys Res Sect B Beam Interact with Mater Atoms 268:187–191. doi: 10.1016/j.nimb.2009.09.020

Krishnamurti GSR, Huang PM, Van Rees KCJ, et al (1995) Speciation of particulate-bound Cadmium of soils and its bioavailability. Analyst 120:659–665. doi: 10.1039/an9952000659

Laclau P (2003) Biomass and carbon sequestration of ponderosa pine plantations and native cypress forests in northwest Patagonia. For Ecol Manage 180:317–333. doi: 10.1016/S0378-1127(02)00580-7

Lal D (1991) Cosmic ray labeling of erosion surfaces: in situ nuclide production rates and erosion models. Earth Planet Sci Lett 104:424–439. doi: 10.1016/0012-821X(91)90220-C

Lal D, Peters B (1967) Cosmic Ray Produced Radioactivity on the Earth BT - Kosmische Strahlung II / Cosmic Rays II. In: Sitte K (ed). Springer Berlin Heidelberg, Berlin, Heidelberg, pp 551–612

Lal R (2008) Carbon sequestration. Philos Trans R Soc B Biol Sci 363:815–830. doi: 10.1098/rstb.2007.2185

Lambers H, Raven JA, Shaver GR, Smith SE (2008) Plant nutrient-acquisition strategies change with soil age. Trends Ecol Evol 23:95–103. doi: 10.1016/j.tree.2007.10.008

Lambers H, Shane MW, Cramer MD, et al (2006) Root structure and functioning for efficient acquisition of phosphorus: Matching morphological and physiological traits. Ann Bot 98:693–713. doi: 10.1093/aob/mcl114

Landeweert R, Hoffland E, Finlay RD, et al (2001) Linking plants to rocks: Ectomycorrhizal fungi mobilize nutrients from minerals. Trends Ecol. Evol. 16:248–254

Lang F, Bauhus J, Frossard E, et al (2016) Phosphorus in forest ecosystems: New insights from an ecosystem nutrition perspective. J Plant Nutr Soil Sci 179:129–135. doi: 10.1002/jpln.201500541

Lang F, Krüger J, Amelung W, et al (2017) Soil phosphorus supply controls P nutrition strategies of beech forest ecosystems in Central Europe. Biogeochemistry 136:5–29. doi: 10.1007/s10533-017-0375-0

Larsen IJ, Montgomery DR, Greenberg HM (2014) The contribution of mountains to global denudation. Geology 42:527–530. doi: 10.1130/G35136.1

Lauer F, Pätzold S, Gerlach R, et al (2013) Phosphorus status in archaeological arable topsoil relicts-Is it possible to reconstruct conditions for prehistoric agriculture in Germany? Geoderma 207–208:111–120. doi: 10.1016/j.geoderma.2013.05.005

Lavkulich LM, Wiens JH (1970) Comparison of Organic Matter Destruction by Hydrogen Peroxide and Sodium Hypochlorite and Its Effects on Selected Mineral Constituents 1. Soil Sci Soc Am J 34:755–758

Law BE, Ryan MG, Anthoni PM (1999) Seasonal and annual respiration of a ponderosa pine ecosystem. Glob Chang Biol 5:169–182. doi: 10.1046/j.1365-2486.1999.00214.x

Lebedeva MI, Fletcher RC, Brantley SL (2010) A mathematical model for steady-state regolith production at constant erosion rate. Earth Surf Process Landforms 35:508–524. doi: 10.1002/esp.1954

Lee FY, Kittrick JA (1984) Elements Associated with the Cadmium Phase in a Harbor Sediment as Determined with the Electron Beam Microprobe1. J Environ Qual 13:337–340

Lin H (2010) Earth ' s Critical Zone and hydropedology : concepts , characteristics , and advances. Hydrol Earth Syst Sci 14:25

Liu XM, Teng FZ, Rudnick RL, et al (2014) Massive magnesium depletion and isotope fractionation in weathered basalts. Geochim Cosmochim Acta 135:336–349. doi: 10.1016/j.gca.2014.03.028

Lucas Y (2001) The Role of Plants in Controlling Rates and Products of Weathering: Importance of Biological Pumping. Annu Rev Earth Planet Sci 29:135–163. doi: 10.1146/annurev.earth.29.1.135

Ma L, Teng FZ, Jin L, et al (2015) Magnesium isotope fractionation during shale weathering in the Shale Hills Critical Zone Observatory: Accumulation of light Mg isotopes in soils by clay mineral transformation. Chem Geol 397:37–50. doi: 10.1016/j.chemgeo.2015.01.010

Maathuis FJ (2009) Physiological functions of mineral macronutrients. Curr Opin Plant Biol 12:250–258. doi: 10.1016/j.pbi.2009.04.003

Maher K (2010) The dependence of chemical weathering rates on fluid residence time. Earth Planet Sci Lett 294:101–110. doi: 10.1016/j.epsl.2010.03.010

Maher K (2011) The role of fluid residence time and topographic scales in determining chemical fluxes from landscapes. Earth Planet Sci Lett 312:48–58. doi: 10.1016/j.epsl.2011.09.040

Maher K, Johnson NC, Jackson A, et al (2016) A spatially resolved surface kinetic model for forsterite dissolution. Geochim Cosmochim Acta 174:313–334. doi: 10.1016/j.gca.2015.11.019

Maher K, von Blanckenburg F (2016) Surface ages and weathering rates from10Be (meteoric) and10Be/9Be: Insights from differential mass balance and reactive transport modeling. Chem Geol 446:70–86. doi: 10.1016/j.chemgeo.2016.07.016

Mahowald N, Jickells TD, Baker AR, et al (2008) Global distribution of atmospheric phosphorus sources, concentrations and deposition rates, and anthropogenic impacts. Global Biogeochem

Cycles 22:1–19. doi: 10.1029/2008GB003240

Marin B, Valladon M, Polve M, Monaco A (1997) Reproducibility testing of a sequential extraction scheme for the determination of trace metal speciation in a marine reference sediment by inductively coupled plasma-mass spectrometry. Anal Chim Acta 342:91–112. doi: 10.1016/S0003-2670(96)00580-6

Marschner P (2011) Marschner's Mineral Nutrition of Higher Plants

Mavromatis V, Prokushkin AS, Pokrovsky OS, et al (2014) Magnesium isotopes in permafrost-dominated Central Siberian larch forest watersheds. Geochim Cosmochim Acta 147:76–89. doi: 10.1016/j.gca.2014.10.009

McCorkle EP, Berhe AA, Hunsaker CT, et al (2016) Tracing the source of soil organic matter eroded from temperate forest catchments using carbon and nitrogen isotopes. Chem Geol 445:172–184. doi: 10.1016/j.chemgeo.2016.04.025

McCulley RL, Jobbágy EG, Pockman WT, Jackson RB (2004) Nutrient uptake as a contributing explanation for deep rooting in arid and semi-arid ecosystems. Oecologia 141:620–628. doi: 10.1007/s00442-004-1687-z

McHargue LR, Damon PE (1991) The global beryllium 10 cycle. Rev Geophys 29:141–158. doi: 10.1029/91RG00072

Meek K, Derry L, Sparks J, Cathles L (2016) 87Sr/86Sr, Ca/Sr, and Ge/Si ratios as tracers of solute sources and biogeochemical cycling at a temperate forested shale catchment, central Pennsylvania, USA. Chem Geol 445:84–102. doi: 10.1016/j.chemgeo.2016.04.026

Meerts P (2002) Mineral nutrient concentrations in sapwood and heartwood: a literature review. Ann For Sci 59:713–722. doi: 10.1051/forest:2002059

Menge DNL, Hedin LO, Pacala SW (2012) Nitrogen and Phosphorus Limitation over Long-Term Ecosystem Development in Terrestrial Ecosystems. PLoS One 7:1–17

Merrill GP (1906) A Treatise on Rocks, Rock-weathering and Soils. Macmillan

Mészáros E (1981) Atmospheric Chemistry. Elsevier

Meyer J, Likens GE (1979) Transport and transformation of phosphorus in a forest stream ecosystem. Ecology 60:1255–1269

Miller EK, Blum JD, Friedland AJ (1993) Determination of soil exchangeable-cation loss and weathering rates using Sr isotopes. Nature 362:438–441. doi: 10.1038/362438a0

Missong A, Bol R, Willbold S, et al (2016) Phosphorus forms in forest soil colloids as revealed by liquid-state 31P-NMR. J Plant Nutr Soil Sci 179:159–167. doi: 10.1002/jpln.201500119

Moir J, Tiessen H (1993) Characterization of Available P by Sequential Extraction. In: Soil Sampling and Methods of Analysis. pp 75–86

Monaghan MC, Krishnaswami S, Turekian KK, Parker PD (1983) 10Be flux to the Earth's surface based on yearly integrated precipitation collection (abstract). Eos Tran AGU 64:

Monaghan MC, McKean J, Dietrich W, Klein J (1992) 10Be chronometry of bedrock-to-soil conversion rates. Earth Planet Sci Lett 111:483–492. doi: 10.1016/0012-821X(92)90198-5

Moore TR, Trofymow JA, Siltanen M, et al (2005) Patterns of decomposition and carbon, nitrogen,

and phosphorus dynamics of litter in upland forest and peatland sites in central Canada. Can J For Res 35:133–142. doi: 10.1139/x04-149

Moulton KL, West J, Berner RA (2000) Solute flux and mineral mass balance approaches to the quantification of plant effects on silicate weathering. Am J Sci 300:539–570

Murphy J, Riley J (1962) A modified single solution method for the determination of phosphate in natural water. Anal Chem Acta 27:31–36. doi: 10.1016/S0003-2670(00)88444-5

Muzikar P, Elmore D, Granger DE (2003) Accelerator mass spectrometry in geologic research. Bull Geol Soc Am 115:643–654. doi: 10.1130/0016-7606(2003)115<0643:AMSIGR>2.0.CO;2

Newman E (1995) Phosphorus inputs to terrestrial ecosystems. J Ecol 83:713–726. doi: 10.2307/2261638

Norton KP, von Blanckenburg F, DiBiase R, et al (2011) Cosmogenic 10Be-derived denudation rates of the Eastern and Southern European Alps. Int J Earth Sci 100:1163–1179. doi: 10.1007/s00531-010-0626-y

O'Neil JR (1986) Theoretical and experimental aspects of isotopic fractionation. Rev Mineral 16:1–40

Oeser M, Weyer S, Horn I, Schuth S (2014) High-precision fe and mg isotope ratios of silicate reference glasses determined in situ by femtosecond LA-MC-ICP-MS and by solution nebulisation MC-ICP-MS. Geostand Geoanalytical Res 38:311–328. doi: 10.1111/j.1751-908X.2014.00288.x

Oeser RA, Stroncik N, Moskwa L, et al (2018) Catena Chemistry and microbiology of the Critical Zone along a steep climate and vegetation gradient in the Chilean Coastal Cordillera. Catena 170:183–203. doi: 10.1016/j.catena.2018.06.002

Opfergelt S, Burton KW, Georg RB, et al (2014) Magnesium retention on the soil exchange complex controlling Mg isotope variations in soils, soil solutions and vegetation in volcanic soils, Iceland. Geochim Cosmochim Acta 125:110–130. doi: 10.1016/j.gca.2013.09.036

Opfergelt S, Georg RB, Delvaux B, et al (2012) Mechanisms of magnesium isotope fractionation in volcanic soil weathering sequences, Guadeloupe. Earth Planet Sci Lett 341–344:176–185. doi: 10.1016/j.chemgeo.2012.07.032

Pagani M, Caldeira K, Berner R, Beerling DJ (2009) The role of terrestrial plants in limiting atmospheric CO2decline over the past 24 million years. Nature 460:85–88. doi: 10.1038/nature08133

Pavich MJ, Brown L, Harden J, et al (1986) 10Be distribution in soils from Merced River terraces, California. Geochim Cosmochim Acta 50:1727–1735. doi: 10.1016/0016-7037(86)90134-1

Pavich MJ, Vidic N (1993) Application of paleomagnetic and 10Be Analyses to Chronostratigraphy of Alpine Glacio-Fluvial Terraces, Sava River Valley, Slovenia. Wiley Online Library

Pearson JA, Knoght DH, Fahey TJ (1987) Biomass and nutrient accumulation during stand development in Wyoming lodgepole pine forests. Ecology 68:1673–1966

Pett-Ridge JC, Derry LA, Barrows JK (2009a) Ca/Sr and 87Sr/86Sr ratios as tracers of Ca and Sr cycling in the Rio Icacos watershed, Luquillo Mountains, Puerto Rico. Chem Geol 267:32–45. doi: 10.1016/j.chemgeo.2008.11.022

Pett-Ridge JC, Derry LA, Kurtz AC (2009b) Sr isotopes as a tracer of weathering processes and dust inputs in a tropical granitoid watershed, Luquillo Mountains, Puerto Rico. Geochim Cosmochim

Acta 73:25–43. doi: 10.1016/j.gca.2008.09.032

Phillips FM, Argento DC, Balco G, et al (2016) The CRONUS-Earth Project: A synthesis. Quat Geochronol 31:119–154. doi: 10.1016/j.quageo.2015.09.006

Pickering WF (1986) Metal ion speciation - soils and sediments (a review). Ore Geol Rev 1:83–146. doi: 10.1016/0169-1368(86)90006-5

Pierson-Wickmann AC, Aquilina L, Weyer C, et al (2009) Acidification processes and soil leaching influenced by agricultural practices revealed by strontium isotopic ratios. Geochim Cosmochim Acta 73:4688–4704. doi: 10.1016/j.gca.2009.05.051

Pogge von Strandmann PAE, Elliott T, Marschall HR, et al (2011) Variations of Li and Mg isotope ratios in bulk chondrites and mantle xenoliths. Geochim Cosmochim Acta 75:5247–5268. doi: 10.1016/j.gca.2011.06.026

Pogge von Strandmann PAE, Opfergelt S, Lai YJ, et al (2012) Lithium, magnesium and silicon isotope behaviour accompanying weathering in a basaltic soil and pore water profile in Iceland. Earth Planet Sci Lett 339–340:11–23. doi: 10.1016/j.epsl.2012.05.035

Pokharel R, Gerrits R, Schuessler JA, et al (2017) Mg Isotope Fractionation during Uptake by a Rock-Inhabiting, Model Microcolonial Fungus Knufia petricola at Acidic and Neutral pH. Environ Sci Technol 51:9691–9699. doi: 10.1021/acs.est.7b01798

Porder S, Vitousek PM, Chadwick OA, et al (2007) Uplift, erosion, and phosphorus limitation in terrestrial ecosystems. Ecosystems 10:158–170. doi: 10.1007/s10021-006-9011-x

Portenga EW, Bierman PR (2011) Understanding earth's eroding surface with 10Be. GSA Today 21:4–10. doi: 10.1130/G111A.1

Poszwa A, Dambrine E, Pollier B, Atteia O (2000) A comparison between Ca and Sr cycling in forest ecosystems. Plant Soil 225:299–310. doi: 10.1023/A:1026570812307

Poszwa A, Ferry B, Dambrine E, et al (2004) Variations of bioavailable Sr concentration and 87Sr/86Sr ratio in boreal forest ecosystems. Biogeochemistry 67:1–20

Ra K, Kitagawa H (2007) Magnesium isotope analysis of different chlorophyll forms in marine phytoplankton using multi-collector ICP-MS. J Anal At Spectrom 22:817. doi: 10.1039/b701213f

Ra K, Kitagawa H, Shiraiwa Y (2010) Mg isotopes in chlorophyll-a and coccoliths of cultured coccolithophores (Emiliania huxleyi) by MC-ICP-MS. Mar Chem 122:130–137. doi: 10.1016/j.marchem.2010.07.004

Raisbeck GM, Yiou F, Finneau M, et al (1981) Cosmogenic 10Be/7Be as a probe of atmospheric transport processes. Geophys Res Abstr EGU Gen Assem 8:1015–1018

Rauret G, López-Sánchez JF, Sahuquillo A, et al (1999) Improvement of the BCR three step sequential extraction procedure prior to the certification of new sediment and soil reference materials. J Environ Monit 1:57–61. doi: 10.1039/a807854h

Reynolds AC, Quade J, Betancourt JL (2012) Strontium isotopes and nutrient sourcing in a semi-arid woodland. Geoderma 189–190:574–584. doi: 10.1016/j.geoderma.2012.06.029

Riebe CS, Granger DE (2013) Quantifying effects of deep and near-surface chemical erosion on cosmogenic nuclides in soils, saprolite, and sediment. Earth Surf Process Landforms 38:523–533. doi: 10.1002/esp.3339

Riebe CS, Hahm WJ, Brantley SL (2017) Controls on deep critical zone architecture: a historical review and four testable hypotheses. Earth Surf Process Landforms 42:128–156. doi: 10.1002/esp.4052

Riebe CS, Kirchner JW, Finkel RC (2004) Erosional and climatic effects on long-term chemical weathering rates in granitic landscapes spanning diverse climate regimes. Earth Planet Sci Lett 224:547–562. doi: 10.1016/j.epsl.2004.05.019

Riebe CS, Kirchner JW, Finkel RC (2003) Long-term rates of chemical weathering and physical erosion from cosmogenic nuclides and geochemical mass balance. Geochim Cosmochim Acta 67:4411–4427. doi: 10.1016/S0016-7037(03)00382-X

Riebe CS, Kirchner JW, Granger DE, Finkel RC (2000) Erosional equilibrium and disequilibrium in the Sierra Nevada, inferred from cosmogenic 26Al and 10Be in alluvial sediment. Geology 28:803–806. doi: 10.1130/0091-7613(2000)28<803:EEADIT>2.0.CO;2

Riotte J, Maréchal JC, Audry S, et al (2014) Vegetation impact on stream chemical fluxes: Mule Hole watershed (South India). Geochim Cosmochim Acta 145:116–138. doi: 10.1016/j.gca.2014.09.015

Röderstein M, Hertel D, Leuschner C (2005) Above- and below-ground litter production in three tropical montane forests in southern Ecuador. J Trop Ecol 21:483–492. doi: 10.1017/S026646740500249X

Roering JJ, Marshall J, Booth AM, et al (2010) Evidence for biotic controls on topography and soil production. Earth Planet Sci Lett 298:183–190. doi: 10.1016/j.epsl.2010.07.040

Ryu JS, Jacobson AD, Holmden C, et al (2011) The major ion, δ44/40Ca, δ44/42Ca, and δ26/24Mg geochemistry of granite weathering at pH=1 and T=25°C: Power-law processes and the relative reactivity of minerals. Geochim Cosmochim Acta 75:6004–6026. doi: 10.1016/j.gca.2011.07.025

Ryu JS, Vigier N, Decarreau A, et al (2016) Experimental investigation of Mg isotope fractionation during mineral dissolution and clay formation. Chem Geol 445:135–145. doi: 10.1016/j.chemgeo.2016.02.006

Scatena FN, Lugo AE (1995) Geomorphology, disturbance, and the soil and vegetation of two subtropical wet steepland watersheds of Puerto Rico. Geomorphology 13:199–213. doi: 10.1016/0169-555X(95)00021-V

Schaller M, Von Blanckenburg F, Hovius N, Kubik PW (2001) Large-scale erosion rates from in situ-produced cosmogenic nuclides in European river sediments. Earth Planet Sci Lett 188:441–458. doi: 10.1016/S0012-821X(01)00320-X

Schauble E (2004) Applying stable isotope fractionation theory to new systems. In: Reviews in Mineralogy and Geochemistry. Mineralogical Society of America, Blacksburg, p 65

Scheuvens D, Schütz L, Kandler K, et al (2013) Bulk composition of northern African dust and its source sediments - A compilation. Earth-Science Rev 116:170–194. doi: 10.1016/j.earscirev.2012.08.005

Schmid I, Kazda M (2002) Root distribution of Norway spruce in monospecific and mixed stands on different soils. For Ecol Manage 159:37–47. doi: 10.1016/S0378-1127(01)00708-3

Schmitt AD, Gangloff S, Labolle F, et al (2017) Calcium biogeochemical cycle at the beech tree-soil solution interface from the Strengbach CZO (NE France): insights from stable Ca and radiogenic Sr isotopes. Geochim Cosmochim Acta 213:91–109. doi: 10.1016/j.gca.2017.06.039

Schmitt AD, Vigier N, Lemarchand D, et al (2012) Processes controlling the stable isotope

compositions of Li, B, Mg and Ca in plants, soils and waters: A review. Comptes Rendus - Geosci. 344:704–722

Schuessler JA, Kämpf H, Koch U, Alawi M (2016) Earthquake impact on iron isotope signatures recorded in mineral spring water Suppl. J Geophys Res Solid Earth 121:8548–8568. doi: 10.1002/2016JB013408

Schuessler JA, Von Blanckenburg F (2014) Testing the limits of micro-scale analyses of Si stable isotopes by femtosecond laser ablation multicollector inductively coupled plasma mass spectrometry with application to rock weathering. Spectrochim Acta - Part B At Spectrosc 98:1–18. doi: 10.1016/j.sab.2014.05.002

Shand P, Darbyshire DPF, Gooddy D, H. Haria A (2007) 87Sr/86Sr as an indicator of flowpaths and weathering rates in the Plynlimon experimental catchments, Wales, U.K. Chem Geol 236:247–265. doi: 10.1016/j.chemgeo.2006.09.012

Shen C, Beer J, Kubik PW, et al (2004) Grain size distribution,10Be content and magnetic susceptibility of micrometer-nanometer loess materials. Nucl Instruments Methods Phys Res B 223–224:613–617. doi: 10.1016/j.nimb.2004.04.113

Shuman LM (1985) Fraction method for soil micro element. Soil Sci 140:11–22

Sierra CA, Müller M, Metzler H, et al (2017) The muddle of ages, turnover, transit, and residence times in the carbon cycle. Glob Chang Biol 23:1763–1773. doi: 10.1111/gcb.13556

Skrivan P, Navraitil T, Burian M (2000) Ten years of monitoring the atmospheric inputs at the Cernokostelecko regions, Central Bohemia. Sci Agric Bohem 31:139–154

Smits MM, Bonneville S, Benning LG, et al (2012) Plant-driven weathering of apatite - the role of an ectomycorrhizal fungus. Geobiology 10:445–456. doi: 10.1111/j.1472-4669.2012.00331.x

Sommer M, Jochheim H, Höhn A, et al (2013) Si cycling in a forest biogeosystem-the importance of transient state biogenic Si pools. Biogeosciences 10:4991–5007. doi: 10.5194/bg-10-4991-2013

Spohn M, Sierra CA (2018) How long do elements cycle in terrestrial ecosystems? Biogeochemistry 1–15. doi: 10.1007/s10533-018-0452-z

Stallard RF, Edmond JM (1983) Geochemistry of the Amazon: 2. The influence of geology and weathering environment on the dissolved load. J Geophys Res 88:9671–9688. doi: 10.1029/JC088iC14p09671; doi:10.1029/JC088iC14p09671

Steiger RH, Jager E (1977) Convention on the use of decay constants in geo- and cosmochronology. Earth Planet Sctence Lett 36:1977

Stewart BW, Capo RC, Chadwick OA (1998) Quantitative strontium isotope models for weathering, pedogenesis and biogeochemical cycling. Geoderma 82:173–195. doi: 10.1016/S0016-7061(97)00101-8

Stone EL, Kalisz PJ (1991) On the maximum extent of tree roots. For Ecol Manage 46:59–102. doi: 10.1016/0378-1127(91)90245-Q

Stone JO (2000) Air pressure and cosmogenic isotope production. J Geophys Res Solid Earth 105:23753–23759. doi: 10.1029/2000JB900181

Swift MJ, Heal OW, Anderson JM (1979) Decomposition in terrestrial ecosystems. Univ of California Press

Takahashi Y, Minai Y, Ambe S, et al (1999) Comparison of adsorption behavior of multiple inorganic ions on kaolinite and silica in the presence of humic acid using the multitracer technique. Geochim Cosmochim Acta 63:815–836. doi: 10.1016/S0016-7037(99)00065-4

Tanner EVJ, Vitousek PM, Cuevas E, Cuevas E (1998) Experimental Investigation of Nutrient Limitation of Forest Growth on Wet Tropical Mountains. Ecology 79:10–22

Taylor S., McLennan S. (1995) The geochemical evolution of the continental crust. Rev Geophys 33:241–265. doi: 10.1029/95RG00262

Teng F-Z (2017) Magnesium Isotope Geochemistry. Rev Mineral Geochemistry 82:219–287. doi: 10.2138/rmg.2017.82.7

Teng FZ, Li WY, Rudnick RL, Gardner LR (2010) Contrasting lithium and magnesium isotope fractionation during continental weathering. Earth Planet Sci Lett 300:63–71. doi: 10.1016/j.epsl.2010.09.036

Tessier A, Campbell PGC, Bisson M (1979) Sequential Extraction Procedure for the Speciation of Particulate Trace Metals. Anal Chem 51:844–851. doi: 10.1021/ac50043a017

Tiessen H (1995) Phosphorus in the global environment: transfers, cycles and management. Chichester (UK) John Wiley & Sons, pp 1–6

Tiessen H, Moir JO (1993) Characterization of available P by sequential extraction. Soil Sampl methods Anal 7:5–229

Tipper ET, Calmels D, Gaillardet J, et al (2012a) Positive correlation between Li and Mg isotope ratios in the river waters of the Mackenzie Basin challenges the interpretation of apparent isotopic fractionation during weathering. Earth Planet Sci Lett 333–334:35–45. doi: 10.1016/j.epsl.2012.04.023

Tipper ET, Gaillardet J, Louvat P, et al (2010) Mg isotope constraints on soil pore-fluid chemistry: Evidence from Santa Cruz, California. Geochim Cosmochim Acta 74:3883–3896. doi: 10.1016/j.gca.2010.04.021

Tipper ET, Galy A, Bickle MJ (2006a) Riverine evidence for a fractionated reservoir of Ca and Mg on the continents: Implications for the oceanic Ca cycle. Earth Planet Sci Lett 247:267–279. doi: 10.1016/j.epsl.2006.04.033

Tipper ET, Galy A, Bickle MJ (2008) Calcium and magnesium isotope systematics in rivers draining the Himalaya-Tibetan-Plateau region: Lithological or fractionation control? Geochim Cosmochim Acta 72:1057–1075. doi: 10.1016/j.gca.2007.11.029

Tipper ET, Galy A, Gaillardet J, et al (2006b) The magnesium isotope budget of the modern ocean: Constraints from riverine magnesium isotope ratios. Earth Planet Sci Lett 250:241–253. doi: 10.1016/j.epsl.2006.07.037

Tipper ET, Lemarchand E, Hindshaw RS, et al (2012b) Seasonal sensitivity of weathering processes: Hints from magnesium isotopes in a glacial stream. Chem Geol 312–313:80–92. doi: 10.1016/j.chemgeo.2012.04.002

Tipping E, Benham S, Boyle JF, et al (2014) Atmospheric deposition of phosphorus to land and freshwater. Environ Sci Process Impacts 16:1608–1617. doi: 10.1039/c3em00641g

Tripler CE, Kaushal SS, Likens GE, Todd Walter M (2006) Patterns in potassium dynamics in forest ecosystems. Ecol Lett 9:451–466. doi: 10.1111/j.1461-0248.2006.00891.x

Turner BL, Lambers H, Condron LM, et al (2013) Soil microbial biomass and the fate of phosphorus during long-term ecosystem development. Plant Soil 367:225–234. doi: 10.1007/s11104-012-1493-z

Uhlig D, Schuessler JA, Bouchez J, et al (2017) Quantifying nutrient uptake as driver of rock weathering in forest ecosystems by magnesium stable isotopes. Biogeosciences 14:3111–3128. doi: 10.5194/bg-14-3111-2017

van der Hammen T, Absy ML (1994) Amazonia during the last glacial. Palaeogeogr Palaeoclimatol Palaeoecol 109:247–261

Vance CP, Uhde-Stone C, Allan DL (2003) Phosphorus acquisition and use: Critical adaptations by plants for securing a nonrenewable resource. New Phytol 157:423–447. doi: 10.1046/j.1469-8137.2003.00695.x

Vesely J, Norton SA, Skrivan P, et al (2002) Environmental Chemistry of Beryllium. Rev Mineral Geochemistry 50:291–317. doi: 10.2138/rmg.2002.50.7

Vitousek P, Chadwick O, Matson P, et al (2003) Erosion and the Rejuvenation of Weathering-derived Nutrient Supply in an Old Tropical Landscape. Ecosystems 6:762–772. doi: 10.1007/s10021-003-0199-8

Vitousek PM, Farrington H (1997) Nutrient limitation and soil development: Experimental test of a biogeochemical theory. Biogeochemistry 37:63–75. doi: 10.1023/A:1005757218475

Vitousek PM, Porder S, Houlton BZ, Chadwick OA (2010) Terrestrial phosphorus limitation: mechanisms, implications, and nitrogen-phosphorsu interactions. Ecol Appl 20:5–15. doi: 10.1890/08-0127.1

von Blanckenburg F (2017) Isotope : Uhren und Fingerabdrücke für das System Erde. Syst Erde, GFZ J 7:6–11. doi: 10.2312/GFZ.syserde.07.01.1

von Blanckenburg F (2005) The control mechanisms of erosion and weathering at basin scale from cosmogenic nuclides in river sediment. Earth Planet Sci Lett 237:462–479. doi: 10.1016/j.epsl.2005.06.030

von Blanckenburg F, Belshaw NS, O'Nions RK (1996) Separation of 9Be and cosmogenic 10Be from environmental materials and SIMS isotope dilution analysis. Chem Geol 129:93–99. doi: 10.1016/0009-2541(95)00157-3

von Blanckenburg F, Bouchez J, Wittmann H (2012) Earth surface erosion and weathering from the 10Be (meteoric)/ 9Be ratio. Earth Planet Sci Lett 351–352:295–305. doi: 10.1016/j.epsl.2012.07.022

von Blanckenburg F, Hewawasam T, Kubik PW (2004) Cosmogenic nuclide evidence for low weathering and denudation in the wet, tropical highlands of Sri Lanka. J Geophys Res 109:1–22. doi: 10.1029/2003JF000049

von Blanckenburg F, Willenbring JK (2014) Cosmogenic nuclides: Dates and rates of earth-surface change. Elements 10:341–346. doi: 10.2113/gselements.10.5.341

von Blanckenburg F, Wittmann H, Schuessler JA (2016) HELGES: Helmholtz Laboratory for the Geochemistry of the Earth Surface. J large-scale Res Facil 2:1–5. doi: 10.17815/jlsrf-2-141

Walker TW, Syers JK (1976) The fate of phosphorus during pedogenesis. Geoderma 15:1–19. doi: 10.1016/0016-7061(76)90066-5

Wallbrink PJ, Murray AS (1996) Distribution and variability of 7Be in soils under different surface cover conditions and its potential for describing soil redistribution processes. Water Resour Res 32:467–476. doi: 10.1029/95WR02973

Wardle DA, Bardgett RD, Klironomos JN, et al (2004a) Ecological Linkages Between Aboveground and Belowground Biota. Science (80-) 304:1629–1633. doi: 10.1126/science.1094875

Wardle DA, Walker LR, Bardgett RD (2004b) Ecosystem properties and forest decline in constrasting long-term chronosequences. Science (80-) 305:509–513

Webster JR, Golladay SW, Benfield EF, et al (1990) Effects of forest disturbance on particulate organic matter budgets of small streams. JN Am Benthol Soc 9:120–140

West AJ, Galy A, Bickle M (2005) Tectonic and climatic controls on silicate weathering. Earth Planet Sci Lett 235:211–228. doi: 10.1016/j.epsl.2005.03.020

West N, Kirby E, Bierman P, et al (2013) Regolith production and transport at the Susquehanna Shale Hills Critical Zone Observatory, part 2: Insights from meteoric ^{10}Be. J Geophys Res Earth Surf 118:1877–1896. doi: 10.1002/jgrf.20121

Whipkey CE, Capo RC, Chadwick OA, Stewart BW (2000) The importance of sea spray to the cation budget of a coastal Hawaiian soil: A strontium isotope approach. Chem Geol 168:37–48. doi: 10.1016/S0009-2541(00)00187-X

Wiederhold JG, Teutsch N, Kraemer SM, et al (2007) Iron isotope fractionation in oxic soils by mineral weathering and podzolization. Geochim Cosmochim Acta 71:5821–5833. doi: 10.1016/j.gca.2007.07.023

Wilcke W, Velescu A, Leimer S, et al (2017) Biological versus geochemical control and environmental change drivers of the base metal budgets of a tropical montane forest in Ecuador during 15 years. Biogeochemistry 136:167–189. doi: 10.1007/s10533-017-0386-x

Wilcke W, Yasin S, Abramowski U, et al (2002) Nutrient storage and turnover in organic layers under tropical montane rain forest in Ecuador. Eur J Soil Sci 53:15–27

Willenbring JK, von Blanckenburg F (2010) Meteoric cosmogenic Beryllium-10 adsorbed to river sediment and soil: Applications for Earth-surface dynamics. Earth-Science Rev 98:105–122. doi: 10.1016/j.earscirev.2009.10.008

Wimpenny J, Colla CA, Yin QZ, et al (2014) Investigating the behaviour of Mg isotopes during the formation of clay minerals. Geochim Cosmochim Acta 128:178–194. doi: 10.1016/j.gca.2013.12.012

Wimpenny J, Gíslason SR, James RH, et al (2010) The behaviour of Li and Mg isotopes during primary phase dissolution and secondary mineral formation in basalt. Geochim Cosmochim Acta 74:5259–5279. doi: 10.1016/j.gca.2010.06.028

Wittmann H, Von Blanckenburg F, Bouchez J, et al (2012) The dependence of meteoric 10Be concentrations on particle size in Amazon River bed sediment and the extraction of reactive 10Be/ 9Be ratios. Chem Geol 318–319:126–138. doi: 10.1016/j.chemgeo.2012.04.031

Wittmann H, Von Blanckenburg F, Dannhaus N, et al (2015) A test of the cosmogenic 10Be(meteoric)/9Be proxy for simultaneously determining basin-wide erosion rates, denudation rates, and the degree of weathering in the Amazon basin. J Geophys Res F Earth Surf 120:2498–2526. doi: 10.1002/2015JF003581

Ziegler K, Chadwick OA, Brzezinski MA, Kelly EF (2005) Natural variations of δ30Si ratios during

progressive basalt weathering, Hawaiian Islands. Geochim Cosmochim Acta 69:4597–4610. doi: 10.1016/j.gca.2005.05.008